CAUSES AND METHODS OF REDUCING DILUTION AT SEABEE GOLD MINE

A Thesis Submitted to the College of

Graduate and Postdoctoral Studies

In Partial Fulfillment of the Requirements

For the Degree of Master of Science

In the Department of Civil, Geological and Environmental Engineering

University of Saskatchewan

Saskatoon

By

NATHAN PAUL SCHARTNER

PERMISSION TO USE

In presenting this thesis in partial fulfillment of the requirements for a Postgraduate degree from the University of Saskatchewan, I agree that the Libraries of this University may make it freely available for inspection. I further agree that permission for copying of this thesis in any manner, in whole or in part, for scholarly purposes may be granted by the professor or professors who supervised my thesis work or, in their absence, by the Head of the Department or the Dean of the College in which my thesis work was done. It is understood that any copying or publication or use of this thesis or parts thereof for financial gain shall not be allowed without my written permission. It is also understood that due recognition shall be given to me and to the University of Saskatchewan in any scholarly use which may be made of any material in my thesis.

Requests for permission to copy or to make other uses of materials in this thesis/dissertation in whole or part should be addressed to:

Head of the Department of Civil, Geological and Environmental Engineering
University of Saskatchewan
3B48 Engineering Building, 57 Campus Drive
Saskatoon, Saskatchewan S7N 5A9
Canada

OR

Dean
College of Graduate and Postdoctoral Studies
University of Saskatchewan
116 Thorvaldson Building, 110 Science Place
Saskatoon, Saskatchewan S7N 5C9
Canada

ABSTRACT

The failure of waste rock from the hangingwall and footwall of open panels dilutes ore grades, creates significant costs for underground mines and can reduce production rates. This research investigates the mechanisms causing dilution from the hangingwall and footwall of panels at SSR Mining's Seabee Gold Mine, located in northern Saskatchewan.

To conduct this research, estimations were made regarding the rock mass conditions and stress in panels so conventional analysis techniques for dilution could be applied. Underground field mapping and lab testing were conducted, and a new methodology was developed to assess large scale joint irregularities. Three joint sets were identified with Q' ranging from 10.6 to 14.1 for the panel hangingwall. An instrumentation program was conducted with both closure stations and an extensometer. New data interpretation techniques were applied which suggested stresses normal to the ore body reached a stress of approximately 92 MPa, prior to panel mining.

Conventional empirical dilution estimation analyses indicated that less than 0.5 metres of dilution should be expected from both the hanging wall and the footwall of all panels assessed at the Seabee Mine. Cavity Monitoring Survey (CMS) data was collected and interpreted and many dilution values were measured to be well in excess of 0.5 metres.

It is known that open panel dilution can be caused by many mechanisms. These mechanisms, or causes of dilution, include:

- rock mass instability due to panel dimensions exceeding stable limits which would be represented by an arch shaped failure;
- panel top sill and bottom sill drifts extending past the ore – waste contact; and,
- blast hole deviation causing the hangingwall and footwall rocks to be blasted.

Each of these mechanisms have characteristic failure or dilution profiles. The approach to this research has been to link the detailed geometry of the hangingwall and footwall surfaces from which dilution has occurred, to the expected failure geometry from the common causes of panel dilution.

This research shows that of the three failure mechanisms listed above, the dominant failure mechanism is based on geometrical instability represented by an arch shaped failure. The failure mechanisms of panel undercutting due to sill drifts extending past the ore – waste contact and blast hole deviation were not found to be significant. Efforts to minimize panel dilution are recommended based on their cause, and these efforts cannot be effective without an understanding of the mechanisms influencing dilution. The methodology developed in this thesis is applicable to all underground hard rock mining operations.

ACKNOWLEDGMENTS

I would like to give my most sincere thank you to Dr. Doug Milne, who exemplified patience while I was writing this thesis.

Thank you to the technical staff and operations team at the Seabee Gold Operation for making this possible. They helped guide me and keep me safe underground when I had no clue what I was doing, or looking for, when I first appeared at the mine. Also, they would oblige me whenever I would ask a really basic question.

TABLE OF CONTENTS

LIST OF FIGURES

LIST OF TABLES

NOTATION

CMS = Cavity Monitoring Survey

MPBX = Multi – point Borehole Extensometer

RQD = Rock Quality Designation

RMR = Rock Mass Rating

Q = Tunnel Quality Index

Jn = Joint Set Number

J_r = Joint Set Roughness

J_a = Joint Set Alteration

J_w = Joint Set Water Reduction

SRF = Stress Reduction Factor

N' = Stability Number

Q' = Modified Tunnel Quality Index with SRF set to 1

A = Factor related to the stress condition

B = Factor related to the primary joint orientation

C = Factor related to the dip of the analysed surface

HR = Hydraulic Radius

As = Surface Area

Ps = Surface Perimeter

UCS = Uniaxial Compressive Strength

$I_{s(50)}$ = Point Load Index corrected to a standard equivalent diameter of 50mm

P = Failure Load

De = Equivalent Core Diameter

K = $I_{s(50)}$ to UCS conversion factor

CHAPTER 1

INTRODUCTION

The failure of waste rock from the hangingwall and footwall of open panels dilutes ore grades, creates significant costs for underground mines, and can reduce production rates. This research investigates the mechanisms causing dilution from the hangingwall and footwall of panels at SSR Mining's Seabee Gold Mine, located in northern Saskatchewan (Figure 1.1). Efforts to minimize panel dilution are recommended based on their cause, and these efforts cannot be effective without an understanding of the mechanisms influencing dilution. The methodology developed in this thesis is applicable to all underground hard rock mining operations. This chapter provides the background to the Seabee Gold Mine, defines dilution, identifies the research objectives and scope of the research, and provides an overview of the thesis document.

1.1 Background

1.1.1 Mine Background and Geology

Seabee Gold Mine is in a narrow vein deposit located at Laonil Lake, Saskatchewan, Canada, approximately 125km northeast of La Ronge. The mine has been in operation since 1991 and is currently owned and operated by SSR Mining Inc. The mine is located in the Glennie Lake Domain of the Canadian Shield. It is a part of the Laonil Lake Instrusive Complex which is a triangular gabbroic intrusive body. The host rock of the area is a medium to fine grained gabbro/granodiorite. The vein structures in the mine are quartz – tourmaline shear structures that have a mineralogical composition of quartz, pyrite, pyrrhotite and chalcopyrite. The gold inclusions occur as flakes and films and are found as replaced pyrite and at the sulphide boundaries (Figure 1.2). The vein structures have a dip of 80 to 90° degrees, to both the east and west, and are 2 to 6m in width (Claude Resources Inc., 2014).

The Seabee Gold Mine is an underground mine with ramp access for personnel transportation, and shaft access for material transport. Current production is approximately 300 tonnes/day at a maximum mining depth of 1400m. Due to the narrow nature of the orebody, mining is longitudinal with development drifts driven in the orebody. Figure 1.3 shows a long section of the entire mine. Noted on this is the location of the panels studied in this thesis, as discussed in Section 1.1.2.

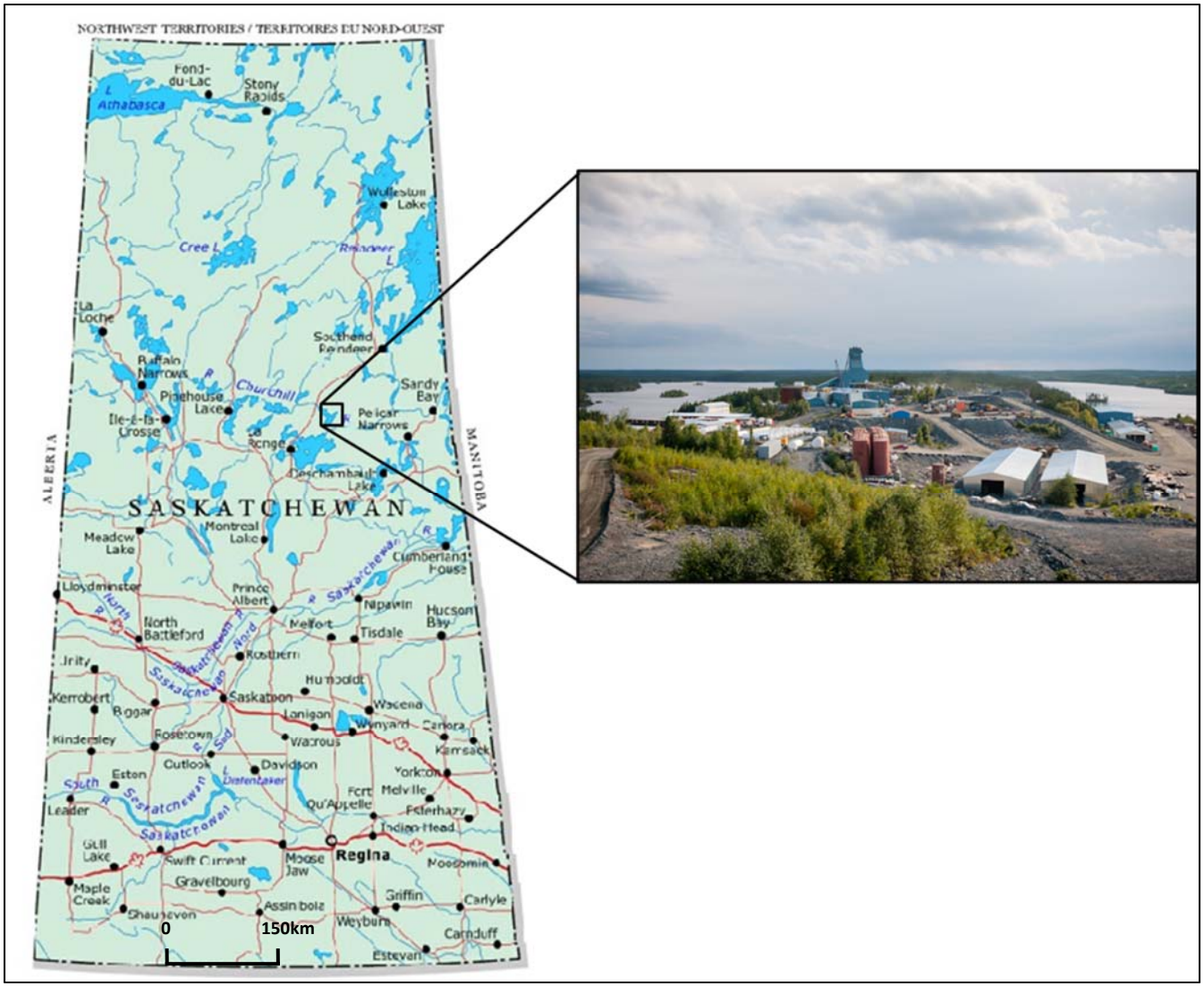

Figure 1.1 Location of Seabee Gold Mine in Saskatchewan (SSR Mining, 2018).

Figure 1.2 Association of gold with sulphide boundaries (no visible gold).

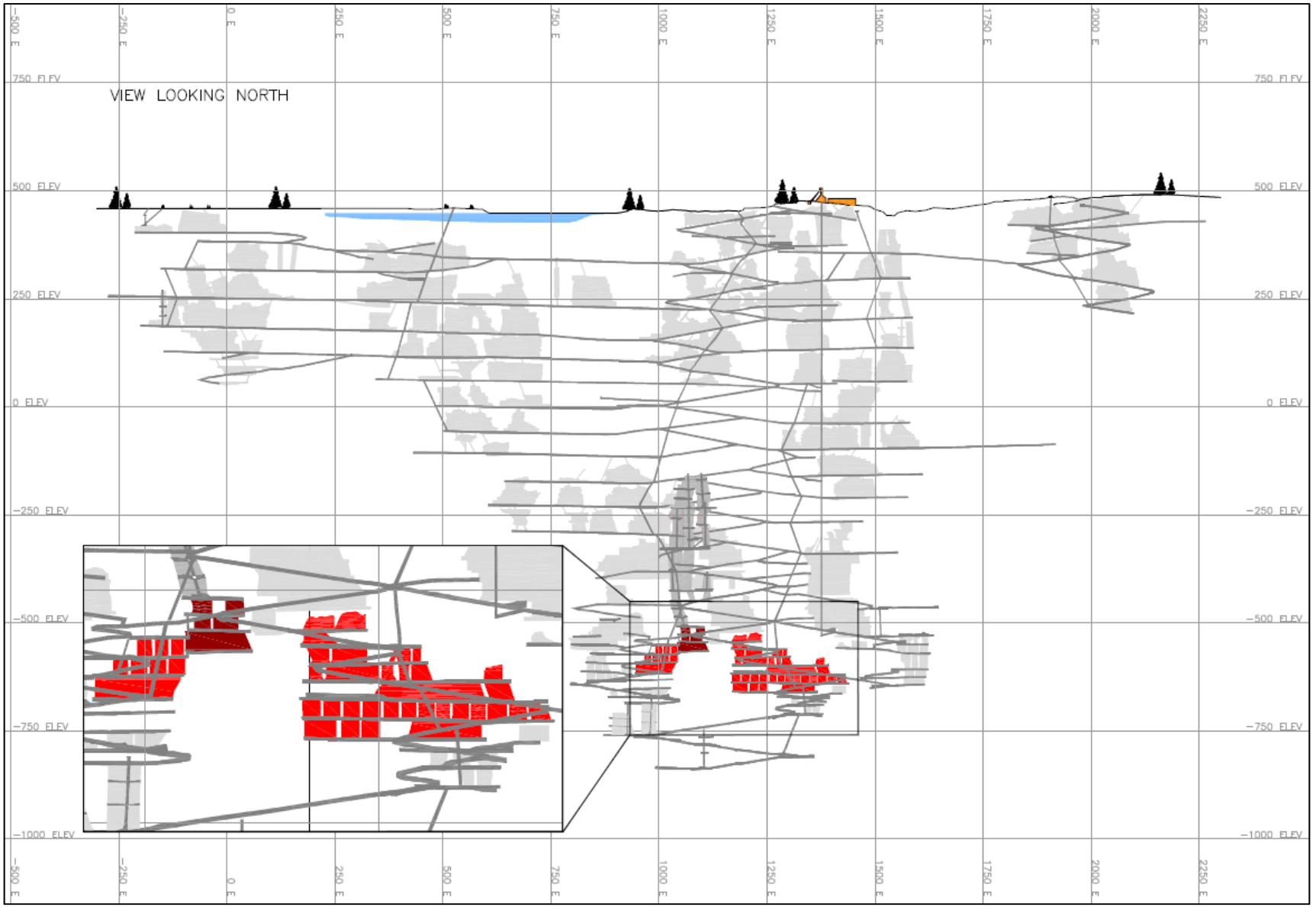

Figure 1.3 Long section of Seabee Gold Mine with panel study area of thesis highlighted in red (SSR Mining Inc., 2018).

1.1.2 Mining Methods

Three primary mining methods have been used at Seabee Gold Mine; as follows:

- shrinkage stoping;
- sublevel open stoping; and,
- modified Avoca.

Shrinkage stoping (Figure 1.4) is a selective hard rock mining method that was used primarily from surface to a depth of 500m. A shrinkage panel is started by driving a haulage drift parallel to the bottom of the panel. Cross–cut drawpoints are driven perpendicular to the haulage drift in intervals that allow for a uniform drawdown of the ore. Mining of the panel begins at the bottom and consists of horizontal lifts that advance towards the top. Ore remains in the panel as this provides a working platform to mine the next lift. When rock is blasted, it increases its volume through swelling by approximately 30 to 40%. This extra volume of rock must be uniformly drawn out of the panel to maintain a constant height from the back to the top of the ore. Shrinkage stoping is a labour intensive mining method that is not easily mechanised. However, using shrinkage stoping reduces dilution and increases ore recovery because operators locate the vertical lifts such that the desired grade of ore is extracted.

Sublevel open stoping is a bulk mining method that is used in all the case study areas. It is the primary mining method below the 500m level. At Seabee Gold Mine, a sublevel open panel is mined longitudinally due to the narrow ore body. It is started by driving an undercut and overcut in the orebody, along the strike length, with a vertical interval of 18m between the floor of the undercut and the back of the overcut. Drilling and blasting is typically performed from the overcut and mucking is performed from the undercut. A vertical slot raise is developed at the beginning of the panel, and production blasts continue until the maximum stable span is opened and a rib pillar of a strike length equal to the ore width is left. The ore is mucked from the undercut after each blast. Once all blasts are complete, the open panel is backfilled with cemented or uncemented rockfill.

Avoca mining is a variant of sublevel open stoping (Figure 1.5). The development is the same for both methods; however, Avoca mining requires access from both sides of the panel on the overcut, one for backfilling and one for drilling and blasting. The difference between sublevel

stoping and Avoca is that the maximum strike length of the open panel is maintained by continuously backfilling at the same rate as the blasting. Therefore, no support pillars are required, which increases recovery.

1.1.3 Case Study Areas

Four case study areas were analysed in this research. They were selected based on the mining schedule, available access, and the quality of data. These areas are: 2b11013, 2b11011, 2c10010 and L62. Figure 1.6 shows the location of the case study areas relative to each other whereas Figure 1.3 shows these panels in relation to the entire orebody.

The first three areas were chosen because cavity monitoring surveys (CMS's) were performed on a large portion of these panels and the area contains at least 3 sublevels. L62 was chosen because of its accessibility for the instrumentation program. The following are general descriptions of each area:

- Case study area 2b11013 is 1100m below surface, 273m on strike and 86m in height. It consists of 4 sublevels and a total of 27 panels. The mining methods used in this area are sublevel open stoping and modified Avoca. Mining commenced in 2010 and was completed in 2013.
- Case study area 2b11011 is 1000m below surface, 72m on strike and 73m in height. It consists of 3 sublevels and 5 panels. The mining methods used in this area are longhole open stoping and Avoca. Mining commenced in 2010 and was completed in 2011.
- Case study area 2c10010 is 1035m below surface, 100m on strike and 71m in height. It consists of 3 sublevels and 12 panels. The mining method used is sublevel open stoping. Mining began at 2c10010 in 2010 and was finished in 2012.
- Case study area L62 is 1000m below surface and 62m on strike. The data collected is from 3 sublevels that each contains 5 panels. The mining methods used are sublevel open stoping and Avoca. Mining began at L62 in 2012 and was completed in 2016.

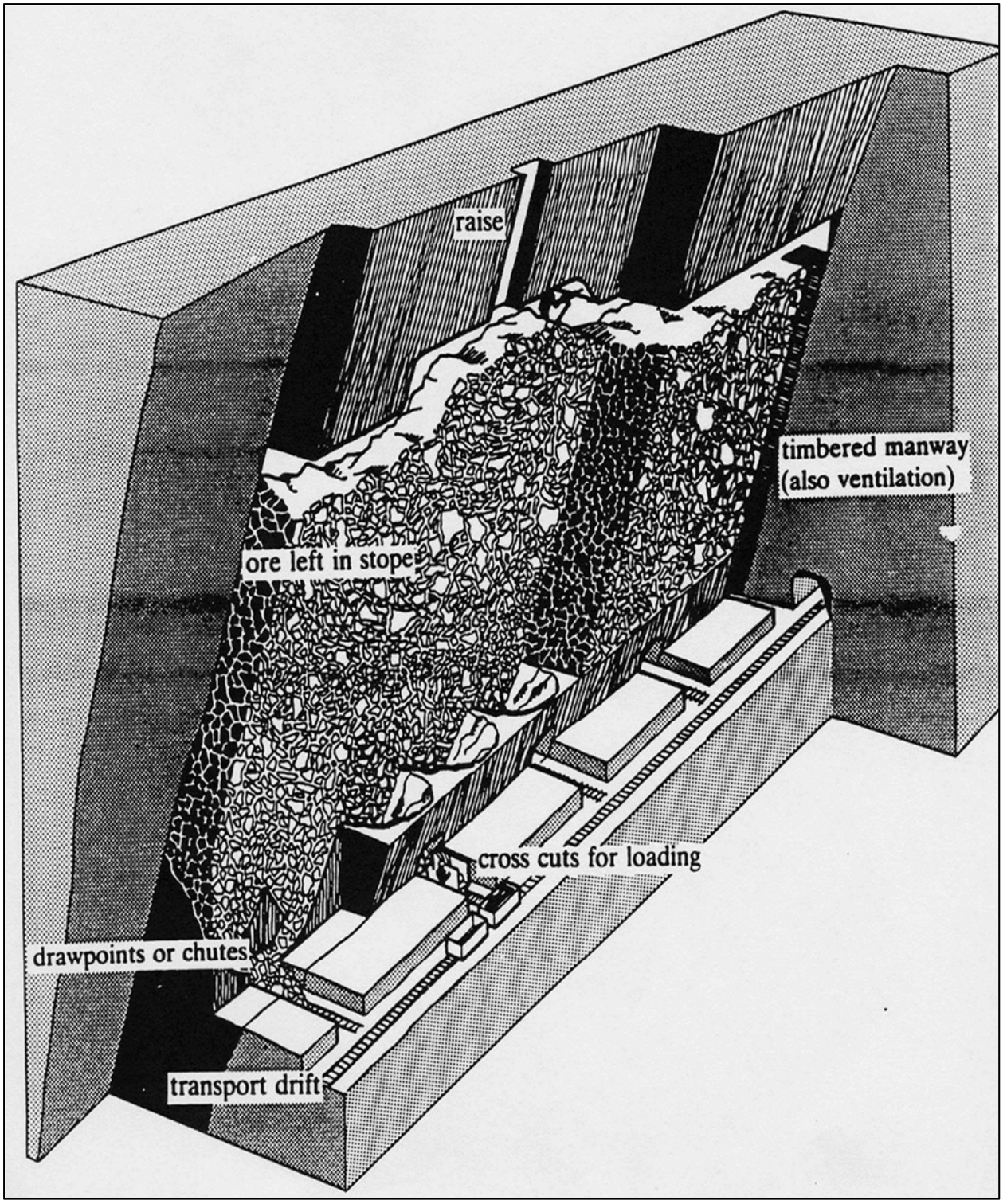

Figure 1.4 Shrinkage stoping with cross cut drawpoints (from Hamrin, 1980).

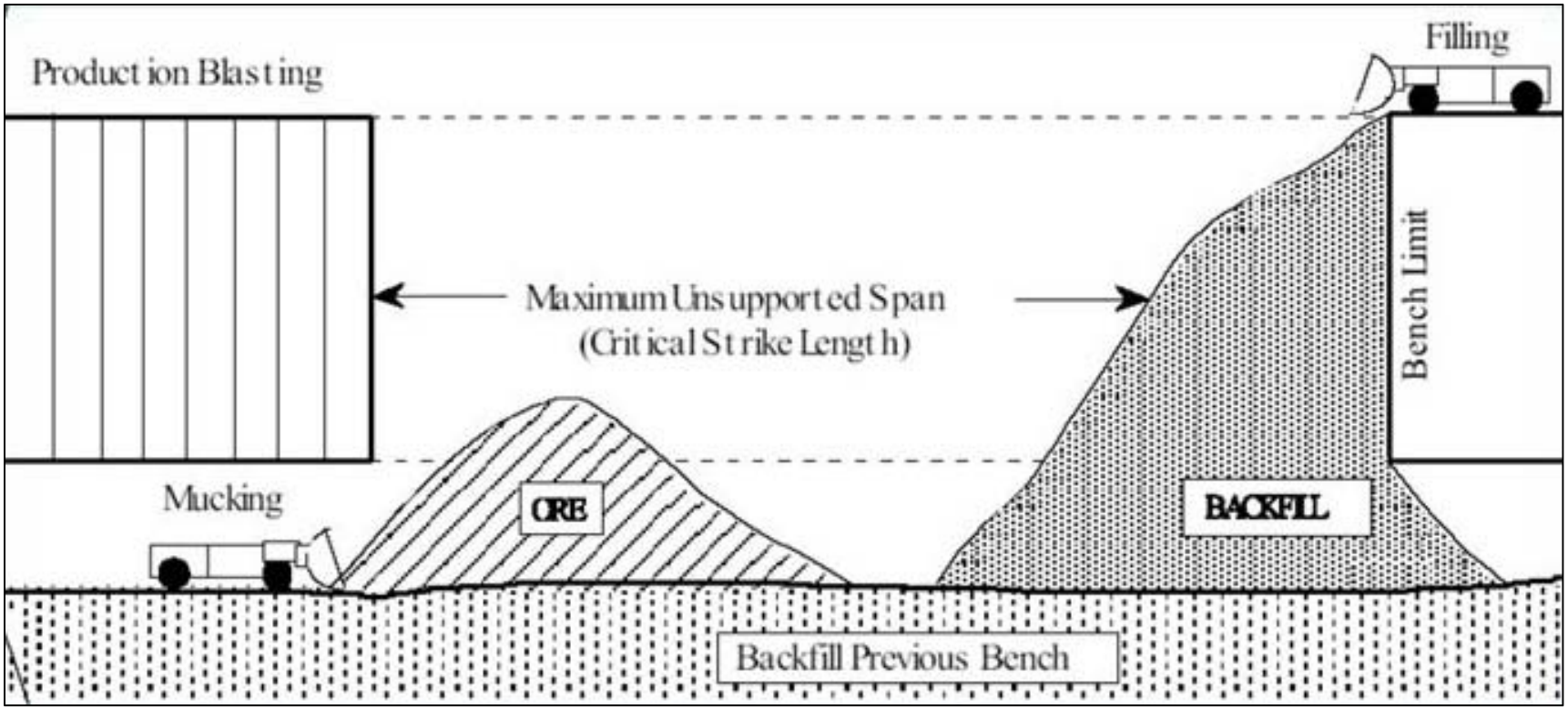

Figure 1.5 Avoca mining showing the access required from both sides on the overcut.

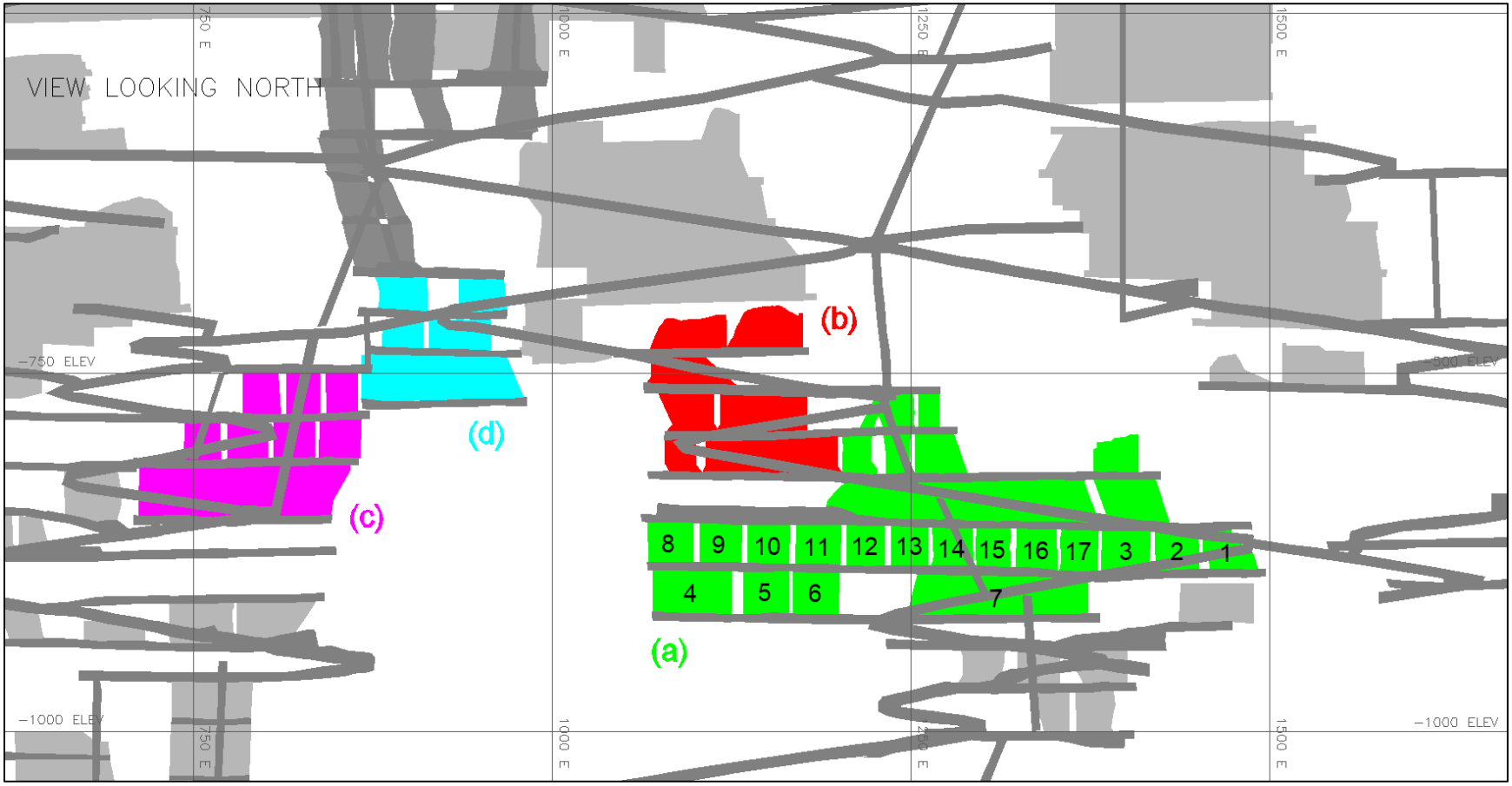

Figure 1.6 Zoomed in view of Figure 1.3 showing location of case study areas: (a) 2b11013, (b) 2b11011, (c) 2c10010 and (d) L62.

1.2 Defining Dilution

Dilution in mining exists when uneconomical waste rock has been mixed with economical ore. Dilution reduces the mill head grade which increases the cash cost of milling, it may reduce recovery, and therefore, increases the cost of the overall mining operations.

Dilution is defined in many ways at different mining operations and is generally expressed as a percentage. Pakalnis (1986) summarized the varying equations for calculating dilution that are used across Canada (Table 1.1). The two most popular ways of defining dilution are Equations 1 and 2 (Scoble and Moss 1994). The main differences between the two methods are that Equation 2 is less sensitive to the amount of waste recovered, and cannot exceed 100%, whereas Equation 1 can. Figure 1.7 shows dilution calculated based on the two equations and plots dilution versus the average width of slough (overbreak) or failure divided by the width of ore. At Seabee Gold Mine, Equation 2 is used to calculate dilution.

Mining dilution takes two general forms: planned and unplanned. Planned dilution occurs because of a varying orebody shape that makes it difficult to extract only ore. Planned dilution is therefore waste rock that is mined within the panel boundaries. The amount of planned dilution mined is a function of drilling and blasting practices, the mining method, and the orebody geometry. Unplanned dilution occurs when waste rock enters the ore stream from outside the planned panel boundaries. The difference between planned and unplanned dilution is shown in Figure 1.8. When using the various methods to calculate dilution from Table 1.1, often only unplanned dilution is defined as waste rock.

Table 1.1 Equations used to define dilution (after Pakalnis 1986).

Equation #	Equation Expression
Eq. 1	Dilution = (Tonnes waste mined) / (Tonnes ore mined)
Eq. 2	Dilution = (Tonnes waste mined) / (Tonnes ore mined + Tonnes waste mined)
Eq. 3	Dilution = (Undiluted in-situ grade as derived from dillholes) / (Sample assay grade at drawpoint)
Eq. 4	Dilution = (Undiluted in-situ grade reserves) / Mill head grades obtained from same tonnage)
Eq. 5	Dilution = (Tonnage mucked - Tonnage blasted) / (Tonnage blasted)
Eq. 6	Dilution = (Backfill tonnage actually placed - Backfill tonnage theoretically required to fill void)
Eq. 7	Dilution = Visually observed and assessed
Eq. 8	Dilution = ("x" amount of meters of footwall slough + "y" amount of hangingwall slough) / (ore width)
Eq. 9	Dilution = (Tons drawn from stope) / (Calculated reserve tonnage) over the last ten years

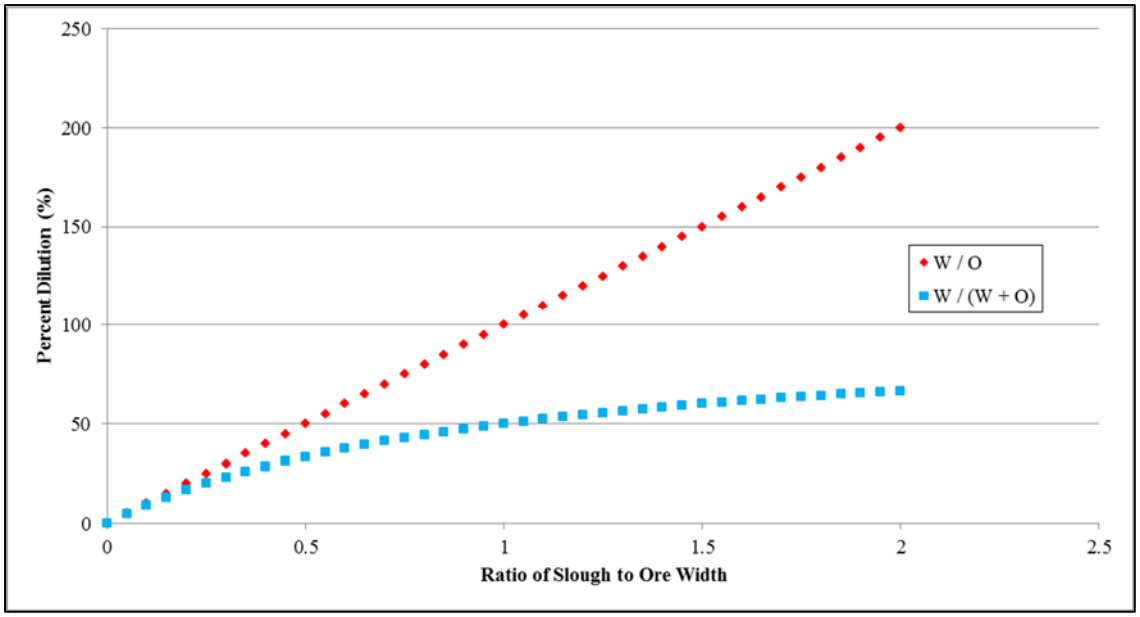

Figure 1.7 Dilution against the ratio of slough to ore width for Equations 1 and 2; where W is waste and O is ore (after Pakalnis et al., 1995).

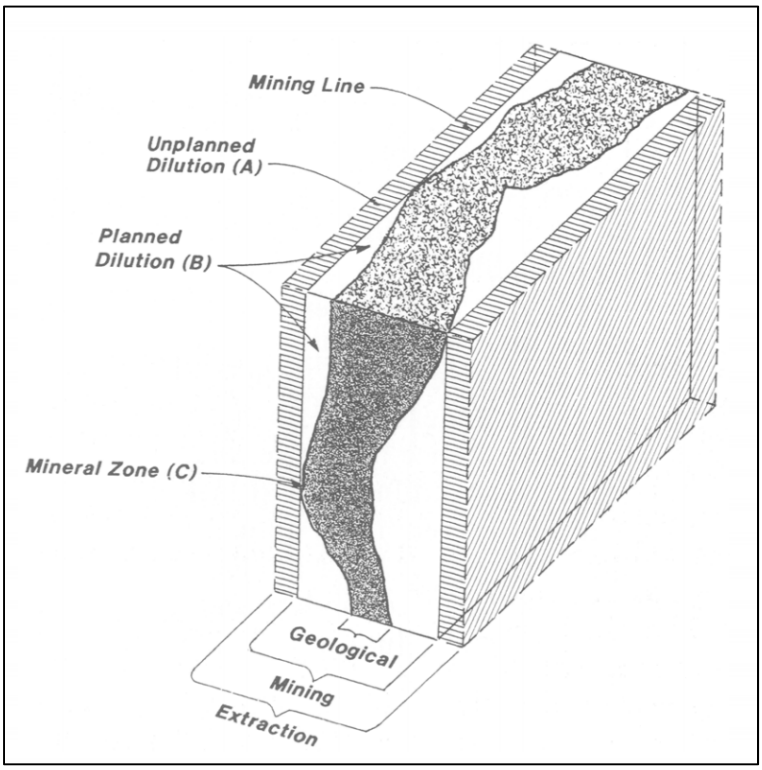

Figure 1.8 Panel showing planned and unplanned dilution (from Scoble and Moss, 1994).

1.2.1 Dilution Economics

The economic impact of unplanned dilution is related to direct and indirect costs. The direct costs of unplanned dilution are related to procurement and operation of the equipment and manpower required to transport and mill the additional material. This includes the mucking, hauling, crushing, hoisting, grinding, and processing. The indirect costs of unplanned dilution are the costs that cannot be quantified or easily attributed to dilution such as increased maintenance on equipment, longer panel cycle times, reduced head grade, increased backfill, increased mining and milling infrastructure, and reduced rate of ore production.

The ability to determine a precise estimate of the total cost of dilution is difficult. Many of the indirect costs are hard to quantify and associate solely with dilution. The cost of dilution can be estimated using direct costs as $25/tonne (Stewart and Trueman, 2008). This is based on the direct costs of mucking and hauling ($7/tonne) and milling ($18/tonne), and will vary for different operations and mining methods.

1.3 Research Objectives

The primary objectives of this research project were to identify the mechanisms of failure for unplanned dilution and propose methods to reduce this dilution.

The sub–objectives required for the study were as follows:

- collect field data to estimate the rock mass properties for rock classification;
- perform laboratory testing to identify the intact rock properties of Seabee Gold Mine;
- identify the effect that induced stress has on dilution;
- identify the causes of dilution at Seabee Gold Mine; and,
- improve the empirical design methods for predicting dilution for thin – veined underground mines.

1.4 Scope and Methodology

This research project included the determination of the mechanism of failure of the panel walls at Seabee Gold Mine through an analysis of rock mass quality, intact rock properties, geometrical extents of panels, induced stress, undercutting, and borehole deviation. The approach used for the analysis was:

- collect field data at Seabee Gold Mine to assess the quality of the rock mass;
- perform laboratory testing to define the properties of the intact rock mass (hangingwall, footwall, and orezone);
- analyse cavity monitoring surveys (CMS's) to quantify the extent of the overbreak and underbreak (the difference between the blasted geometry and the planned geometry);
- analyse surveys of the development drifts to identify the extent of undercutting; and,
- perform field instrumentation programs that include multi – point borehole extensometers (MPBX's) and converge stations to provide data to estimate the induced stress in the panels.

Not included in the scope of this research project was the effect of blasting on the rock mass and the resulting dilution caused by blasting, or the time dependent nature of failure of the rock mass.

1.5 Thesis Overview

This thesis is organized into six chapters. The following is an outline of the chapters in the thesis.

Chapter 1 – Introduction provides background information on Seabee Gold Mine, the case study area, mining methods in use at Seabee Gold Mine, and dilution. The problem is defined and the research objectives are stated.

Chapter 2 – Literature Review provides a review of the pertinent literature for this thesis. This includes an overview of various rockmass classifications systems, orebody delineation methods, induced stress of the study area, instrumentation that was used and empirical methods that have been applied for panel stability.

Chapter 3 – Data Collection categorizes the different methods used to collect data for calculating the amount of panel overbreak/underbreak, rock mass classification, panel deformation, induced stress, and laboratory testing.

Chapter 4 – Induced Stress Around Open Panels is a discussion on how induced stress will affect the amount of dilution from each panel. Included are the methods used to measure the induced stress in the field, numerical modelling that was performed, the classification of the case histories based on the induced stress and a summary of the work.

Chapter 5 – Analysis of Dilution Using Empirical Design Methods is a discussion on the use of existing empirical design methods to predict dilution at Seabee Gold Mine. The methodology used to create a new empirical method for predicting dilution based on the relative geometric stability of a point on the panel wall is also discussed. The case history data is applied to this method and the results are analysed.

Chapter 6 – Conclusions summarises the key findings and results and provides recommendations for continuing research into dilution at thin – veined mines.

CHAPTER 2

LITERATURE REVIEW

This chapter reviews the literature relevant to the work performed in this thesis. To be reviewed in this chapter are:

- the various methods of rock mass classification that are commonly used in hard rock mining;
- the development of the empirical methods used to determine the stability of open panels;
- the empirical methods used to predict the amount of dilution from open panels; and,
- the effect of induced stress on the stability of open panels.

2.1 Rock Mass Classification

Many rock mass classification methods are used in mine design. The most common techniques to help estimate the properties of underground openings are summarized. In all methods, the area under assessment must be differentiated into zones with similar rock mass properties which are called structural domains. The size of the zone that is to be classified must make practical sense according to the requirements of the activities of the area. Activities that are sensitive to the risk of rock mass failure might be classified using relatively small areas while less sensitive projects might be classified over large areas. The boundaries between zones with similar rock mass properties often coincide with large scale structural features such as faults, dykes, or shears or a change in rock type.

2.1.1 Rock Quality Designation (RQD)

RQD (Rock Quality Designation) is a measure of the degree of jointing as a percentage of competent rock greater than 10 centimetres long in a given length of core (core run) (Deere, 1964). RQD was developed to provide an estimate of required tunnel support based on the rock mass quality from drill core logs.

RQD is dependent on the direction of the drill hole with respect to the orientation of the joints or fractures present. The orientation of the drill hole can significantly change the estimation of RQD of the rock mass. To get the most relevant RQD estimation, the borehole orientation

should be perpendicular to the orientation of the joint surfaces of interest. The calculation of the RQD of the rock mass is for the in situ undisturbed rock mass. The drill core can be damaged through the drilling and handling process. Only natural joints that would exist in situ should be included in the RQD estimation.

The calculated RQD can have a range from 0 – 100 which represents a rock mass quality of poor to excellent, respectively. The RQD values and their respective rock mass quality descriptors are given in Table 2.1 and illustrated in Figure 2.1.

It is possible to estimate the RQD of the rock mass through a volumetric calculation using the joints visible on the exposed surfaces of the rock mass (Palmström, 1982). The RQD that is based on the number of discontinuities per cubic metre of rock mass (Jv) is given by the relationship:

$$RQD = 115 - 3.3J_v \tag{2.1}$$

where:

Jv is the *number of discontinuities per cubic metre of the rock mass*.

It is important to include only the natural joints that would exist in situ and to not include damage to the rock mass due to blasting. Calculating RQD using this volumetric method reduces the directional dependency of the drill hole method and allows the practitioner to ignore small joints.

2.1.2 Rock Mass Rating (RMR)

The original RMR (Rock Mass Rating) classification was developed by Bieniawski in 1976. In addition to what became known as the RMR_{76} (Bieniawski, 1976), Bieniawski developed the RMR_{89} which proposed some modifications to the values attributed to the parameters of the RMR_{76} system (Bieniawski, 1989). At Seabee Gold Mine, the system that is commonly applied is RMR_{76}. RMR is a single value rating from 8 to 100 that represents the strength of the rockmass.

Table 2.1 Descriptions and ratings for the RQD parameter (after Barton et al., 1976).

ROCK QUALITY DESIGNATION	RQD
Very Poor	0 - 25
Poor	25 - 50
Fair	50 - 75
Good	75 - 90
Excellent	90 - 100

* Where RQD is reported or measured as ≤ 10 (including 0) a nonimal value of 10 is used to evaluate Q in Eq. 2.2

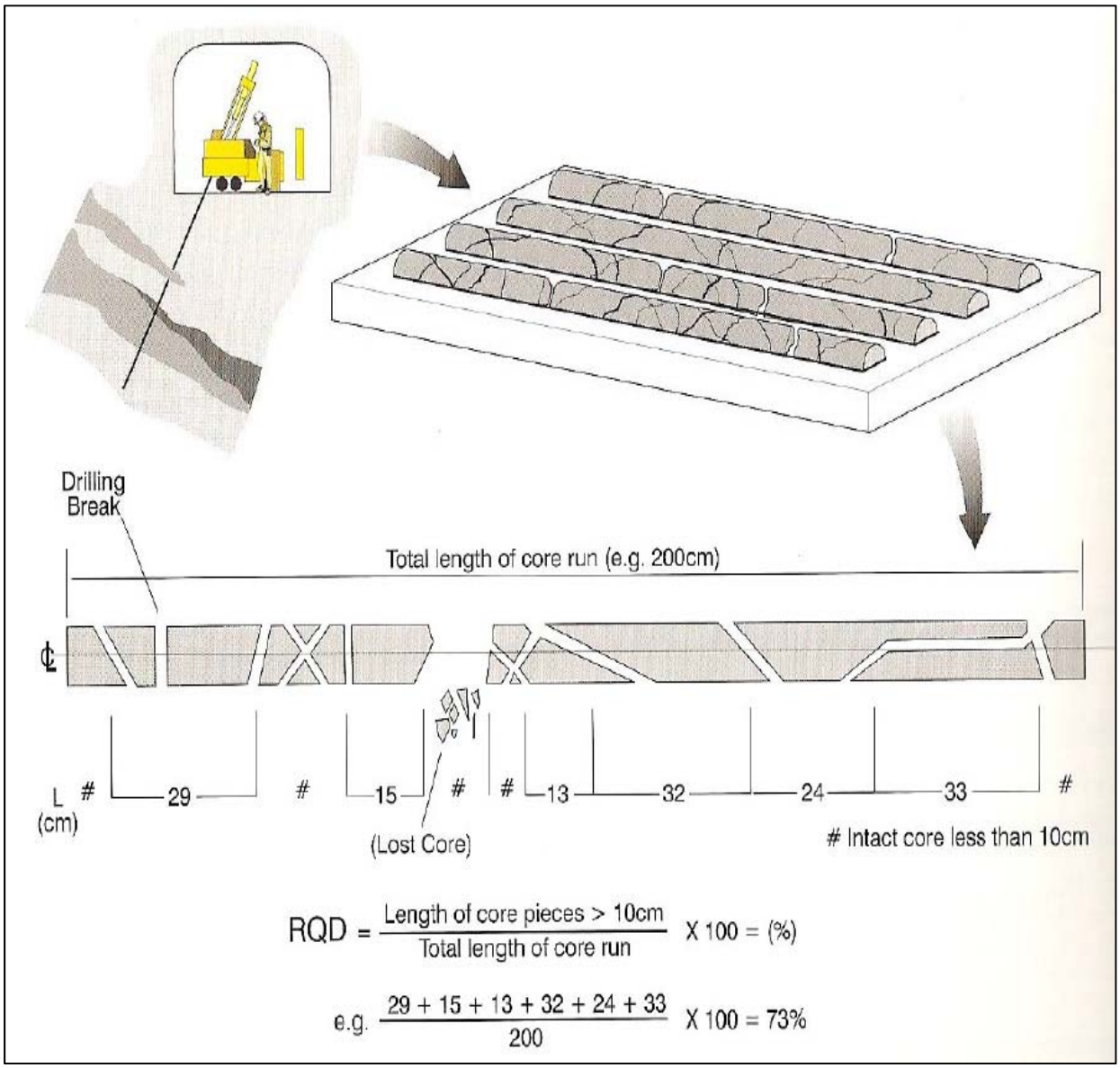

Figure 2.1 Measurement of RQD (after Hutchinson and Diederichs, 1996).

RMR is the sum of ratings given to different properties of the rock mass which include: UCS (unconfined compressive strength), RQD, amount of water present, joint spacing, joint alteration and joint orientation with respect to the surface under design. Table 2.2 summarizes the parameters used to estimate RMR_{76} (Bieniawski, 1976). These different ratings for the properties are given different numerical weighting that are dependent on their influence to the stability of the rock mass. The RMR value is applied to the rock mass after it has been separated into structural domains.

2.1.3 NGI Tunnel Quality Index (Q)

The *Tunnel Quality Index* (Q) was developed to quantify the stability of a tunnel based on joint properties, ground water conditions and induced stresses in the rockmass (Barton et al., 1974). The Q value is calculated from the following equation that is based on approximately 200 case histories of underground excavations:

$$Q = \frac{RQD}{J_n} \times \frac{J_r}{J_a} \times \frac{J_w}{SRF} \tag{2.2}$$

where:

RQD	is the *Rock Quality Designation*;
J_n	is the *Joint Set Number*;
J_r	is the *Joint Set Roughness*;
J_a	is the *Joint Set Alteration*;
J_w	is the *Joint Set Water Reduction*; and,
SRF	is the *Stress Reduction Factor*.

The RQD is a representation of the joint spacing in the rockmass and is as described in Section 2.1.1. The values use to calculate Eq. 2.2 are the actual RQD percentage for the rockmass and range from 0 – 100 for a very poor RQD to an excellent RQD, respectively. For the Q system, a minimum value of RQD greater to or equal than 10 is applied (Barton et al., 1974).

The parameter that represents the *Joint Set Number* (J_n) accounts for the number of joint sets and the amount of random jointing that are present in the rock mass under study. The values associated with J_n range from 0.5 for a massive rock mass with no jointing to a value of 20 for

crushed, earthlike rock. The full range of values is given in Table 2.3. The presence of joint sets is often determined through rock mass joint mapping and visualizing the data using stereonet plotting. The joint sets can be determined through clustering of data points on the stereonet; while random joints can be determined by a general spread of data points throughout the plot.

The *Joint Roughness Number* (J_r) represents the small and large scale joint surface roughness and it is estimated for the most unfavourable joint set orientation with respect to stability. The values of J_r range from 0.5 for a slickensided planar joint surface to a value of 4 for discontinuous joints. The full range of values is shown in Table 2.4.

Originally, Barton et al. (1974), defined three classes of small scale roughness (rough, smooth, and slickensided) and two large scale types of roughness (undulating and planar). Milne et al. (1991) adapted a graph developed by Barton (1981) into areas that quantified the small scale roughness ($J_{r/r}$) and the large scale roughness ($J_{r/w}$). The product of these parameters produces J_r. This modified graph can be seen in Figure 2.2.

The *Joint Alteration Number* (J_a) represents the degree of surface alteration and the amount and slipperiness of mineral coatings on the surface of joints that are most critical to the stability of the surface being evaluated. These values range from 0.75 for a joint that has been tightly healed to 10.0 – 20.0 for joint surfaces that have infillings with > 5mm thickness of gouge or clay. An abbreviated list of the values that are most important for hard rock mining is given in Table 2.5. A comprehensive list of values for differing joint alterations can be found in Barton et al. (1974).

The *Joint Water Reduction* (J_w) represents the effect that groundwater has on the reduction of effective stress on the joint sets, as well as the washing out of joint fillings. The values for Jw can range from 1.0 for dry excavations to 0.1 – 0.05 for exceptionally high inflow or pressure that continues without decay (Table 2.6).

The *Stress Reduction Factor* (SRF) represents the destabilizing effect that low or high confining stress conditions can have on a rock mass. The SRF term also assesses the effect of weak zones, such as shears and faults, which can reduce stability by reducing confining stresses in the rock mass. The most favourable conditions have SRF values between 0.5 – 2.0 which represents a competent rock mass with a moderate confining stress. The worst conditions have SRF values

between 10 – 20 and this represents areas that have multiple occurrences of weakness zones containing clay and loose surrounding rock or heavy rock burst areas (Table 2.7).

Table 2.2 The Rock Mass Rating Classification Table (after Bieniawski, 1976).

A. CLASSIFICATION PARAMETERS AND THEIR RATINGS

PARAMETER			RANGES OF VALUES						
1	Strength of intact rock material	Point-load strength index	> 8 MPa	4 - 8 MPa	2 - 4 MPa	1 - 2 MPa	For this low range - uniaxial compressive test is preferred		
		Uniaxial compressive strength	> 200 MPa	100 - 200 MPa	50 - 100 MPa	25 - 50 MPa	10 - 25 MPa	3 - 10 MPa	1 - 3 MPa
	Rating		15	12	7	4	2	1	0
2	Drill core quality RQD		90% - 100%	75% - 90%	50% - 75%	25% - 50%	< 25%		
	Rating		20	17	13	8	3		
3	Spacing of joints		> 3 m	1 - 3 m	0.3 - 1 m	50 - 300 mm	< 50 mm		
	Rating		30	25	20	10	5		
4	Condition of joints		Very rough surfaces. Not continuous, No separation, Hard joint wall rock	Slightly rough surfaces. Separation < 1 mm. Hard joint wall rock	Slightly rough surfaces. Separation > 1 mm. Soft joint wall rock.	Slickensided surfaces, OR Gouge < 5 mm thick, OR Joint open 1-5 mm. Continuous joints.	Soft gouge > 5 mm thick. OR Joint open > 5mm. Continuous joints.		
	Rating		25	20	12	6	0		
5	Ground water	Inflow per 10 m tunnel length	None		< 25 litres/min	25 - 125 litres/min	> 125 litres/min		
		Ratio $\frac{\text{Joint water pressure}}{\text{major principal stress}}$	OR 0		OR 0.0 - 0.2	OR 0.2 - 0.5	OR > 0.5		
		General conditions	OR Completely dry		OR Moist only (Interstitial water)	OR Water under moderate pressure	OR Severe water problems		
	Rating		10		7	4	0		

B. RATING ADJUSTMENT FOR JOINT ORIENTATIONS

Strike and dip orientations of joints		Very favourable	Favourable	Fair	Unfavourable	Very unfavourable
Ratings	Tunnels	0	-2	-5	-10	-12
	Foundations	0	-2	-7	-15	-25
	Slopes	0	-5	-25	-50	-60

C. ROCK MASS CLASSES DETERMINED FROM TOTAL RATINGS

Rating	100 ← 81	80 ← 61	60 ← 41	40 ← 21	< 20
Class No.	I	II	III	IV	V
Description	Very good rock	Good rock	Fair rock	Poor rock	Very poor rock

D. MEANING OF ROCK MASS CLASSES

Class No.	I	II	III	IV	V
Average stand-up time	10 years for 5 m span	6 months for 4 m span	1 week for 3 m span	5 hours for 1,5 m span	10 minutes for 0,5m span
Cohesion of the rock mass	> 300 kPa	200 - 300 kPa	150 - 200 kPa	100 - 150 kPa	< 100 kPa
Friction angle of the rock mass	> 45°	40° - 45°	35° - 40°	30° - 35°	< 30°

Table 2.3 Descriptions and ratings for the J_n parameter (after Barton et al., 1974).

JOINT SET NUMBER	J_n
Massive, no or few joints	0.5 - 1
One joint set	2
One joint set plus random	3
Two joint sets	4
Two joint sets plus random	6
Three joint sets	9
Three joint sets plus random	12
Four or more joint sets, 'sugar cubed'	15
Crushed rock, earthlike	20

Table 2.4 Descriptions and ratings for the J_r parameter (after Barton et al., 1974).

JOINT ROUGHNESS NUMBER	J_r
Discontinuous joints	4
Rough or irregular, undulating	3
Smooth, undulating	2
Slickensided, undulating	1.5
Rough or irregular, planar	1.5
Smooth, planar	1.0
Slickensided, planar	0.5
Zone containging clay minerals thick enough to prevent rock wall contact	1.0
Sandy, gravelly or crushed zone thick enough to prevent rock wall contact	1.0

Table 2.5 Descriptions and ratings for the J_a parameter (after Barton et al., 1974).

JOINT ALTERATION NUMBER	J_a
Tightly healed	0.75
Surface staining only	1.0
Slightly altered joint walls, sparse mineral coating	2.0 - 3.0
Low friction coating (chlorite, mica, talc, clay) < 1mm thick	3.0 - 6.0
Thin gouge, low friction or swelling clay 1 - 5mm thick	6.0 - 10.0
Thick gouge, low friction or swelling clay > 5mm thick	10.0 - 20.0

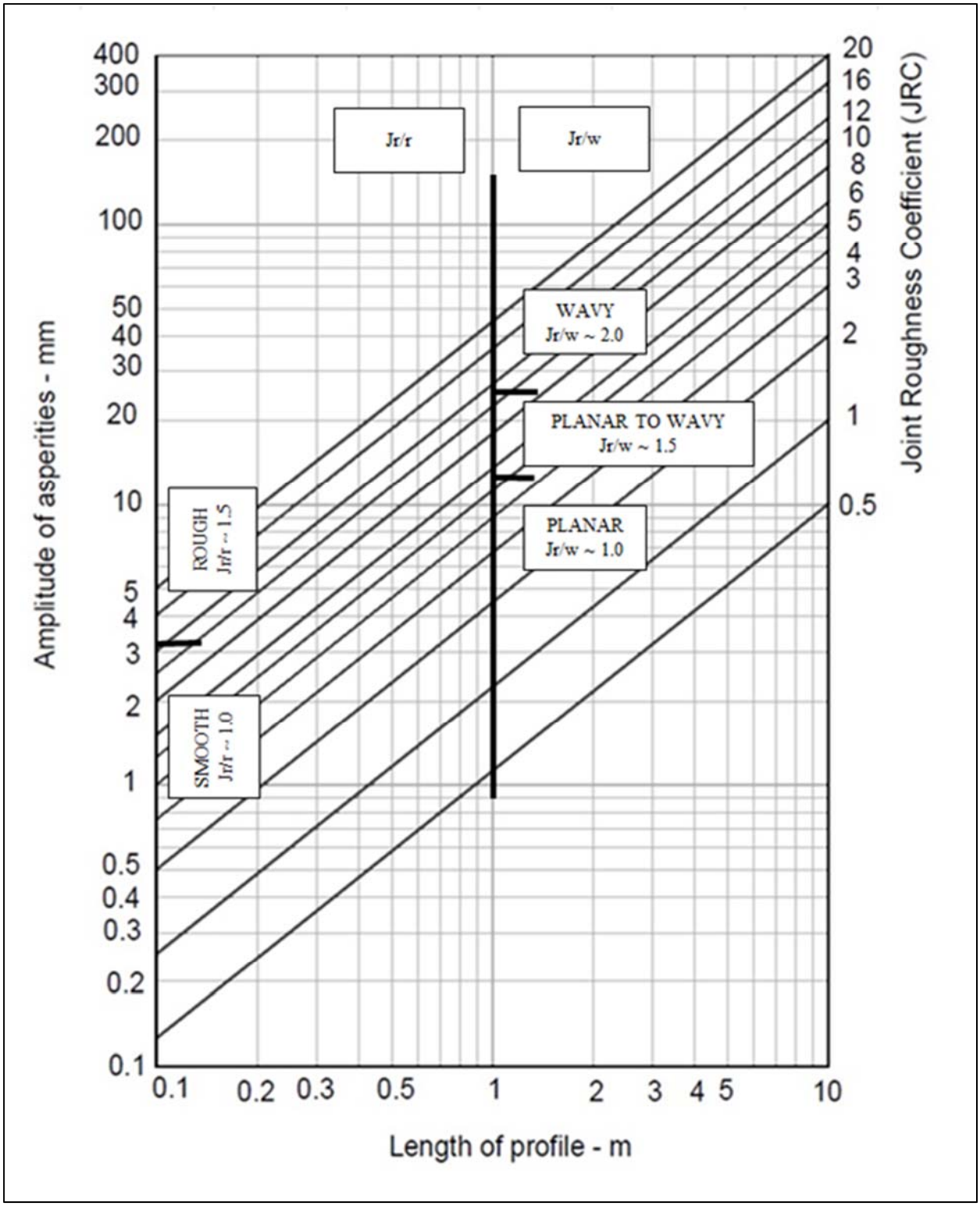

Figure 2.2 The JRC Chart depicting the Jr/r values and the Jr/w values (from Milne et al., 1991).

Table 2.6 Descriptions and ratings for the J_w parameter (after Barton et al., 1974).

JOINT WATER REDUCTION	J_w
Dry excavations or minor inflow < 5L/min locally Medium inflow or pressure	1.0
Large inflow or pressure with unfilled joints	0.66
Large inflow or pressure with outwash of joint fillings	0.5
Large inflow or pressure with outwash of joint fillings	0.33
Exceptionally high inflow or pressure, decaying with time after excavation	0.2 - 0.1
Exceptionally high inflow or pressure, continuing without noticeable decay	0.1 - 0.05

Table 2.7 Descriptions and ratings for the SRF parameter (after Barton et al., 1974).

STRESS REDUCTION FACTOR	SRF
(a) Weakness zones intersecting excavation	
Multiple occurrences of weakness zones containing clay or chemically disintigrated rock, very loose surround rock (any depth)	10
Single weakness zones containing clay, or chemically disintegrated rock (depth of excavation ≤ 50m)	5
Single weakness zones containing clay, or chemically disintegrated rock (depth of ≥ 50m)	2.5
Multiple shear zones in competent rock (clay free), loose surrounding rock mass (any depth)	7.5
Single shear zones in competent rock (clay free) (depth of excavation ≤ 50m)	5
Single shear zones in competent rock (clay free) (depth of excavation > 50m)	2.5
Loose open joints, heavily jointed or 'sugar cube' etc. (any depth)	5
(b) Competent rock, rock stress problems	
Low stress, near surface	2.5
Medium stress	1
High stress, very tight structure (usually favourable to stability may be unfavourable to wall stability)	0.5 - 2.0
Mild rock burst (massive rock)	5 - 10
Heavy rock burst (massive rock)	10 - 20

Eq. 2.2 contains three quotients and each represents a factor affecting the stability of the rock mass. The first quotient, RQD/J_n, is a rough characterization of the average block size (Barton et al., 1974). The stability of the rock mass is partially governed by the average size of the blocks within the rock mass. The use of RQD/J_n was initially developed by Cecil (1970) who plotted case studies of unsupported span widths against RQD and found a large amount of scatter in the data. It was then found that the correlation improved when RQD was divided by the number of joint sets present in an area. While RQD is the representation of intact block size, J_n is a representation of the degrees of freedom of movement. Combining these terms shows that a rockmass with a low RQD when confined with limited degrees of freedom is just as stable as a rockmass with a high RQD and multiple degrees of freedom for movement.

The second quotient in Eq. 2.2, J_r/J_a, is a characterization of the dilatancy and shear strength of the joint surfaces. The joint roughness on the small and intermediate scale was viewed positively due to the increasing of dilatancy that accompanies shearing. Alternatively, joint alteration and joint filling was viewed negatively due to the reduction of shear strength from potentially lower friction angles of the joint surfaces. This quotient should be applied to the joint set most critical to the stability of the rockmass, which is generally joint sets that strike sub-parallel to the opening surface under consideration.

The final quotient of J_w/SRF is a characterization of the stress state of the rockmass. The pressure of water present will potentially destabilize the rockmass, partially due to the resulting effective stress. Also, the differing levels of in situ stresses of the surrounding rockmass and potential zones of weakness can also lead to stress related instability.

2.2 Empirical Open Panel Design Methods for Stability

In the authors' experience, there are three main methodologies for the design of open panels: empirical, numerical, and analytical methods, with empirical methods being more widely used by the mining industry. Empirical methods use case histories of open panel performance to predict future panel performance. The expected performance of the open panel is assessed based on a quantifiable measurement (ie. a measurement of dilution) or a qualitative assessment of stability (ie. stable, unstable, caved). These measurements or assessments allow for the creation of a failure criterion.

Empirical methods are well suited to the design of open panels because of the difficulty of quantifying the engineering properties of the rockmass. An engineered material such as steel or concrete is designed to engineering specifications whereas a rockmass is highly variable in its properties.

2.2.1 Mathews Design Method

The Mathews Stability Graph was the first empirical open panel stability graph and was developed by Mathews et al. (1981) (Figure 2.3). This graphical approach was developed for the Canada Centre for Mineral and Energy Technology (*CANMET*) to predict the stability of open spans for deep (> 1000m) open panels and was based on 50 case histories. On the graph the Stability Number*, N*, is plotted against the Hydraulic Radius*, HR*, (or the Shape Factor*, S*).

The *N* stability number is a unitless value used to assess the stability of an opening's surface. It incorporates the in situ stress condition, major joint orientation, the dip of the given surface, and a rock quality measure*, Q*'. *Q*' is similar to *Q* (Section 2.1.3) except the *SRF* factor is set to 1. The stability number is calculated as follows:

$$N = Q' \times A \times B \times C \tag{2.2}$$

where:

- *N* is the *Stability Number*;
- *Q'* is the *Tunnel Quality Index with SRF set to 1*;
- *A* is the *Factor related to the stress condition*
- *B* is the *Factor related to the primary joint orientation;* and,
- *C* is the *Factor related to the dip of the analysed surface*.

The *A* factor is a representation of the stress condition and intact strength of the rockmass so the *SRF* factor is ignored in *Q'*. It is based on the ratio of uniaxial compressive strength of the intact rock to the induced stress parallel to the panel opening (σ_c/σ_1). In order to best identify the induced stress condition parallel to the panel opening, a numerical stress analysis should be used. The *A* factor can be determined from this ratio based on the graph presented in Figure 2.4. The *A*

factor reduces with a higher induced stress relative to the rock strength to reflect the increased instability of the rock mass due to increasing stress.

The *B* factor is a measure of the orientation of the joint set that is most critical to stability of the opening surface (critical joint), and is based on the angle between the opening surface and the critical joint. This is based on the concept that the opening will be most stable when structure is perpendicular to the opening surface, will be least stable when at a shallow angle to the opening (20°), and will gain some stability when parallel to the opening surface. The panel gains stability when structure is parallel because of the potential failure mode switch to a beam failure rather than a sliding or cantilever failure. The values attributed to the different angles are seen in Figure 2.5.

The *C* factor is a representation of the effect of gravity on the stability of the opening. This was premised on the idea that there is greater potential of failure (due to falling, slabbing and gravity) on a horizontal surface than a vertical surface. *C* factor can be determined by the graph presented in Figure 2.6, or, or equivalently by using the following equation:

$$Factor\ C = 8 - 7\cos(DipAngle) \tag{2.3}$$

The second term used in Mathews Stability Graph is the hydraulic radius (*HR*) or shape factor (*S*) of the opening surface (Eq. 2.4). The *HR* is a measure of the relative geometric stability of the open panel. An increase in the dimensions of the panel will increase the *HR* and will decrease the inherent stability of the opening. Increasing the aspect ratio of the dimensions will converge the *HR* to a constant which equals half the span.

$$HR\ or\ S = A_r P \tag{2.4}$$

where:

HR is the *Hydraulic Radius*;
A_r is the *Surface Area*; and
P is the *Surface Perimeter*.

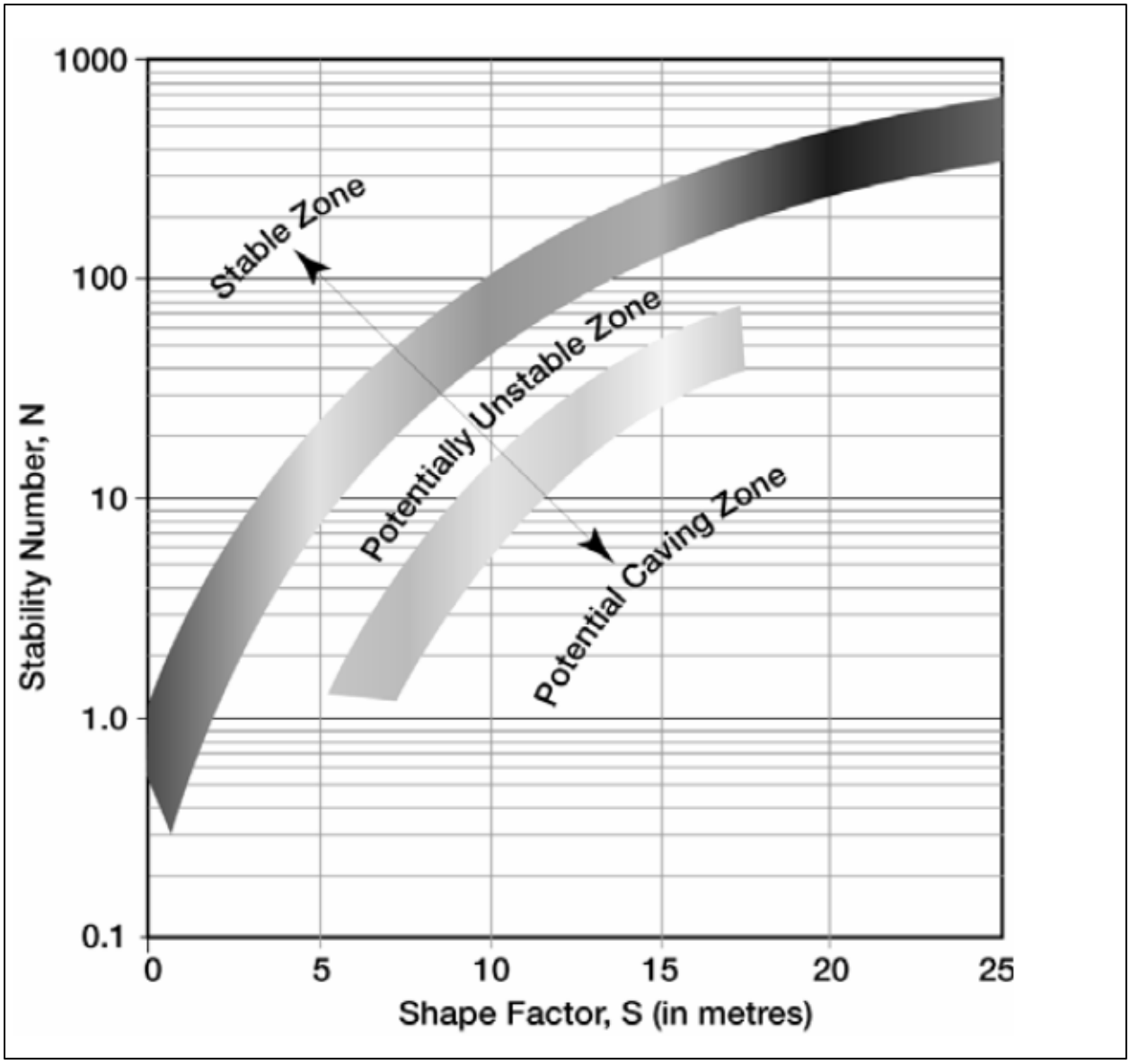

Figure 2.3 The Mathews Stability Graph (from Stewart, 2005, after Mathews et al., 1981).

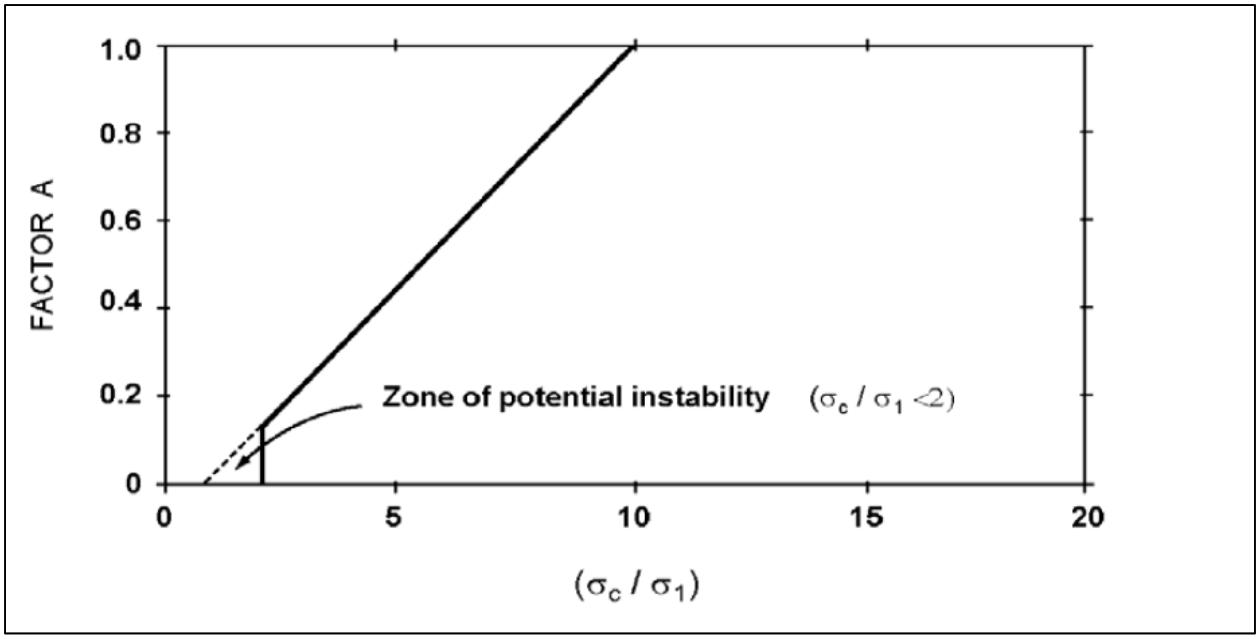

Figure 2.4 Graph to determine Factor A (from Nickson, 1992, after Mathews et al. 1981).

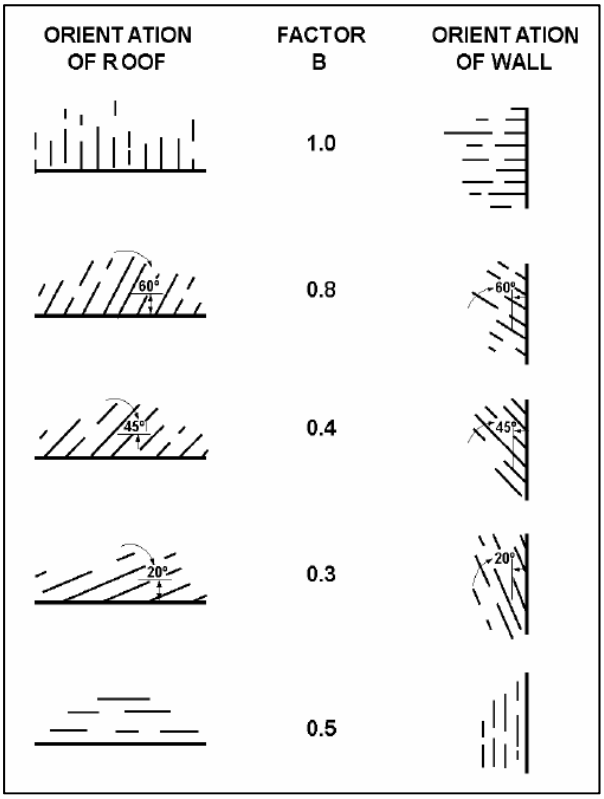

Figure 2.5 Values of Factor B (from Nickson, 1992, after Mathews et al., 1981).

2.2.2 Modified Stability Graph Method

The Modified Stability Graph was developed by Potvin (1988) and later Nickson (1992) from the Mathews Stability Graph design method. Potvin (1988) added an additional 176 case histories to the stability graph that were obtained from 40 Canadian mines. A transition zone was added between the *Stable* and *Caved* zones on the graph; with the additional case histories further defining the limits of the failure criterions. Potvin's Modified Stability Graph can be seen in Figure 2.7. Potvin (1988) also modified the input parameters used for the calculation of the stability number (Figure 2.8). The *A* factor was modified to provide a minimum value of 0.1 for any σ_c/σ_1 ratio of less than 2. The *B* factor was converted to a graphical form similar to the *A* and *C* factors and the x-axis compensates for the strike of the critical joint set relative to the strike of the opening, based on the premise that the greater the difference in strike angle of the joint set to the opening the greater the stability will be.

Nickson (1992) continued the development of the Modified Stability Graph by studying the effects of cablebolt support on the stability of open panels. To the supported case histories that were accumulated by Potvin (1988), Nickson added an additional 46 case histories, and further delineated the Modified Stability Graph by adding the zones of *Stable with Support* and the *Supported Transition Zone* (Figure 2.9). Nickson added additional statistical rigour not present in previous versions of the stability graph to define the new zones.

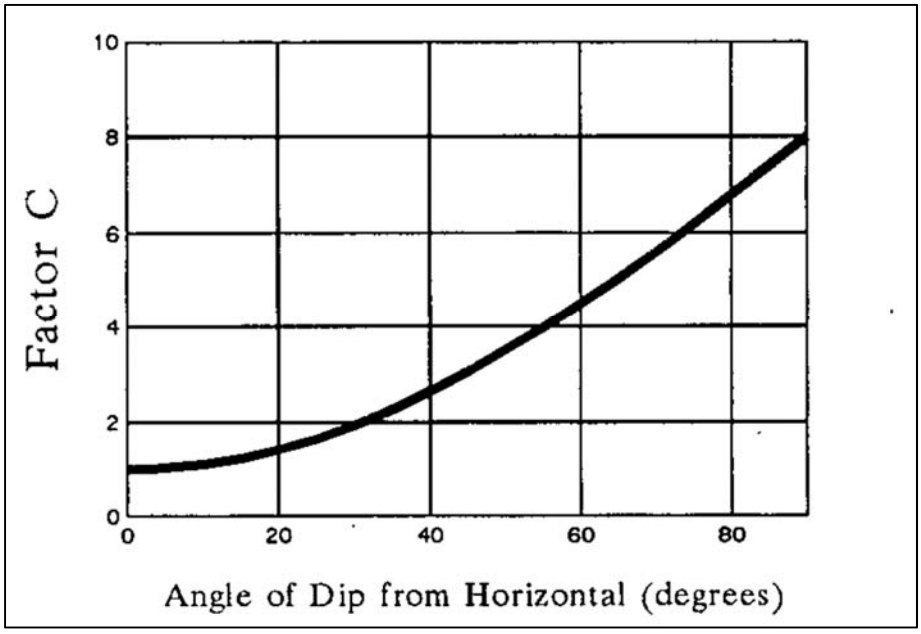

Figure 2.6 Graph to determine Factor C (from Nickson, 1992, after Mathews et al., 1981).

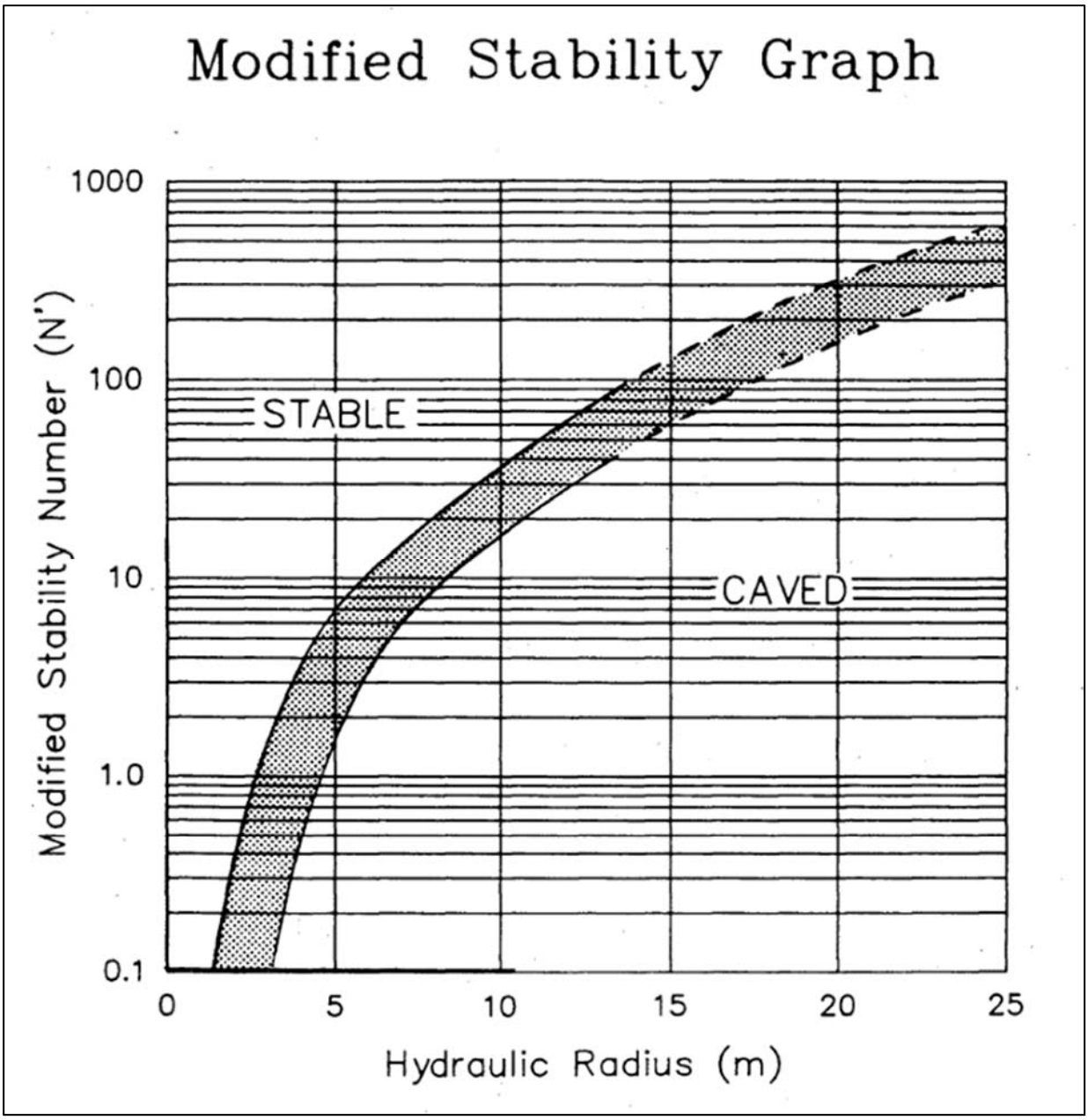

Figure 2.7 The Modified Stability Graph (from Potvin, 1988).

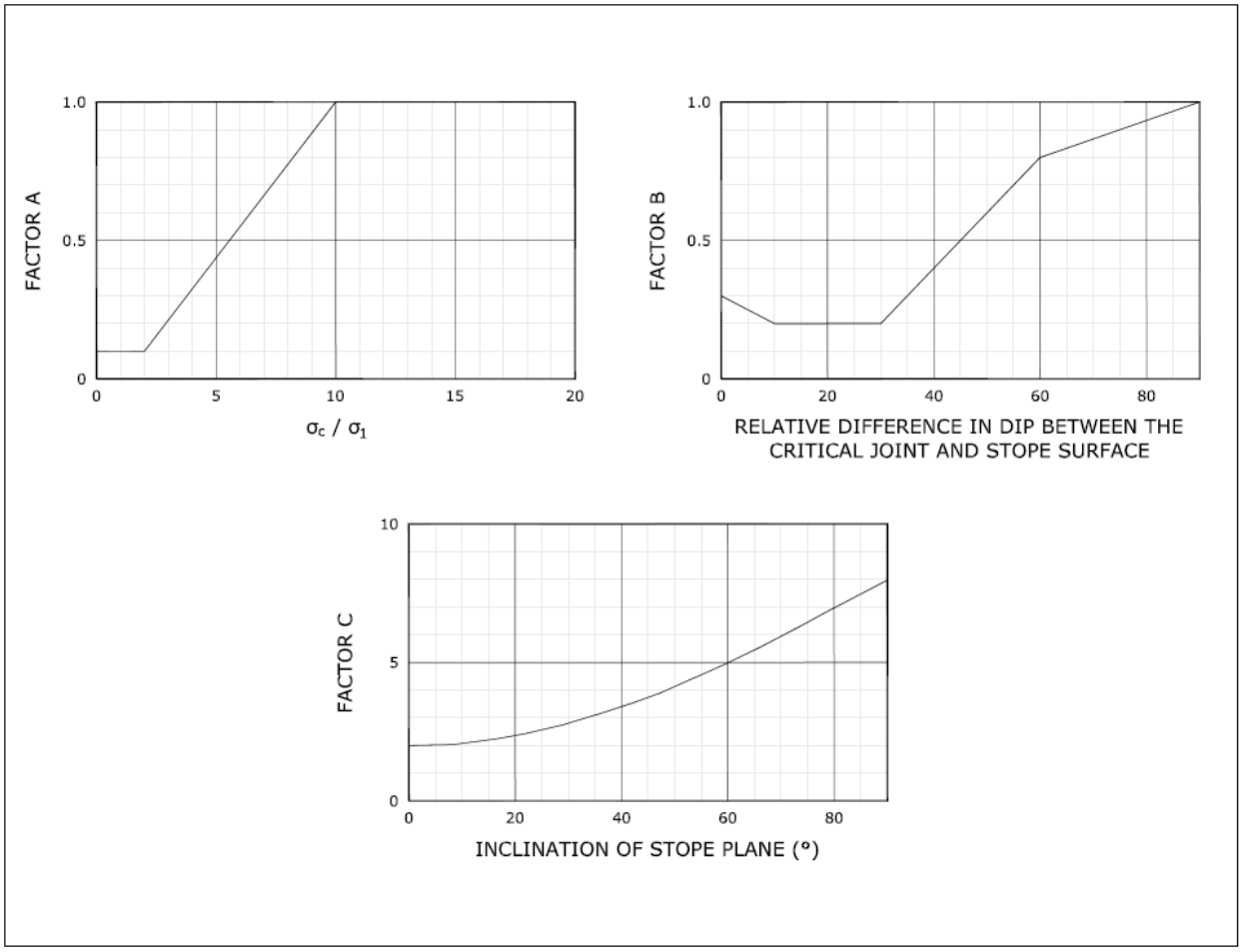

Figure 2.8 Modified input parameters to calculate N' for the modified stability graph (after Nickson, 1992, after Potvin, 1988).

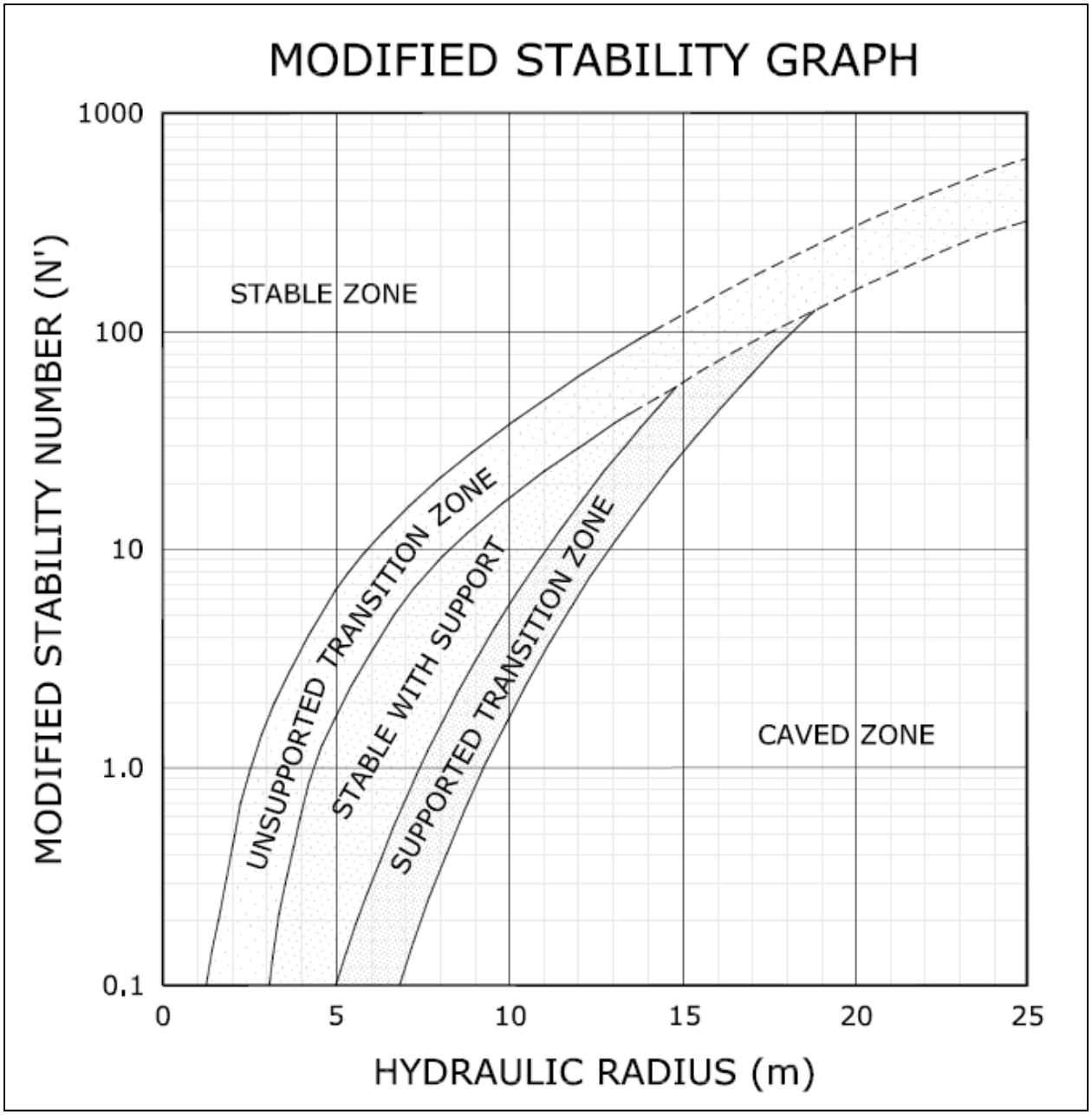

Figure 2.9 The Modified Stability Graph (after Nickson, 1992).

2.3 Dilution Design for Open Panels

In addition to the efforts that were made to predict the stability of open panels, work has also been performed to predict the amount of dilution that could be expected from an open panel.

2.3.1 Dilution Design Method

Pakalnis (1986) developed the dilution design method based on 133 case histories from Ruttan Mine in Canada, as shown in Figure 2.10. This method is based on the RMR_{76} classification system and is one of the first methods to estimate dilution that is not based on stable / unstable predictions. This method empirically predicts the dilution for three different panel types experienced at Ruttan Mine: isolated, rib, and echelon. A dilution equation was generated for each panel type which considered RMR_{76}, exposure rate, and exposed area. The RMR_{76} term represents the quality of the rockmass, the exposure rate accounts for the deterioration of the rockmass with respect to time, and the exposed area considers the geometric stability of the opening. The three equations based on panel type are as follows:

for isolated panels;

$$Dilution = 8.6 - 0.09(RMR) - 13.2(ExposureRate) + 0.0038(AreaExpose) \quad \text{(Eq. 2.5)}$$

for rib panels; and,

$$Dilution = 15.8 - 0.18(RMR) - 7.7(ExposureRate) + 0.0026(AreaExpose) \quad \text{(Eq. 2.6)}$$

for echelon panels;

$$Dilution = 10.3 - 0.13(RMR) - 14.8(ExposureRate) + 0.003(AreaExpose) \quad \text{(Eq. 2.7)}$$

2.3.2 ELOS Stability Chart

Clark (1998) developed a quantitative method to compare dilution for open panels with different ore thicknesses called *Equivalent Linear Overbreak and Slough,* ELOS. ELOS provides a measurement of dilution that is independent of the panel thickness. A visual representation of converting the overbreak from an open panel into ELOS is shown in Figure 2.11. ELOS is calculated from the simple equation:

$$ELOS = \frac{Volume\ of\ Slough\ from\ Stope\ Surface}{Stope\ Height\ \times Wall\ Strike\ Length} \quad \text{(Eq. 2.8)}$$

The ELOS Stability chart was developed using 85 case histories and is built upon previous work on stability graphs (Clark, 1998). Similar to the other stability charts, it plots N' vs HR; however, rather than estimating whether the panel is stable / caved, the ELOS of the panel is estimated instead. The zones representing ELOS on the graph were developed using logistic regression and neural networks of the case history data. The ELOS Stability chart is shown in Figure 2.12.

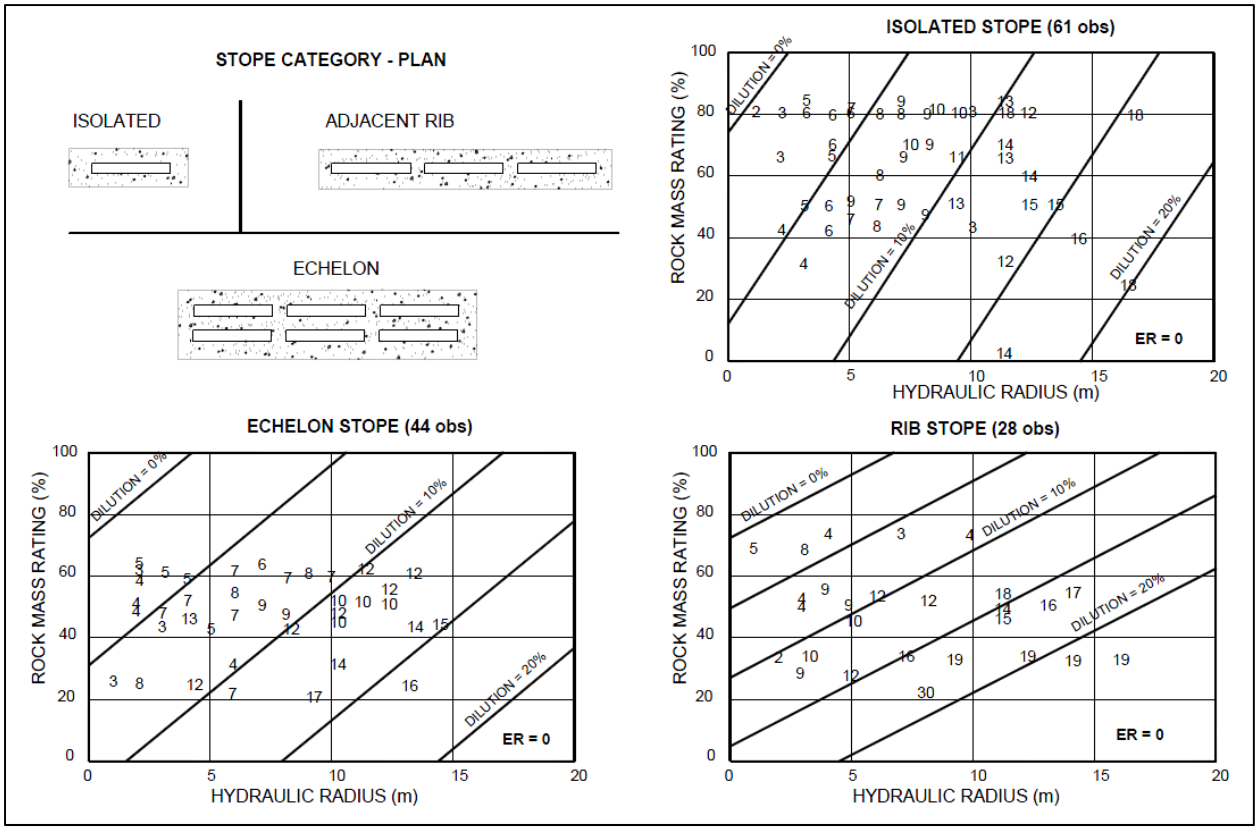

Figure 2.10 Graphical representation of dilution anaylsis (from Capes, 2006, after Pakalnis, 1993).

2.3.3 Modified Dilution Graph

Capes (2009) continued the development of the ELOS methodology by collecting an additional 169 case histories of panels with an HR less than 10m and a wide range of rockmass conditions. Using the additional case histories, a logistic regression and classification analysis was used to redefine the ELOS lines on the graph. These lines represented an 80% correct prediction of ELOS for the case histories used. The Modified Dilution Graph is shown in Figure 2.13.

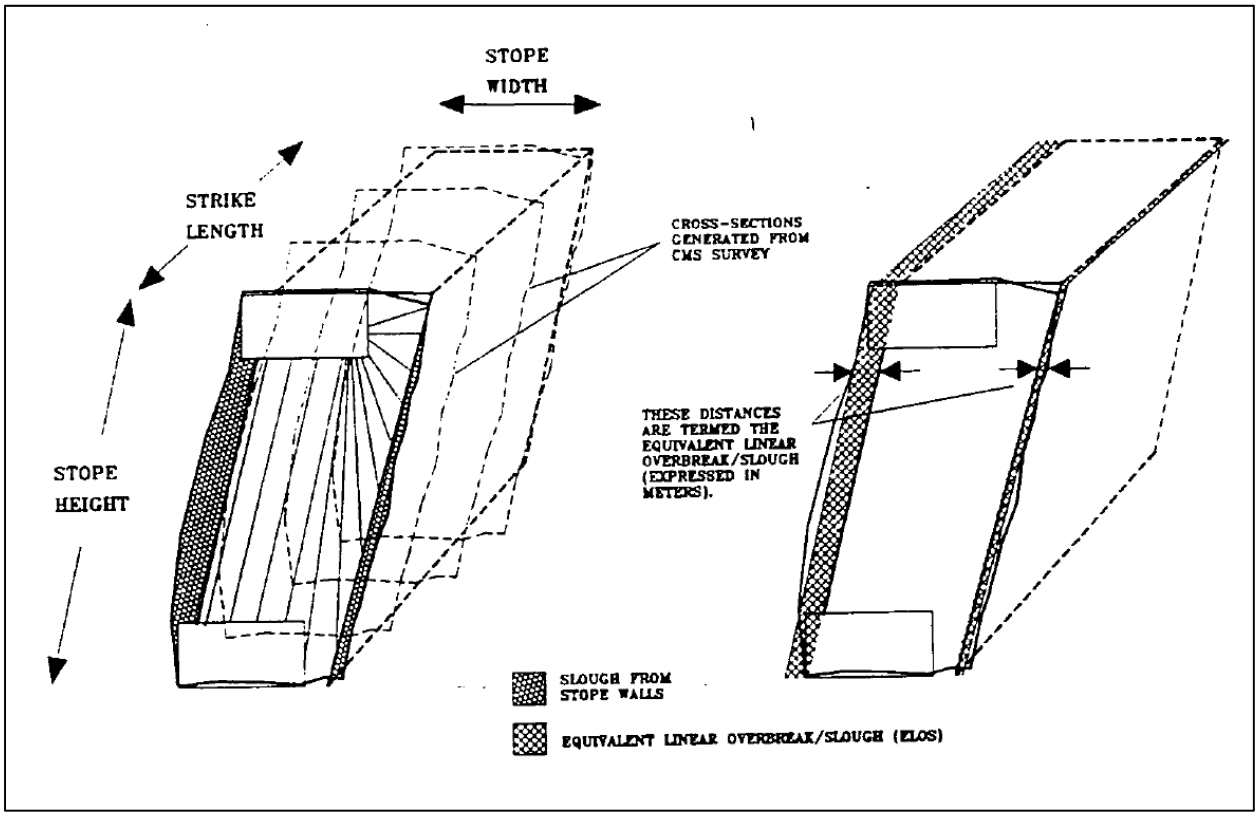

Figure 2.11 Schematic describing the calculation of ELOS (from Clark, 1998).

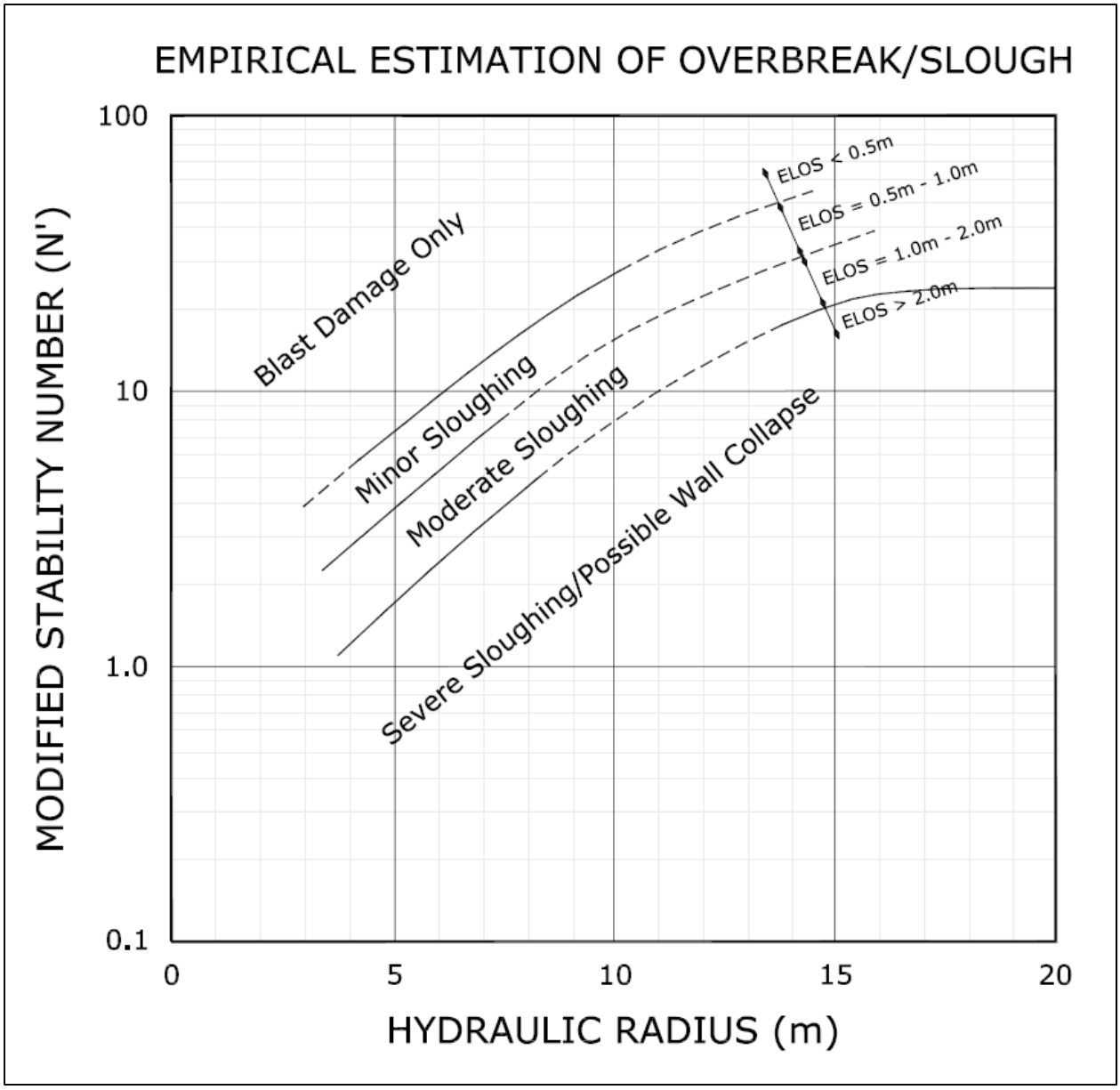

Figure 2.12 Empirical ELOS design chart (after Clark, 1998).

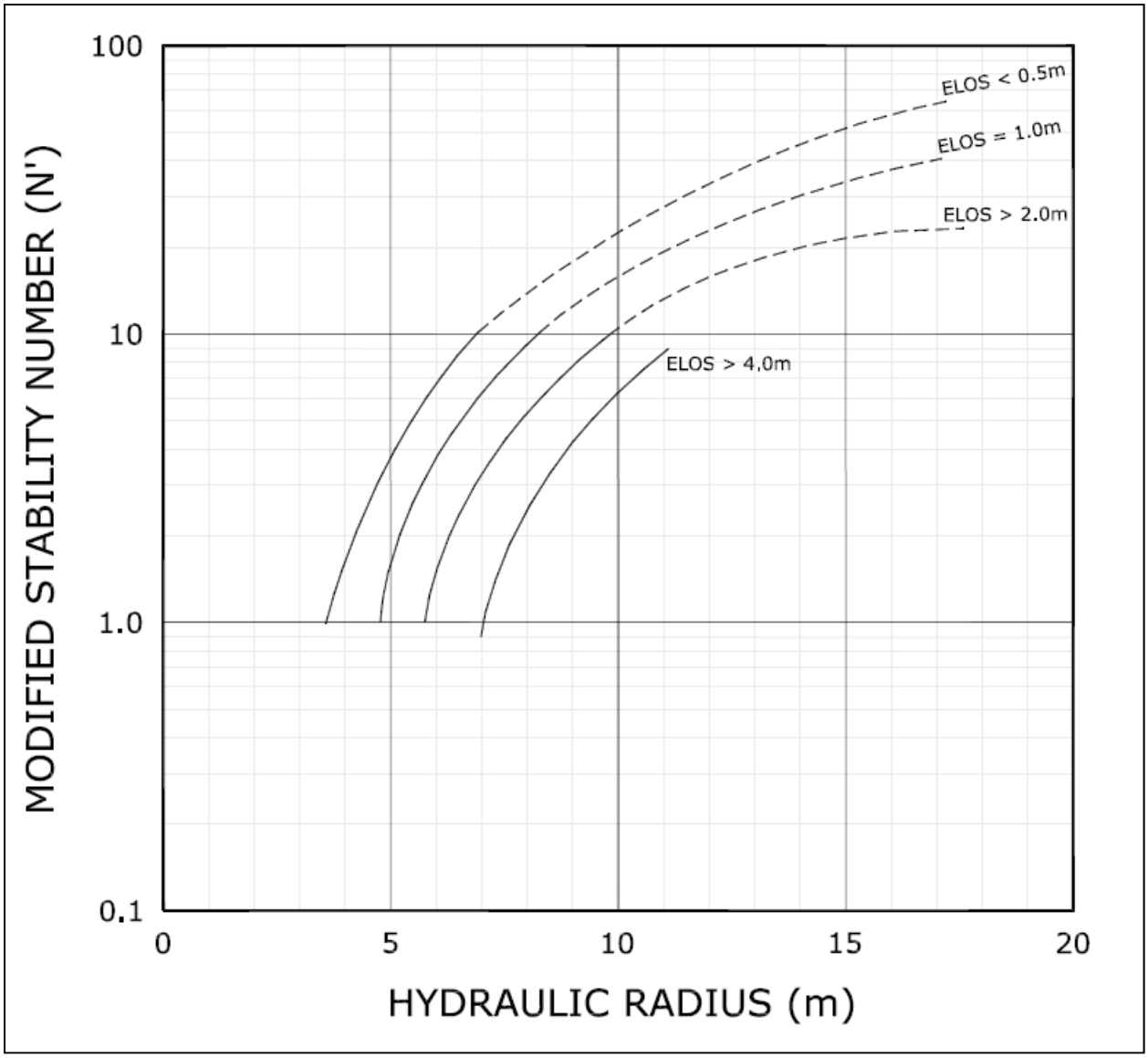

Figure 2.13 Modified Dilution Graph (after Capes, 2009).

2.4 Induced Stress in Open Panels

There are two components of stress that can result in instability of the open panel: high induced stresses that leads to stress damage of the rockmass, and stress relaxation of the panel walls that leads to reduced confinement of the rockmass. Work has been performed that examines the effects of both high induced stress and stress relaxation on panel walls and their effects on the performance of the stability of the open panels.

2.4.1 Stress Flows around an Opening

When an opening is created in a rock mass the in situ stresses will be re-distributed around the opening. Hoek and Brown (1980) describe this re-distribution of the stresses around an opening as conceptually analogous to undisturbed water flowing in a stream that encounters an obstacle. This conceptual model of stress flow around an opening is shown in Figure 2.14. In the same way that the water accelerates around the object in the stream to create fast moving water, stress will "flow" around the opening to create zones of compression or high induced stress. When the water flows around the object it will also form areas of slow moving water upstream and downstream of the object in the same way that stress will create zones of tension or de-stress the rockmass. The stressed and de-stressed (relaxed) zones will be induced in each principal induced stress direction with the greatest influence from the maximum principal induced stress.

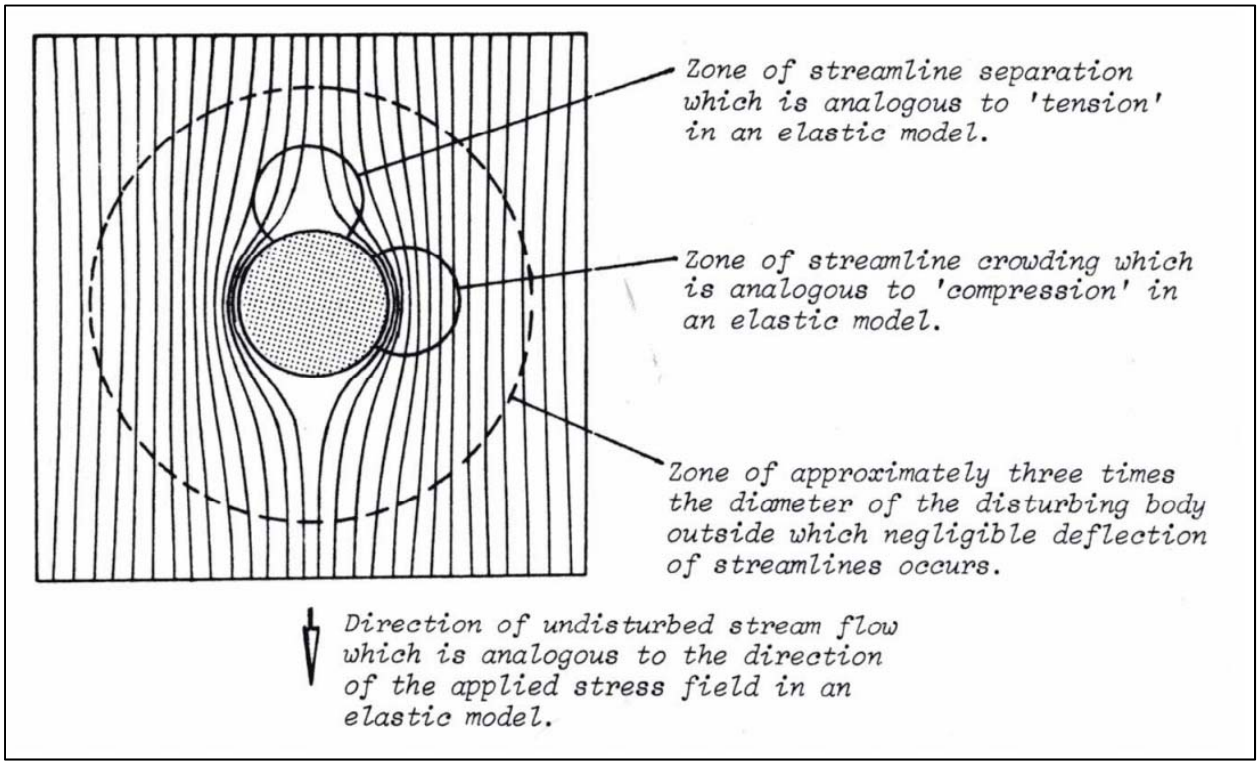

Figure 2.14 Conceptual stress flows around an excavation (from Hoek and Brown, 1980).

2.4.2 Stress History in Panel Brows

Due to the use of incremental blasting of longhole rings in narrow vein open panels, there is the potential for high induced stress in the brow to continuously move with the blasting of the panel, as shown in Figure 2.15 (Stewart, 2005). Every blast has the potential to damage the rockmass in the hangingwall and footwall adjacent to the brow. As the blasting of the panel continues, this potentially damaged rockmass in the walls becomes exposed with a potentially greater chance of failure due to the damage. Due to the configuration of narrow vein panels, blasting longhole rings is often done in small increments, which exposes more of the hangingwall and footwall to increased induced stress. A long section showing the sequence of blasting in a narrow vein longhole panel, and the subsequent brows that are formed, is shown in Figure 2.15. The stress state of the walls of the panel are accounted for in all the versions of the stability graph; however, they only consider the stress state of the wall post-mining (Mathews et al., 1981; Potvin, 1988; Nickson, 1992; Clark, 1997; Capes, 2006).

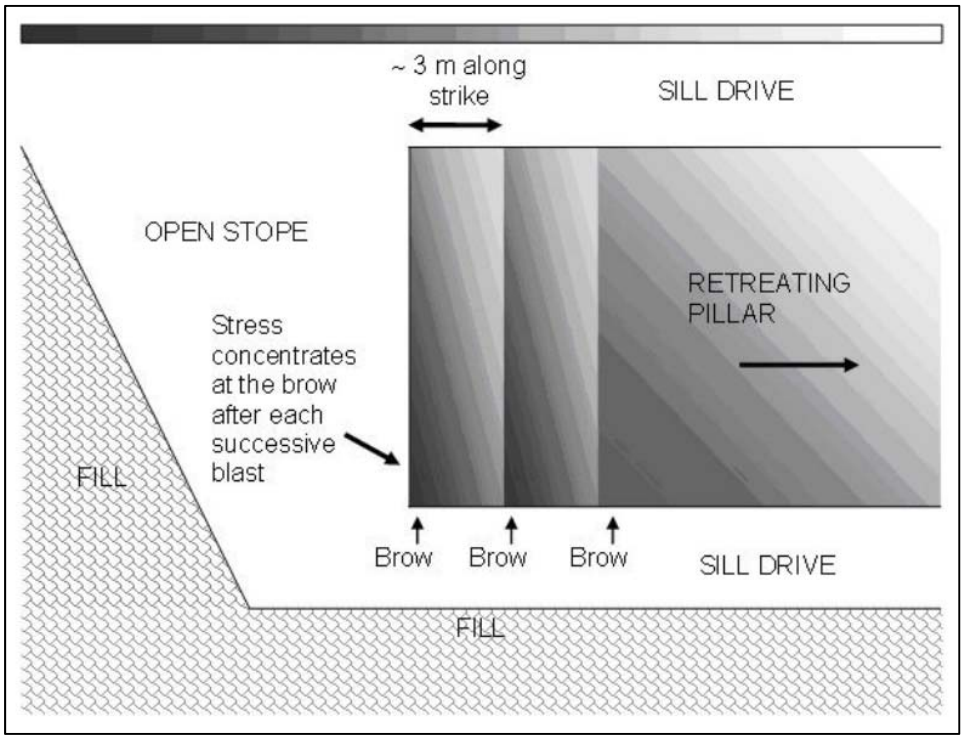

Figure 2.15 Long section of incremental blasting of a panel, showing how each brow is exposed to induced stresses (darkness of shading represents increase in induced stress) (from Stewart, 2005).

2.5 Summary

This chapter reviewed the literature on rock mass classification, empirical methods to predict the stability of open panels, the empirical methods to predict the amount of dilution expected from open panels, and the effect of induced stresses on open panels.

The work on rock mass classification that was reviewed includes the following classification methods of the rock mass: rock quality designation (RQD), the rock mass rating (RMR), and the NGI tunnel quality index (Q and Q'). These methods build upon similar characteristics of the rockmass to create a classification system. The RMR and Q system both incorporate the RQD of the rockmass that represents the frequency of jointing structure. RMR and Q both add additional rockmass characteristics such as: intact rock strength, joint surface condition, the number of joint sets present, groundwater, and various adjustments for orientation and location of the opening.

The empirical methods that predict panel stability incorporate these classification systems and add additional factors to adjust for the modes of failure that the panel wall could experience; kinematic failure due to the orientation of the joint structure (accounted for with Factors B and C) and rockmass / stress related failure (accounted for with rock mass classification and Factor A). The geometric and scale-related stability of the opening is then accounted for by using the hydraulic radius of the opening. The empirical methods build upon each other and add additional case histories to further populate the graphs, improve delineation of the stability zones, and apply statistical analysis.

The empirical methods to predict panel dilution are also built upon the stability graph methods; however, instead of using zones that delineate stability, they incorporate zones that delineate the amount of dilution. The ELOS method compares the amount of dilution in a panel, independent of its geometry. This is especially useful for thin-veined open panels, which are particularly sensitive to calculations involving a percent dilution as seen in Figure 1.6. Similar to the empirical stability graphs, the dilution graphs have been improved with the addition of case histories and rigorous statistical analysis to delineate the ELOS zones.

The work on stress histories on the brow of the open panel was also reviewed. The pre-mining stress in the panel walls is considered in Factor A of the empirical methods. However the stress

history method considers the stress in the walls as the mining front of the brow is continually moving.

The following chapter discusses the laboratory testing performed on rock from Seabee Gold Mine, and the data collection and analysis of induced stress around the open panels.

CHAPTER 3

DATA COLLECTION

This chapter presents a discussion on the data collected at the Seabee Gold Mine case study areas. Presented in this section are:

- the methodology for collecting joint data information;
- a summary of the data collected; and,
- the laboratory testing results on the different zones.

3.1 Joint Data Collection Methodology

The stability of the open panels can be quantified by the amount of dilution that the panel will experience. The panel stability is influenced by the panel geometry and the interaction between the orientation of the panel walls and joint surfaces. This section will discuss the collection of the joint data.

Joint data was collected from Seabee Mine to help quantify the rock mass behaviour and entered into a joint database for analysis. This data was critical for understanding the rock mass behaviour, to determine the transition between instability governed by discrete blocks bound by joints, and to assess overall rock mass failure through unravelling of the panel walls. To predict the likelihood of structural failure, the orientation of the joint surfaces must also be accurately measured. To generate a rock classification, the joint frequency, roughness, and alteration must be measured. Collecting joint data throughout production areas of the mine helps refine the empirical methods discussed in Section 2.3.

The methodology used for joint data collection was focused on collecting key parameters from the rock mass in order to aid in the characterization of the rock mass. These parameters were later used for the calculation of potential structural failure and for rock mass classification. The locations within the production area that were chosen for joint data collection were limited by the production practices and the access that was available and included development access to the overcuts and undercuts. The joint sets of primary concern are those that run parallel to the open panel surface and these sets are most easily identified when mapping a development drift that is orientated perpendicular to the open panel surface. For each panel discussed in Section 1.1

(Figure 1.5), the distance that could be mapped was approximately 20m from the entrance of the access to the undercut/overcut drift. The accesses that were available for measuring joint surfaces were:

- 2b10010 #1,2, and 3 access;
- 2b11009 #3 access;
- 2b11011 #1,2 and 3 access;
- 2b11011 #2 sill;
- 2b11013 #4,5,6 and 7 access; and,
- L62 990 level.

The data parameters that were collected are shown in Figure 3.1. The instrumentation used for the collection of this data include:

- Clar compass;
- profile or carpenter comb; and,
- folding ruler.

The dip and dip direction of the joint surfaces were recorded with the Clar compass with respect to mine north (43° west of true north). The planarity of the joint surface was recorded by measuring the maximum amplitude of the joint surface as a variation from planar, as measured from a datum defined by the ruler lying across the joint surface. The roughness of the joint surface was measured using the carpenter comb and recorded as a JRC for a 10 cm length. The infilling, ends visible, joint length, amount of water present, and an estimation of block size were recorded based on visual observations.

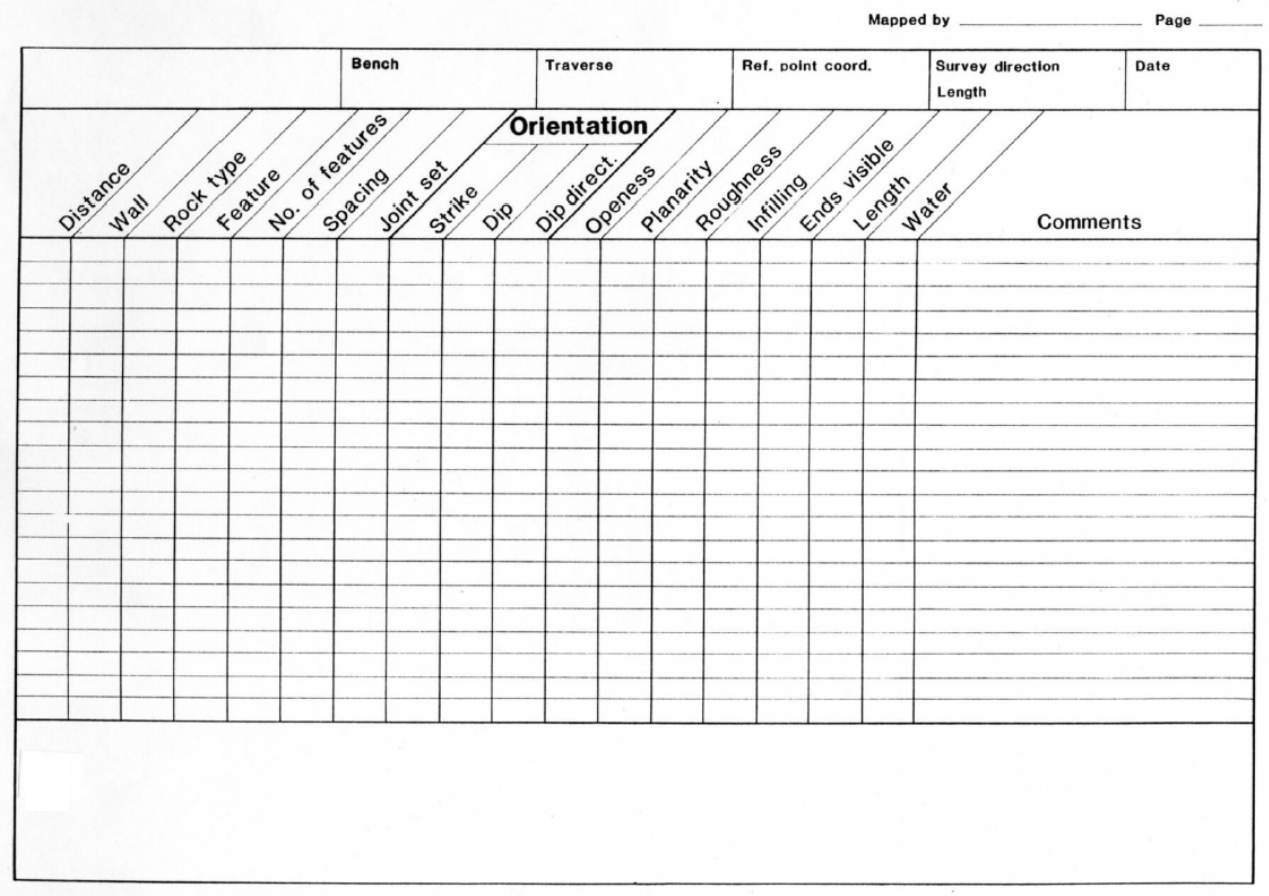

Figure 3.1 Example sheet for the recording of joint surface data collection.

3.2 Cavity Monitoring System (CMS)

To quantify the amount of dilution from a panel, the Cavity Monitoring System (CMS) was used to create a 3D image of the empty panel. The CMS surveys provided a database from which overbreak/underbreak could be calculated for the open panels. This database of dilution data is critical for the assessment of panel performance as it allows for the quantification of whether there was lost revenue from mining the panel which could be caused by weak rock being mucked with the ore and/or ore left in the panels. Additionally, this data is required for the development of the empirical methodology of predicting panel performance and so was analysed for this thesis.

3.2.1 Limitations of the CMS

The largest limitation to the CMS survey is its inability to measure to objects that are not in the line of sight of the survey instrument; which is especially a problem in narrow vein mining. This

creates shadows or pockets where there is no data recorded because the line of sight of the CMS station was blocked by an object (Figure 3.2). A list of common underground conditions that can create a blockage have been summarized by Clark (1998):

- blasted muck on the floor of the undercut or walls;
- mesh hanging from the walls;
- protruding ground support and support services;
- extreme fog and dust;
- backfill on the undercut if the survey is not taken immediately after blasting, or ore on the undercut if the survey is taken to soon; and,
- irregular shaped open panels (bends in the ore along the dip or strike).

In narrow vein mining, the two most significant factors of those listed are backfill in the open panel and irregular shaped open panels. Often in narrow vein mines, there is limited area to store excess waste rock and operations cannot wait for a CMS survey to be completed before they must begin backfilling the open panel. If the team performing the CMS survey is unable to get to the panel within the same day that the open panel is finished blasting and mucking, it can often already be filled from 1/4 to 1/3 with backfill. This will hide a large portion of the open panel walls from the CMS survey. Additionally, in narrow vein mines the effect of an irregular open panel more easily creates shadowing on the CMS survey than an open panel of similar HR but larger ore width. This effect can be seen in Figure 3.2. A narrow width open panel limits the angle between the laser line of sight and the panel wall, a shadow then occurs if the angle to the irregularity is equal to or greater than the angle that the laser is hitting the panel surface. With a wide width panel, these angles soon become so large that they have no effect on the CMS survey.

The scanning angle increment is the final variable that limits the accuracy of the CMS survey and this is controllable by the user. This effect can be seen by comparing Figure 3.2 with Figure 3.3. The larger the incremental degree scanning angle, the worse the resolution will be away from the station. A larger degree scanning angle is sometimes chosen to limit the scanning time of the survey.

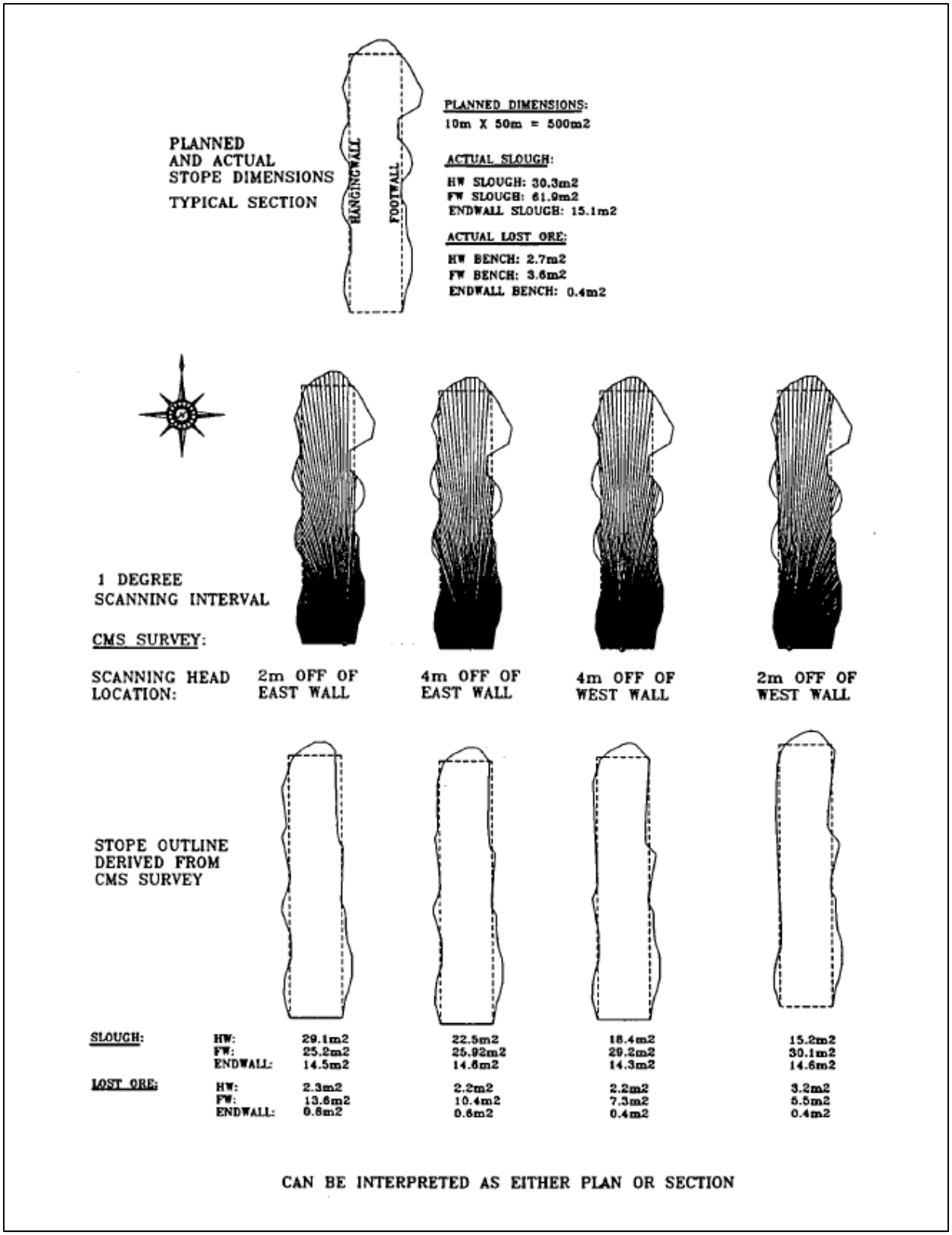

Figure 3.2 Schematic showing the line of sight limitations of the CMS (from Clark, 1998).

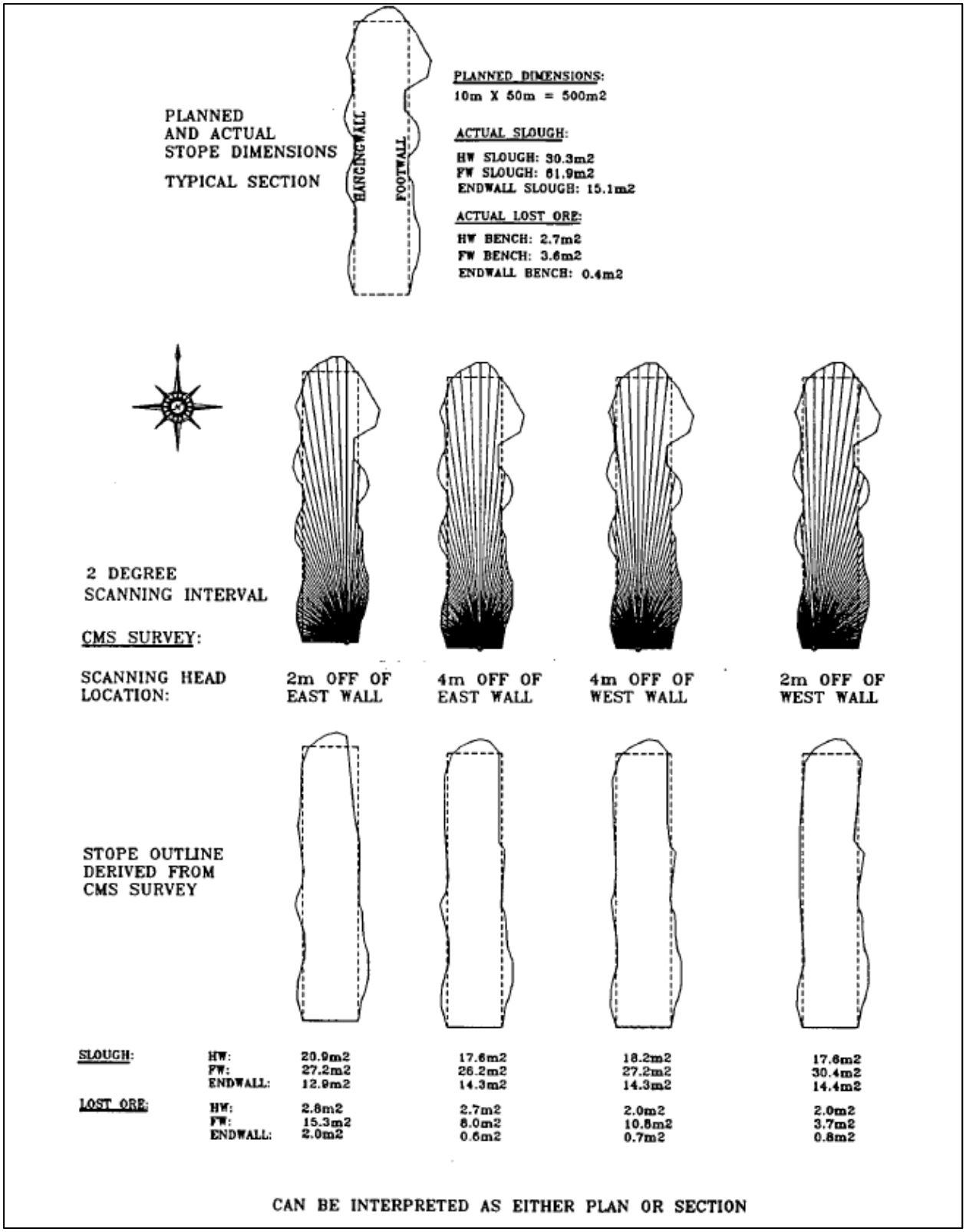

Figure 3.3 Schematic showing the line of sight limitations with a 2° interval (from Clark 1998).

3.2.2 Data Collection

The data was collected from three case study areas: 2b11013, 2c10010, and 2c11011 (Figure 1.5). The CMS was performed as soon as possible after mucking so that wall failure due to exposure time was not a significant factor. The CMS station should be extended into the panel at a location that maximises the coverage area and minimizes shadowing. The CMS should also be surveyed from control points so that its position within the open panel is accurate. The CMS can then survey the finished panel walls and the data can be processed on surface.

This procedure to obtain a CMS of the open panel took approximately 1-2 hours. Once the data was processed and transferred into the main computer system, it was analysed to determine the amount of overbreak and underbreak that occurred in that open panel. This was achieved by overlaying the CMS survey onto the designed open panel in AutoCAD. Sections were then cut perpendicularly through the open panel on 1.5m intervals and the amount of overbreak and underbreak could be seen in these sections. Figure 3.4 is an example of a cut section in AutoCAD that shows overbreak and underbreak. The panels from the case history locations were analysed using this method as part of this research.

The data from each section was then analysed to determine the average ELOS per blast ring by taking the overbreak area and dividing by the height of the sections from the bottom of the overcut to the top of the undercut. This is as per the procedure described in Section 2.3.2. This data can then be presented in bar graph form as seen in Figure 3.5 and 3.6. The bar graphs are presented with the ring number for the production holes presented on the x – axis. These rings are spaced with a 1.5m burden along the strike of the panel. The panels are separated by rib pillars which are represented by the boundaries of the boxes within the graph. The bars in Figure 3.5 and 3.6 represent the ELOS on the north and south walls of the panel respectively. The bar graphs for each panel in the study can be found in Appendix A. The ELOS data was presented in the bar graph format in order to easily identify trends in the data that can provide information on where dilution is occurring. It can be seen in both Figure 3.5 and 3.6 that in the majority of the panels, there is relatively little dilution close to the pillars (adjacent to the boxes), and the majority of the dilution occurs towards the center of the panels. In Figure 3.5 and 3.6, Panels 3, 4, 5 and 9, are not shown due to poor CMS data that was obtained. This relates to the limitations of the CMS (Section 2.3.1), where too many shadows were present in the CMS data.

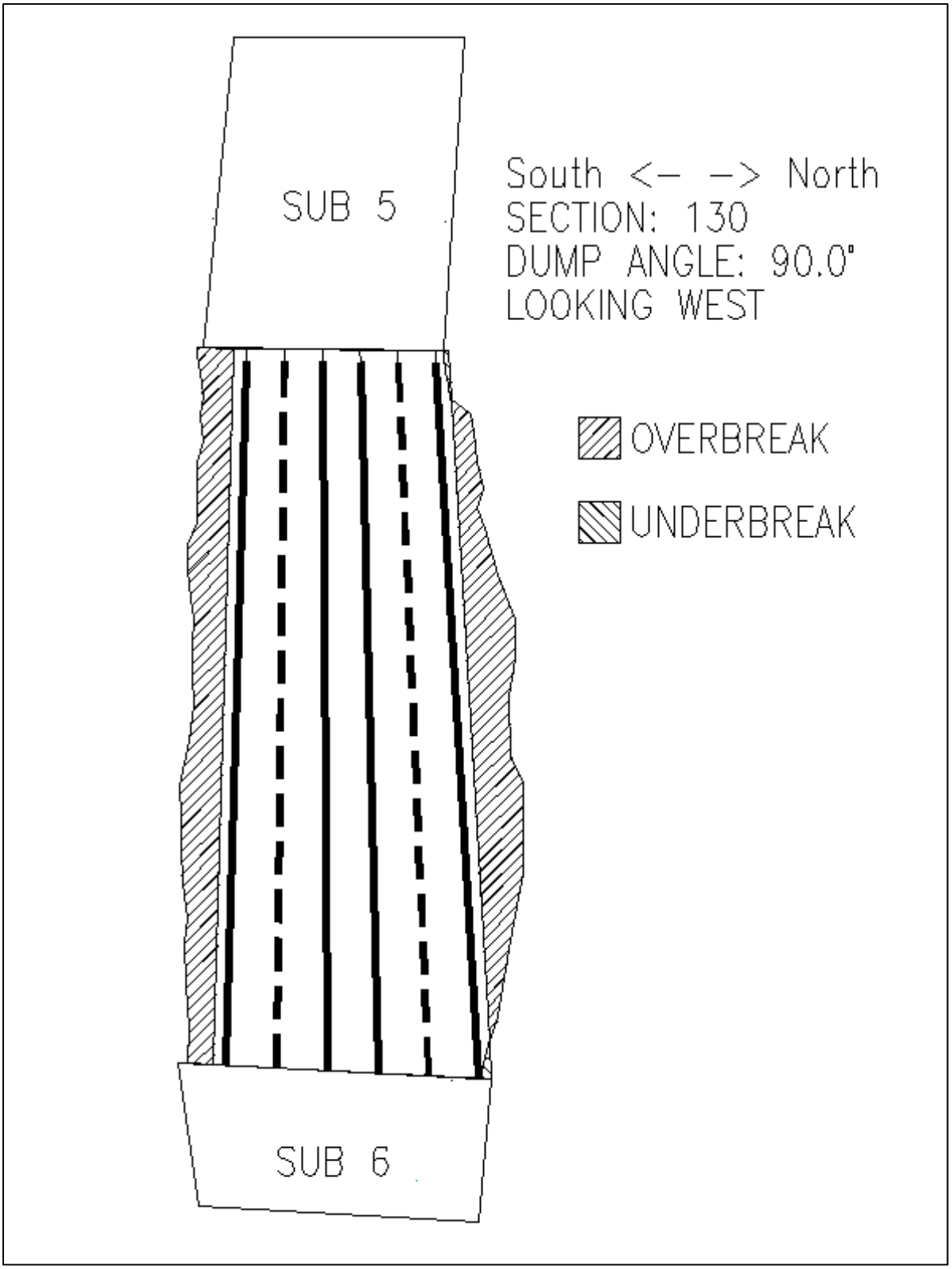

Figure 3.4 A single section from 2b11013 5-6 Panel 10 that depicts the overbreak and underbreak in the open panel.

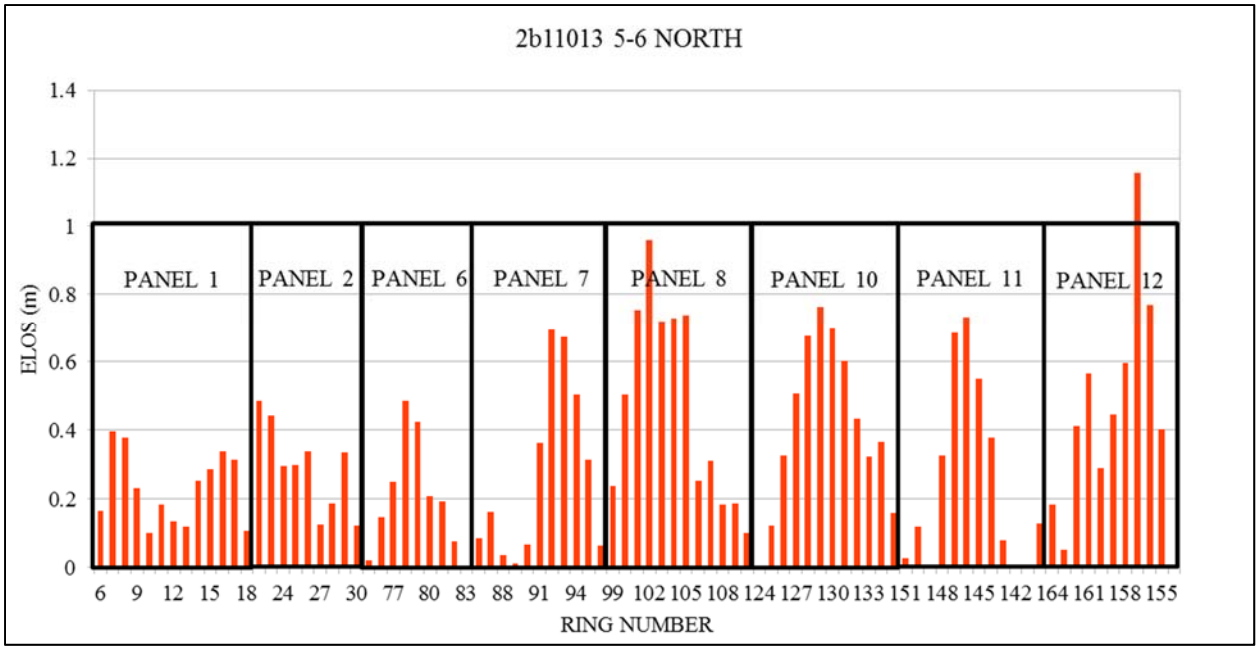

Figure 3.5 A bar graph showing the ELOS against ring number for 2b11013 5-6 north wall.

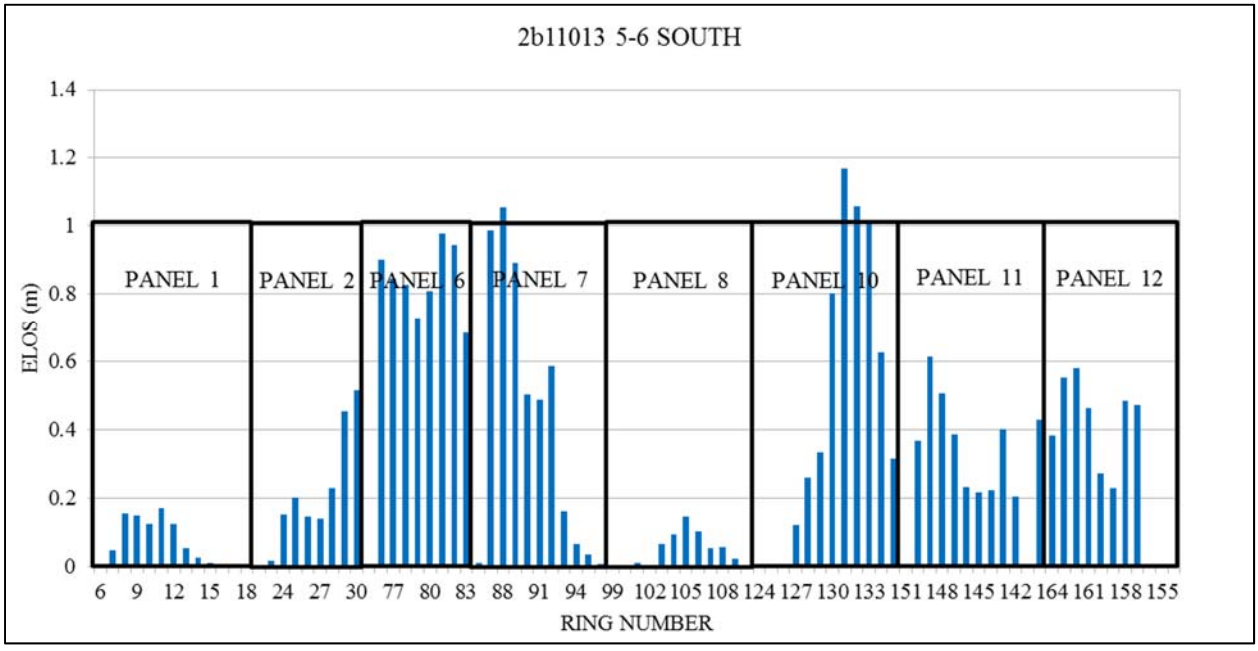

Figure 3.6 A bar graph showing the ELOS against ring number for 2b11013 5-6 south wall.

3.3 Joint Data Collection in Case Study Areas

The data that was collected, and location, is summarized in Figure 3.7. This also includes a stereonet of the joint orientations and a modified JRC chart of joint roughness. Summary plan views for all areas the data was collected from can be found in Appendix B.

As part of this research, the JRC-Joint Amplitude chart (Figure 2.2) was modified for field data applications. During data collection there was difficulty in measuring, or finding, joints that were 1m in length or greater. Joints of that length are required in order to classify the $J_{r/w}$ (joint waviness) as the waviness category on the graph does not extend below 1m. The $J_{r/w}$ category lines were extended to smaller joint profile lengths using Equation 3.1 (Barton and Bandis, 1982) and results are shown in Figure 3.7. The zone for estimating $J_{r/w}$ was extended to include joint profile lengths between 0.3m and 1.0m. It was felt that profile lengths less than 0.3m could not reliably represent joint waviness.

$$JRC_n = JRC_o \left(\frac{L_n}{L_o}\right)^{-0.02JRC_o} \tag{3.1}$$

where:

JRC_n is the *scaled JRC*;

JRC_o is the *original JRC*;

L_o is the *dimension of the surface used to measure* JRC_o; and,

Ln is the *dimension of the actual sliding surface*.

This data was also used in the calculation of N' of the rock mass for each area. This data was summarized in conjunction with the CMS surveys performed and open panel geometries and is shown in Table 3.1. It is of note that all areas that were mapped were dry to moist which gives a J_w value of 1.0 for all measurements taken.

A full summary of the collected data for the case study panels that includes the panel geometry (strike length, exposed panel height, hydraulic radius, orebody dip, ore width, and stability number), the level and number of panels mined adjacent to the panel, and the dilution data for the panel is given in Tables 3.2 and 3.3. A full summary of the recorded joint information including RQD, Jn, Jr/r, Jr/w, Jr, Ja, Jw and Q' is given in Table 3.4.

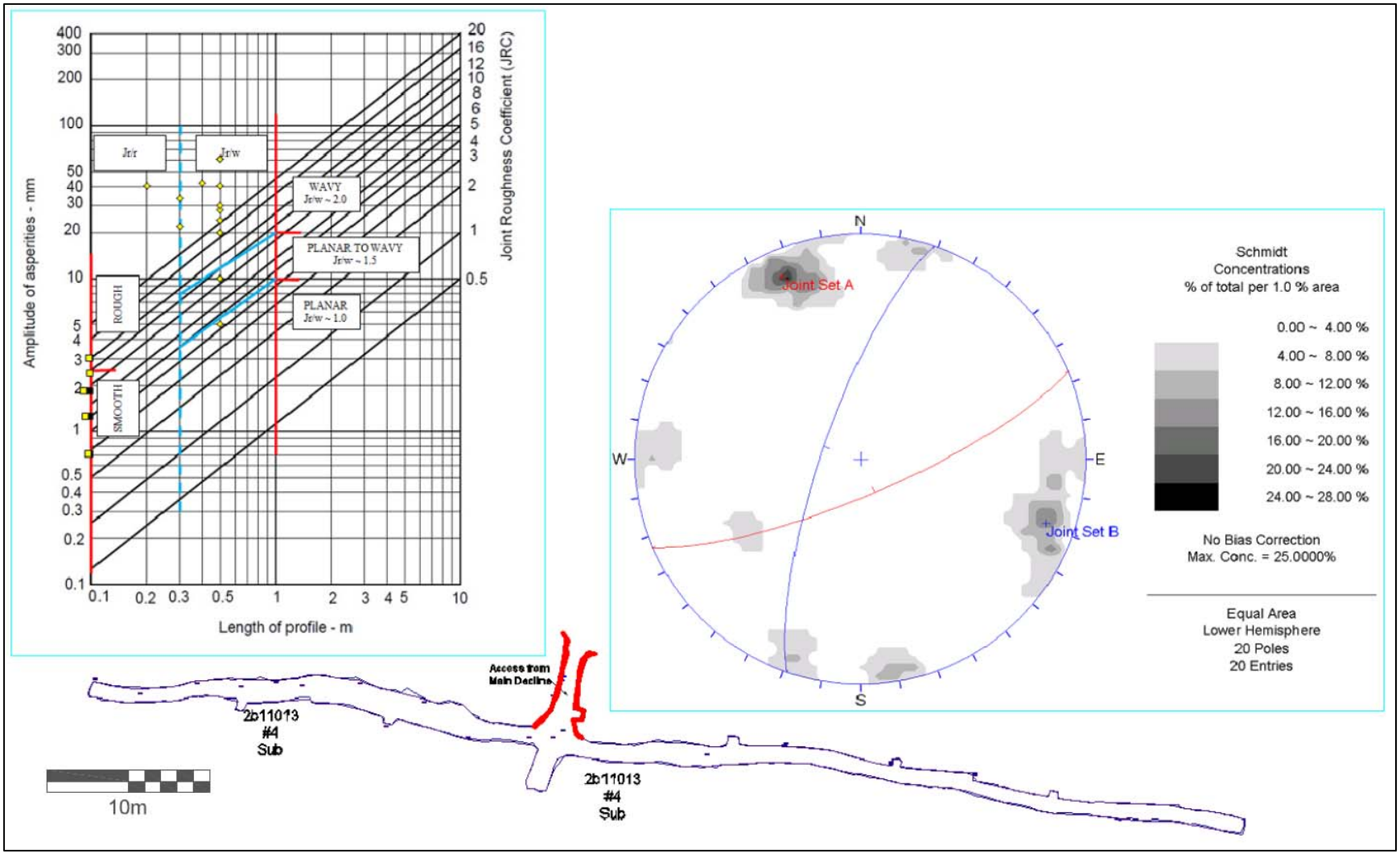

Figure 3.7 Joint mapping data collected from 2b11013 #4 access shown in plan view.

Table 3.1 Panel summary sheet for 2b11013 5-6 Panel 12 (after Wang, 2004).

SEABEE MINE 2b11013 5-6 Panel 12 STOPE SUMMARY				
General	Wall		South	
	Strike Length		18	m
	Exposed Height		16.7	m
	Hydraulic Radius (HR)		4.38	m
	Dip		81	degress
	Ore Width		3.2	m
	N'		17.5	
Stope Situation	Level		2	
	Adjacent Mined	**0** side / **1** side / **2** sides	1	
Dilution	O/B Volume		96.4	m^3
	ELOS Avg.		0.328	m

Table 3.2 Panel information summary for all available case histories.

	General							Stope Situation		Dilution	
Stope	Wall	Strike Length (m)	Exposed Height (m)	Hydraulic Radius	Dip (°)	Ore Width (m)	N'	Level	Adjacent Mined	O/B Volume (m^3)	ELOS Avg. (m)
2b11013 6-7 Panel 1	North	32.9	18.9	6	87	3.24	16.8	1	0	103.2	0.204
2b11013 6-7 Panel 1	South	32.9	18.9	6	87	3.24	16.8	1	0	173.6	0.346
2b11013 6-7 Panel 2	North	20.5	18.7	4.7	78	6.04	16.8	1	1	58.4	0.14
2b11013 6-7 Panel 2	South	20.5	18.7	4.7	78	6.04	16.8	1	1	535	1.321
2b11013 6-7 Panel 3	North	19.5	19.3	4.7	87	6	16.8	1	1	2.3	0.004
2b11013 6-7 Panel 3	South	19.5	19.3	4.7	87	6	16.8	1	1	247.2	0.741
2b11013 6-7 Avoca	North	N/A	17.8	4.5	88	2.79	16.8	1	1	259.3	0.511
2b11013 6-7 Avoca	South	N/A	17.8	4.5	88	2.79	16.8	1	1	88.4	0.168
2b11013 5-6 Panel 1	North	23	17.2	4.88	84	2.14	17.5	2	0	71.2	0.218
2b11013 5-6 Panel 1	South	23	17.2	4.88	84	2.14	17.5	2	0	22.2	0.068
2b11013 5-6 Panel 2	North	17.9	17.2	4.42	88	1.8	17.5	2	1	68.1	0.29
2b11013 5-6 Panel 2	South	17.9	17.2	4.42	88	1.8	17.5	2	1	49.2	0.208
2b11013 5-6 Panel 6	North	13.2	17	3.65	82	2.8	17.5	2	1	52.4	0.217
2b11013 5-6 Panel 6	South	13.2	17	3.65	82	2.8	17.5	2	1	198.4	0.815
2b11013 5-6 Panel 7	North	16.8	16.7	4.17	83	3.4	17.5	2	1	93.7	0.27
2b11013 5-6 Panel 7	South	16.8	16.7	4.17	83	3.4	17.5	2	1	148.7	0.434
2b11013 5-6 Panel 8	North	16.3	17.2	4.18	80	5	17.5	2	1	132.8	0.535
2b11013 5-6 Panel 8	South	16.3	17.2	4.18	80	5	17.5	2	1	11.9	0.047
2b11013 5-6 Panel 10	North	19.3	17.6	4.61	82	3.6	17.5	2	1	144.8	0.441
2b11013 5-6 Panel 10	South	19.3	17.6	4.61	82	3.6	17.5	2	1	157.9	0.486
2b11013 5-6 Panel 11	North	16.4	17.6	4.24	81	3.8	17.5	2	1	75.5	0.262
2b11013 5-6 Panel 11	South	16.4	17.6	4.24	81	3.8	17.5	2	1	86.2	0.277
2b11013 5-6 Panel 12	North	18	16.7	4.38	81	3.2	17.5	2	1	120.5	0.409
2b11013 5-6 Panel 12	South	18	16.7	4.38	81	3.2	17.5	2	1	96.4	0.328
2c10010 1-2 Panel 1	North	13.7	17.1	3.8	89	3.6	17.5	3	-	91.5	0.3
2c10010 1-2 Panel 1	South	13.7	17.1	3.8	89	3.6	17.5	3	-	13.9	0.045
2c10010 2-3 Panel 1	North	21.3	17.5	4.8	87	4.2	18.2	2	-	160.4	0.543
2c10010 2-3 Panel 1	South	21.3	17.5	4.8	87	4.2	18.2	2	-	2.8	0.01

Table 3.3 Panel information summary for all available case histories (continued).

	General							Stope Situation		Dilution	
Stope	Wall	Strike Length (m)	Exposed Height (m)	Hydraulic Radius	Dip (°)	Ore Width (m)	N'	Level	Adjacent Mined	O/B Volume (m^3)	ELOS Avg. (m)
2c10010 2-3 Panel 2	North	22.9	17.5	4.9	86	3.9	18.2	2	-	63.1	0.148
2c10010 2-3 Panel 2	South	22.9	17.5	4.9	86	3.9	18.2	2	-	144.4	0.342
2c10010 2-3 Panel 3	North	24	17.8	5.1	88	3.2	18.2	2	-	64.6	0.197
2c10010 2-3 Panel 3	South	24	17.8	5.1	88	3.2	18.2	2	-	101.4	0.307
2c10010 3-4 Panel 1	North	17.2	16.5	4.2	85	3.5	17.6	1	-	106.6	0.327
2c10010 3-4 Panel 1	South	17.2	16.5	4.2	85	3.5	17.6	1	-	43.7	0.134
2c10010 3-4 Panel 2	North	16.3	16.5	4.1	80	4.6	17.6	1	-	108.3	0.365
2c10010 3-4 Panel 2	South	16.3	16.5	4.1	80	4.6	17.6	1	-	71.9	0.241
2c10010 3-4 Panel 3	North	8.5	16.5	2.8	87	2.9	17.6	1	-	121.5	0.281
2c10010 3-4 Panel 3	South	8.5	16.5	2.8	87	2.9	17.6	1	-	66.8	0.155
2c10010 3-4 Panel 4	North	17.1	16.5	4.2	86	4	17.6	1	-	128.8	0.437
2c10010 3-4 Panel 4	South	17.1	16.5	4.2	86	4	17.6	1	-	97.9	0.339
2c10010 3-4 Panel 5	North	21.9	17.2	4.8	89	2.5	17.6	1	-	61.8	0.194
2c10010 3-4 Panel 5	South	21.9	17.2	4.8	89	2.5	17.6	1	-	207.3	0.654
2b11011 1UP Panel 1	North	24.9	18	5.2	84	3.8	17.4	4	-	100.1	242
2b11011 1UP Panel 1	South	24.9	18	5.2	84	3.8	17.4	4	-	170.4	0.397
2b11011 1UP Panel 2	North	23.5	18	5.1	86	4.1	17.4	4	-	91.5	0.223
2b11011 1UP Panel 2	South	23.5	18	5.1	86	4.1	17.4	4	-	388.6	1.073
2b11011 1-2 Panel 1	North	18.1	17.8	4.5	89	2.7	16.7	3	-	-	0.184
2b11011 1-2 Panel 1	South	18.1	17.8	4.5	89	2.7	16.7	3	-	-	0.641
2b11011 2-3 Panel 1	North	18	18.2	4.5	87	3.1	17.2	2	-	-	0.101
2b11011 2-3 Panel 1	South	18	18.2	4.5	87	3.1	17.2	2	-	-	0.149
2b11011 2-3 Panel 2	North	27.9	18.2	5.5	86	3.4	17.2	2	-	-	0.257
2b11011 2-3 Panel 2	South	27.9	18.2	5.5	86	3.4	17.2	2	-	-	0.392
2b11011 3-4 Panel 1	North	14.1	16	3.7	89	3.5	18.9	1	-	-	0
2b11011 3-4 Panel 1	South	14.1	16	3.7	89	3.5	18.9	1	-	-	0.533
2b11011 3-4 Panel 2	North	12.9	16	3.6	88	3.8	18.9	1	-	-	0.257
2b11011 3-4 Panel 2	South	12.9	16	3.6	88	3.8	18.9	1	-	-	0.539

Table 3.4 Full joint information that was recorded at Seabee Gold Mine.

Stope	# Joints Recorded	RQD	Jn	Jr/r	Jr/w	Jr	Ja	Jw	Q'
2b11013 #4 Access	20	75	12	1	2	2	1	1	12.5
2b11013 #5 Access	23	90	12	1	1.5	1.5	1	1	11.3
2b11013 #6 Access	28	80	12	1	2	2	1	1	13.3
2b11013 #7 Access	10	85	12	1	1.5	1.5	1	1	10.6
2b11011 #1 Access	20	75	12	1	2	2	1	1	12.5
2b11011 #2 Access	9	90	12	1	1.5	1.5	1	1	11.3
2b11011 #2 Sill	11	90	12	1	1.5	1.5	1	1	11.3
2b11011 #3 Access	20	75	12	1.5	1.5	2.25	1	1	14.1
2c10010 #1 Access	26	100	12	1	1.5	1.5	1	1	12.5
2c10010 #2 Access	21	75	12	1	2	2	1	1	12.5
2c10010 #3 Access	18	80	12	1	2	2	1	1	13.3

3.4 Laboratory Testing of Core Samples for Intact Rock Properties

A laboratory testing program for estimating rock strength properties was conducted on 30.5mm diameter core samples taken from the Seabee Gold Mine. The core samples, from diamond drill holes U11-037 and U11-357, encompass the three zones of interest for panel stability considerations: the hangingwall, footwall and orezone. The core boxes were shipped to the University of Saskatchewan rock mechanics lab and cut to testing length according to ASTM standards.

The following five tests were performed on the core: point load index test, Brazilian, triaxial, ultrasonic velocity and the uniaxial compressive strength (UCS). The rock properties obtained included UCS, tensile strength, internal angle of friction, cohesive strength and elastic properties. Raw data is contained in Appendix C and the results are summarized by zone in Sections 3.4.6 to 3.4.8.

3.4.1 Uniaxial Compressive Strength (UCS) Test

The purpose of the UCS test was to obtain the strength of the core sample under axial load, with no confinement. The samples were tested in a Tinius – Olsen testing machine with a corresponding data logging system for load and strain, when required. A constant loading rate was applied until sample failure occurred. The testing procedure followed was ASTM D7012-10 (2008). Each sample had a minimum length to diameter ratio of 2. Two variations of the UCS test were performed. The first was with strain gauges attached to the sample to calculate the static elastic modulus and Poisson's ratio of the core sample. The second variation was without strain gauges to obtain the UCS of the sample alone. Five samples were tested with strain gauges for each zone and five samples were tested without strain gauges. The raw data is shown in the appendix in Tables C.1 to C.15.

3.4.2 Point Load Index Test

The point load test is a quick and inexpensive test designed to find an index value for rock strength. It is used as an alternative to UCS since sample preparation is much easier. The testing procedure followed was ASTM D5731-08 (2008). The number of core samples tested ranged from 19 to 21 samples per structure. The raw data is tabulated in Appendix C, Tables C.13 to

C.15. The point load results were correlated to UCS using and $I_{s(50)}$ that was calculated using Equation 3.2 as follows:

$$I_s = \frac{P}{{D_e}^2} \tag{3.2}$$

where:

I_s is the *Point Load Index*;

P is the *Failure Load (N)*; and

D_e is the *Equivalent Core Diameter (mm)*.

I_s is then corrected for size to $I_{s(50)}$ (the equivalent of 50mm core diameter) by multiplying by the size correction factor, F. The conversion factor, K, was found by correlating the UCS data and $I_{s(50)}$ data using the relationship expressed in Equation 3.3 as:

$$UCS = K \times I_{s(50)} \tag{3.3}$$

3.4.3 Brazilian Test

The purpose of the Brazilian test was to obtain the tensile strength of the core sample. The testing procedure followed was ASTM D3967-08 (2008), using the Tinius – Olsen testing machine. Peak load and sample dimensions were used to calculate the splitting tensile strength. The number of core samples tested for each structure was 10. The samples were cut to a length – to – diameter ratio of between 0.4 – 0.7. The results are summarized in Tables C.4 to C.6.

3.4.4 Triaxial Test

The purpose of the triaxial testing was to measure the confined compressive strength over a range of confining pressures. Results from multiple tests were used to define the strength envelope for each of the structures, thereby providing the cohesion and internal angle of friction, and the angle of the failure plane. The testing procedure followed was ASTM D7012-10 (2010).

The number of core samples tested for each structure was 4. Each sample had a minimum length – to – diameter ratio of 2. Each sample was protected against oil penetration using a rubber jacket. The protected sample was placed into the triaxial cell between loading platens. The cell was filled with hydraulic oil and placed into the loading frame. A confining pressure was applied to the sample and the axial load was increased until the sample failed. The peak load was used to calculate the strength of the sample at each confining stress. The results are contained in Tables C.1 to C.3 and plotted in Figures C.16 to C.18.

3.4.5 Ultrasonic Velocity Test

The purpose of the Ultrasonic Velocity test was to estimate the dynamic elastic constants of the UCS and triaxial core samples. The non – destructive testing procedure followed was ASTM D2845-08 (2008). Fourteen samples were tested for each structure. For the procedure, 1MHz P and S – wave velocity transducers and lead foil were positioned at each end of the samples that were placed in a loading frame. A load of 1 tonne was applied to ensure good contact between the sample and transducer. Travel time of the waves between transducers was measured using an oscilloscope. The true travel time through the sample was obtained by subtracting the correction for zero transducer time. Velocity and dynamic elastic properties were calculated using the sample dimensions and P and S wave travel time. The results are contained in Tables C.7 to C.9.

3.4.6 Hangingwall Structure Results

The total number of core samples tested in the hangingwall structure was 43. Table 3.5 provides the location where each sample was taken, specimen dimensions and test type, and sample densities. The corresponding raw data is found in Appendix C. The average density of the hangingwall structure was 2950 ± 95kg/m^3.

A conversion factor, K, of 18 can be used to estimate UCS from the point load test results, based on this testing. Assumed values of K are usually between 22 and 24, however, calibrating the K value by conducting both tests from samples cut from a single length of core provides a site specific calibration. The UCS to indirect tensile strength ratio was approximately 7.7. A photograph of a Brazilian sample is shown in Figure 3.8. The average static elastic modulus was 43 ± 11GPa and the dynamic was 54 ± 6GPa. It is typical of laboratory data that the static modulus is lower than the dynamic modulus because they measure elastic properties at much

different loading rates. The internal angle of friction from the triaxial test was found to be 45° and the cohesion 12MPa using the Mohr – Coulomb plot in Figure 3.9. Figure 3.10 shows a failed sample. A summary of the testing results is in Table 3.6.

Table 3.5 Information on core samples from the hangingwall structure.

Sample Name	Hole Number	Depth (m)	Test Type	Length (mm)	Diameter (mm)	Volume (m^3)	Mass (g)	Density (kg/m^3)
HW1	U11-037	162.15	Triaxial	69.51	30.49	5.08E-05	157.43	3102
HW2	U11-037	162.25	Triaxial	69.56	30.52	5.09E-05	153.24	3011
HW3	U11-037	162.35	Triaxial	69.61	30.52	5.09E-05	155.7	3057
HW4	U11-037	162.45	Triaxial	71.26	30.5	5.21E-05	157.08	3017
HW5	U11-037	162.70	UCS	68.73	30.52	5.03E-05	152.6	3035
HW6	U11-037	162.95	UCS	68.87	30.5	5.03E-05	148.18	2945
HW7	U11-037	163.05	UCSstrain	67.52	30.55	4.95E-05	146.31	2956
HW8	U11-037	164.05	UCS	71.22	30.51	5.21E-05	145.45	2793
HW9	U11-037	164.20	UCS	70.22	30.49	5.13E-05	148.59	2898
HW10	U11-037	163.95	UCSstrain	68.03	30.5	4.97E-05	137.33	2763
HW11	U11-357	165.00	Brazilian	19.70	30.52	1.44E-05		
HW12	U11-357	165.94	Brazilian	19.37	30.51	1.42E-05		
HW13	U11-357	165.97	Brazilian	20.00	30.55	1.47E-05		
HW14	U11-357	166.01	Brazilian	20.50	30.51	1.50E-05		
HW15	U11-357	166.04	Brazilian	19.23	30.55	1.41E-05		
HW16	U11-357	172.05	UCS	67.60	30.24	4.86E-05	144.53	2977
HW17	U11-357	172.12	UCSstrain	68.26	30.24	4.90E-05	144.84	2954
HW18	U11-357	172.19	UCSstrain	71.84	30.23	5.16E-05	146.76	2846
HW19	U11-357	172.26	UCSstrain	67.44	30.24	4.84E-05	144.77	2989
HW20	U11-357	172.00	Brazilian	11.88	30.28	8.55E-06		
HW21	U11-357	172.01	Brazilian	13.41	30.21	9.61E-06		
HW22	U11-357	172.03	Brazilian	13.93	30.22	9.99E-06		
HW23	U11-357	172.04	Brazilian	12.22	30.24	8.78E-06		
HW24	U11-357	172.05	Brazilian	14.02	30.25	1.01E-05		
AVERAGE								2953 ± 95

Table 3.6 Summary of testing results for the hangingwall structure.

Zone / Box	Conversion Factor, K	UCS Point Load (MPa)	UCS (MPa)	Tensile Strength (MPa)	Static E (GPa)	Static ν	Dynamic E (GPa)	Dynamic ν	Φ	C (MPa)
HW / U11-037	18	100 ± 19 (10)	102 ± 53 (6)		43 ± 9 (2)	.29 ± .06 (2)	56 ± 10 (10)	.23 ± .03 (10)		
HW / U11-357	18	109 ± 29 (9)	100 ± 5 (4)	13 ± 2.4 (10)	43 ± 12 (3)	.19 ± .08 (3)	51 ± 3 (4)	.28 ± .01 (4)		
AVERAGE*	18	105 ± 25	102 ± 41	13 ± 2.4	43 ± 11	.23 ± .09	54 ± 9	.24 ± .03	45°	12

**Averages are calculated from all test results*

()Number of tests completed

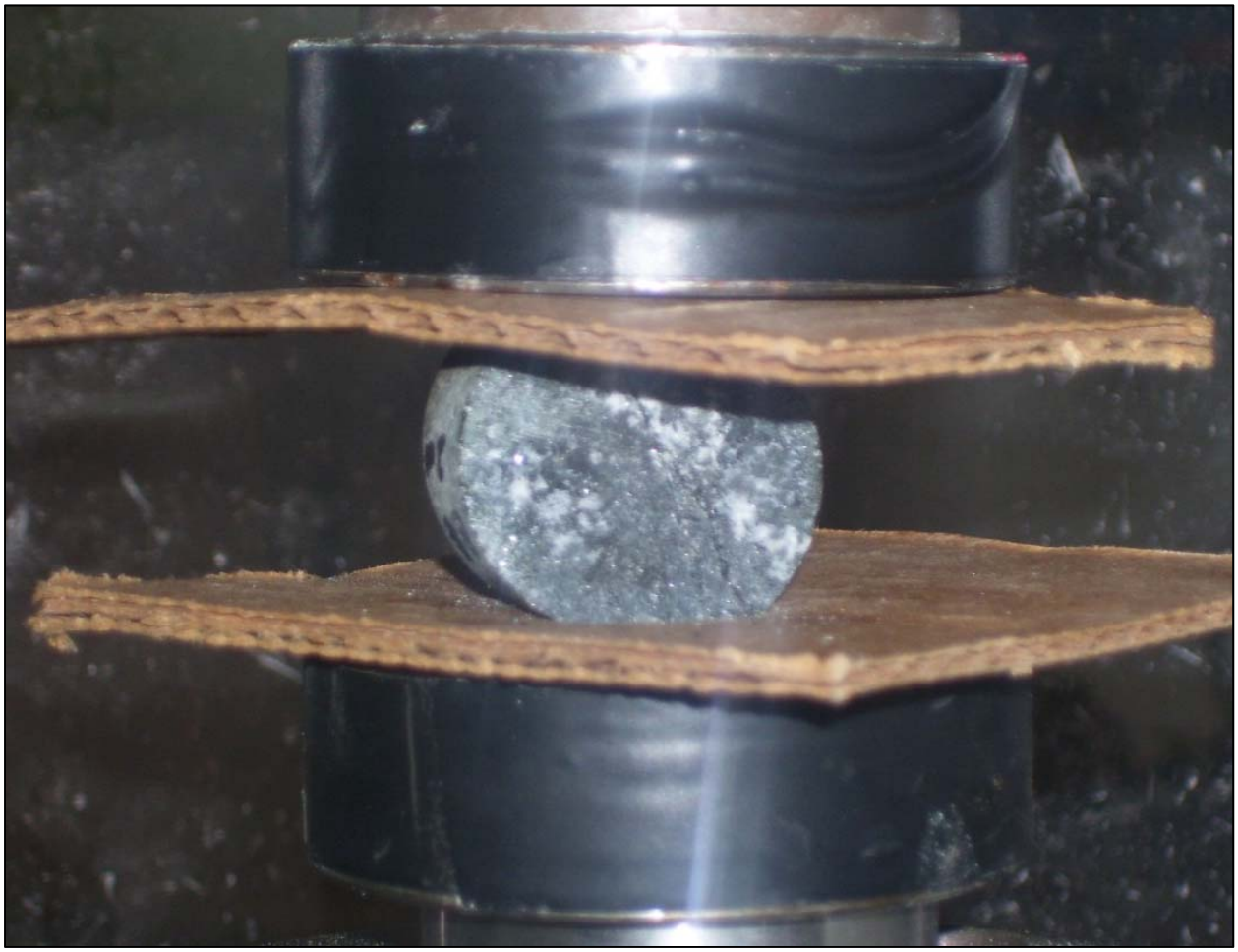

Figure 3.8 Failure of sample HW11 after the Brazilian test.

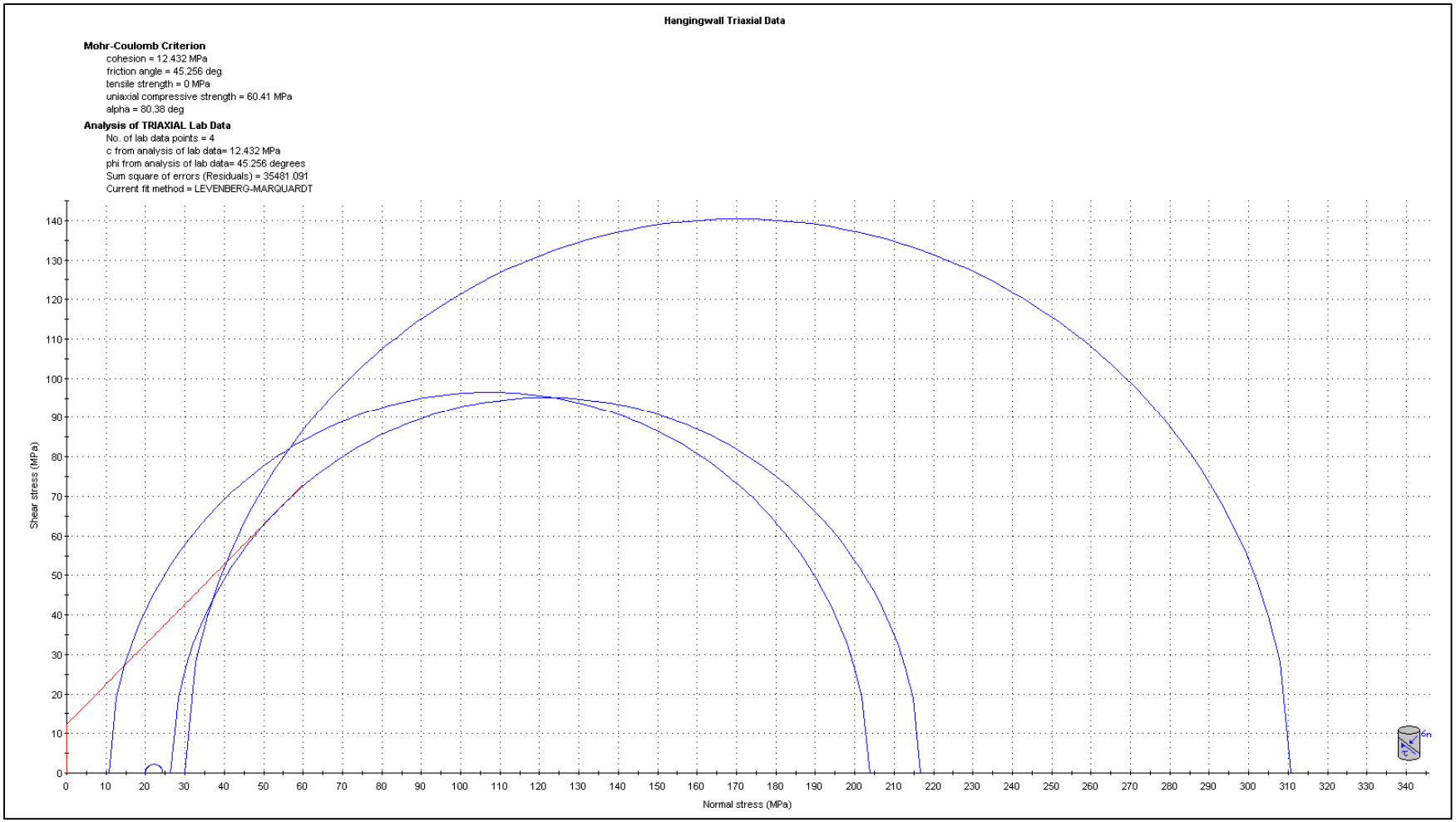

Figure 3.9 Mohr – Coulomb plot of triaxial results for the hangingwall with analysis results.

Figure 3.10 Failure plane on sample HW2 after the triaxial test.

3.4.7 Footwall Structure Results

45 core samples were tested in the footwall structure. Table 3.7 provides the sample locations, specimen dimensions and test type, and sample densities. The corresponding raw data is found in Appendix C (Figures C.6 – C.10, Tables C.2, C.5, C.8, C.11 and C.14). The average density of the footwall structure based on 24 tests was 2930 ± 34kg/m^3.

A conversion factor, K, of 17 can be used to estimate UCS from the point load test results, based on this testing. The UCS to indirect tensile strength ratio was approximately 11.1. The average static elastic modulus was 77 ± 18GPa and the dynamic was 67 ± 11GPa. It is typical of laboratory data that the static modulus is lower than the dynamic modulus because of the difference in measuring techniques; however, the footwall samples possibly had a larger frequency of micro-fractures which would increase the time for the acoustic waves to travel through the sample and therefore lower the dynamic elastic modulus. Evidence for this also

exists in the stress-strain graph of sample FW17 shown in Figure 3.11 where there is a discrepancy in the data where there was possibly movement along a microfracture. The internal angle of friction from the triaxial test was found to be 48° and the cohesion 30MPa using the Mohr – Coulomb plot in Figure 3.12. A photograph of a failed sample is shown in Figure 3.13. A summary of the results is contained in Table 3.8.

3.4.8 Orezone Structure Results

The total number of core samples tested in the orezone structure was 44. Table 3.9 provides the location from which each sample was taken, specimen dimensions and test type, and sample densities. The corresponding raw data is found in Appendix C (Figures C.11 – C.15, Tables C.3, C.6, C.9, C.12 and C.15). The average density of the orezone structure was 2972 ± 32kg/m^3.

Based on the test results, a conversion factor, K, of 8 can be used to estimate UCS from the point load test results, based. The lower conversion factor is likely due to the orezone being composed of a different rock type (quartz zones interspersed with granodiorite) than the hangingwall and footwall rock type (granodiorite). The UCS to indirect tensile strength ratio was approximately 4.0. The average static elastic modulus was 35 ± 18GPa and the dynamic was 55 ± 9GPa. It is typical of laboratory data that the static modulus is lower than the dynamic modulus because of the difference in measuring techniques. The internal angle of friction from the triaxial test was found to be 57° and the cohesion was 23MPa using the Mohr – Coulomb plot in Figure 3.14. A photograph of a failed sample is shown in Figure 3.15. A summary of the results can be seen in Table 3.10

Table 3.7 Information on core samples from the footwall structure.

Sample Name	Hole Number	Depth (m)	Test Type	Length (mm)	Diameter (mm)	Volume (m^3)	Mass (g)	Density (kg/m^3)
FW1	U11-037	174.06	Triaxial	68.64	30.5	5.01E-05	151.32	3017
FW2	U11-037	174.15	Triaxial	70.37	30.5	5.14E-05	151.73	2951
FW3	U11-037	174.30	Triaxial	68.57	30.52	5.02E-05	146.83	2927
FW4	U11-037	174.42	Triaxial	69.00	30.48	5.03E-05	148.91	2958
FW5	U11-037	174.60	UCSstrain	70.48	30.5	5.15E-05	151.05	2933
FW6	U11-037	174.74	UCS	70.27	30.48	5.13E-05	150.44	2934
FW7	U11-037	174.87	UCS	67.83	30.48	4.95E-05	145.44	2939
FW8	U11-037	176.11	UCS	67.34	30.5	4.92E-05	144.88	2945
FW9	U11-037	176.22	UCS	68.14	30.5	4.98E-05	144.39	2900
FW10	U11-037	175.66	UCSstrain	70.34	30.5	5.14E-05	147.32	2867
FW11	U11-357	174.07	Brazilian	18.65	30.51	1.36E-05		
FW12	U11-357	177.96	Brazilian	18.38	30.54	1.35E-05		
FW13	U11-357	177.98	Brazilian	21.65	30.52	1.58E-05		
FW14	U11-357	178.00	Brazilian	19.80	30.55	1.45E-05		
FW15	U11-357	178.02	Brazilian	18.10	30.53	1.33E-05		
FW16	U11-357	154.80	UCS	70.07	30.49	5.12E-05	148.48	2902
FW17	U11-357	154.87	UCSstrain	69.48	30.48	5.07E-05	148.38	2927
FW18	U11-357	154.94	UCSstrain	69.26	30.5	5.06E-05	147.50	2915
FW19	U11-357	155.01	UCSstrain	68.47	30.5	5.00E-05	145.30	2905
FW20	U11-357	154.70	Brazilian	12.93	30.5	9.45E-06		
FW21	U11-357	154.71	Brazilian	14.35	30.5	1.05E-05		
FW22	U11-357	154.73	Brazilian	14.69	30.52	1.07E-05		
FW23	U11-357	154.74	Brazilian	15.66	30.51	1.14E-05		
FW24	U11-357	154.76	Brazilian	15.34	30.51	1.12E-05		
AVERAGE								2930 ± 34

Table 3.8 Summary of testing results for the footwall structure.

Zone / Box	Conversion Factor, K	UCS Point Load (MPa)	UCS (MPa)	Tensile Strength (MPa)	Static E (GPa)	Static ν	Dynamic E (GPa)	Dynamic ν	Φ	C (MPa)
FW / U11-037	22	169 ± 45 (10)	171 ± 48 (6)		75 ± 12 (2)	.20 ± .05 (2)	62 ± 7 (10)	.17 ± .06 (10)		
FW / U11-357	11	90 ± 22 (11)	90 ± 35 (4)	12.8 ± 2.6 (10)	78 ± 21 (4)	.21 ± .11 (4)	76 ± 15 (4)	.22 ± .05 (4)		
AVERAGE*	17	138 ± 35	139 ± 59	12.8 ± 2.6	77 ± 18	.21 ± .09	67 ± 11	.18 ± .06	48°	30

**Averages are calculated from all test results*

()Number of tests completed

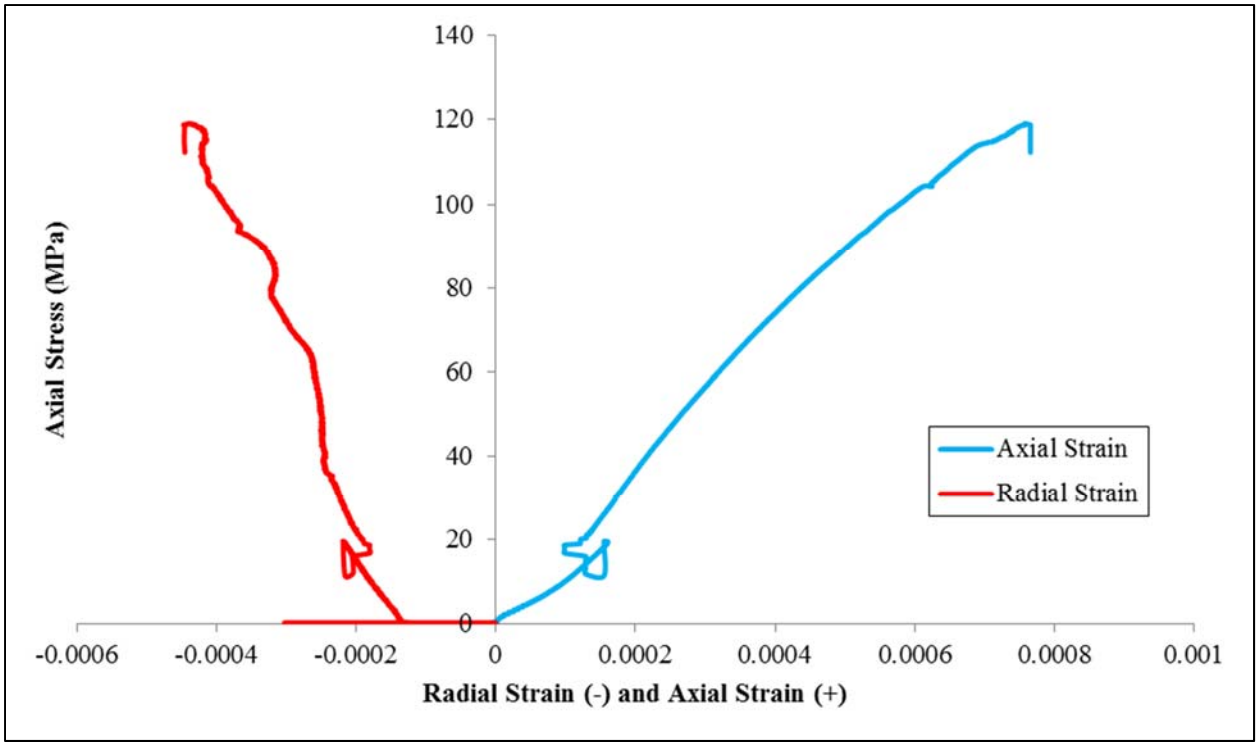

Figure 3.11 Stress – strain graph for sample FW17 showing an inconsistent stress – strain curve.

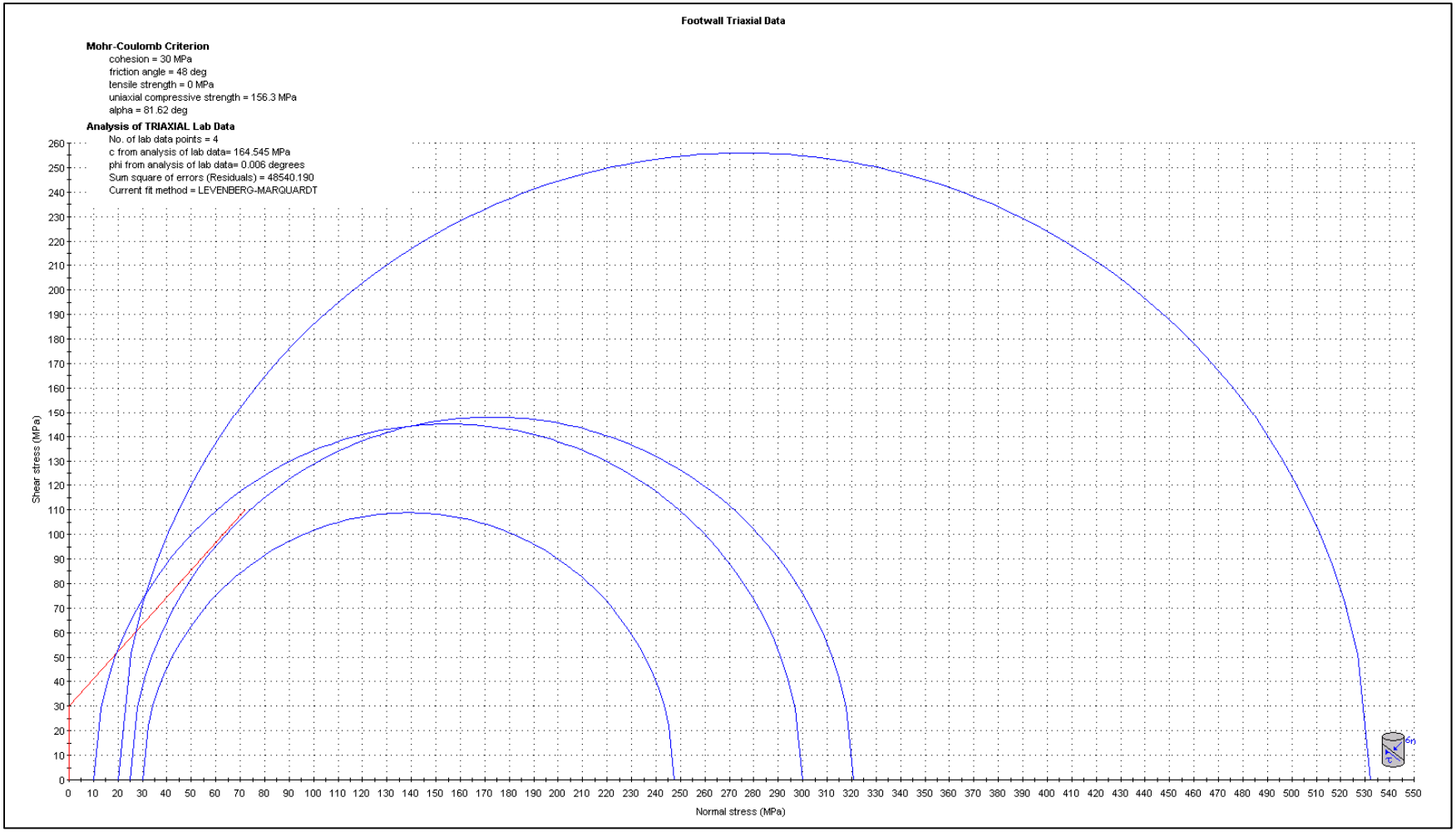

Figure 3.12 Mohr – Coulomb plot of triaxial results for the footwall with analysis results.

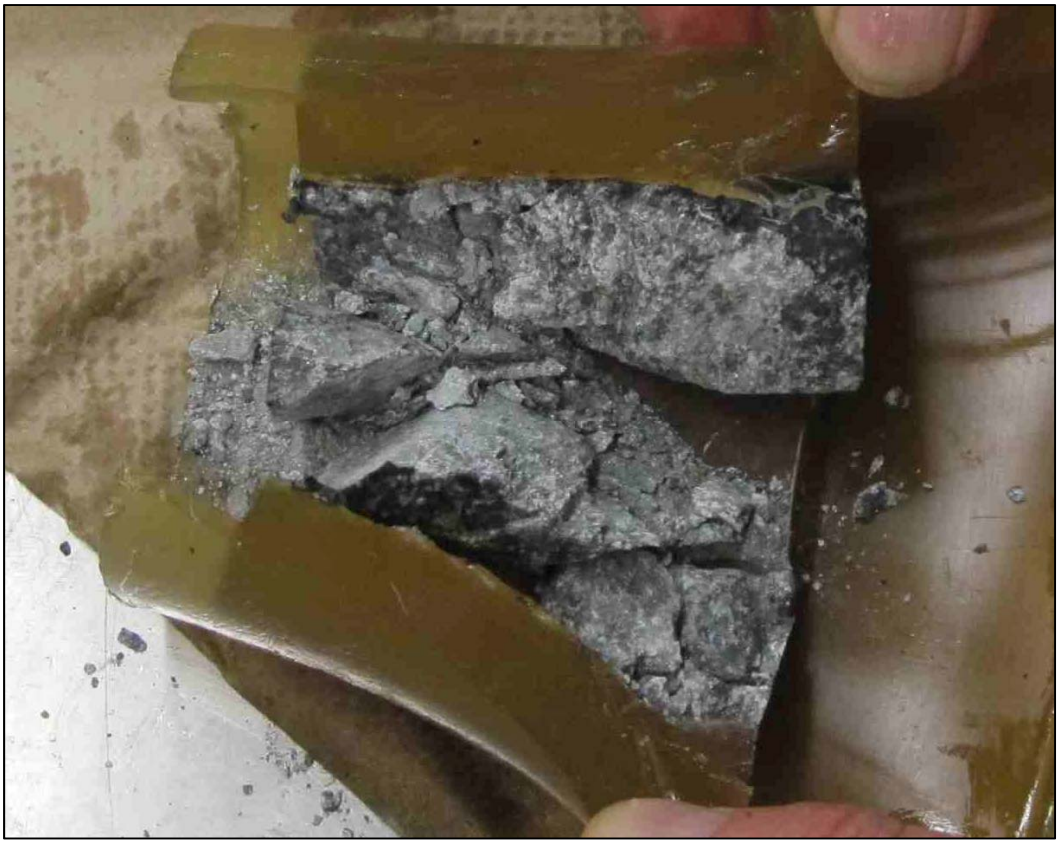

Figure 3.13 Failure of sample FW2 after the triaxial test.

Table 3.9 Information on core samples from the orezone structure.

Sample Name	Hole Number	Depth (m)	Test Type	Length (mm)	Diameter (mm)	Volume (m^3)	Mass (g)	Density (kg/m^3)
OZ1	U11-037	170.60	Brazilian	11.95	30.52	8.74E-06		
OZ2	U11-037	170.61	Brazilian	15.58	30.51	1.14E-05		
OZ3	U11-037	170.63	Brazilian	13.56	30.55	9.94E-06		
OZ4	U11-037	170.64	Brazilian	14.79	30.51	1.08E-05		
OZ5	U11-037	170.66	Brazilian	13.16	30.55	9.65E-06		
OZ6	U11-037	170.67	Brazilian	14.35	30.5	1.05E-05		
OZ7	U11-037	170.68	Brazilian	13.50	30.5	9.86E-06		
OZ8	U11-037	170.70	Brazilian	14.50	30.5	1.06E-05		
OZ9	U11-037	170.71	Brazilian	13.94	30.5	1.02E-05		
OZ10	U11-037	170.73	Brazilian	13.28	30.5	9.70E-06		
OZ11	U11-357	165.10	Triaxial	69.85	30.22	5.01E-05	149.35	2981
OZ12	U11-357	165.30	Triaxial	68.52	30.24	4.92E-05	148.70	3022
OZ13	U11-357	165.90	Triaxial	69.68	30.23	5.00E-05	148.66	2972
OZ14	U11-357	166.10	Triaxial	70.74	30.2	5.07E-05	151.11	2982
OZ15	U11-357	166.30	UCS	69.48	30.18	4.97E-05	148.07	2979
OZ16	U11-357	165.45	UCS	67.45	30.3	4.86E-05	140.56	2890
OZ17	U11-357	166.50	UCS	73.43	30.23	5.27E-05	155.67	2954
OZ18	U11-357	165.65	UCS	69.75	30.21	5.00E-05	150.55	3011
OZ19	U11-357	165.65	UCS	67.32	30.23	4.83E-05	143.20	2964
OZ20	U11-357	168.60	UCSstrain	66.90	30.21	4.80E-05	141.90	2959
OZ21	U11-357	168.75	UCSstrain	68.87	30.18	4.93E-05	147.34	2991
OZ22	U11-357	168.90	UCSstrain	68.22	30.18	4.88E-05	146.81	3008
OZ23	U11-357	171.10	UCSstrain	68.77	30.24	4.94E-05	144.84	2932
OZ24	U11-357	171.30	UCSstrain	69.20	30.25	4.97E-05	147.63	2968
AVERAGE								2972 ± 32

Table 3.10 Summary of testing results for the orezone structure.

Zone / Box	Conversion Factor, K	UCS Point Load (MPa)	UCS (MPa)	Tensile Strength (MPa)	Static E (GPa)	Static ν	Dynamic E (GPa)	Dynamic ν	Φ	C (MPa)
OZ / U11-037				17.6 ± 2.0 (10)						
OZ / U11-357	8	71 ± 26 (20)	70 ± 18 (10)		35 ± 18 (5)	.17 ± .05 (5)	55 ± 9 (14)	.21 ± .04 (14)	57°	23

()Number of tests completed

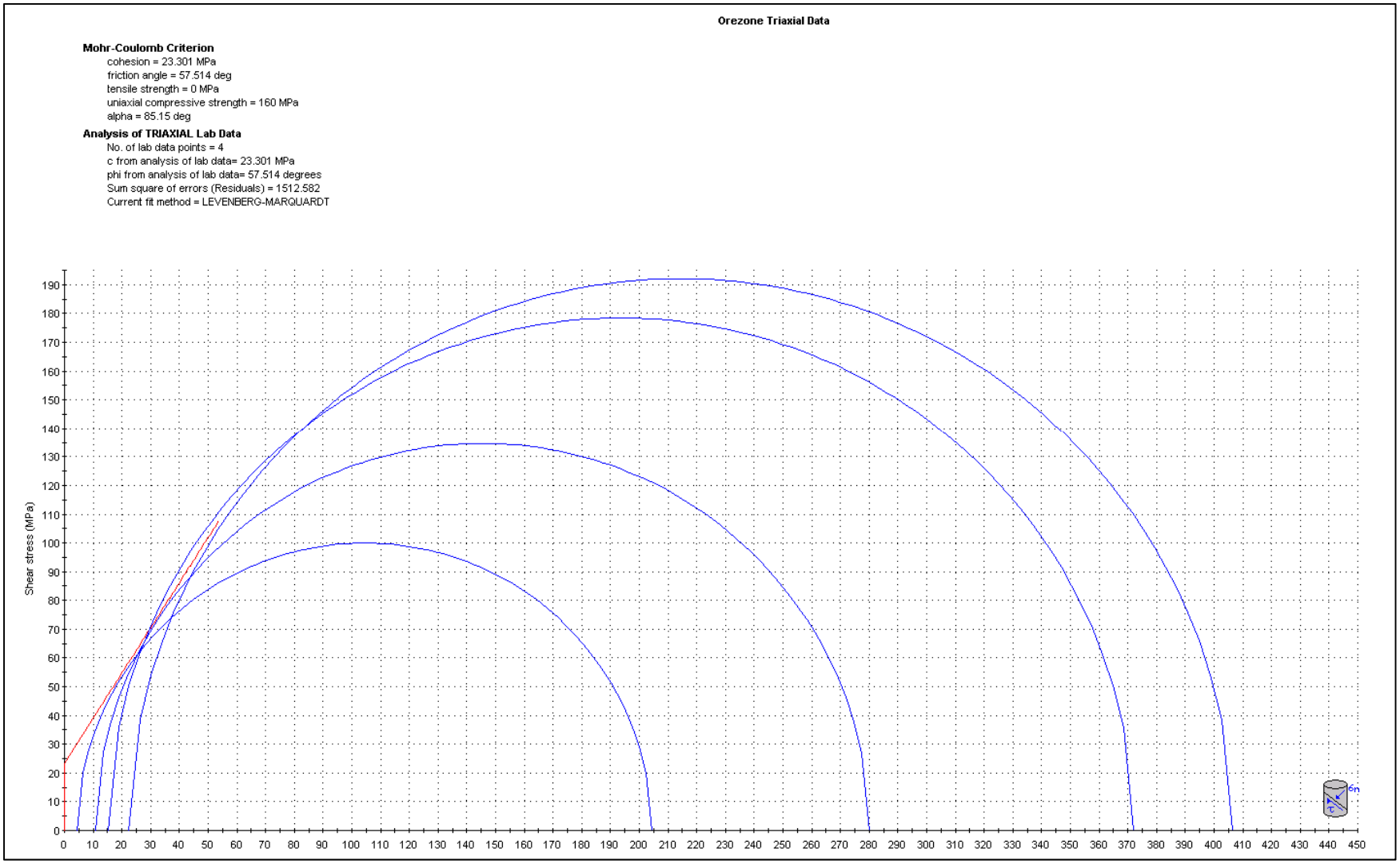

Figure 3.14 Mohr – Coulomb plot of triaxial results for the orezone with analysis results.

Figure 3.15 Failure of sample OZ14 after the Triaxial test.

3.5 Measurement of Induced Stress Around Open Panels

An instrumentation program was developed with the goal of monitoring changes in deformation of the rockmass which could then be related to changes in induced stress. To measure the effect of induced stress on the stope, two types of instrumentation were installed: a simple, inexpensive three-point closure station system that could be installed anywhere in the mine, and a sophisticated and more precise Multi – Point Borehole Extensometer which was installed at focused areas. Sections 3.5.1 and 3.5.2 discuss these methods in greater detail.

3.5.1 Data Collection from Three Point Closure Stations

The deformation of an excavation can be measured with a three point closure station. At three points on the wall of a circular tunnel (points A, B and C), a wedge anchor is firmly installed so that it remains a fixed point on the wall. The distance between each anchor is defined as chords AB, AC and BC. Additional mining in the area creates changes in the principal stresses ($\Delta\sigma_1$ and $\Delta\sigma_2$), which in turn deform the tunnel walls. The application of these stresses on the circular

tunnel creates an elliptical distortion proportional to the applied stress. The fixed points of A, B and C move with the deformation of the tunnel and the resulting change in length of the chords is AC', AB' and BC' can be used to calculate the strain, $\varepsilon_{AB,}$ using Equation 3.4:

$$\varepsilon_{AB} = \frac{AB - AB'}{AB} \tag{3.4}$$

The change in deformation of the chord length can be measured using a tape extensometer (Figure 3.16). The tape is attached to hooks on two of the fixed point wedge anchors and tensioned to the indicated limit for the tape extensometer to provide repeatability of measurements. This process is then repeated for the other two chord lengths at that closure station. The tape extensometer used at Seabee Gold Mine has an accuracy of ±0.05mm and a repeatability of ±0.05mm. The fixed locations on the walls were placed by drilling a smooth hole with a hammer drill and inserting 6" wedge anchors that were threaded with eye bolts.

A closure station was installed in 2b11013 Sublevel 5; on top of the pillar between Panel 3 and 4 (Figure 3.17). It was installed on August 27, 2012 in the location seen in Figure 3.17. Mining commenced with the first blast of the slot on September 4, 2012 and the slot was finished on September 5, 2012. The panel production blasts continued until September 9, 2012 and mine engineering personnel took measurements one day after each blast. The recorded measurements are in Table 3.11.

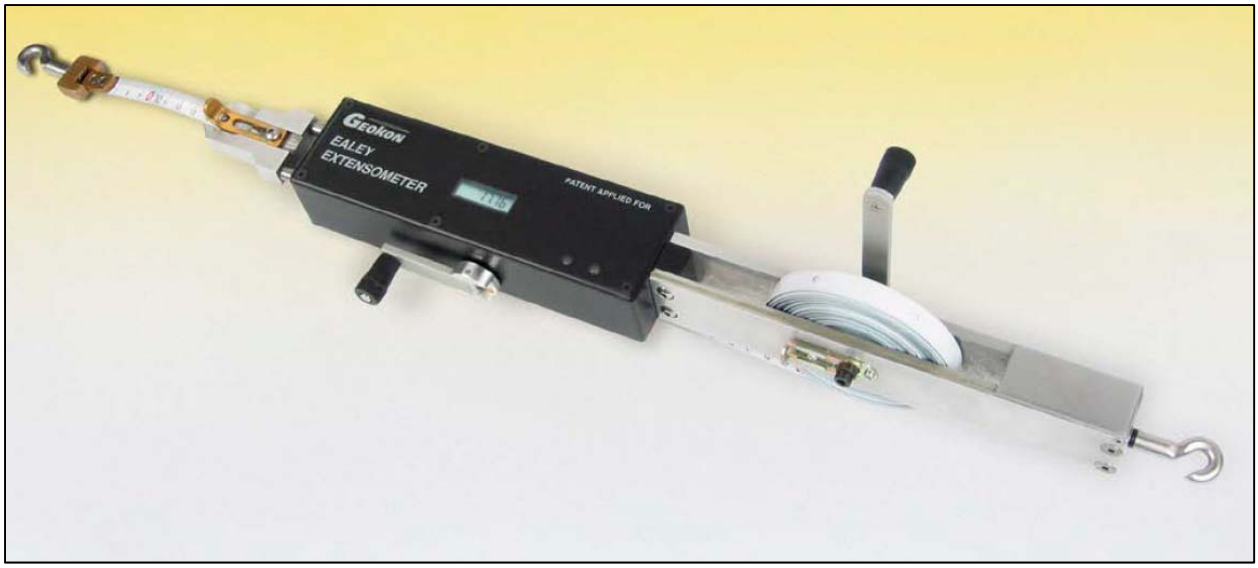

Figure 3.16 Picture of tape extensometer that shows the digital micrometer, tension, hooks and tape. (from Geokon Inc., 2012)

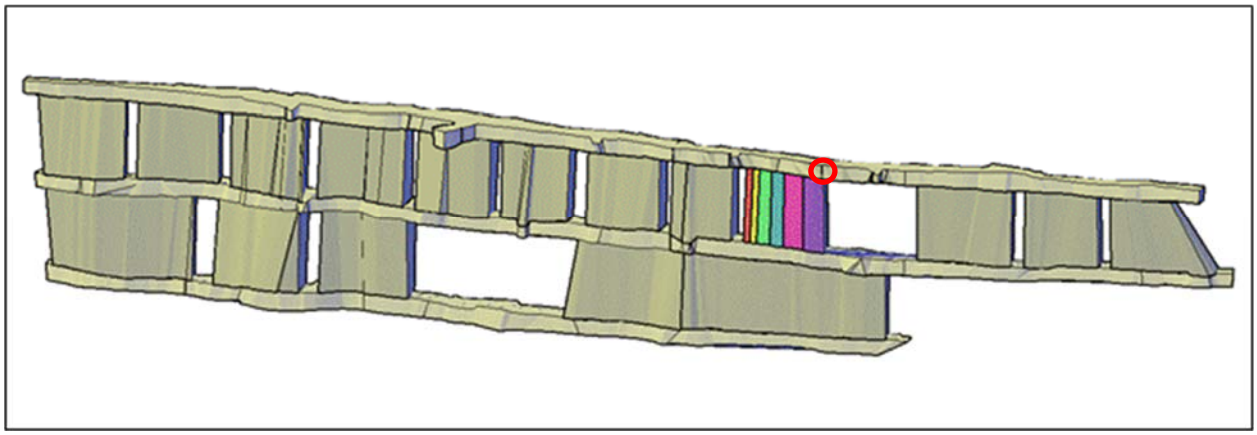

Figure 3.17 Illustration of 2b11013 5-6 showing blasting from left to right and the location of the closure station in the red circle.

Table 3.11 Data collected for the closure station at 2b11013.

	Chord A - C				Chord A - B				Chord B - C			
Date	Tape (m)	Vernier (mm)	Dial (mm)	Total (m)	Tape (m)	Vernier (mm)	Dial (mm)	Total (m)	Tape (m)	Vernier (mm)	Dial (mm)	Total (m)
27-Aug-12	3.50	7	0.15	3.50715	5.75	13	0.75	5.76375	6.00	4	0.40	6.00440
05-Sep-12	3.50	5	0.60	3.50560	5.75	16	0.30	5.76630	6.00	3	0.05	6.00305
07-Sep-12	3.50	2	0.90	3.50290	5.75	15	0.85	5.76585	6.00	2	0.70	6.00270
08-Sep-12	3.50	3	0.20	3.50320	5.75	16	0.65	5.76665	6.00	0	0.05	6.00005
09-Sep-12	3.50	2	0.40	3.50240	5.75	12	0.20	5.76220	6.00	0	0.25	6.00025
10-Sep-12	3.50	1	0.55	3.50155	5.75	11	0.80	5.76180	6.00	0	0.10	6.00010

3.5.2 Data Collection of Multipoint – Borehole Extensometers (MPBXs)

Multi – Point Borehole Extensometers (MPBXs) are used to record relative deformations in areas where there is no access for closure or tape readings. Extensometers were installed in the L62 zone of the mine (Figure 3.18). Three MPBXs were installed, one in each of the following areas; the 1000-1010 level, 990-1000 level, and 970-990L in September 2012. Readings were recorded on a data logger at 10min intervals. The data from the data loggers was downloaded at approximately 6 month intervals. The data from the first two MPBXs was unusable due to what is assumed as installation and/or manufacturer errors due to the fact that the data was erratic.

The MPBX installed between levels 970 – 990 level was collared from a drift with the toe of the extensometer located in the centre of the planned panel. The orientation of the borehole, with respect to the open panel, can be seen in Figure 3.18 and Figure 3.19, which is approximately 45° from perpendicular in both plan view and long section. The date of installation for this MPBX is September 19, 2012. The data logger was attached to the instrument and was set to record data from each of the nodes every 10 minutes.

The readings taken from this MPBX were recorded in increments of $1/100^{th}$ of a volt. In order to convert these voltage readings into displacements the following equation, provided by the vendor (MDT), was used:

$$\delta_n = (127)\frac{V_n - V_o}{500} \tag{3.5}$$

where:

δ_n is the *cumulative displacement of the node (mm)*;

V_n is the *current voltage reading of the nodes*; and

V_o is the *original voltage reading*.

Cumulative displacements are plotted in Figure 3.20, where positive numbers are tension and negative numbers are in compression. The cumulative displacement values were then converted to cumulative strain using Equation 3.4. The results are shown in Figure 3.21.

This MPBX exhibits the displacement behaviour that is expected based on the in situ changing stress field. That is, the MPBX went into compression as the mining front approached and caused an increase in the induced stress. After the mining front passed the MPBX (blast 8), the nodes entered into tension. This corresponds to a lower induced stress field of the zone in relaxation. This is seen in Figure 3.22. These displacements values shown are the first MPBX reading taken after a blast was initiated, allowing for the identification of the immediate (within 10 minutes) response of the rockmass due to the induced stress change.

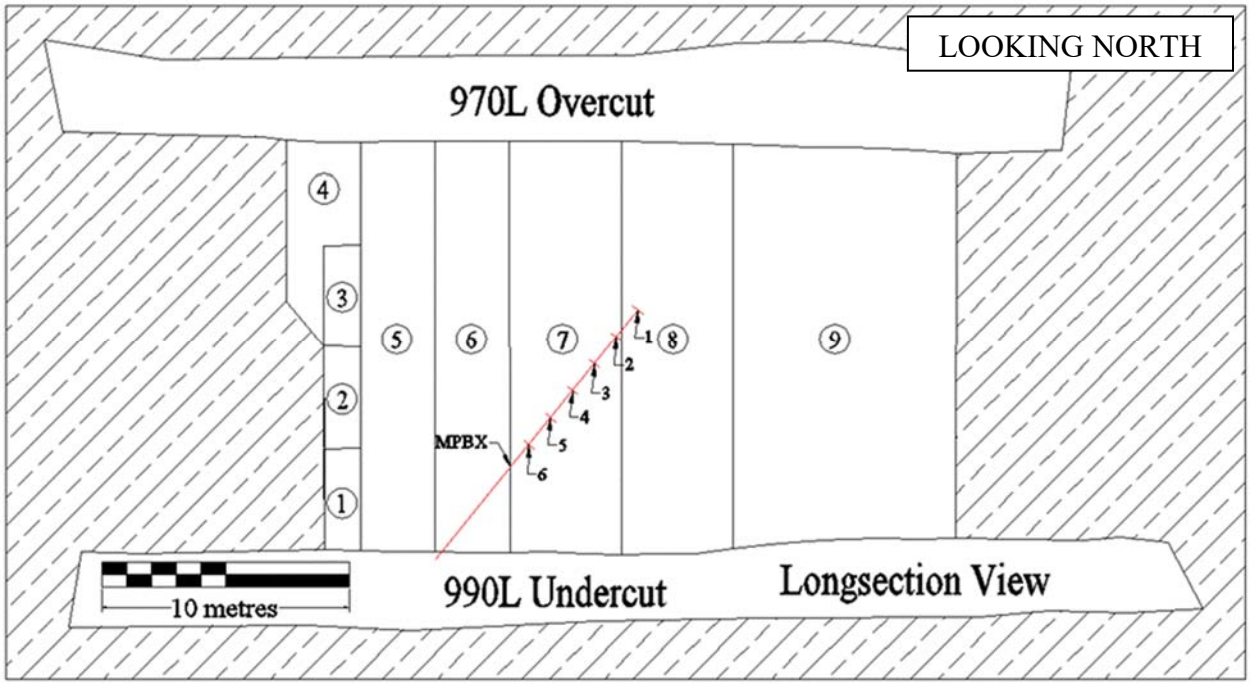

Figure 3.18 Longsection view of L62 970-990 after all 9 blasts were complete, showing the location of the MPBX.

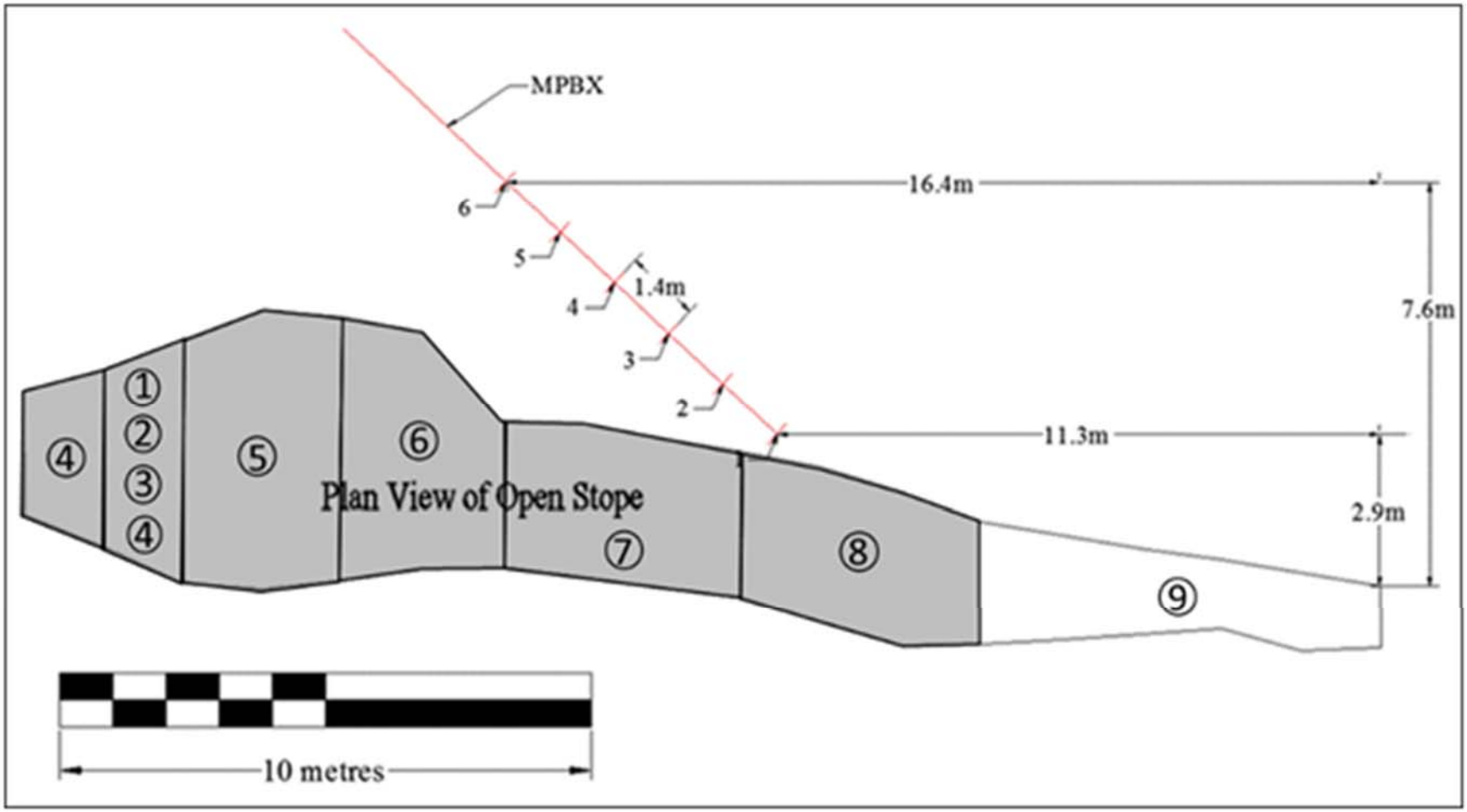

Figure 3.19 Plan section view of L62 970-990 showing the orientation of the MPBX.

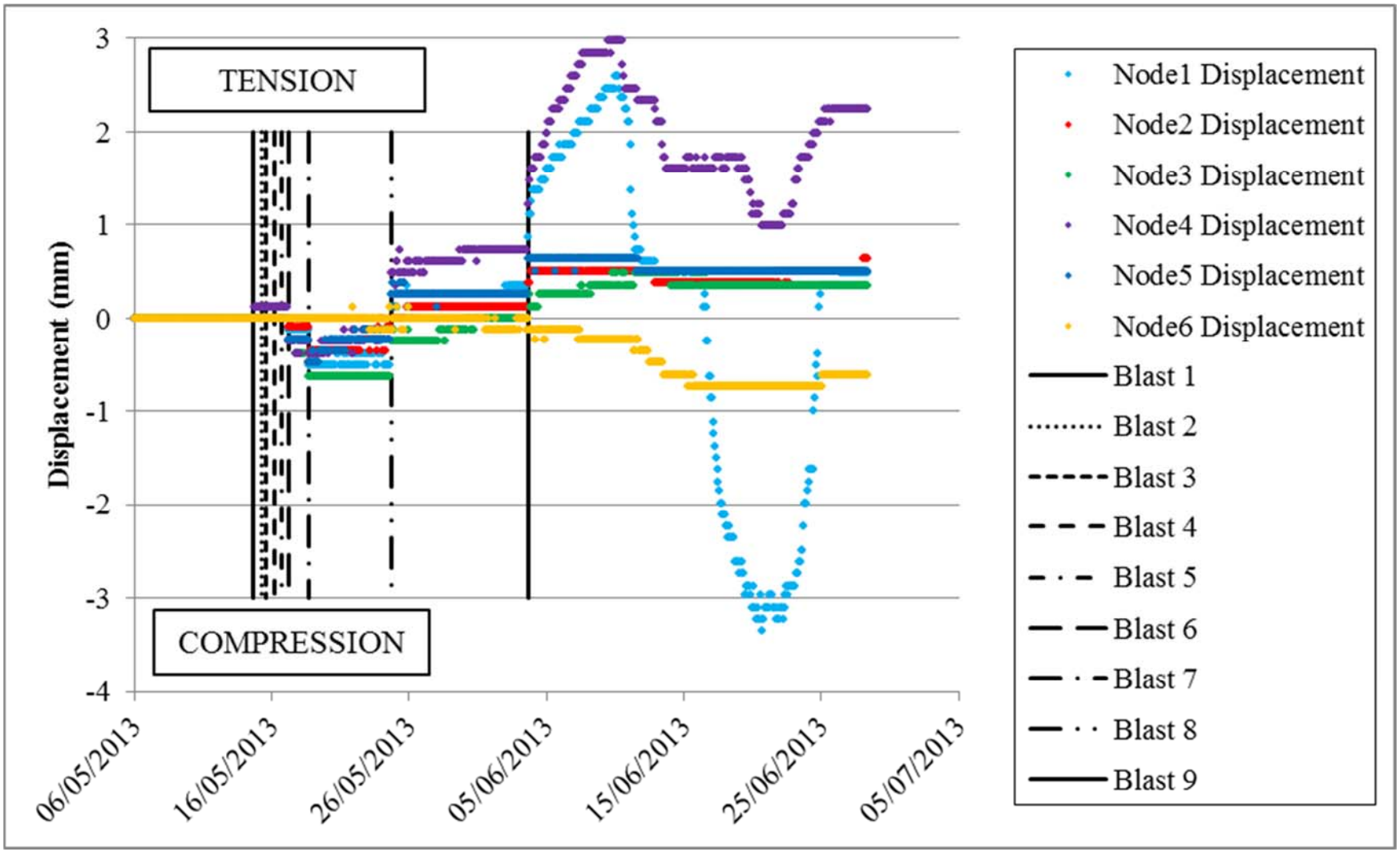

Figure 3.20 Cumulative displacement plot of the L62 970-990 MPBX.

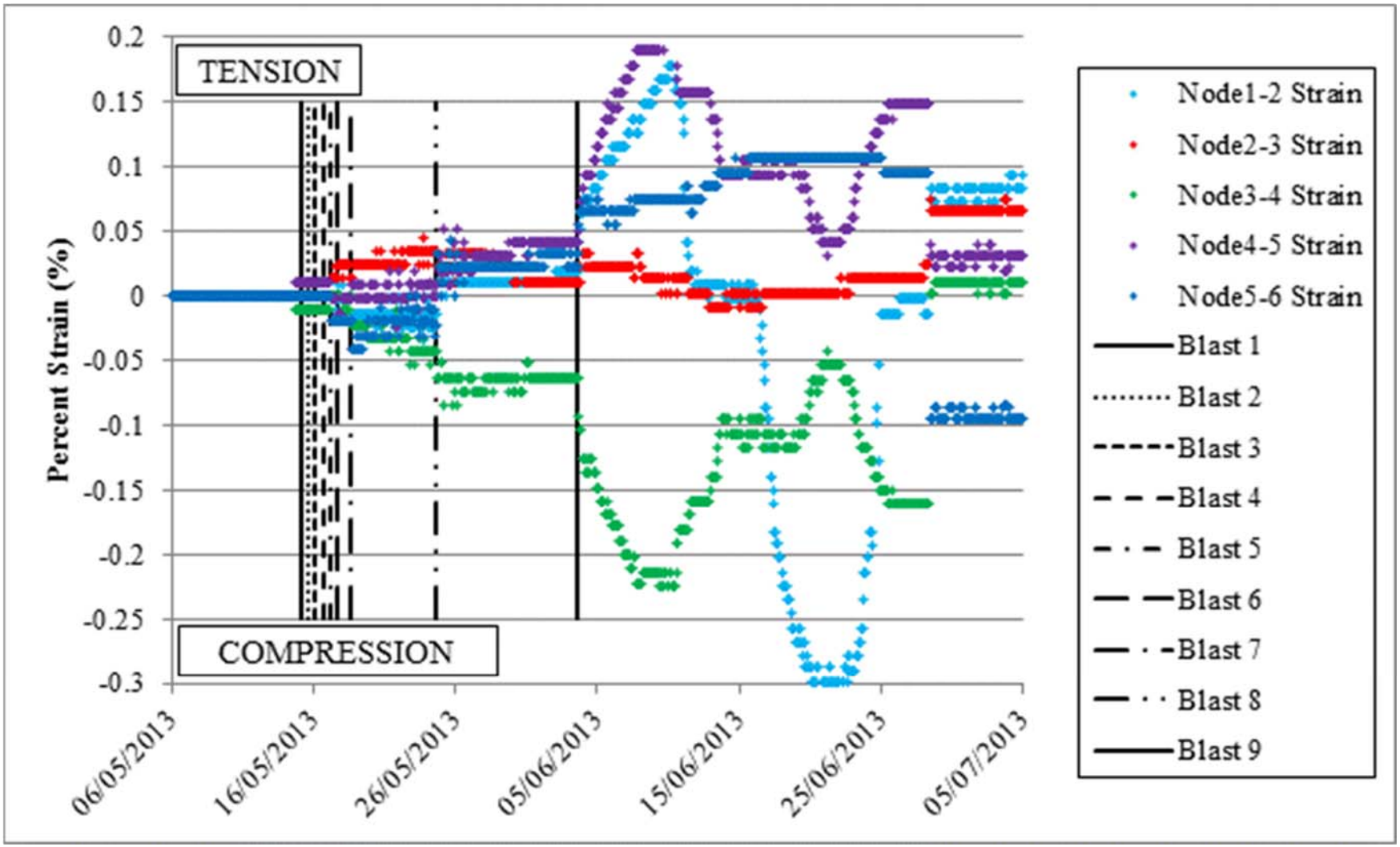

Figure 3.21 Strain plot of the L62 970-990 MPBX.

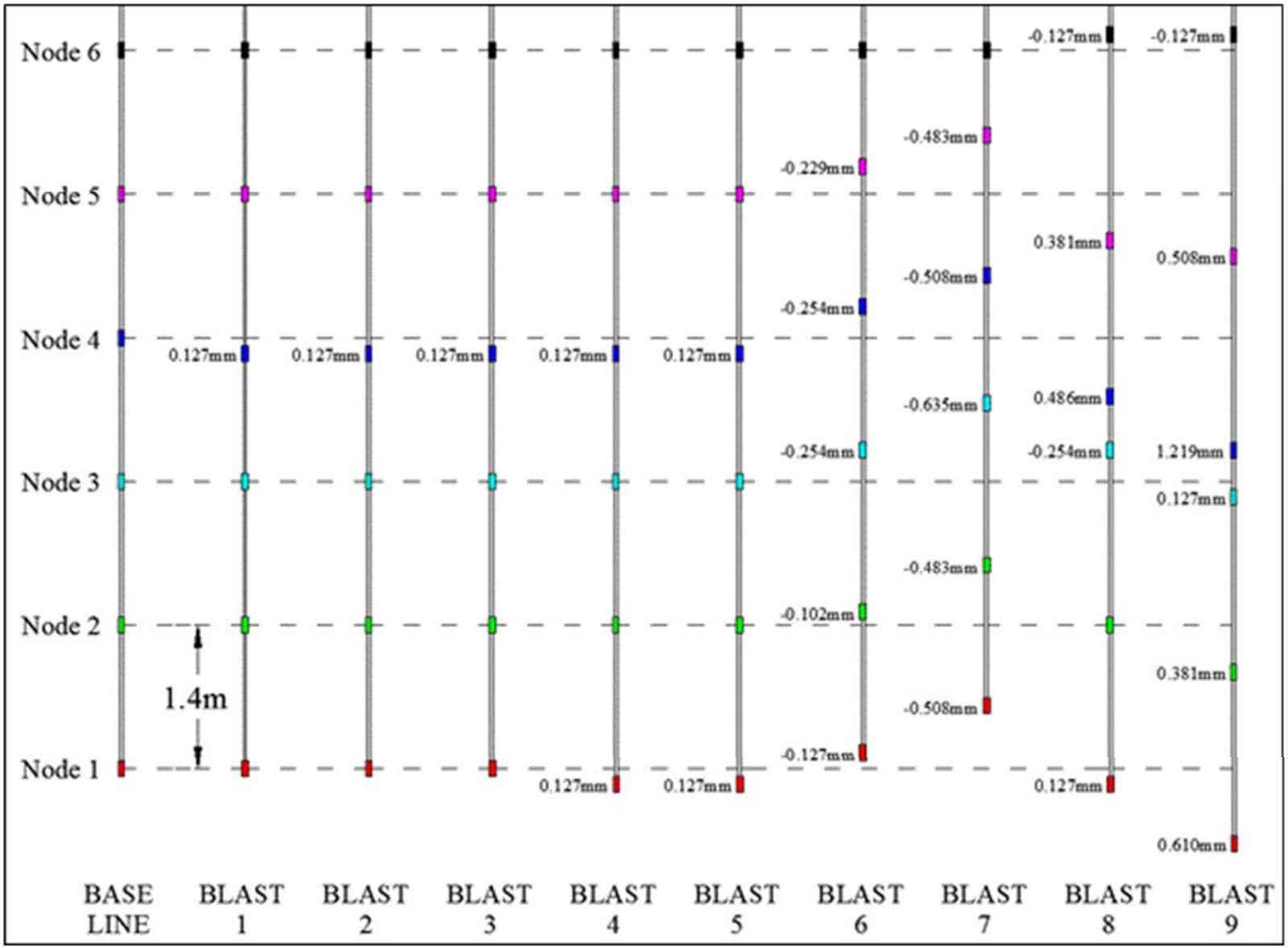

Figure 3.22 Cumulative displacement at each node location after each blast of the L62 970-990 panel.

3.6 Summary

This chapter provided information on the data collection in this study. The data that was collected from Seabee Gold Mine included CMS, joint and rockmass properties, information on the panel geometry, laboratory data on the rockmass, and instrumentation data (three – point closure stations and MPBXs). This data was collected over a period of 2 years between 2010 and 2012.

As part of this research the JRC-Joint Amplitude chart was modified for field applications. The chart was modified to extend the criteria of joint waviness as joints greater than one meter in length were not often encountered in the field.

The CMS data that was collected is crucial to quantify the amount of dilution for each panel. The data was gathered for 28 panels which provided data for 56 panel walls. In conjunction with the CMS data, panel geometry was collected for the analysis of dilution in Chapter 5.

Laboratory testing was performed on core that was brought from Seabee Gold Mine to the University of Saskatchewan. The core was separated into three domains: hangingwall, footwall and orezone. The tests that were performed were: UCS, point load, Brazilian tensile, triaxial, and ultrasonic velocity. The purpose of the tests was to quantify the rockmass properties for numerical modelling in Chapter 4 and empirical methods used in Chapter 5.

Instrumentation was installed to obtain data on the movement of the rockmass as a result of induced stress changes. A three – point closure station and an MPBX were installed at two separate locations of the mine, and the data was collected as the mining front approached the instrument. This data is analyzed in Chapter 4 to quantify the induced stress change that occurs in the rockmass due to mining activity, and then analysed in Chapter 5 to determine if induced stress has an effect on the amount of dilution in a panel.

CHAPTER 4

INDUCED STRESS AROUND OPEN PANELS

An instrumentation program was developed with the objective of monitoring changes in deformation of the rockmass, and then relating the deformation to changes in induced stress. Stress is one of the major factors driving instability around underground openings and may not be adequately accounted for in the current empirical design methods for estimating dilution. To obtain an estimate of the stress state in the vicinity of the Seabee panels under study, three point closure stations were used, as well as multi-point extensometers. Closure stations use relatively inexpensive equipment and can be installed anywhere in the mine. The closure data was coupled with data from more expensive borehole extensometers. The stress data was used in conjunction with dilution data and analysed to determine if any relationship exists between induced stress changes and dilution.

4.1 Analysis of Three Point Closure Station Data

To analyse the closure station data that was gathered, a program called "Converge" was used to convert the three measured minor strains into the principal strains and stresses (Milne & Milne, 1993). Solving for the two principal strains and stresses from the three secondary chord strains can be done using a strain gauge rosette, Hooke's Law and the Kirsch solution (Kirsch, 1898), and described by Goodman (1980) in Appendix A2. The required inputs for "Converge" are the elastic properties of the rock mass (Young's modulus and Poisson's ratio), and a spreadsheet containing the microstrains from the three directions of closure and their corresponding angle of orientation. Using these inputs, "Converge" outputs the principal strains, principal stresses, and their angle of orientation from horizontal.

There are two main challenges associated with estimating stress change using this approach. The first difficulty is estimating an appropriate value for Young's modulus and Poisson's ratio for the measured deformations. For a small tunnel in a competent rock mass with wide joint spacing approaching the tunnel diameter, Young's modulus equal to the intact rock modulus would be appropriate. For a less competent rock mass with a closer joint spacing relative to the tunnel diameter, a Young's modulus closer to that of the overall rock mass would be appropriate. For

the Seabee rock mass, an RMR_{76} of 75 is observed and was used with Equation 4.1 (Bieniawski, 1989) to give an estimated modulus 50 GPa.

$$E_{rock\ mass} = 2 \times RMR_{76} - 100 \tag{4.1}$$

A second difficulty associated with the analysis of induced stresses in circular tunnels is that few underground mining excavations are circular. To determine the effect that a square tunnel will have on the induced stresses, in comparison to a circular tunnel, an empirical approach was used. In the empirical study the variable that is being considered is the K_i ratio. The K_i ratio is the ratio of induced stresses that have caused the deformation measured at the closure station, measured in a plane perpendicular to the tunnel direction. To determine the magnitude of difference in induced stress, Examine2D was used to model a 10 m square drift with the parameters of a depth of 1000 m, unit weight of 0.027 MN/m^3, E of 50 GPa and a Poisson's Ratio of 0.2.

Two geometric correction scenarios were modelled where the orientation of the induced principal stresses were different. The first orientation scenario was with the maximum induced stress parallel to horizontal. The second scenario was with the maximum induced stress oriented at 45 ° from horizontal (counterclockwise).

The results of the first scenario can be seen in Table 4.1 and in graphical form in Figure 4.1. The values of both $\Delta\sigma_1$ and $\Delta\sigma_3$, calculated with "Converge", are higher than the actual values modelled with Examine2D. This is because the deformation readings were taken from the center of the walls and back, which responds under a stress change with more deformation than would occur with a circle. The graph can be used to correct the principal stresses calculated by "Converge" by reducing them based on the ratios found on the y-axis. This is accomplished by calculating the K_i ratio from the "Converge" output of induced stresses. The Ki ratio is then found on the graph and $\Delta\sigma_1$ and $\Delta\sigma_3$ are reduced by their corresponding ratios.

The results of the second scenario can be seen in Table 4.2 and in graphical form in Figure 4.2. The results indicate that for the maximum induced stress, the orientations of the principal stresses that act on the opening does not have a significant difference if the opening is a circular

or a square. "Converge" will calculate stress change values 1.3 – 1.6 times higher for any K_i ratio.

Table 4.1 Results of empirical study on the geometric correction at 0° to horizontal.

	Sigma1 (MPa)			Sigma3 (MPa)		
Induced K Ratio	Converge	Examine2D	Ratio	Converge	Examine2D	Ratio
1	8.1	5.0	1.62	8.1	5.0	1.62
2	14.5	10.0	1.45	9.4	5.0	1.87
3	20.4	15.0	1.36	10.4	5.0	2.09
4	26.8	20.0	1.34	11.6	5.0	2.33
5	33.3	25.0	1.33	12.9	5.0	2.59
6	39.8	30.0	1.33	14.3	5.0	2.86
7	45.9	35.0	1.31	15.3	5.0	3.06
8	52.7	40.0	1.32	16.9	5.0	3.37
9	58.9	45.0	1.31	18.0	5.0	3.60
10	66.1	50.0	1.32	19.8	5.0	3.97
11	72.2	55.0	1.31	21.0	5.0	4.20
12	78.8	60.0	1.31	22.5	5.0	4.49
13	84.9	65.0	1.31	23.5	5.0	4.70
14	91.6	70.0	1.31	25.1	5.0	5.01
15	98.3	75.0	1.31	26.6	5.0	5.31

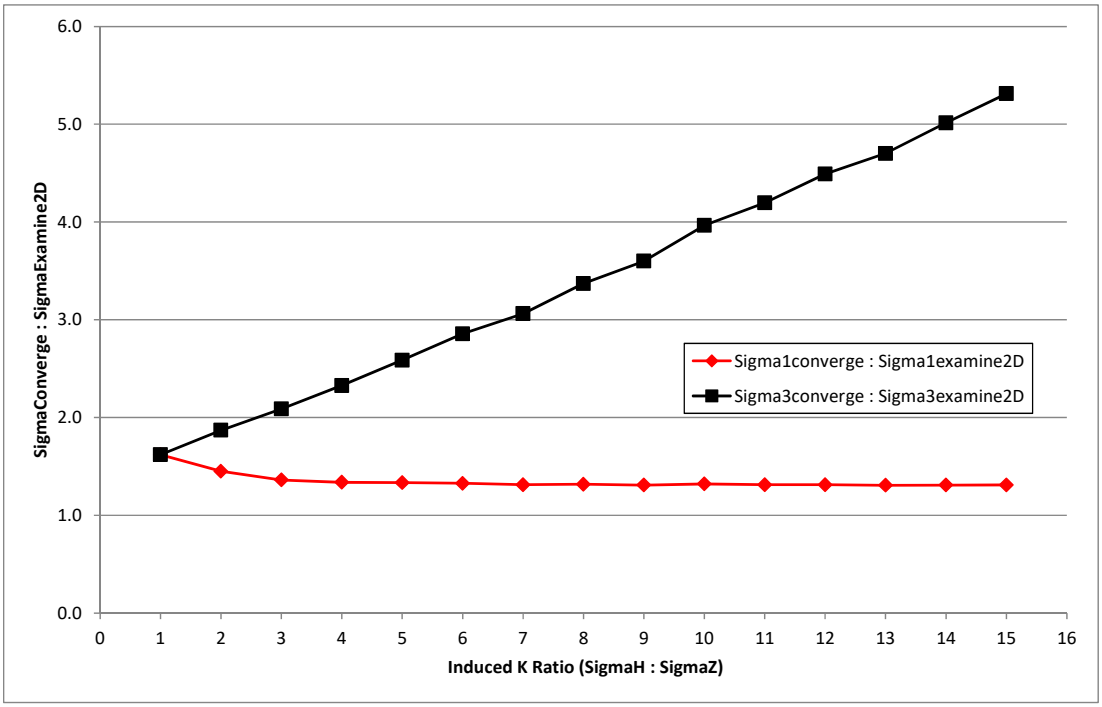

Figure 4.1 Geometric correction ratios of induced stresses of "Converge" to the numerical model at 0° to horizontal.

Table 4.2 Results of empirical study on the geometric correction at 45° to horizontal.

	Sigma1 (MPa)			Sigma3 (MPa)		
Induced K Ratio	Converge	Examine2D	Ratio	Converge	Examine2D	Ratio
1	7.9	5.0	1.58	7.9	5.0	1.58
2	16.1	10.0	1.61	7.6	5.0	1.52
3	24.3	15.0	1.62	7.4	5.0	1.48
4	32.5	20.0	1.63	7.0	5.0	1.40
5	40.7	25.0	1.63	6.7	5.0	1.34
6	48.8	30.0	1.63	6.4	5.0	1.28
7	57.0	35.0	1.63	6.1	5.0	1.22
8	65.1	40.0	1.63	5.7	5.0	1.14
9	73.2	45.0	1.63	5.4	5.0	1.08
10	81.4	50.0	1.63	5.1	5.0	1.02
11	89.5	55.0	1.63	4.8	5.0	0.96
12	97.7	60.0	1.63	4.4	5.0	0.88
13	105.9	65.0	1.63	4.2	5.0	0.84
14	114.1	70.0	1.63	3.9	5.0	0.78
15	122.2	75.0	1.63	3.6	5.0	0.72

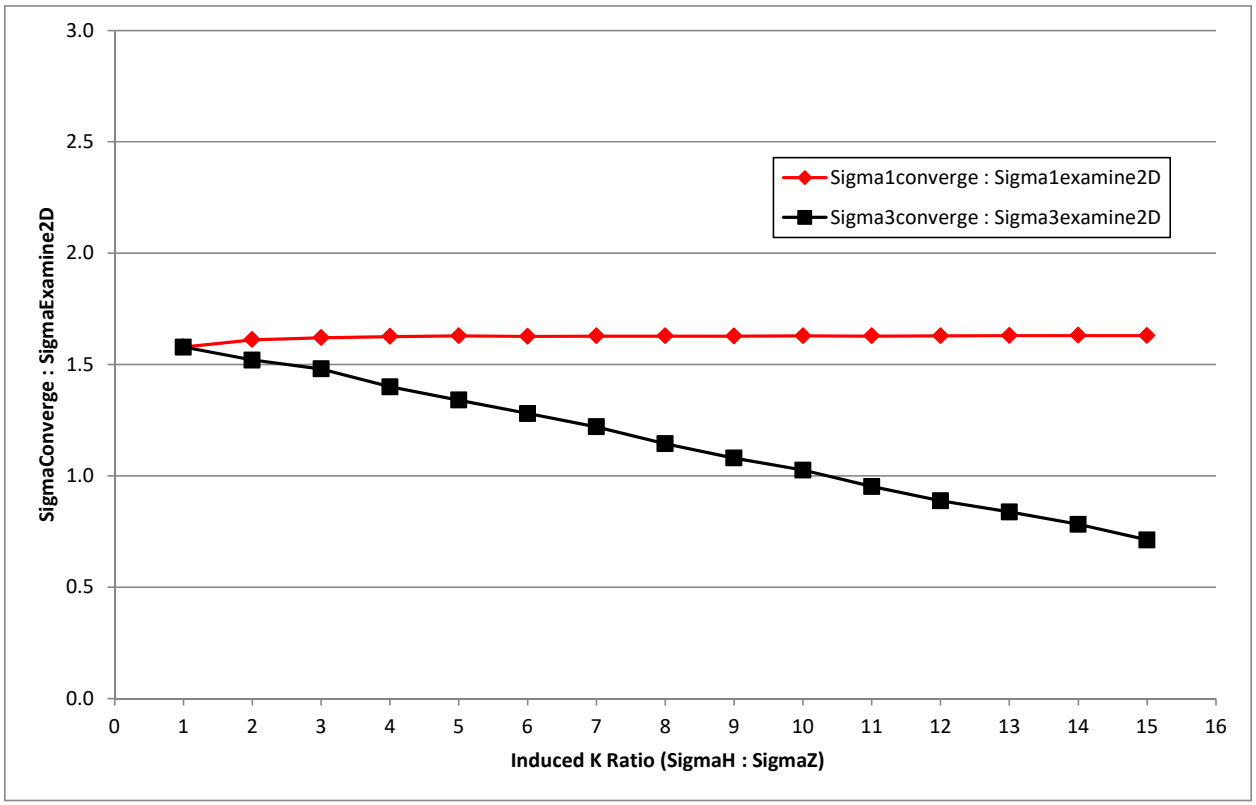

Figure 4.2 Geometric correction ratios of induced stresses of "Converge" to the numerical model at 45° to horizontal.

Using the closure data obtained in Chapter 3, and the methods described above, the maximum uncorrected principal stress change was estimated at 56 MPa and the minimum at 30 MPa. Using the correction from Figure 4.1, the maximum principal stress change was reduced to 39 MPa and the minimum to 16 MPa. It is interesting to note that the maximum principal stress change neared its peak after the first primary blast of the panel while the minimum principal stress change did not see a large change until the third primary blast. To identify the total maximum and minimum stress from the estimated in situ stress and induced stress, a two dimensional stress transformation was performed using the method described in Hoek and Brown (1980), the results of which can be seen in Table 4.4. The maximum total stress change that is experienced during mining activities in the overcut is estimated at 92 MPa. This is below the UCS of 120 MPa that was tested for the rock. The rock mass had not failed in the overcut at the time of an inspection after the September blast.

Table 4.3 Principal stress changes at the overcut at 2b11013 #5 sill.

	Microstrain			Principal Strain Change		Direction	Principal Stress Change			Corrected Principal Stress Change	
Date	AB	AC	BC	ε_1	ε_3	θ	σ_1	σ_3	Induced K Ratio	σ_{1C}	σ_{3C}
27-Aug-12	0	0	0	0	0	0	0	0	-	0	0
5-Sep-12	442	-442	391	1083	-637	29	25	-7	-4	19	-3
7-Sep-12	1212	-364	616	1808	-476	36	49	6	8	37	2
8-Sep-12	1126	-503	724	1964	-708	33	51	1	51	39	1
9-Sep-12	1354	269	691	1541	261	45	50	25	2	35	13
10-Sep-12	1597	338	716	1735	338	49	56	30	2	39	16

Table 4.4 Summation of the stresses at the overcut at 2b11013 #5 sill.

	Corrected Principal Stress Change			In Situ Stress			Summation of Stress Change		
Date	σ_{1C}	σ_{3C}	Angle	σ_1	σ_3	Angle	σ_1	σ_3	Angle
27-Aug-12	0	0	0	62	31	0	62	31	0
05-Sep-12	19	-3	29	62	31	0	72	37	18
07-Sep-12	37	2	36	62	31	0	88	44	26
08-Sep-12	39	1	33	62	31	0	89	44	26
09-Sep-12	34	13	45	62	31	0	88	53	18
10-Sep-12	39	16	49	62	31	0	92	56	20

4.2 Analysis of Extensometer Data

In conjunction with the drift closure data, 3 extensometers were installed to monitor the hanging wall response to approaching mining and eventual undercutting by a mined panel. As mentioned in Section 3, two of the extensometers did not provide useable data. The remaining extensometer recorded the hangingwall response to mining block L62 between the 970 level and 990 level. Challenges with drill access required the extensometer hole to be drilled at approximately 45° to the panel strike and 45° to the panel dip direction.

To simplify the interpretation of the extensometer data, it was assumed that the recorded deformation is due to movement of the hanging wall normal to the plane of panel hanging wall. This assumption will ignore changes to the hanging wall stress with panel mining for stresses oriented parallel to the panel (horizontally and vertically), as these stress changes should be minor due to the narrow nature of the panels.

To relate recorded anchor movements to stresses, the anchor deformations must be interpreted as strains between anchors. As discussed, the extensometer is installed at an oblique angle to the panel hanging wall so the interpretation of the recorded deformation is more challenging. For the extensometer in the hanging wall of L62, installed at 45° to both the strike and dip of the panel, the anchors that are 1.4m apart would be 1.4m x (sin 45° x sin 45°) apart in the direction normal to the panel (0.7m apart).

If it is assumed that the anchors will only move in the direction of the extensometer rods. 1mm of recorded movement, measured between anchors 1.4m apart, would give 0.7% strain. If it is assumed that extensometer anchors would move in the direction normal to the panel hangingwall, 1mm of movement between the anchors that are 1.4m apart, in the direction of the extensometer, would correspond to anchors 0.7m distance apart in the direction normal to the panel. To record the strain normal to the panel, 1mm of measured movement between anchors 1.4m apart would give 1.4% strain (1mm/0.7m), or double the strain recorded between anchors in the extensometer direction.

It is expected that the second strain estimating approach is correct since the hanging wall rock mass is much stiffer than the extensometer. This means that the plotted strains are one half of the actual strains normal to the panel hanging wall.

The strains normal to the panel (normal strains) will reflect the increasing stress as mining approaches the extensometer anchor location. The effect of blast 7 (Figure 3.19) on the strain between anchors 1 and 2 is approximately 0.012% compressive strain along the extensometer, or twice as much normal to the stope (0.024%). With the assumption that the principal stresses do not change significantly parallel to the stope, the stress increase due to blast 7, approximately 2 metres from the hanging wall can be expressed by Equation 4.2:

$$\sigma_n = \epsilon_n \times E \tag{4.2}$$

where: E = Young's modulus (50GPa from rockmass classification); and,
ϵ_n~ strain (0.02% in compression after blast 7).

The stress increase due to blast 7 is therefore approximately 10MPa based on the rockmass elastic modulus and strain calculated from the MPBX.

Note that the minimum incremental change in strain reading is approximately 0.01%, as shown in Figure 3.21. This suggests that the reading accuracy is approximately 0.01% or a displacement of approximately 0.1 mm.

Figure 3.18 shows the panel configuration after blast 8 when all of the extensometer anchors have been undercut by the panel hanging wall. For strain due to elastic relaxation between anchors close to the open panel, and at a significant distance from the end of the open panel, Equations 4.3 and 4.4 can be used to estimate the pre-mining stress close to a spherical cavity (Milne, 1997). Using a spherical simplification for a tabular excavation can only be a reasonable approximation when both the distance between anchors considered and the furthest anchor from the excavation are small relative to the extent of the opening.

$$\varepsilon_r = \left(\frac{\sigma_r (1 + \upsilon)}{E}\right) \tag{4.3}$$

Or

$$\sigma_r = \left(\frac{(\varepsilon_r \times E)}{(1+\upsilon)}\right) \tag{4.4}$$

Using a Young's modulus for the rockmass of 50GPa and a strain in tension of 0.02% gives a stress change of ~11MPa.

It should be noted that 11MPa is less than the expected virgin in situ stress normal to the panel hanging wall. This panel case history is at a depth of approximately 1000 metres so the vertical stress would be approximately 30MPa and the stress normal to the panel would expect to range between 30 and 75MPa, based on conditions common to the rocks in the Canadian Shield. It should also be noted that the smallest measurable displacement would change the estimated stress by about 100%, so from this perspective, the estimated stresses are surprisingly close to the expected values. Unfortunately, this approach does not provide useful insight into stress conditions at the mine.

4.3 Numerical Modelling Using ExamineTAB

The calculation of induced stresses present within a panel prior to mining was performed using the numerical modelling program ExamineTAB (Curran et al., 1991). ExamineTAB is a pseudo 3D displacement discontinuity program for calculating stresses and displacements around tabular ore bodies in a direction normal to the plane of the ore body. To analyse the induced stresses before mining a panel, the excavated rock (including the mined out sills) were drafted in AutoCAD and imported into ExamineTAB. The mining block that was analyzed using the numerical modelling was 2b11013, which is the same block shown in Figure 3.18.

The rock properties used for the analysis are shown in Figure 4.3. Also shown as input in Figure 4.3 are the in situ stresses in the mining block prior to mining any of the panels. At this point, the only excavated rock is from the sills used to access the block. When modelling adjacent panels in this mining block, the rib pillars were modelled as excavated rock. The reason for this is that the rib pillars between panels are only 3m wide and are designed as failed pillars. The expectation is that the stress within pillars will be much higher than the strength of the rock and

that when they fail, stress will be unable to transfer through the failed rock. The rest of the 17 panels that were modelled are included in Appendix D.

4.3 Classification of Case Histories Based on Induced Stress

The induced pre-mining stress in the 17 panels that were modelled using the ExamineTAB program were used to classify the panels into stress categories. The classification of panels based on the pre-mining induced stress allows for the comparison of dilution numbers for those panels based on induced stress. It was expected that lower pre-mining induced stress would result in lower amounts of dilution. The higher induced stress could cause failure or damage in the rock mass before mining, effectively lowering the rock mass classification resulting in more wall failure to occur once it is mined.

Classification of the panels based on induced stress is difficult because the induced stresses vary across the panel extent. Because of this difficulty, the panels were classified based on the estimated area of the panel with a modelled induced stress higher than 100MPa, immediately prior to mining. The panels were classified into 3 groups: classification 1 is under 15% area, classification 2 is between 16 – 50% area, and classification 3 is over 50% area. These limits were chosen to break up the panels into 3 fairly equally groupings of stress conditions. Table 4.5 shows the percent area of each panel that was estimated to have higher than 100 MPa induced stress, as calculated from ExamineTAB.

The results that are presented in this table correspond to the stresses expected with the mining steps. The panel numbers named here are in reference to the order that they were mined out. When Panel #1 was to be mined (east side of the mining block), there was only the excavation of the sills that would provide a small amount of induced stress in the panel prior to mining (Figure 4.3). Panels #2 and #3 were then mined out on the same level as Panel #1 would have small amounts of induced stress in the locations that are adjacent to the panels that were already excavated (Figure 4.4).

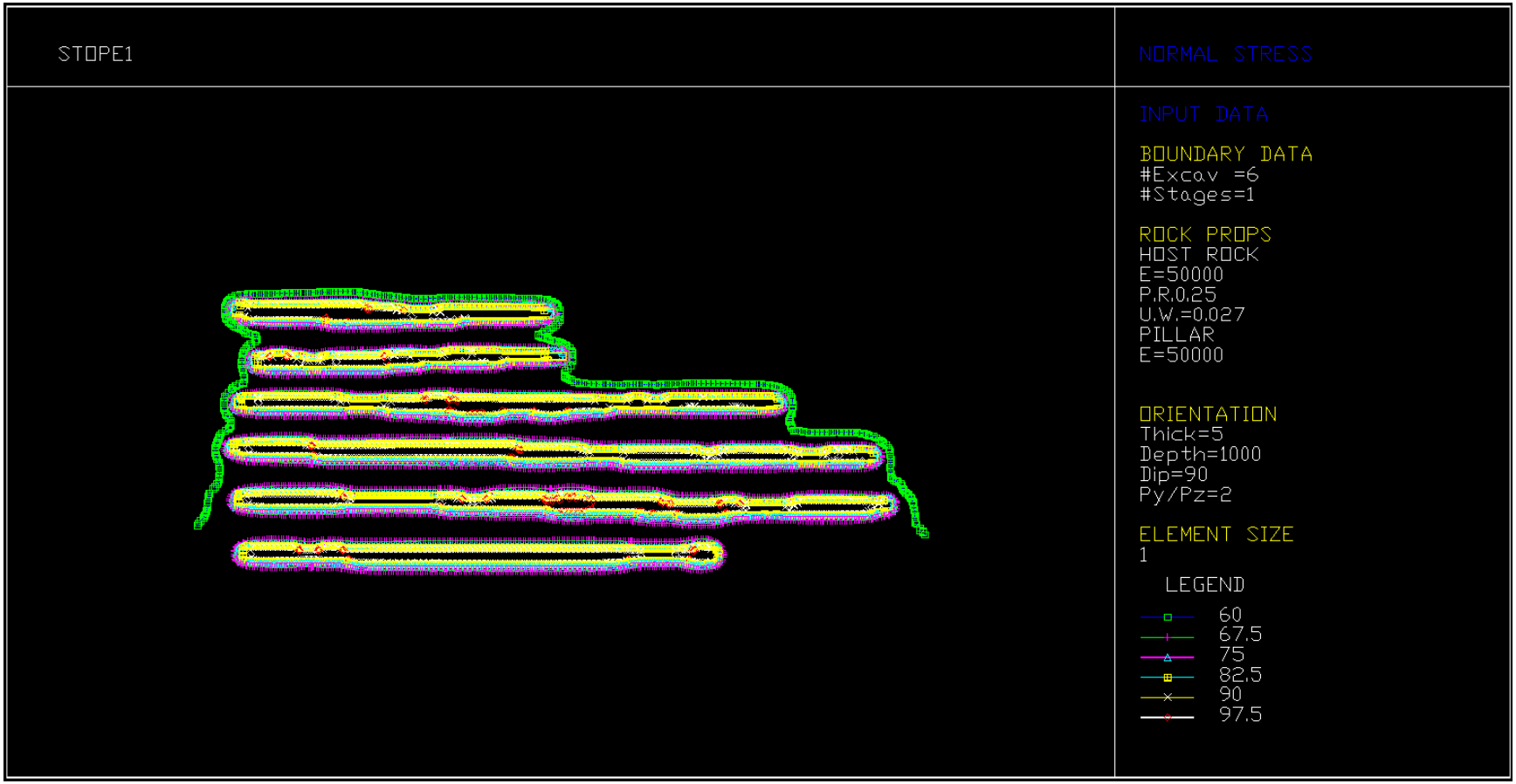

Figure 4.3 Induced stresses around the sill excavations at 2b11013 block prior to any panels being mined out.

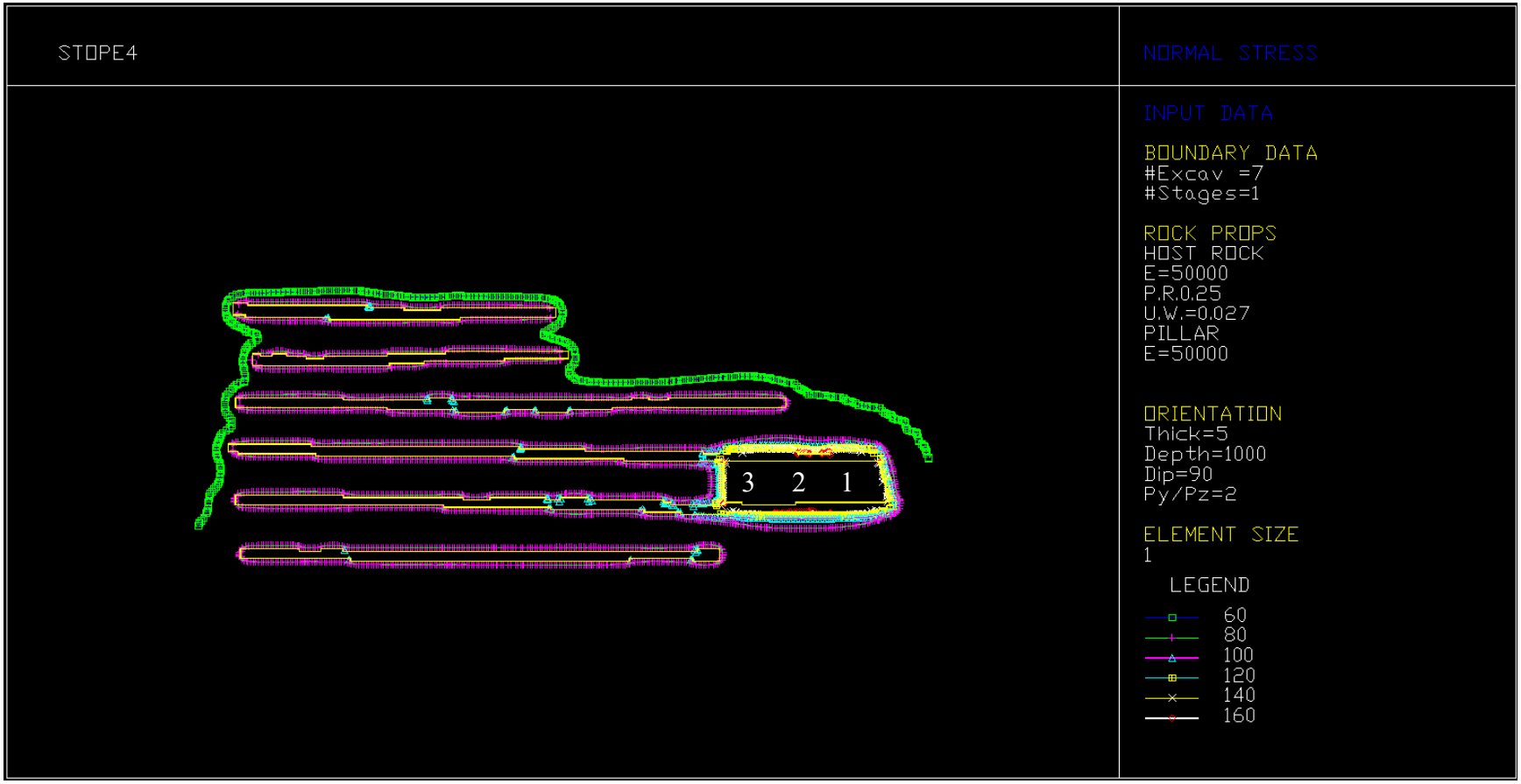

Figure 4.4 Induced stresses after Panels #1-3 have been mined out on the east side.

Panel #4 was then excavated on another level on the far west side of the mining block from Panel #1. The distance from Panel #3 to Panel #4 is quite large and therefore Panel #4 is still in a similar stress situation to that of Panel #1 before it was mined. Panels #5-6 are mined adjacent to Panel #4 on the bottom level and the induced stress prior to mining those panels is influenced mostly by the proximity to Panel #4 (Figure 4.5).

Panel #7 does not have much induced stress influence because of the large pillar left between it and Panel #6 (Figure 4.6). Panel #8 has a similar stress situation to that of Panels #2 or #5. There is still only one panel adjacent to it and provides only a small amount of induced stress, however, this time the adjacent panel is from below. The first large increase in induced stress occurs in Panel #9; where there are now two adjacent panels that cause higher induced stress flow into the panel. Both Panels #8 and #5 are causing a high induced stress to occur in the bottom and left hand side of the panel (Figure 4.6).

This trend now occurs throughout the rest of the panels with an anomaly of Panel #12; however, upon closer examination it is noted that Panel #12 sits on top of the pillar between Panel #6 and #7, which causes it to have only one adjacent panel on the left hand side (Figure 4.7). The final panel to be mined out also has the expectedly highest amount of induced stress. Panel #17 (shown as the pillar adjacent to Panel #16) has three adjacent panels that have been previously excavated, and those areas are now flowing the stress into the Panel #17 area. Overall, the relative amounts of induced stress in each panel are as expected (Table 4.5 and 4.6).

The panels in 2b11013 can then be classified based on the classification system mentioned; Table 4.6 shows the classification of the panels. There are seven panels in Classification 1, six panels in Classification 2, and four panels in Classification 3. With the panels classified based on induced stress, a possible correlation between the amount of dilution and the induced stress can be assessed. The comparison between induced stress within the panel and dilution will be discussed further in Chapter 5.

It is important to note that for this analysis, the initial input values are not of great significance since the point of the analysis is to identify relative changes in stress in the panels. The results are categorized based on their relative stress changes.

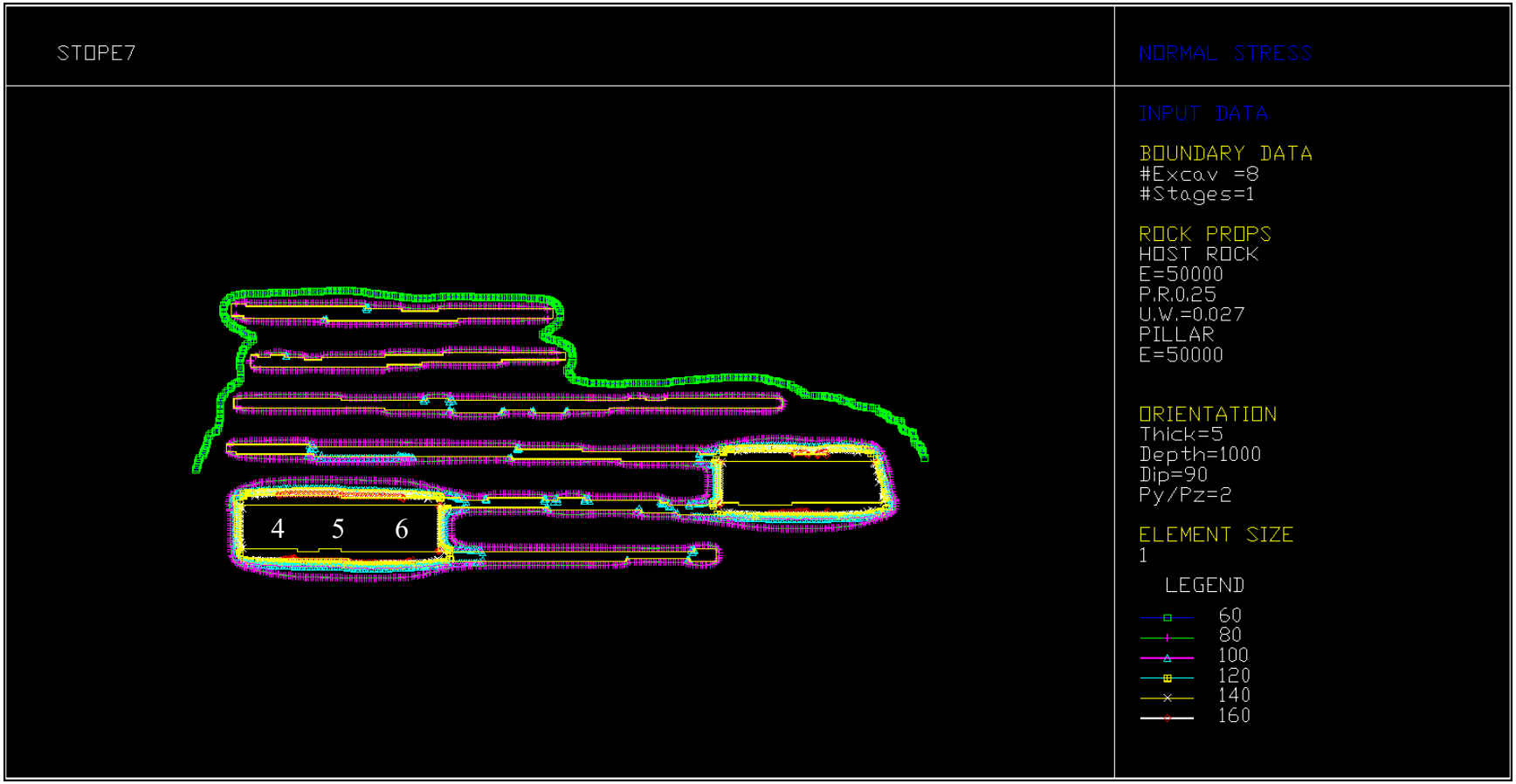

Figure 4.5 Induced stresses after Panels #4-6 have been mined out on the west side.

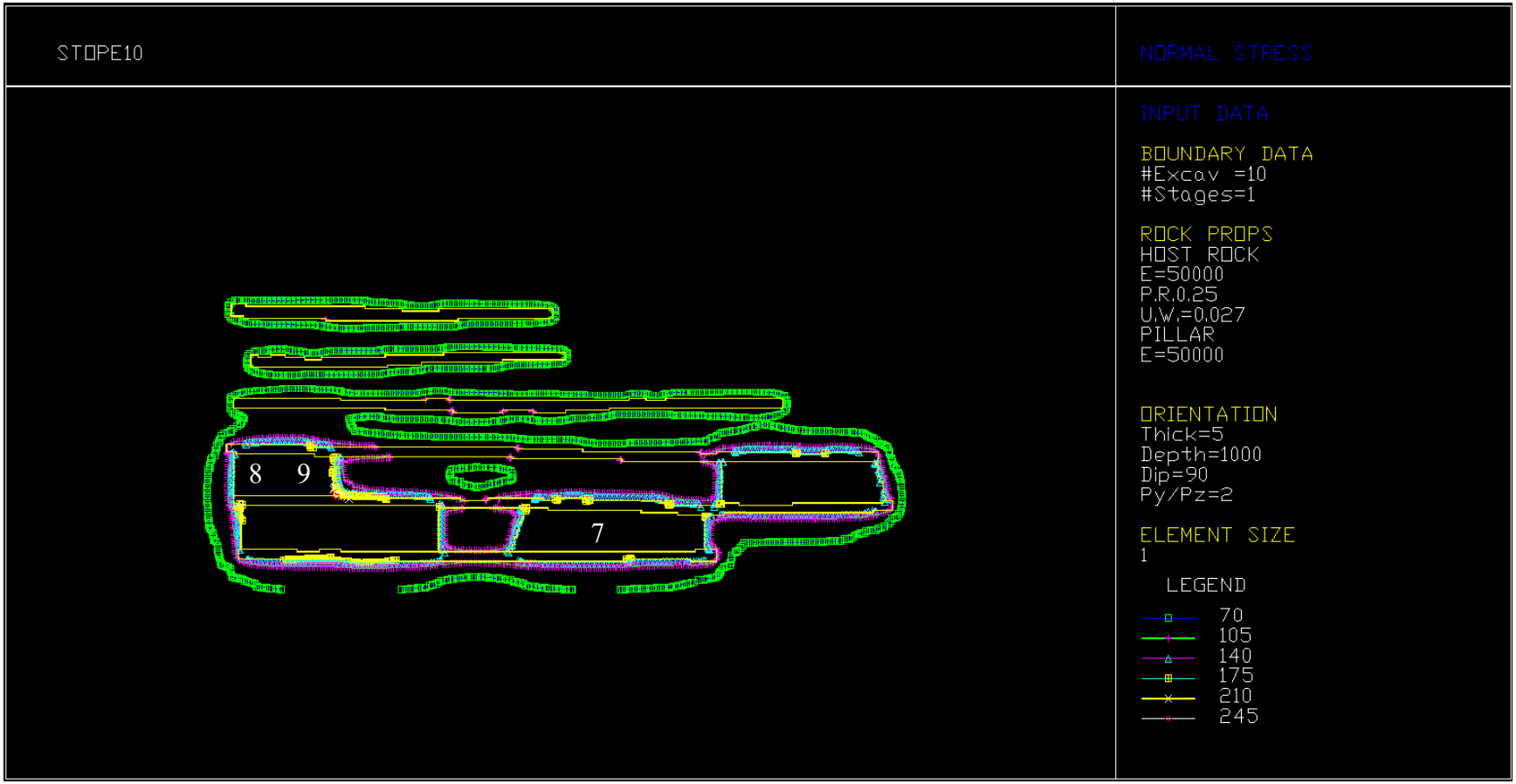

Figure 4.6 Induced stresses after Panels #7-9 have been mined out.

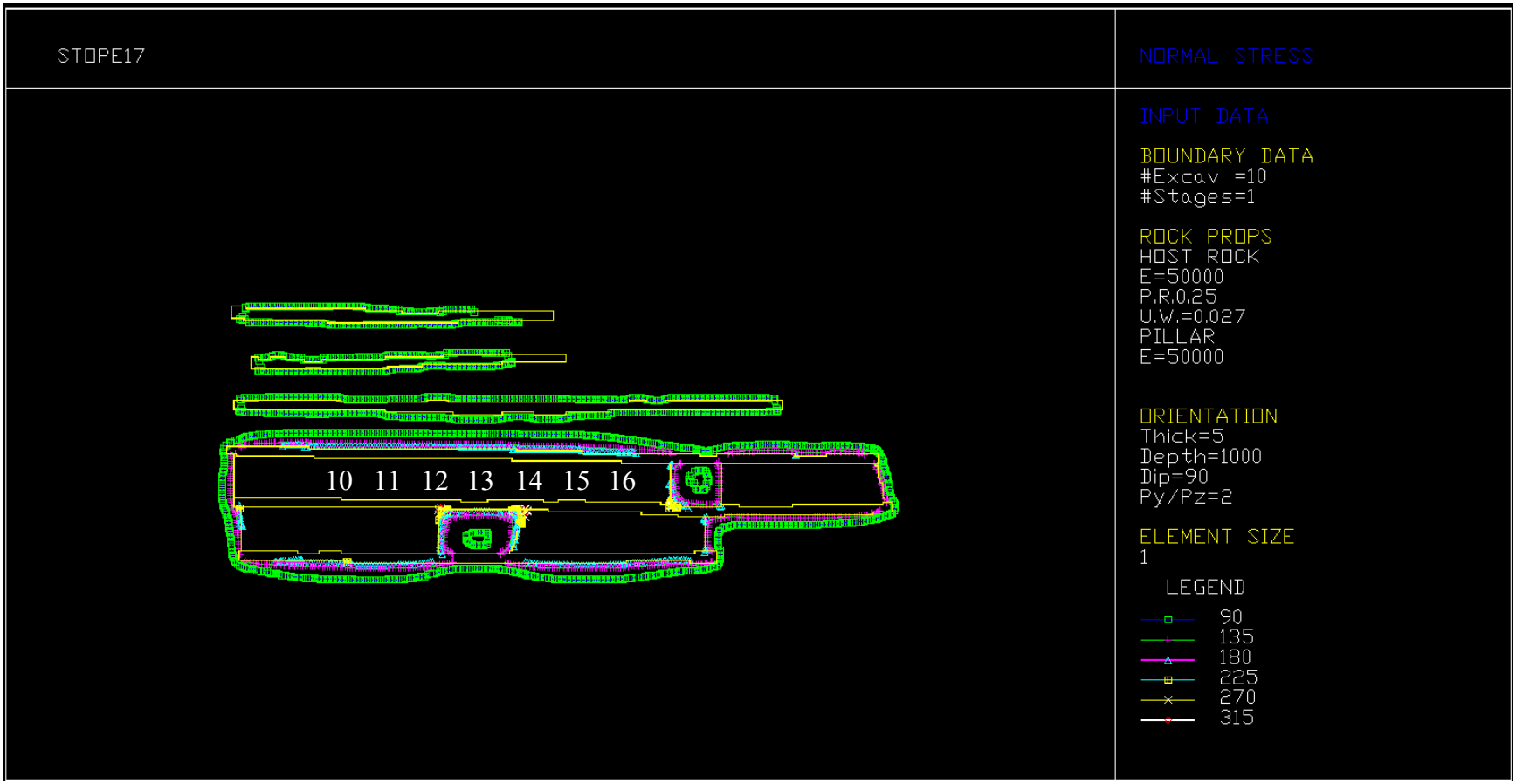

Figure 4.7 Induced stresses after Panels #10-16 have been mined out.

Table 4.5 Percentage of the area of the panel higher than 100MPa.

Stope #	Stope Area (m^2)	Area Over 100MPa (m^2)	Percent of Stope Over 100MPa (%)
1	380	0	0
2	370	47	13
3	370	52	14
4	592	0	0
5	461	50	11
6	428	63	15
7	1271	0	0
8	360	43	12
9	328	178	54
10	335	164	49
11	409	164	40
12	333	71	21
13	313	157	50
14	318	154	48
15	268	161	60
16	336	197	59
17	383	293	77

Table 4.6 Classification of panels based on amount of induced stress.

Classification	Stope #	Stope Area (m^2)	Percent of Stope Over 100MPa (%)
1	1	380	0
1	4	592	0
1	7	1271	0
1	5	461	11
1	8	360	12
1	2	370	13
1	3	370	14
2	6	428	15
2	12	333	21
2	11	409	40
2	14	318	48
2	10	335	49
2	13	313	50
3	9	328	54
3	16	336	59
3	15	268	60
3	17	383	77

4.4 Summary

To use the three – point extensometer data that was gathered from Seabee Gold Mine, a methodology was developed to convert the displacement readings into the changes in principal stresses. To account for the difference in circular openings rather than square opening that are more common in mining, an empirical method was developed to obtain a ratio that could be applied to the calculated principal stress changes to estimate actual stress change. Extensometer data was also interpreted to give estimates of induced stress and the stress state prior to mining. It was found that the extensometer data was not accurate enough to produce useful results.

A numerical model was also used to calculate the amount of induced stress present in panel areas prior to mining. The changes in induced stress are caused by mining out adjacent panels which re-distributes the stresses. The panels were then classified according to the amount of induced stress.

The next chapter is an analysis of dilution in the study panels. The classification of panels by induced stress will be analysed to determine if there is any trend of increasing dilution with increased stress; dilution will be analysed using existing empirical design methods; and a new method of analysing dilution in narrow vein mines proposed and evaluated.

CHAPTER 5

ANALYSIS OF DILUTION DATA USING EMPIRICAL DESIGN METHODS

This chapter presents the analysis of the dilution data from the Seabee Gold Mine case study areas. The current empirical methods of predicting dilution are inadequate for thin veined orebodies where predicted dilution is < 0.5m. A new method of determining dilution was created that identifies dilution at points over the panel wall instead of predicting a single average dilution for the entire panel. This section includes the following:

- an initial analysis using Clark's ELOS method of predicting dilution based on previous case histories;
- an analysis of panel dilution based on the classification of the panels by pre-mining stress levels;
- the introduction of the terms used in a new method of determining dilution using a detailed surface dilution analysis conceptual model; and,
- the analysis of the panels from the 2b11013 mining block using the new method of detailed surface dilution analysis data.

5.1 Analysis Using Clark's ELOS Method

The CMS data, panel geometries, and joint data collection for the three stoping blocks (2b11013, 2b11011, and 2c10010) were analysed. The Hydraulic Radius versus Modified Stability Numbers from Tables 3.1 and 3.2 were plotted on the Modified Dilution Graph to determine the distribution of actual dilution compared to the predicted dilution (Figure 5.1). The distribution of data shows that the N' and HR of the panels is approximately 16-19 and 3-6m, respectively.

The N' values vary due to the variability of the Q' measured during data collection. These narrow ranges of values fall within the predicted ELOS of < 0.5m for all panels. Whereas, the actual ELOS ranges from < 0.1m to > 0.5m (minimum ELOS is 0.01m and maximum ELOS is 1.3m). The gradient of predicted ELOS on the Modified Dilution Graph is not refined enough to be useful for thin veined orebodies where experienced dilution is often less than 0.5m but still of a significant economic impact to the mining operations. The next section investigates the effect of pre-mining stress on hanging wall dilution.

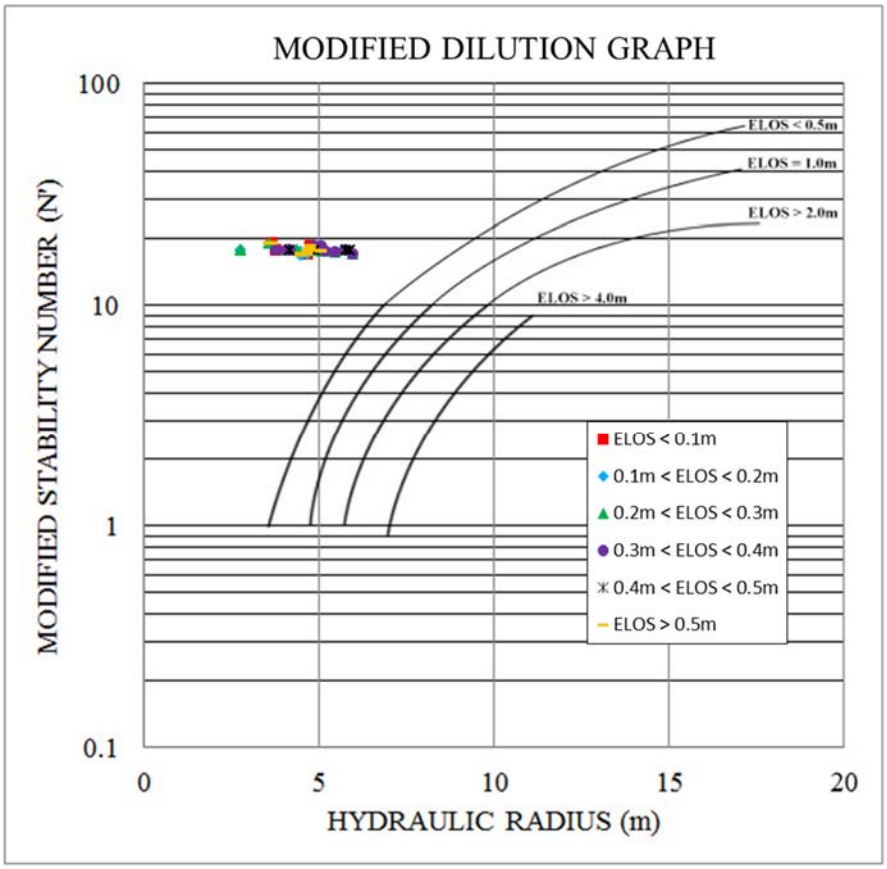

Figure 5.1 Modified Dilution Graph depicting ELOS for the 56 Seabee Gold Mine case study panels in this study (after Capes, 2009).

5.2 ELOS Dilution Analysis using the Induced Stress Classifications

To identify the effect of pre-mining induced stress on panel dilution, the stress classification system from Table 3.7 was applied to the geometry of each panel. This comparison of dilution based on stress classification is shown in Figure 5.2. If the ELOS of each panel was affected by the pre-mining induced stress, it would be expected that classification #1 (which contained the panels with the least amount of pre-mining stress) would have a lower ELOS than classification #2 and classification #3 (which had the highest amount of pre-mining stress). What is seen in Figure 5.2 is no discernible trend going from classification #1 to #3 on the north wall or the south wall dilution. There are panels of high and low ELOS in all three classifications. This indicates that pre-mining stress is not a significant factor for determining the amount of ELOS in a panel. In all cases, the predicted dilution was less than 0.5m so it was not necessary to compare the difference between actual and predicted dilution.

5.3 Methodology of Increasing the Spatial Density of Panel Dilution Data

A current shortcoming with the Modified Dilution graph is the lack of delineation of ELOS in the range < 0.5m. Since dilution greater than 0.5m can give a high percent dilution and is often considered excessive for narrow vein panels, this is a particularly important area of the dilution graph.

The empirical dilution prediction techniques explicitly account for dilution from rockmass instability through the N' term; whereas, the average amount of dilution caused by drill hole deviation, blast damage, and undercutting are implicitly accounted for through the empirical approach that incorporates the average effect of these parameters on the case histories used to develop the technique. More detailed information can be obtained from studying the spatial location of dilution on the HW and FW surfaces and is a focus of this research. In addition, the depth of underbreak (DoU), or the ore left on panel walls, can further assist in determining the factors influencing the behaviour of panel walls.

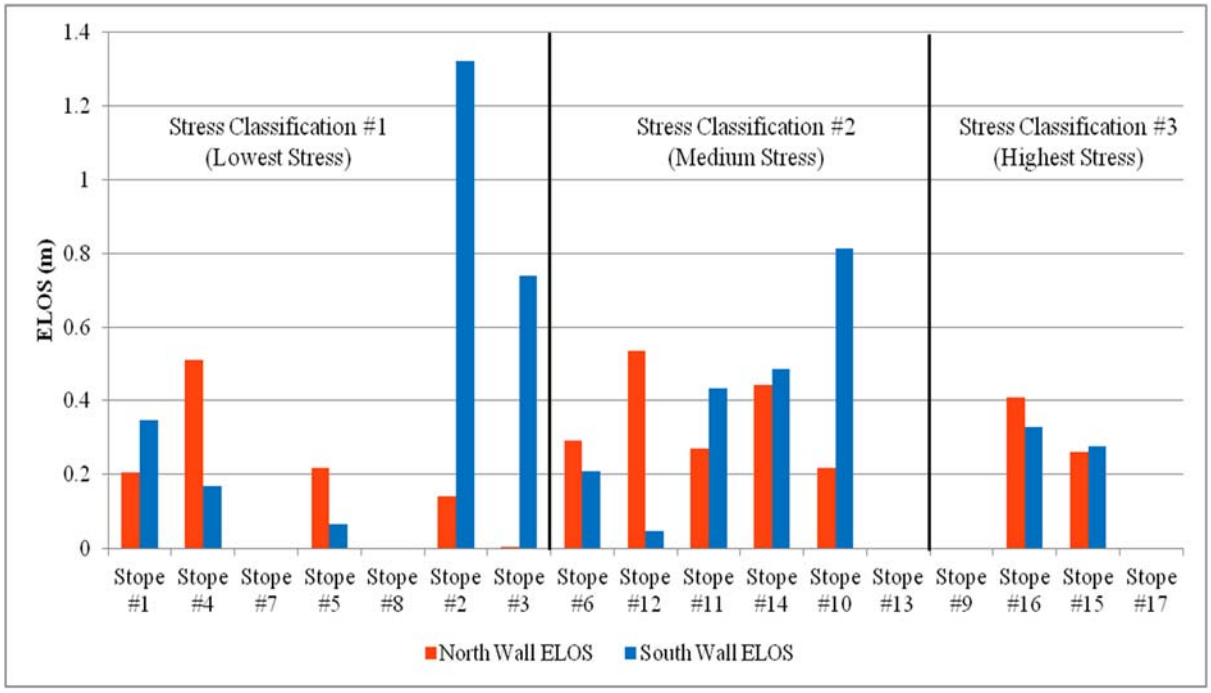

Figure 5.2 Comparison of ELOS for each 2b11013 panel based on its stress classification (blank panels did not have a CMS).

The first of two variables that were used to increase the spatial resolution of dilution data is the Effective Radius Factor (ERF) (Milne et al., 1996). The ERF replaces the HR as a measure of the geometric stability of an openings surface. HR was replaced due to several drawbacks to the term, as follows:

- it is difficult to apply a HR to an irregularly shaped surface; and,
- the HR can only provide one measurement at the centre of the panel, representing the overall stability of the panel.

ERF is calculated by measuring the distance from any point on the panel surface to the supporting abutments. This measure of the distance to the supporting abutments can be found by using a number of rays, n, projected at set angles, θ, and recording the distance to the abutment, r_θ as shown in Figure 5.3 and 5.4 and Equation 5.1:

$$\text{ERF} = \frac{.5}{\frac{1}{n}\sum_{\theta-1}^{n}\left(\frac{1}{r_\theta}\right)} \tag{5.1}$$

The ability to calculate a geometric stability at any point of the panel surface provides the ability to relate dilution to the stability of the point with regards to its distance from an abutment. The ERF value is greatest at the centre of the stope and smallest at an abutment. If the distance to a wall is zero, the denominator becomes infinity, and ERF tends to zero.

The second variable that was used is a new term called the Depth of Slough (DoS). DoS is a linear measure of dilution at any point on the panel surface. DoS augments the ELOS term for a quantification of the amount of dilution occurring. ELOS is calculated by cutting a cross-section of a panel and taking the area of the overbreak and dividing by the height of the panel as shown in Figure 5.5. The benefits of the ELOS methodology for calculating dilution is its ability to provide an objective measure of dilution that can be directly compared to other cases. The drawback of the ELOS method is that it can only be calculated over a single surface or section of the surface.

The DoS term is calculated in a similar manner to ELOS. Cross sections of the open panel are cut at regular intervals that match the grid pattern used to find the ERF values (a grid of 1.5m x 1.5m was used for this study). Within the cross section, the linear amount of dilution is taken at the intervals equivalent to the grid spacing (Figure 5.6). This process of calculating dilution allows for the same objective comparisons between panels as the ELOS method but additionally allows for dilution to be compared spatially across the rest of the panel surface. With the two terms of ERF and DoS defined, it is now possible to compare the spatial distribution of stability over a panel surface to the corresponding dilution at that same point. The next section will explain the conceptual model created to estimate maximum overbreak from various causes.

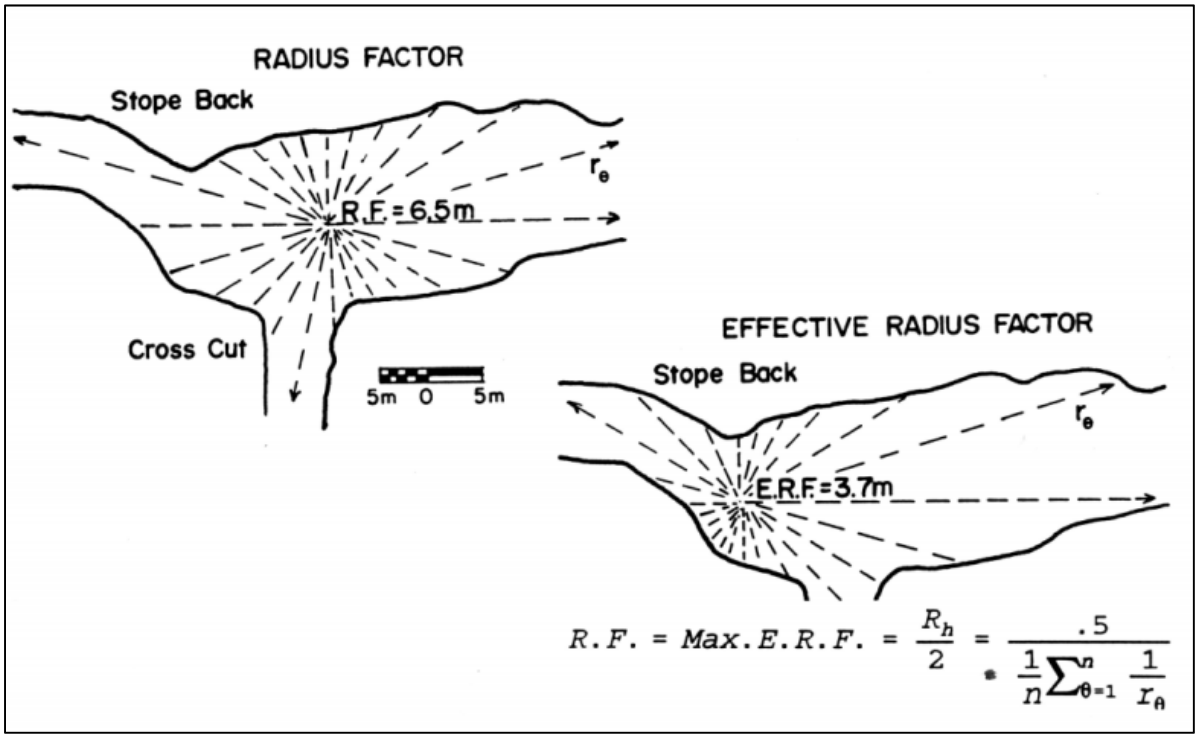

Figure 5.3 Panel back showing the radius factor and effective radius factor (from Milne, 1997).

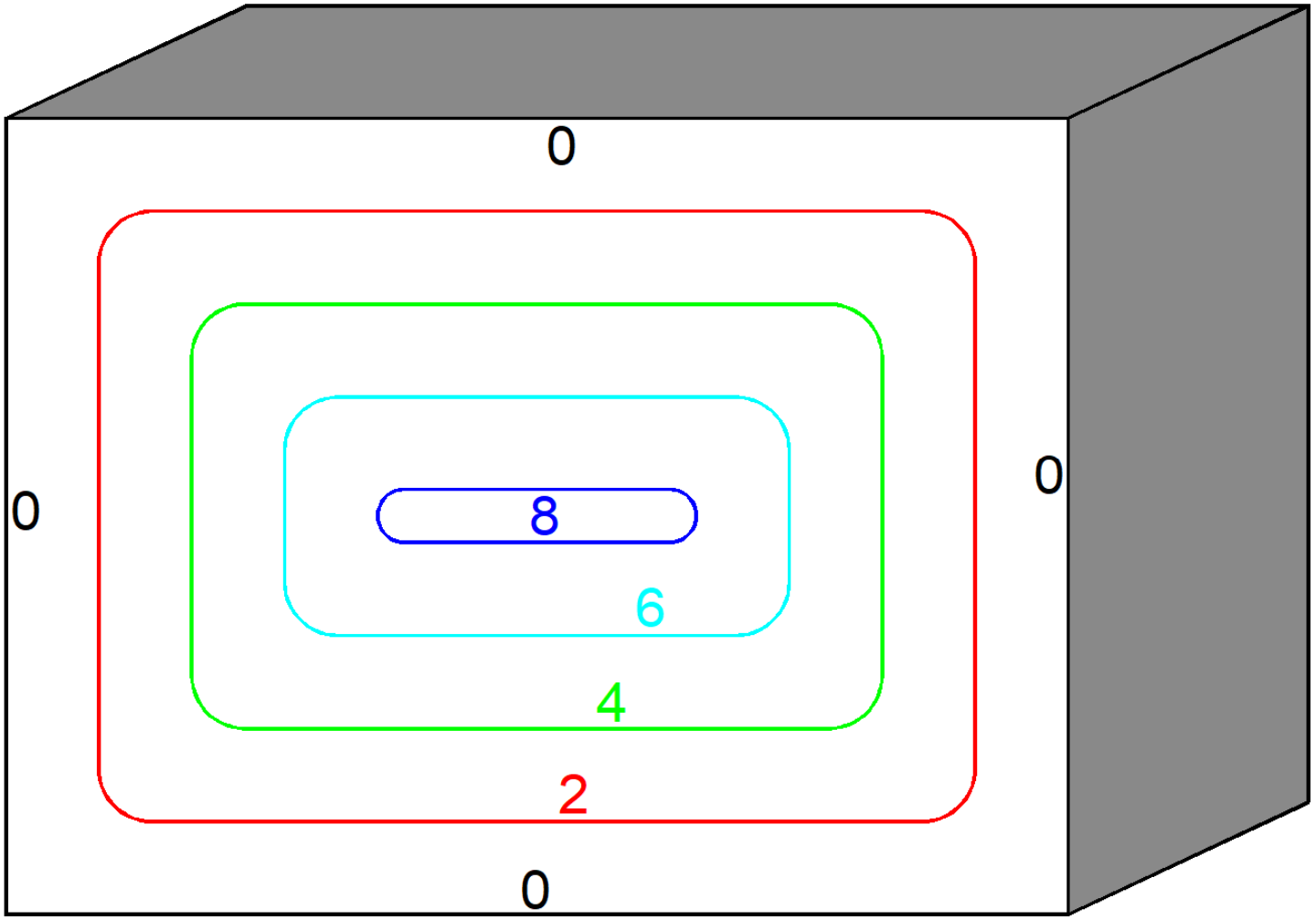

Figure 5.4 Conceptual model of the ERF contours where an ERF of 0 is at the abutments and the maximum ERF is at the centre.

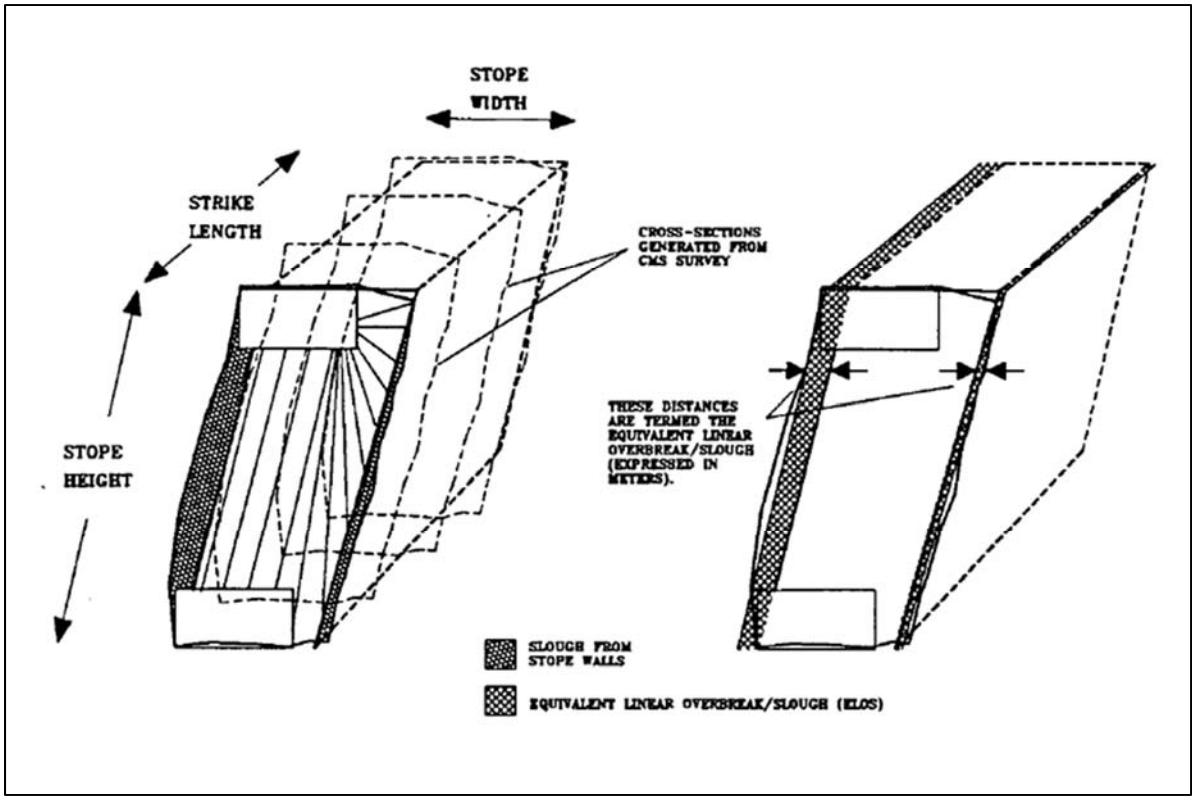

Figure 5.5 Schematic showing the calculation of ELOS (from Clarke 1998).

5.4 Creation of a Conceptual Dilution Model for the Open Panels

A conceptual model was created to compare the actual data plotted against a hypothetical model of expected overbreak. The three failure mechanisms that are spatially controlled factors that were expected to have the largest influence on panel dilution are:

- geometrical instability represented by an expected arch shaped failure;
- borehole deviation; and,
- panel undercutting due to the sill width being greater than the panel width.

5.4.1 Conceptual Model of Arch Shaped Failure

This study represents the geometrical instability in the wall of a stope with the shape of a parabola as shown in the left hand wall of Figure 5.7. This shape was chosen because the panel wall should progress to an arched shaped (Milne, 1997). Using this shape provides a failure envelope where there is no failure at the pillar walls and maximum failure in the panel centre

(Figure 5.7). The shape of the parabola was calculated based on the ELOS of either the north panel wall or south panel wall.

5.4.2 Conceptual Model of Borehole Deviation

Borehole deviation is expected to increase with increased drilling distance from the collar on the overcut. No data exists at Seabee Gold Mine on the extent of borehole deviation for the production blast holes. Based on a hole size of 2.5", it was estimated that the borehole would deviate up to 4% of the drilling distance at the end of the drill hole (Hamrin, 1995). This results in a maximum deviation of 0.72m for a 16m drillhole. The shape of the deviation was modelled using a quadratic equation (Milne, 1997) (Figure 5.8):

$$\text{Borehole Deviation} = 0.72\text{m} = 0.0028 \times (\text{Distance from Collar})^2 \quad (5.2)$$

Blast damage is also implicitly included with the borehole deviation in the conceptual model. It is assumed that the blast damage will be constant throughout the panel and will follow a similar shape as the borehole deviation.

Taking the total effect of borehole deviation on the failure profile would result in no net change in total dilution because it is assumed that the borehole deviation has an equally likely chance to deviate to any angle from the designed borehole location (Figure 5.9). This assumption is required due to the lack of borehole deviation monitoring performed at Seabee Gold Mine.

Often in production longhole drilling, the borehole will have a preferential deviation due to drill rotation, joint orientations, and differing material properties from the orebody to the host rock. For example, with the primary joint set following a similar strike and dip as the ore structure, the borehole deviation will likely deviate along the same plane as the strike of the orebody rather than away or into the orebody. If the primary joint set has a dip steeper than the dip of the orebody but along the same strike, the borehole will likely want to deviate into the orebody and along the strike of the orebody. But as noted above, without measurements on the deviation of the borehole at Seabee Gold Mine, it has been assumed that the borehole will deviate in all directions, with equal likelihood.

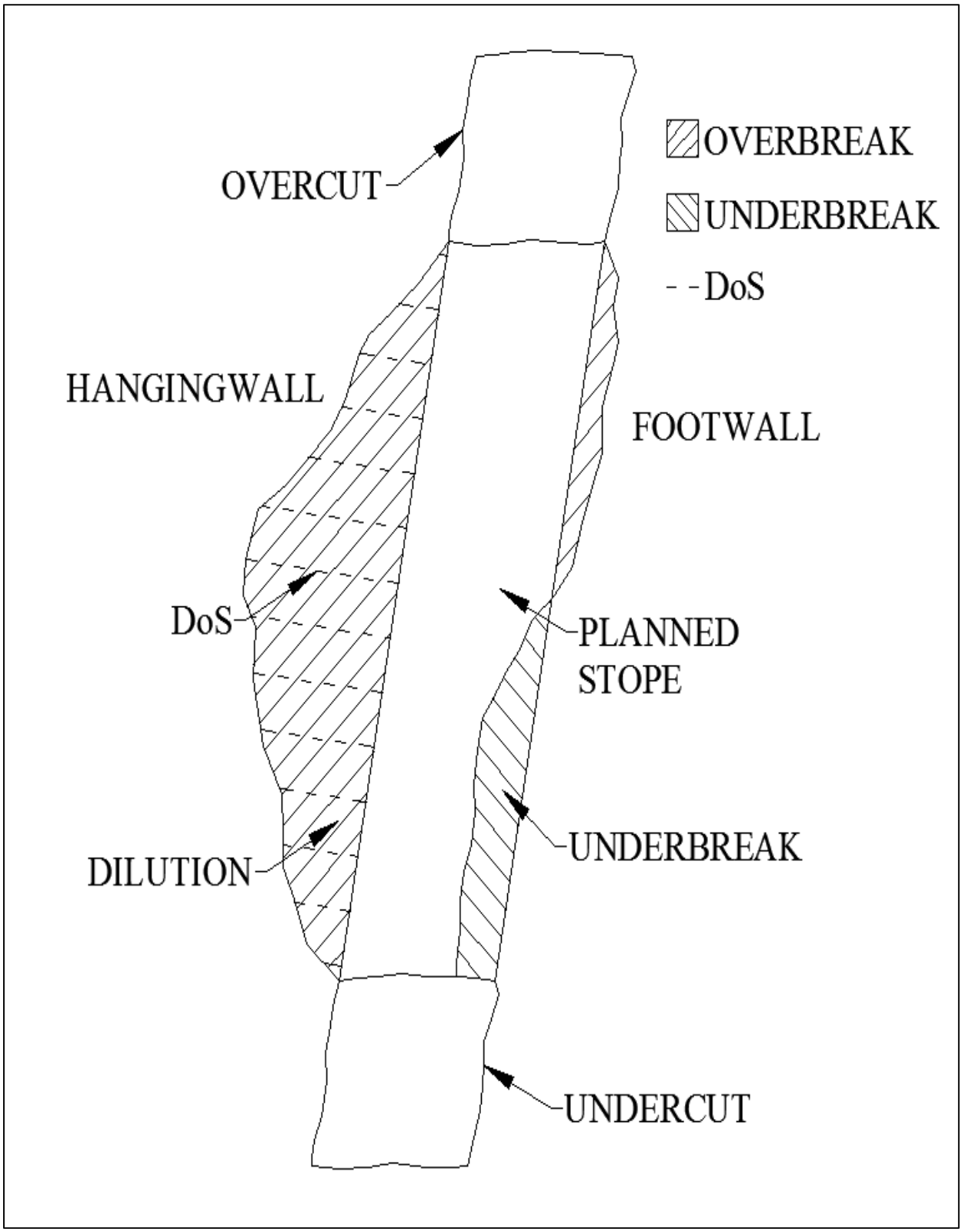

Figure 5.6 Schematic showing the calculation of DoS.

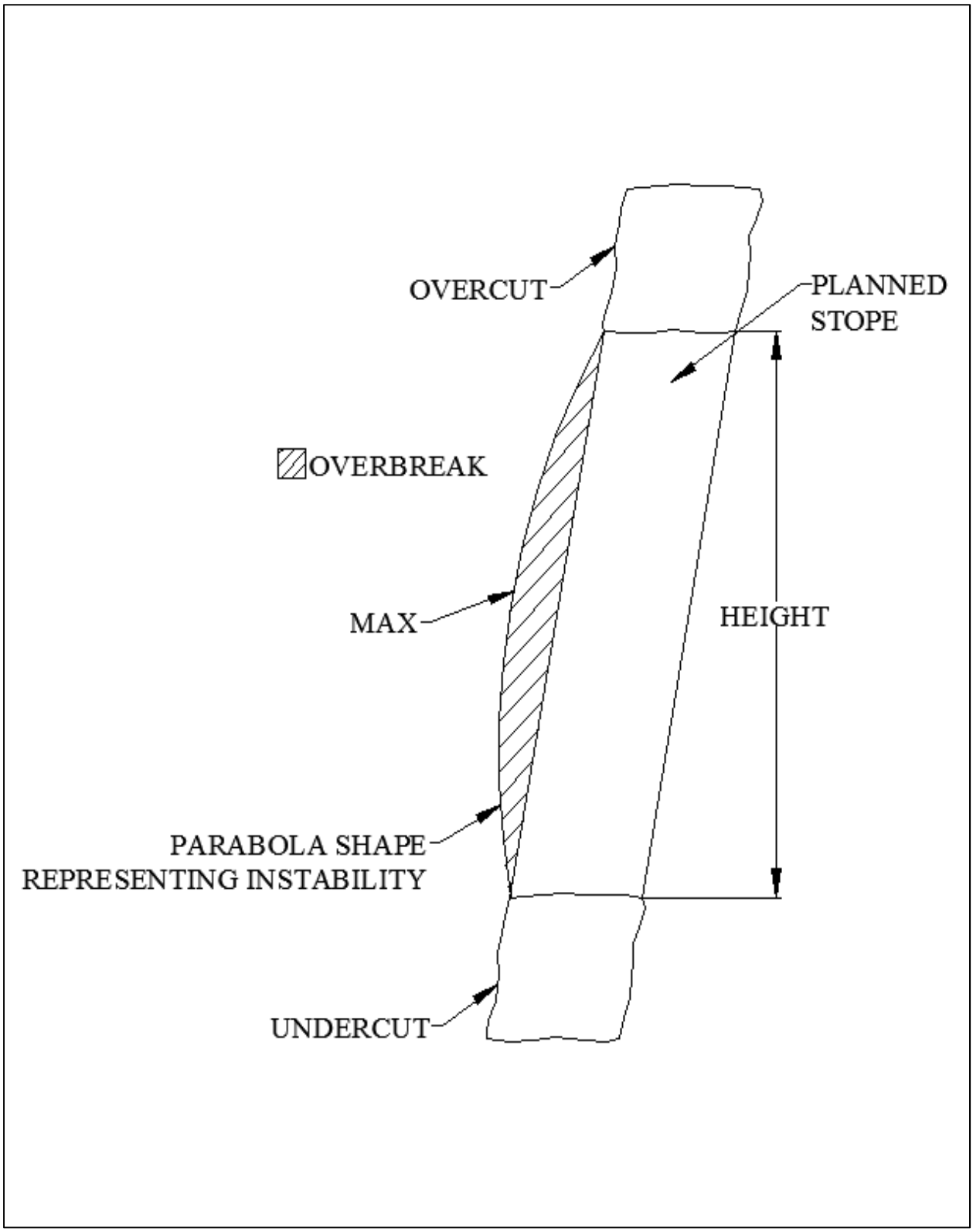

Figure 5.7 Cross section view of conceptual model of arch failure.

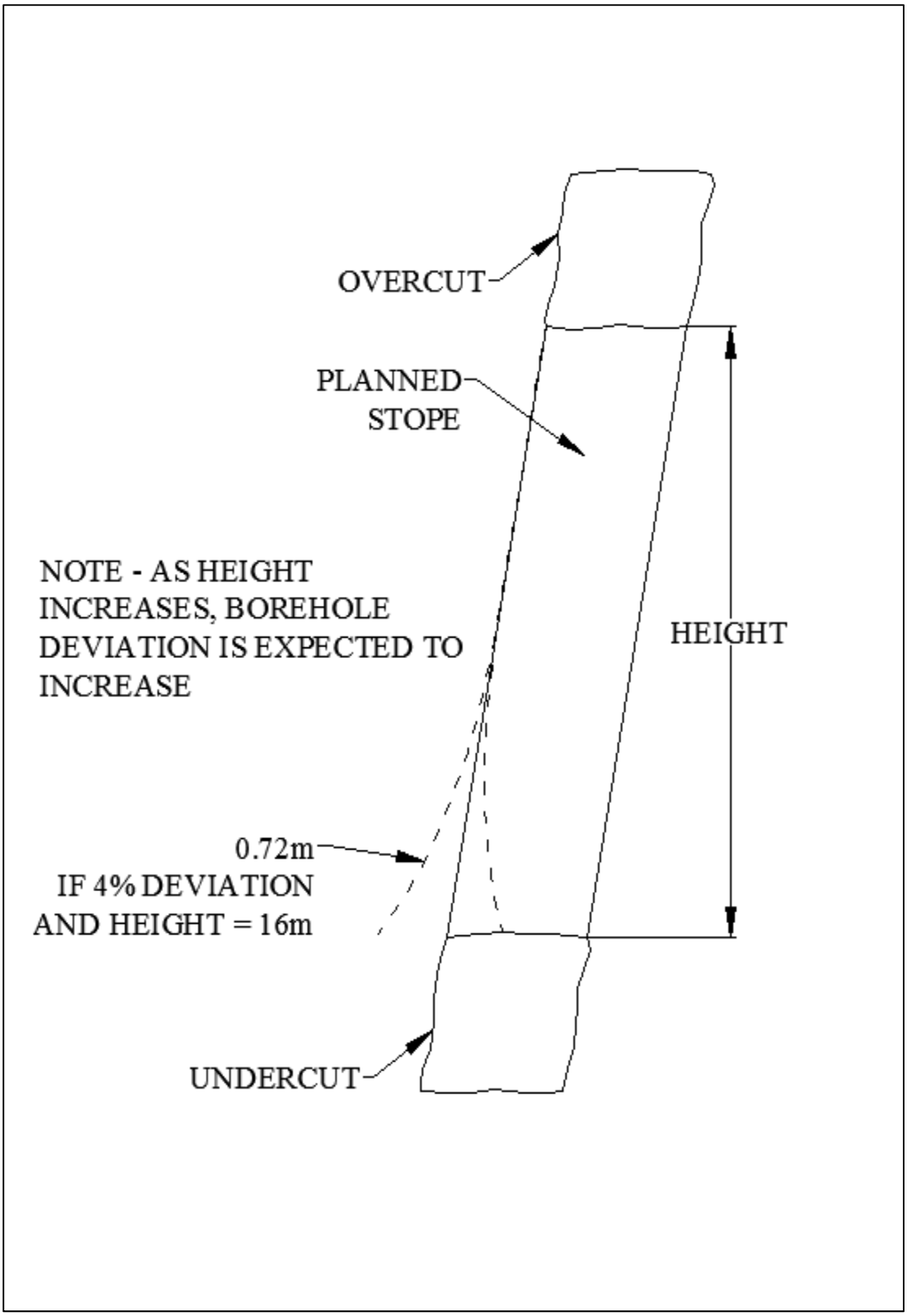

Figure 5.8 Cross section view of conceptual model of borehole deviation.

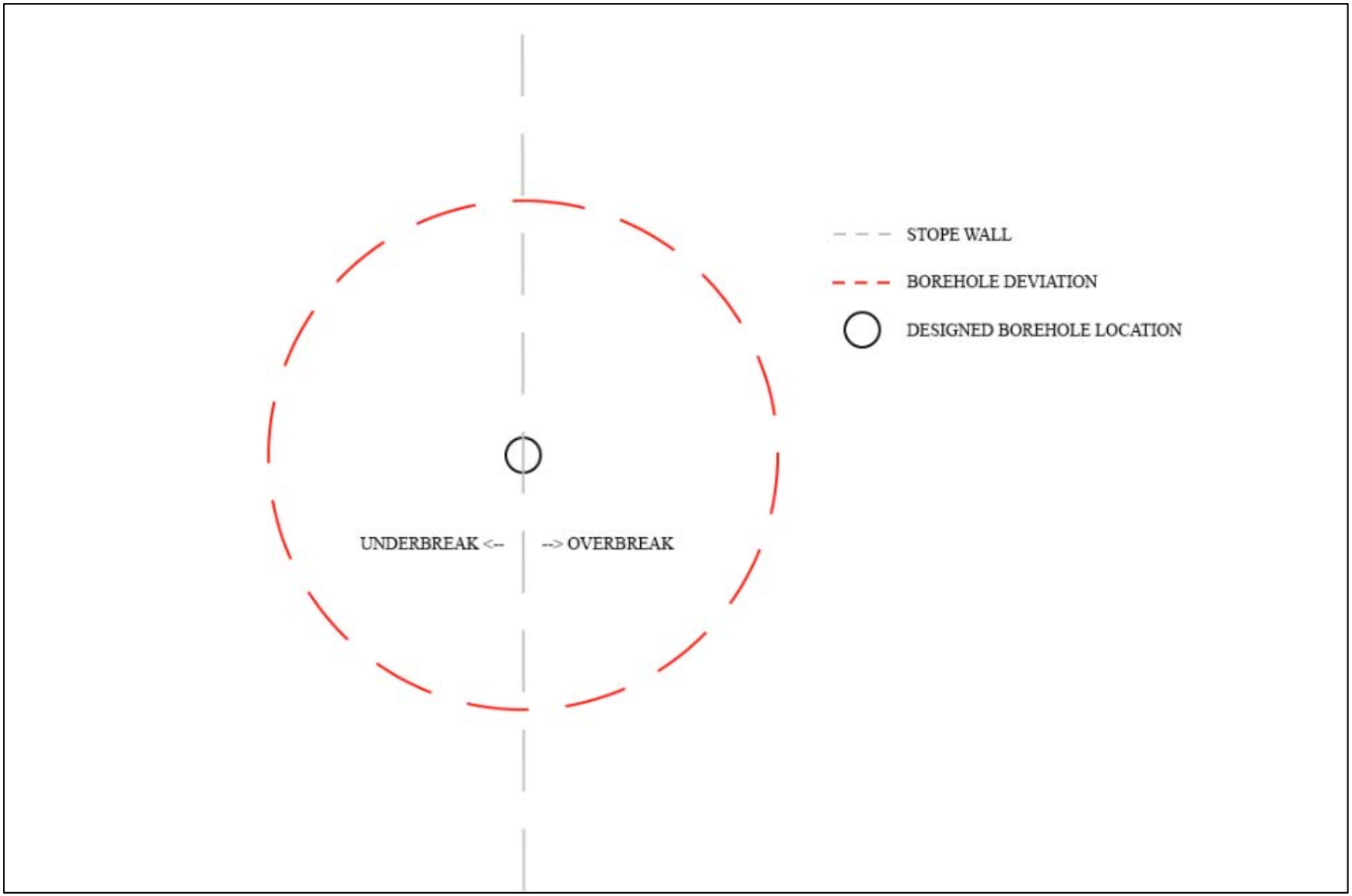

Figure 5.9 Plan view of possible locations of borehole deviation from the designed borehole location, at bottom sill of Figure 5.7.

5.4.3 Conceptual Model of Undercutting

Undercutting was calculated by taking the average amount of undercutting of the panel wall, at the overcut and undercut on each wall. Figure 5.10 represents how the average undercutting was plotted on a panel surface. The undercutting extends from the abutment of the designed panel wall to the abutment at the existing panel wall and it is expected for the panel wall to tend to fail to this free face.

Undercutting is only added to conceptual models containing a single panel as the amount of undercutting is calculated on a per panel basis.

5.4.4 Conceptual Model of all the Panels and of a Single Case Study

A conceptual model of potential slough combining both the arch failure and borehole deviation scenarios was created for the 2b11013 case history database (Figure 5.11). This model is based on the worst case scenario of maximum borehole deviation even though an average value would be preferred in design. The average dimensions of this stope are: 48m strike by 24m high.

As discussed in Section 5.4.2, the maximum drill hole divation is 0.72m into the hangingwall and represents overbreak. The minimum deviation is -0.72m into the orebody and represents underbreak. These are plotted as dashed lines.

With the stope dimensions of this case history applied using Equation 5.1, the maximum ERF is estimated at 8m and the minimum is 0m. For this calculation, a grid spacing for calculating ERFof 1.5m x 1.5m was used throughout the stope. The maximum value of 8m is calculated at the centre of the stope as shown in Figure 5.3. The minimum value of zero is at the abutments of the stope as described in Section 5.4.1

When the actual stope data was analysed, the average value of undercutting for the entire panel was calculated from sections that were 1.5m apart. For every section, the undercutting at the top sill and bottom sill was determined and averaged, so that a single value could be assigned as per Figure 5.10. The average undercutting of all the sections was averaged and the stope was assigned an undercutting value of 0.3m.

Figure 5.12 shows the upper bound for expected overbreak for a particular panel in the study area depicted in Figure 5.11. The underbreak is removed as this is not the worst case scenario. The overbreak at any ERF value is the sum of the arch based failure, undercutting, and maximum expected borehole deviation. At the abutments with an ERF value of 0, the depth of potential slough is only attributed to undercutting. As the ERF approaches its maximum value, the potential slough is attributed to all three scenarios of arch based failure, undercutting and borehole deviation. At the bottom of the stope, the arch based failure is reduced but borehole deviation increases. This indicates that there is higher expected dilution at the bottom of the stope where the borehole deviation is greater than the top of the stope where the boreholes are collared.

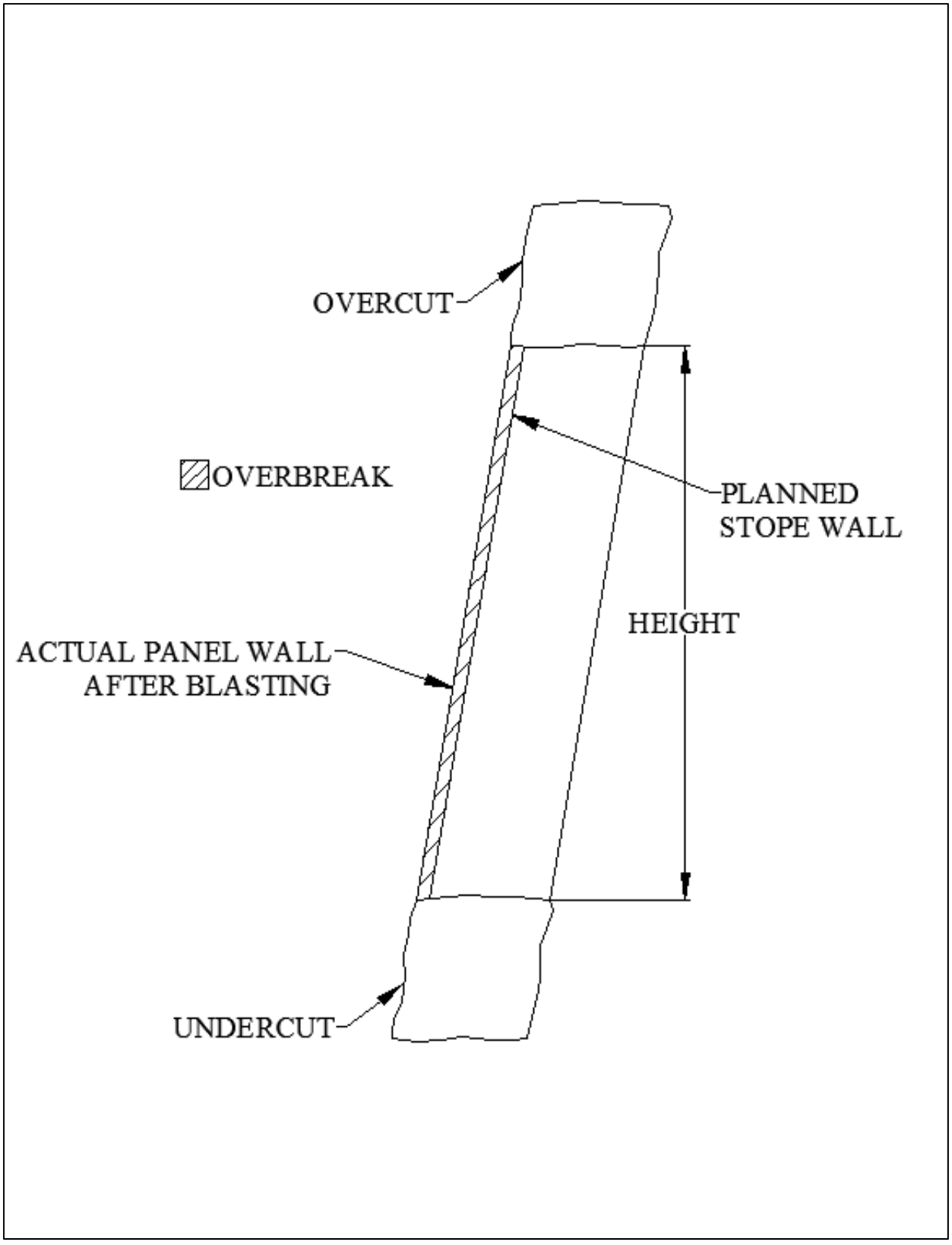

Figure 5.10 Cross section view of conceptual model of undercutting.

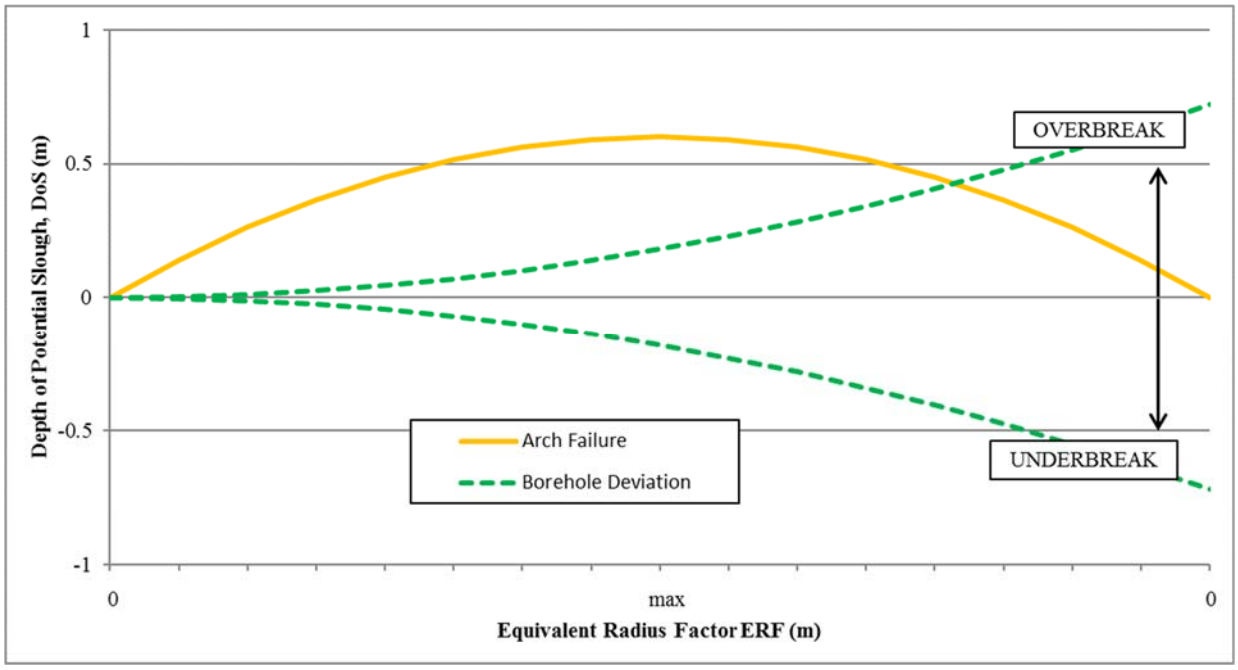

Figure 5.11 Conceptual model of the upper and lower bound for the entire case study area.

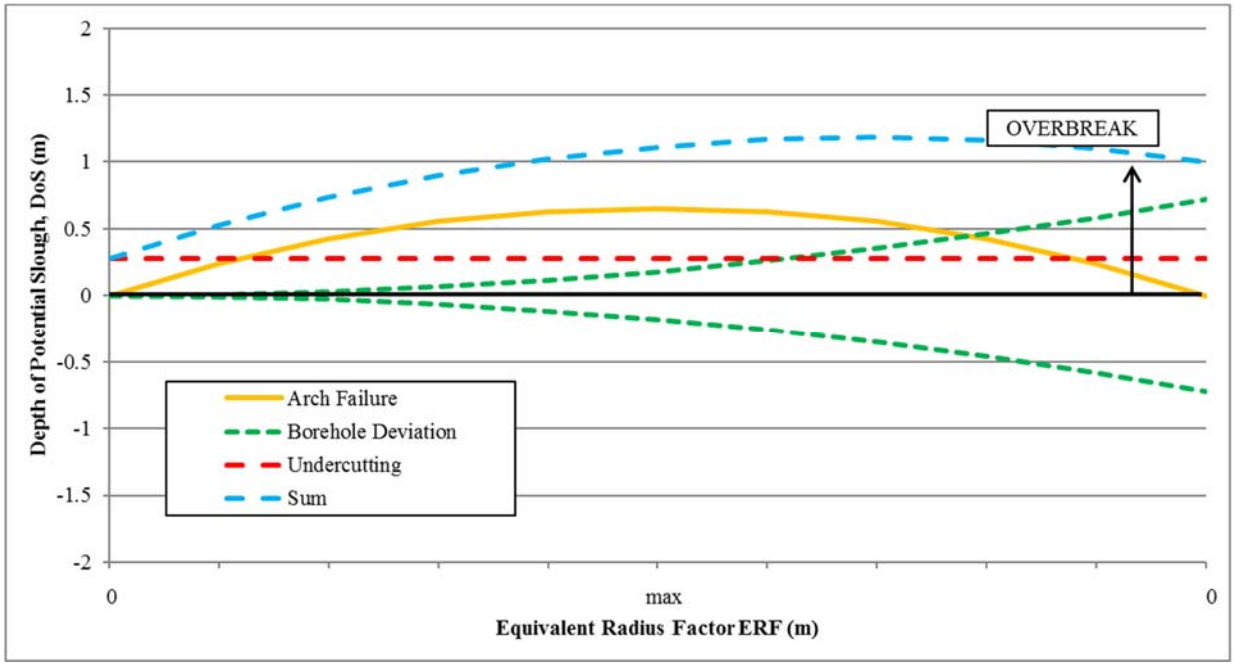

Figure 5.12 Conceptual model of the upper bound of overbreak for single panel; including the undercutting.

5.4.5 X-Axis of the Conceptual Model

The x-axis of the Figure 5.11 and Figure 5.12 increases from the left side to a midpoint and then decreases again. This is due to the nature of attempting to graphically represent the 2D spatial data of the panel onto a single axis of the graph.

As shown in Figure 5.4, ERF has a value of 0 on the abutments, and increases as the point gets further from the abutments. The dashed line represents the two vertical halves of the panel; the top half of the panel is represented on the left hand side of the graph (Figure 5.11 and 5.12). For example, any value of 0 that is on the top half of the panel will be represented by a single value of 0 on the left hand side of the graph, any value of 2 on the top half the panel will be represented by a single value of 2 on the left hand side of the graph, etc. The opposite then follows for any ERF value on the bottom half of the panel; i.e., it will be represented on the right hand side of the graph.

The reason for choosing to split the panel into a top half and a bottom half rather than a left half and a right half is due to the representation of the borehole deviation on the graph. The important aspect of borehole deviation for this study is its effect on the dilution of the panel, and so only deviation into and out of the plane of the panel is of importance. Representing the left side and right side of the graph with the top half and bottom half of the panel, respectively, allows for an increasing or decreasing amount of borehole deviation as the graph goes from left to right. Since the left hand side of the graph represents the top of the panel, borehole deviation will always be zero as the hole is collared at the top of the panel. If a different representation of the panel within the graph was chosen, then an average borehole deviation would have to be shown, which is not as ideal as showing the actual borehole deviation through the panel.

The other two mechanisms of dilution (geometric instability and undercutting) are not influenced by the method of plotting on the graph, as they are both vertically and horizontally symmetrical.

5.5 Analysis of the High Resolution Dilution Model against the Conceptual Model

The entire 2b11013 case study area (Figure 1.5) was plotted onto the chart of "Depth of Potential Slough versus ERF" to determine how the entire dataset matches against the model. The data (Figure 5.13) can be represented by the equation:

$$DoS = -0.0066ERF^2 + 0.0928ERF - 0.047 \quad (5.2)$$

This equation is represented by a population size of 4230 data points and has an R^2 of 0.04 which is very small (regression was done using the trendline function in Excel). The 4230 data points were gathered from the 13 panels of the stoping block 2b11013. The R^2 of the data corresponds to the visual appearance of the data; the data very generally follows an arch shape, but at any point along the x-axis, corresponding to ERF values, each ERF value can correspond to a large range of DoS values. The line provides a very similar shape of failure as the arching mode of failure. There is minimal amounts of underbreak or overbreak near the abutments at an ERF of 0, and large amounts of overbreak at the maximum ERF.

There is consistently a large amount of underbreak for any value of ERF with this dataset. Based on the conceptual model, there should only be a minor amount of borehole deviation that could account for the underbreak, and this would be completely offset by the arch failure being at maximum at that point. This odd behaviour can be explained after spending time with the production drillers at Seabee Gold Mine. In the design phase of the longhole design, the mine planner often designs the hole layout to have the minimal amount of clearance from the wall to the drill because the sill was driven at the exact dimensions of the orebody. When the production driller sets up to drill those holes along the wall, he often cannot get the drill in the designed location due to protruding wall rock that reduces his wall clearance. In this case, the driller will set up the drill as close as possible to the designed wall offset and recalculate the hole design as best as possible. If he miscalculates or uses the original design dip and dump, it would result in underbreak from the designed panel shape.

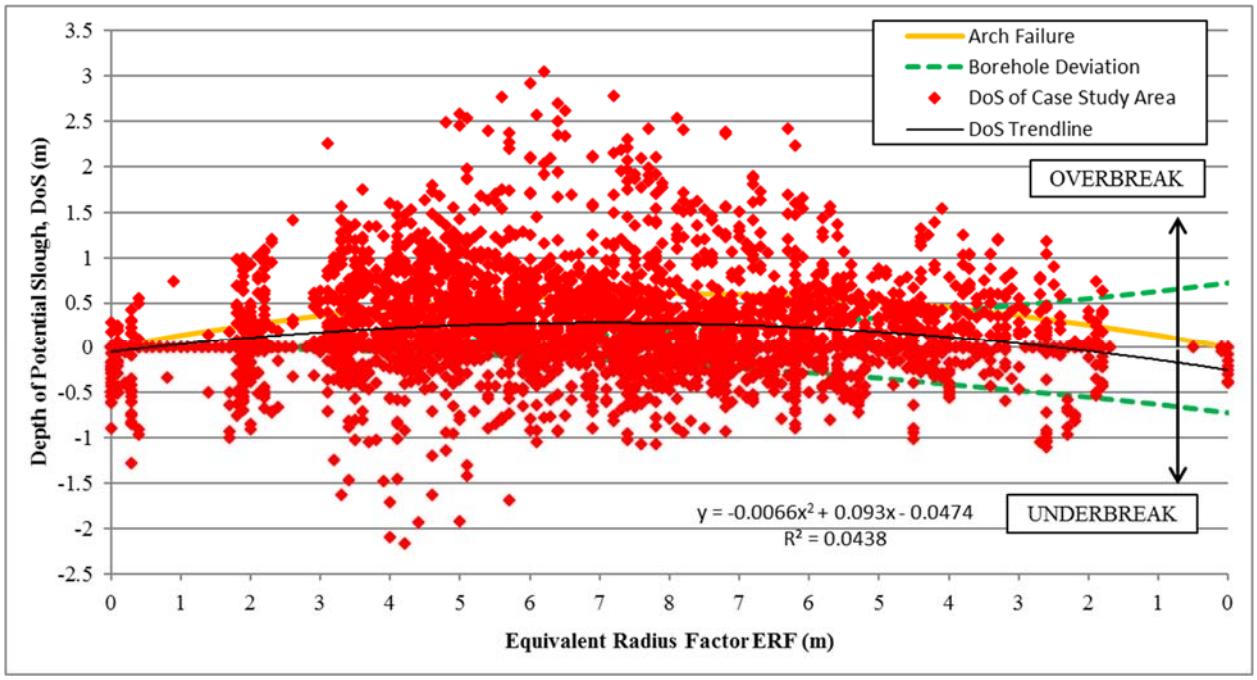

Figure 5.13 DoS for each ERF value for the case history database of 2b11013.

To reduce the noise in the dataset that is seen in Figure 5.13, the data was refined to produce an average value of DoS for all the data points with the same x-axis value (ERF values on the left side of the graph were not combined with ERF values on the right side of the graph). The average values can be seen in Figure 5.14 where the trend of the plotted data provides a similar shape to the conceptual model of the arch failure and is represented by the equation:

$$DoS = -0.0089ERF^2 + 0.132ERF - 0.112 \tag{5.3}$$

This equation is represented by a population size of 132 data points and has an R^2 of 0.37. Taking the average of all the data points provides a clearer understanding of the different mechanisms of failure in the various parts of the panel. The underbreak near the panel pillars at an ERF of 0 is approximately 0.25m. The trend of increasing depth of slough towards the centre of the panel is also clearer than the graph of all the data. Where Figure 5.13 indicates all the possibilities of the range of overbreak and underbreak for a given ERF, Figure 5.14 provides the most likely average amount of overbreak or underbreak.

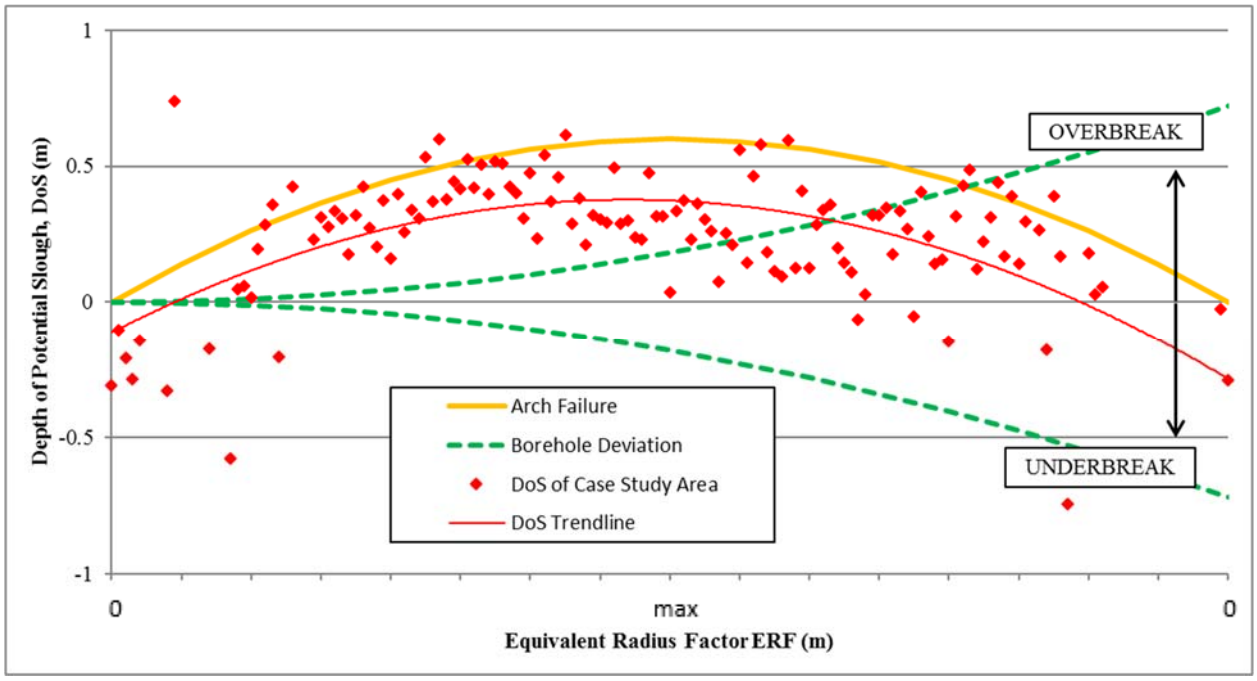

Figure 5.14 Average DoS for each ERF value for the case history database of 2b11013.

The same techniques that were used to reduce the noise in the dataset for all the panels, was also used for the dataset of Panel 10 – Sublevel 5-6 in the 2b12013 block. The average values of the depth of slough for each ERF can be seen in Figure 5.15. The trend of the dataset can be described by the equation:

$$DoS = -0.0448ERF^2 + 0.4446ERF - 0.554 \quad (5.4)$$

This equation is represented by a population size of 58 data points and has a R^2 of 0.63. Again the trend of the dataset closely matches the arch failure conceptual mechanism. Although it is interesting that it did not match the sum of all the sources of slough. The sum of the failures for an individual panel also included the undercutting of the panel walls by the silling development, which was calculated to add an additional 0.3m of slough along all values of ERF. Because the dataset does not give any indication of matching the sum of the dataset, it can be assumed that undercutting did not affect the amount of dilution for this panel. This is consistent with visual inspections of panels after blasting.

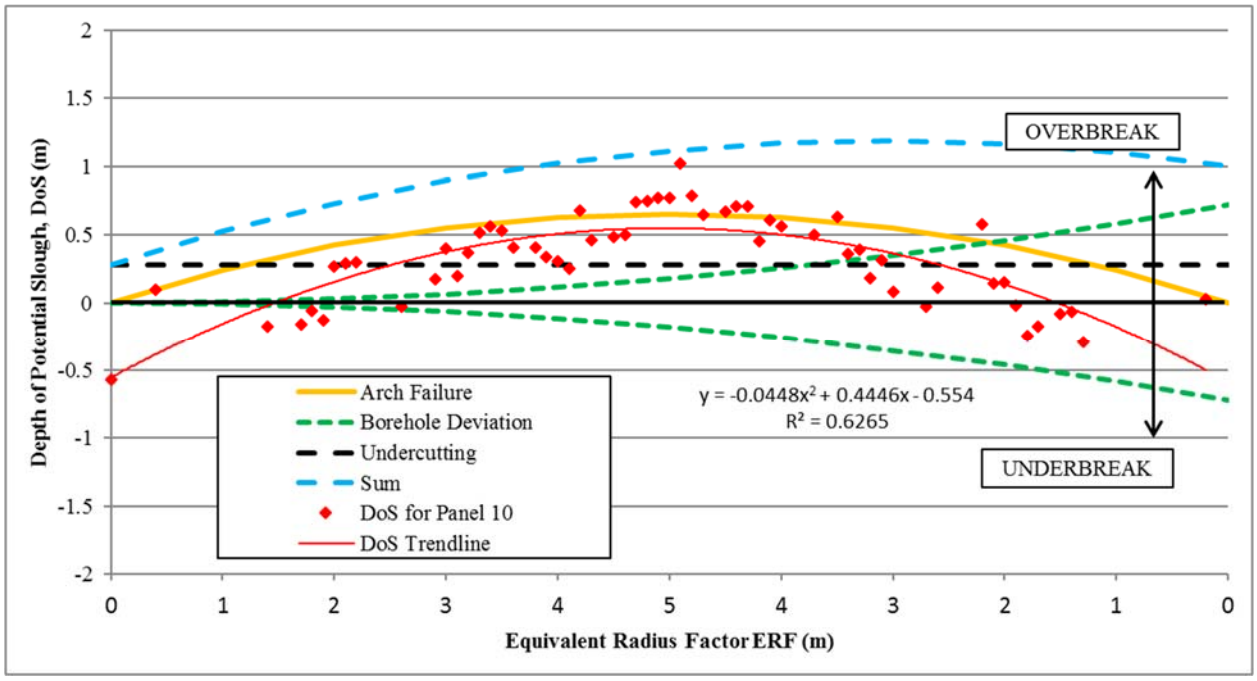

Figure 5.15 Average DoS for each ERF value for the Panel 10, Sublevel 5-6 in 2b12013.

5.6 Summary

In summary, three stoping blocks were identified as case study locations with suitable CMS data for this study. Three of the mining blocks (2b11013, 2b11011, and 2c10010) were used in the traditional ELOS vs. HR method, and one block (2b11013) was used with the new method of dilution analysis.

It was determined that the traditional method of ELOS vs. HR would not work for this panel dataset because of the limited range of HR and N' values with the dataset encompassed. Because the size of the panels did not vary significantly, a method of determining the amount of dilution at a single point rather than for the entire panel was devised. The ERF term was used instead of HR, and DoS was used instead of ELOS.

The effect of pre-mining stress was analysed against ELOS. The classification system used in Chapter 3 was used to group the panels together into pre-mining stress categories, and ELOS was plotted for the north and south wall of each panel. No trend was determined from this analysis, and it was determined that pre-mining stress was not a significant factor contributing to dilution for those panels.

A conceptual model was created to analyse to the dataset with a new method. The conceptual model contained the mechanisms of failure that are anticipated for these panels: arch failure (due to rockmass instability), borehole deviation, and undercutting.

This new method of dilution analysis was applied against the conceptual model using the data base from one of the stoping areas. Too much scatter was found, so the scatter was reduced by taking the average of the DoS for each value of ERF. This provided a clear trend of dilution that matched the arch mechanism of failure. The same method was applied to a single panel within the dataset, where an undercutting correction was also applied. The results were similar to the entire dataset, however, undercutting was shown to not significantly influence dilution in this particular case study.

CHAPTER 6

CONCLUSION

Unplanned open panel dilution is a major issue and cost for underground mining. For narrow vein mines, this issue is more acute as relatively small amounts of dilution can severely change the economics of the operation.

The initial objectives of the research included collecting field data to estimate rockmass properties, measuring field deformation to estimate induced stress changes, performing laboratory testing to identify the intact rock properties and, where possible, improving the interpretation of this data. This interpreted data was then coupled with observed hangingwall and footwall dilution to:

- assess existing empirical methods of dilution estimation;
- quantify the effect of pre-mining induced stress on dilution; and,
- develop new approaches for prediction the causes of dilution for the Seabee Mine.

Existing empirical methods of dilution estimation were not sufficiently accurate to predict dilution in the narrow Seabee ore. Pre-mining stress levels were shown to have no quantifiable effect on hanging wall and footwall dilution.

A new method was developed for interpreting the failure geometry of panels after dilution has occurred. The method linked the depth of slough (DoS) of a point on the hangingwall or footwall surface, to the effective radius factor (ERF) of that point. Based on the trend between ERF and DoS, the dilution could be linked to rock mass instability, blast hole deviation and/or hanging wall undercutting. Findings from the Seabee Mine suggest that undercutting of the panel hangingwall and footwall did not significantly influence dilution. A generally arched failure occurred, suggesting rock mass instability. Of note is that ore was often left in the panel close to the overcut drift, highlighting problems getting the blast hole drill set-up close enough to the hanging wall contact.

Other outcomes of this thesis include:

- Modified the JRC chart for easier use in field applications. The $J_{r/w}$ lines were extended for smaller joint profiles so that determining the proper $J_{r/w}$ is more methodical;
- Collected field data including CMS, joint properties, panel geometries for 28 panels for dilution analysis;
- Collected field data for three – point closure stations and MPBX instrumentation that recorded the displacement of the rock as mining activity changed the induced stresses; and,
- Analysed the three – point closure data to determine the induced stress in the panel as the mining front approaches the instrumentation location. Also, used numerical modelling to determine the pre – mining induced stress in a panel due to the mining of panels in the area prior and categorize the panels based on the amount of induced stress.

6.1 Recommendations for Future Work

This research has created a new method of predicting and evaluating dilution for panel walls in thin – vein underground mines using ERF and DoS. The method can be used to evaluate a group of panels or individual panels. The recommended future work for this topic are:

- increase the number of individual panels analysed;
- perform the new methodology on panels of different hydraulic radius. Panel sizes at Seabee Gold Mine were limited and no data was gathered on panels of large hydraulic radius;
- Perform a more rigorous statistical analysis on the results of the new method to determine its efficacy.

A specific recommendations for Seabee mine is to investigate the possibility of increasing the overcut width to allow the blast hole drill to set up closer to the hangingwall and footwall contact. Data suggests that undercutting the hangingwall by at least 0.3m does not significantly decrease stability. Increasing the overcut width could result in improved blasting for greater ore recovery, without risking significant increased dilution.

REFERENCES

ASTM. (2008). *D2845-08 Standard Test Method for Laboratory Determination of Pulse Velocities and Ultrasonic Elastic Constants of Rock.* West Conshohocken: ASTM International.

ASTM. (2008). *ASTM D3967-08 Standard Testing Method for Splitting Tensile Strength of Intact Rock Core Specimens.* West Conshohocken: ASTM International.

ASTM. (2008). *ASTM D5731-08 Standard Test Method for Determination of the Point Load Strength Index of Rock and Application to Rock Strength Classifications.* West Conshohocken: ASTM International.

ASTM. (2010). *D7012-10 Standard Test Method for Compressive Strength and Elastic Moduli of Intact Rock Core Specimens under Varying States of Stress and Temperatures.* West Conshohocken: ASTM International.

Barton,N. (1981). Shear-strength investigations for surface mining, 3rd International Conference on Stability in Surface Mining, Vancouver, ch. 7: 171-192, AIME.

Barton, N., Lien, R., and Lunde, J. (1974). Engineering classification of rock masses for the design of tunnel support. *Rock Mechanics* (6) 189-236.

Barton, N., and Bandis, S. (1982). Effects of block size on the shear behavior of jointed rock. *The 23rd US symposium on rock mechanics (USRMS)*. American Rock Mechanics Association.

Bieniaswski, Z.T. (1975). The point – load test in geotechnical practice. *Engineering Geology* (9) 1-11.

Bieniawski, Z. T. (1976). Rock mass classification of jointed rock masses. *Exploration for Rock Engineering. Johannesburg: Balkema*, *97*, 106.

Bieniawski, Z. T. (1989). *Engineering rock mass classifications: a complete manual for engineers and geologists in mining, civil, and petroleum engineering*. John Wiley & Sons.

Capes, G. W. (2009). *Open stope hangingwall design based on general and detailed data collection in unfavourable hangingwall conditions*. PhD thesis. University of Saskatchewan.

Clark, L. M. (1998). *Minimizing dilution in open stope mining with a focus on stope design and narrow vein longhole blasting.* PhD thesis. University of British Columbia.

Cecil, O. S. (1970). Correlation of rock bolt shotcrete support and rock quality parameters in Scandinavian tunnels, PhD thesis. University of Illinois.

Deere, D. U. (1964). Technical description of rock cores for engineering purpose. *Rock Mechanics and Engineering Geology*, *1*(1), 17-22.

Geokon Inc. (2012). "Geokon/Ealey Tape Extensometer Data Sheet." 2012 http://www.geokon.com/content/datasheets/1610_Tape_Extensometer.pdf (accessed August 19, 2013)

Goodman, R.E. (1980). *Introduction to Rock Mechanics*. Michigan: Wiley.

Hamrin, H. (1980). *Guide to underground mining methods and applications*. Stockholm: Atlas Copco.

Hamrin, H. (1995). Precision drilling extends the range of long hole blasting. *The Int. Symp. on mine planning and equipment selection* (pp. 89-96).

Hoek, E., & Brown, E. T. (1980). *Underground excavations in rock* . Institution of Mining and Metallurgy.

Hutchinson, D.J., and Diederichs, M. S. (1996). *Cablebolting in underground mines*. Richmond, Canada: BiTech Publishers Ltd.

Kirsch, C. (1898). Die theorie der elastizitat und die bedurfnisse der festigkeitslehre. *Zeitschrift des Vereines Deutscher Ingenieure*, *42*, 797-807.

Mathews, K. E. Hoek, D.C. Wyllie, D.C. Stewart, S.B.V. (1980). Prediction of stable excavation spans for mining at depths below 1000 metres in hard rock. Report to Canada Centre for Mining and Energy Technology (CANMET), Department of Energy and Resources; DSS File No. 17SQ.23440-0-90210. Ottawa.

Milne, D. M., Pakalnis, R. C., and Lunder, P. J. (1996). Approach to the quantification of hanging-wall behaviour. *Transactions of the Institution of Mining and Metallurgy. Section A. Mining Industry*, *105*.

Milne, D. M. (1997). *Underground design and deformation based on surface geometry.* PhD thesis. University of British Columbia.

Nickson, S. D. (1992). *Cable support guidelines for underground hard rock mine operations.* PhD thesis. University of British Columbia.

Pakalnis, R. (1986). *Empirical stope design at Ruttan Mine*. PhD thesis. University of British Columbia.

Pakalnis, R., Poulin, R., and Vongpaisal, S. (1995). Quantifying dilution for underground mine operations. *Proceedings, CIM AGM 1995.* Halifax, Nova Scotia.

Palmstrom, A. (2005). Measurements of and correlations between block size and rock quality designation (RQD). *Tunnelling and Underground Space Technology*, *20*(4), 362-377.

Potvin, Y. (1988). *Empirical open stope design in Canada.* PhD thesis. University of British Columbia.

Scoble, M.J., and Moss, A. (1994). Dilution underground bulk mining: implications for production management, mineral resource evaluation II: methods and case histories. *Geological Society Special Publication*, (79) 95-108.

Stewart, P. C. (2005). *Minimising dilution in narrow vein mines*. PhD thesis. University of Queensland.

SSR Mining Inc. (2018). Internal document.

SSR Mining Inc. (2018). SSR Mining. Retrieved from SSR Mining: http://www.ssrmining.com/operations/production/seabee/ (accessed October 14, 2018)

Vos, I. and Siddorn, J. (2009). Seabee Gold Mine summary of observations. SRK Consulting (Canada) Inc.

Wang, J. (2004). Influence of *stress, undercutting, blasting and time on open stope stability and dilution*. PhD thesis. University of Saskatchewan.

APPENDIX A

ELOS BAR GRAPHS

This portion of the appendices provides the figures from the ELOS of each individual ring from the Seabee Gold Mine case study areas.

Figures A.1 to A.18 provide the ELOS data for each ring that was analysed using the CMS data for each panel in the case study areas.

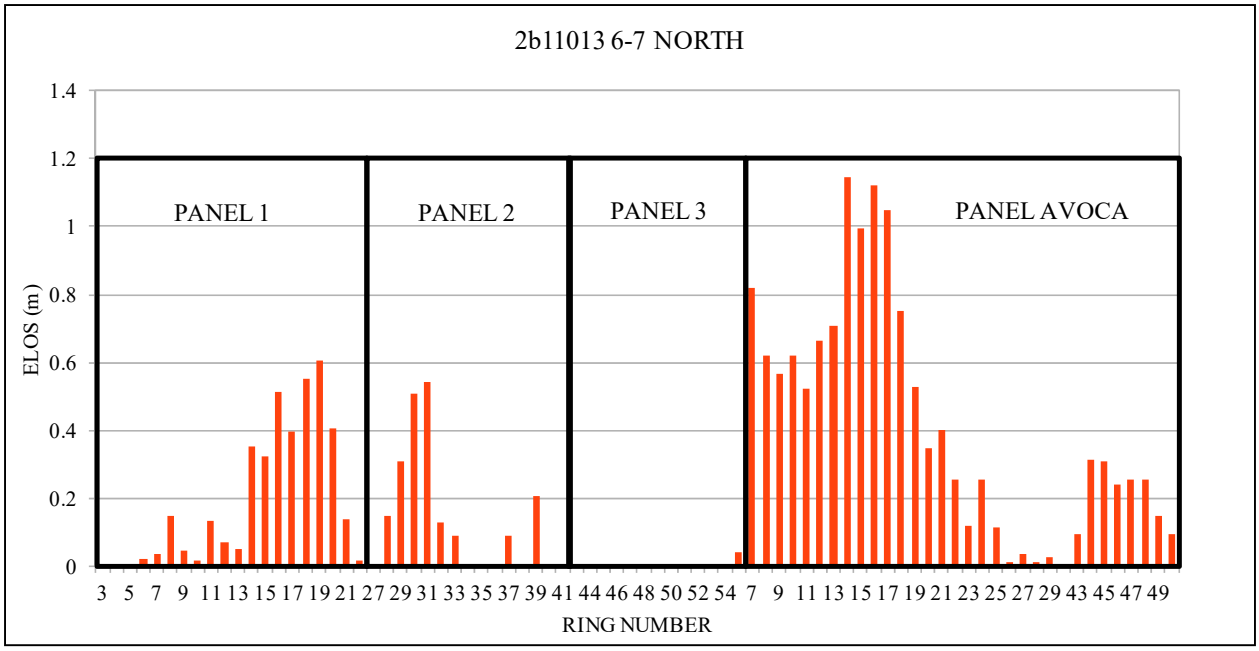

Figure A.1 A bar graph showing the ELOS against ring number for 2b11013 6-7 north wall.

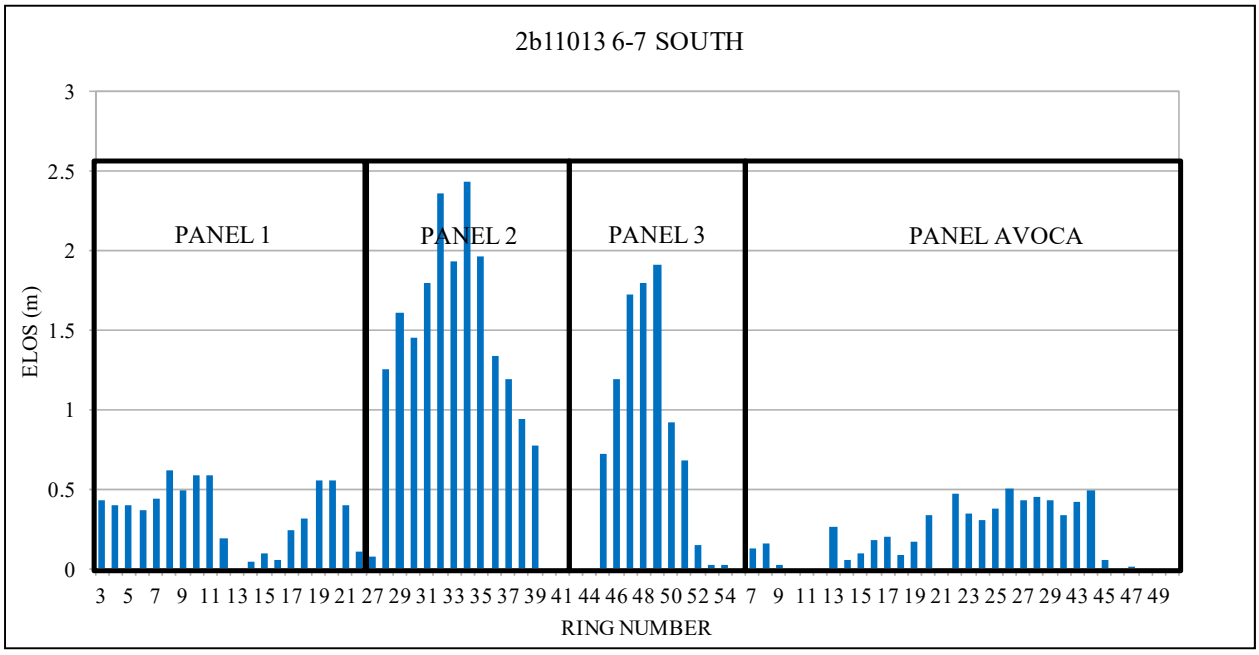

Figure A.2 A bar graph showing the ELOS against ring number for 2b11013 6-7 south wall.

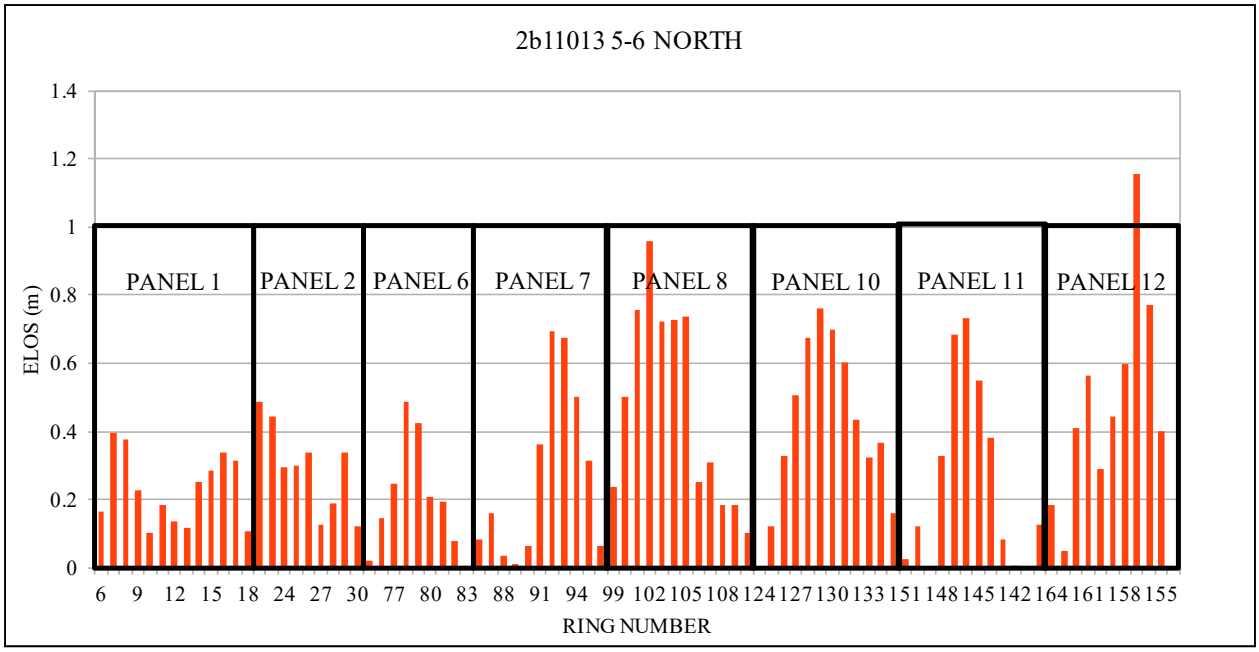

Figure A.3 A bar graph showing the ELOS against ring number for 2b11013 5-6 north wall.

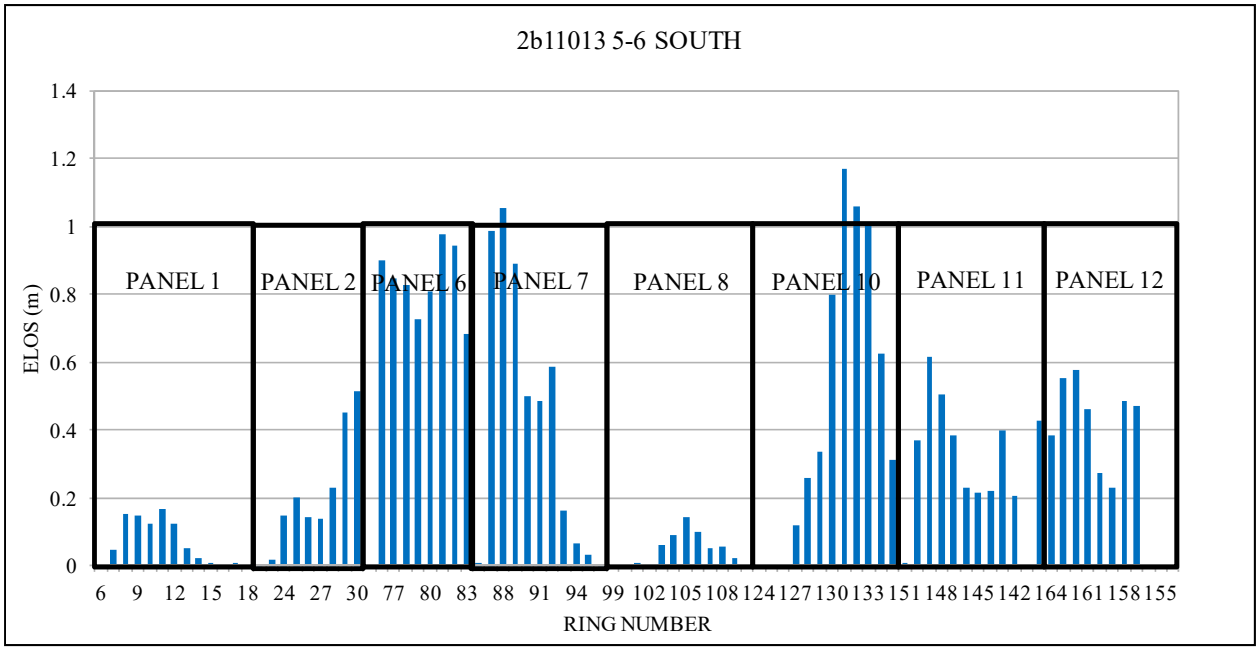

Figure A.4 A bar graph showing the ELOS against ring number for 2b11013 5-6 south wall.

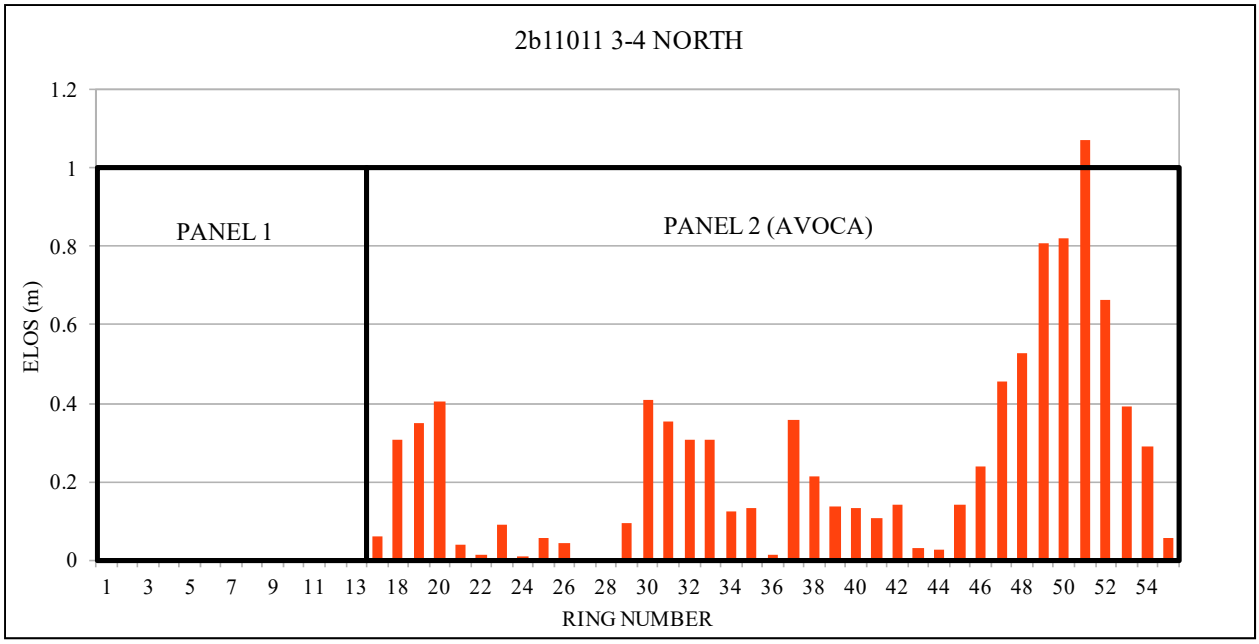

Figure A.5 A bar graph showing the ELOS against ring number for 2b11011 3-4 north wall.

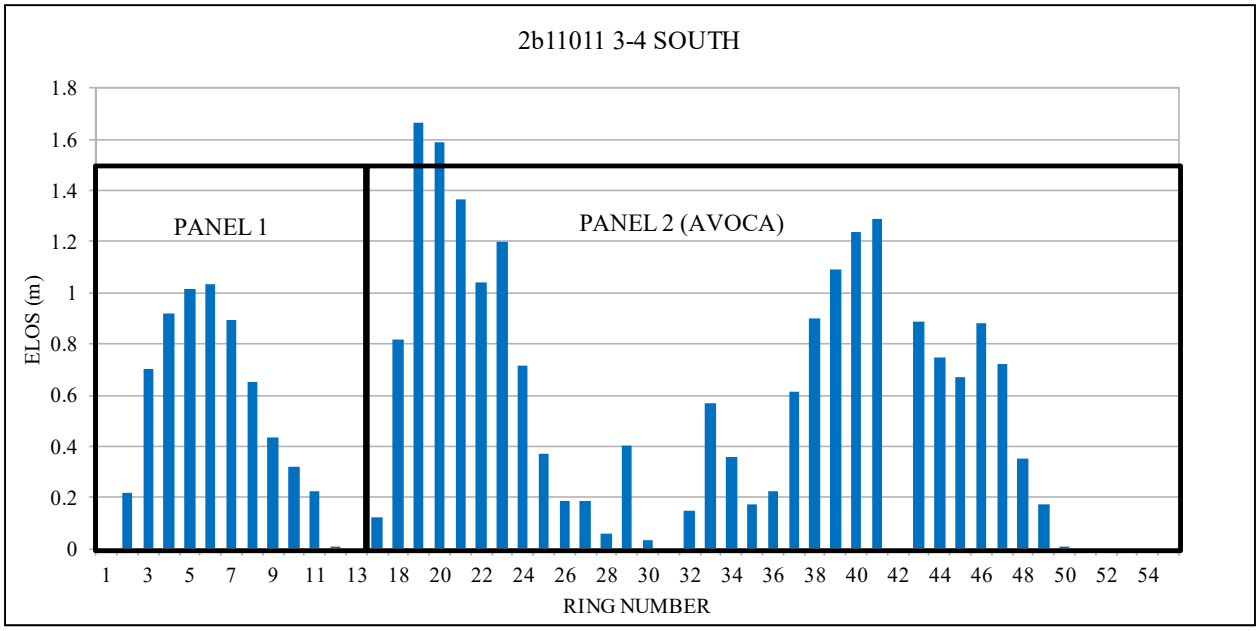

Figure A.6 A bar graph showing the ELOS against ring number for 2b11011 3-4 south wall.

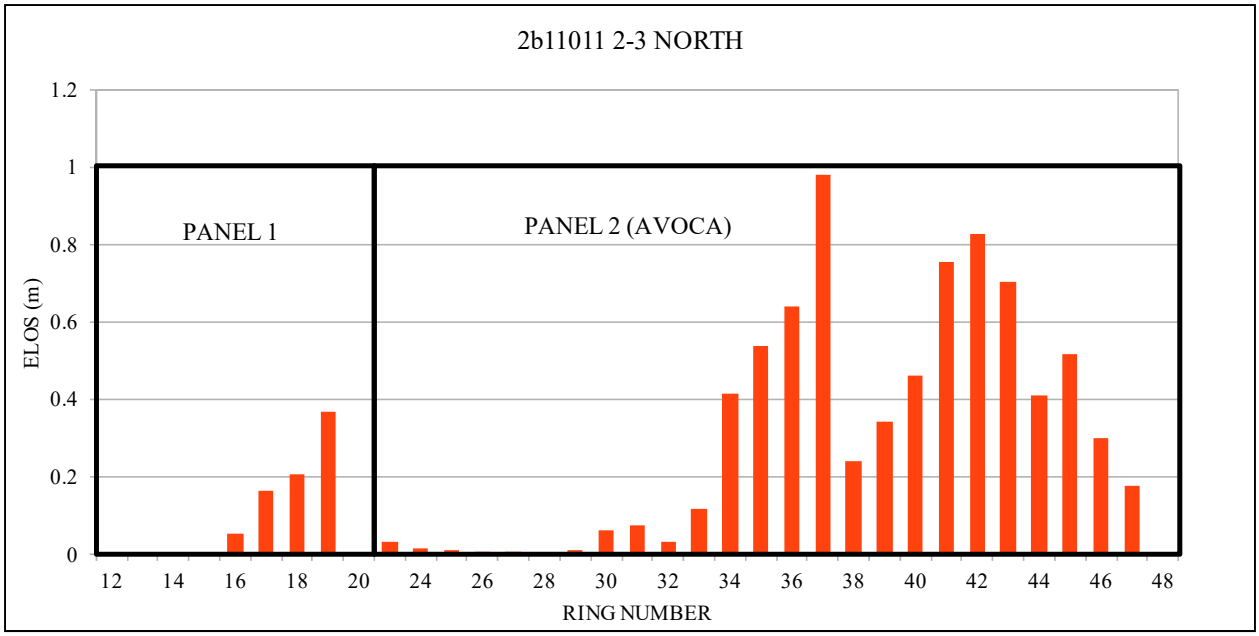

Figure A.7 A bar graph showing the ELOS against ring number for 2b11011 2-3 north wall.

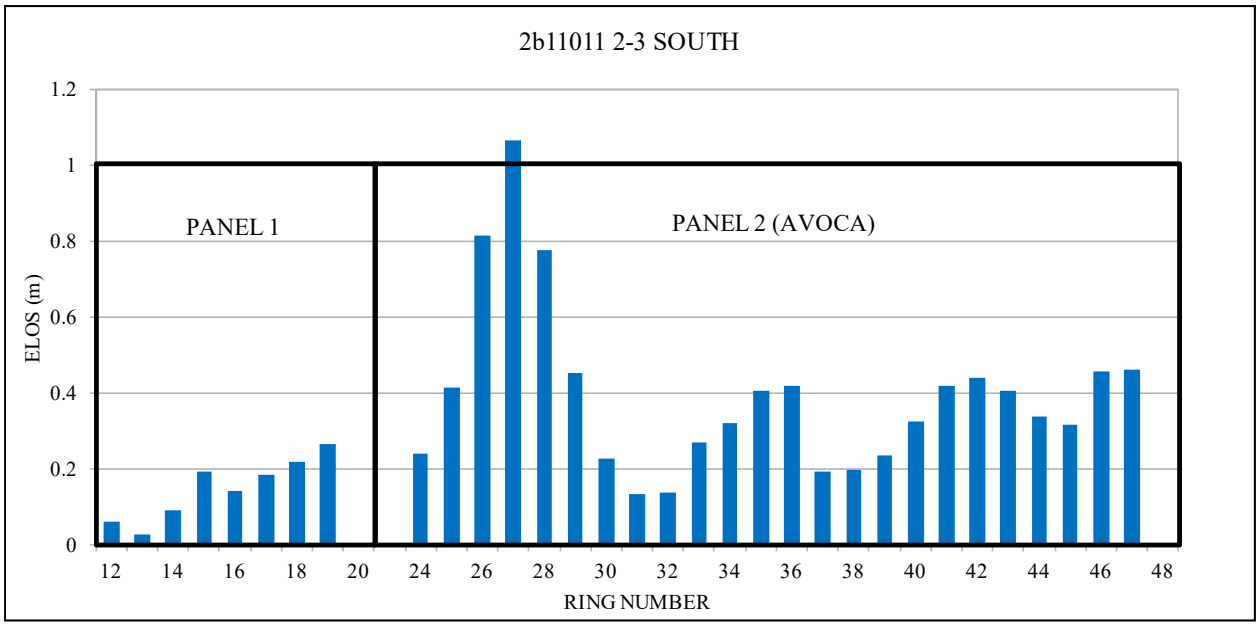

Figure A.8 A bar graph showing the ELOS against ring number for 2b11011 2-3 south wall.

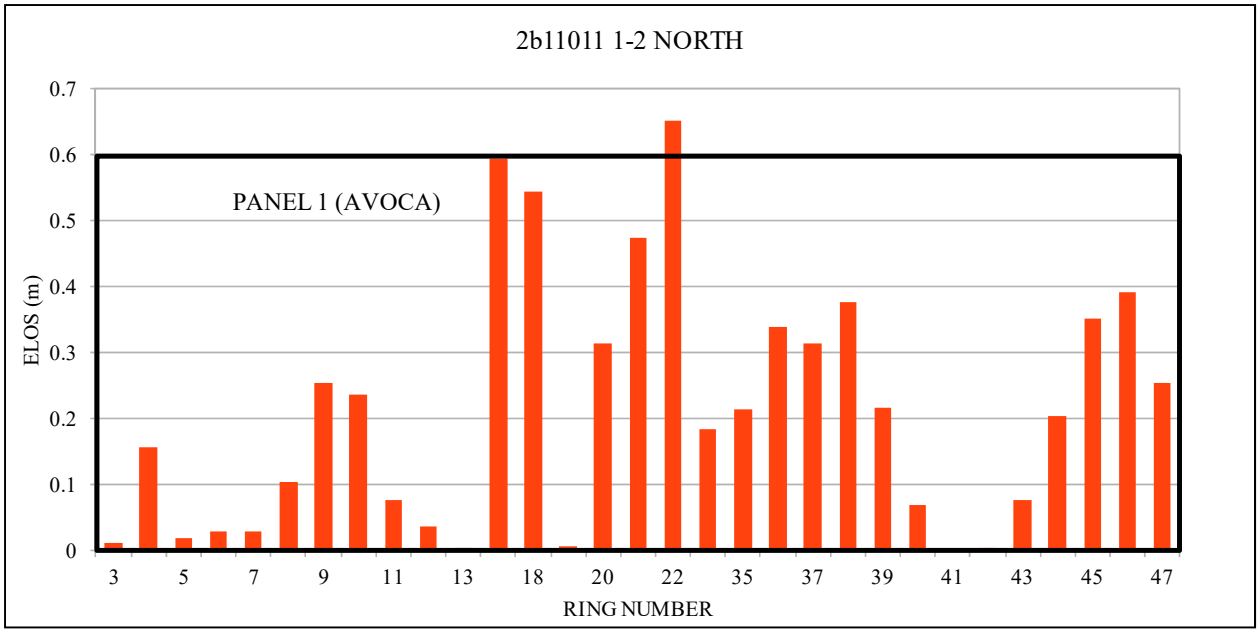

Figure A.9 A bar graph showing the ELOS against ring number for 2b11011 1-2 north wall.

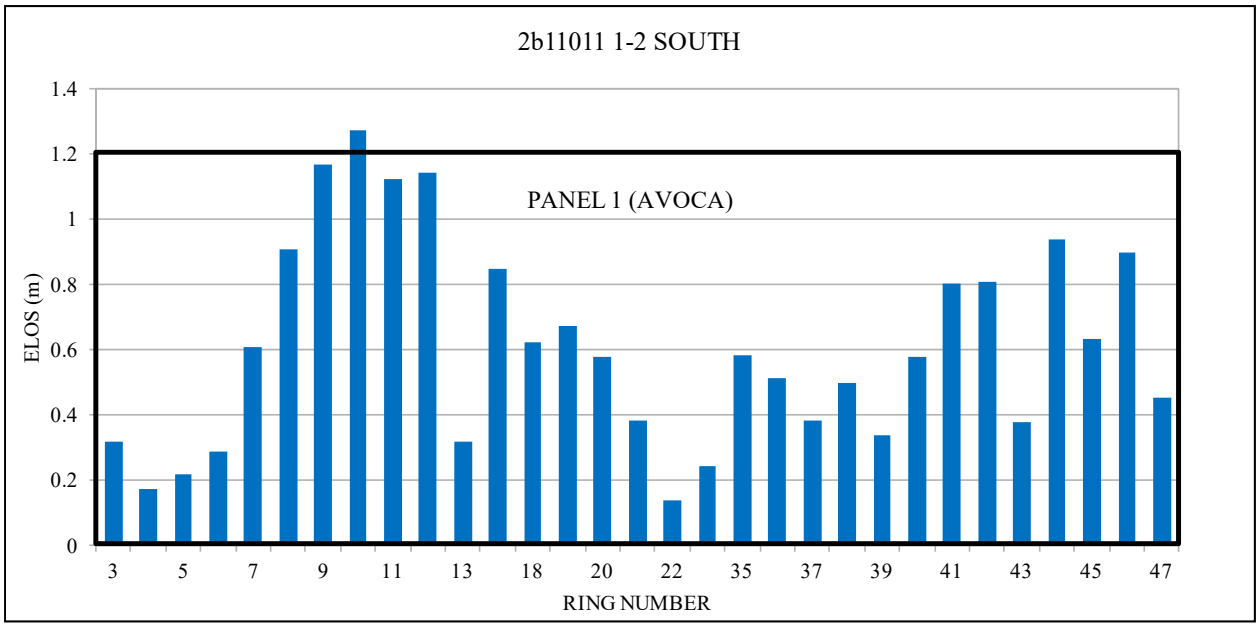

Figure A.10 A bar graph showing the ELOS against ring number for 2b11011 1-2 south wall.

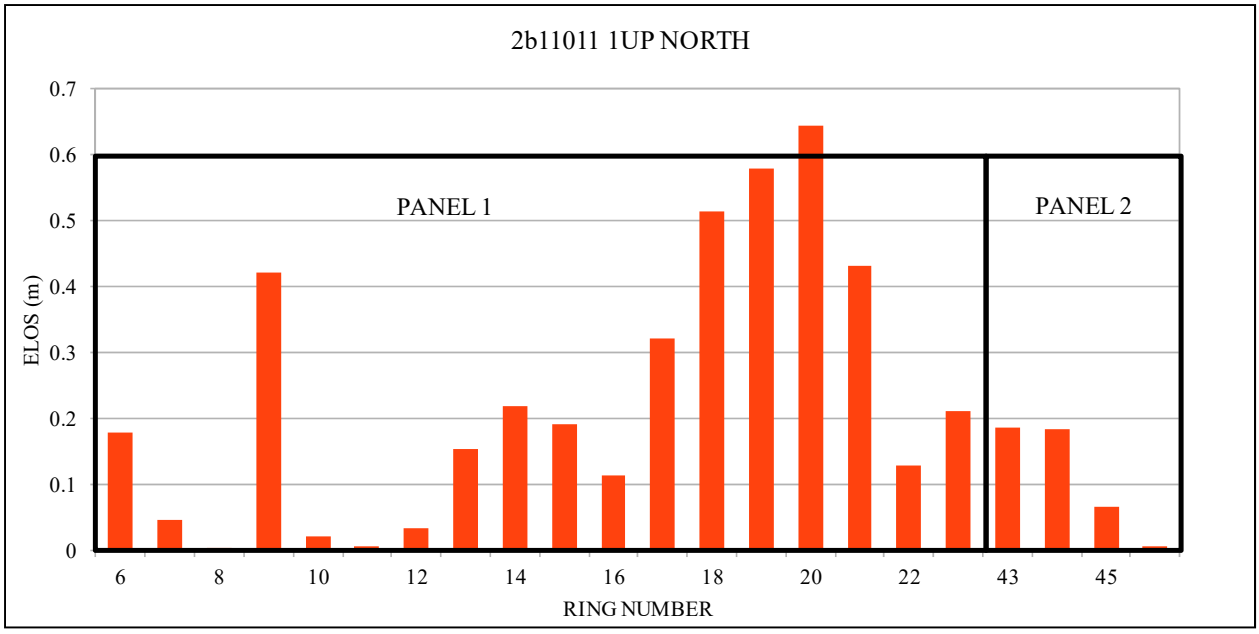

Figure A.11 A bar graph showing the ELOS against ring number for 2b11011 1UP north wall.

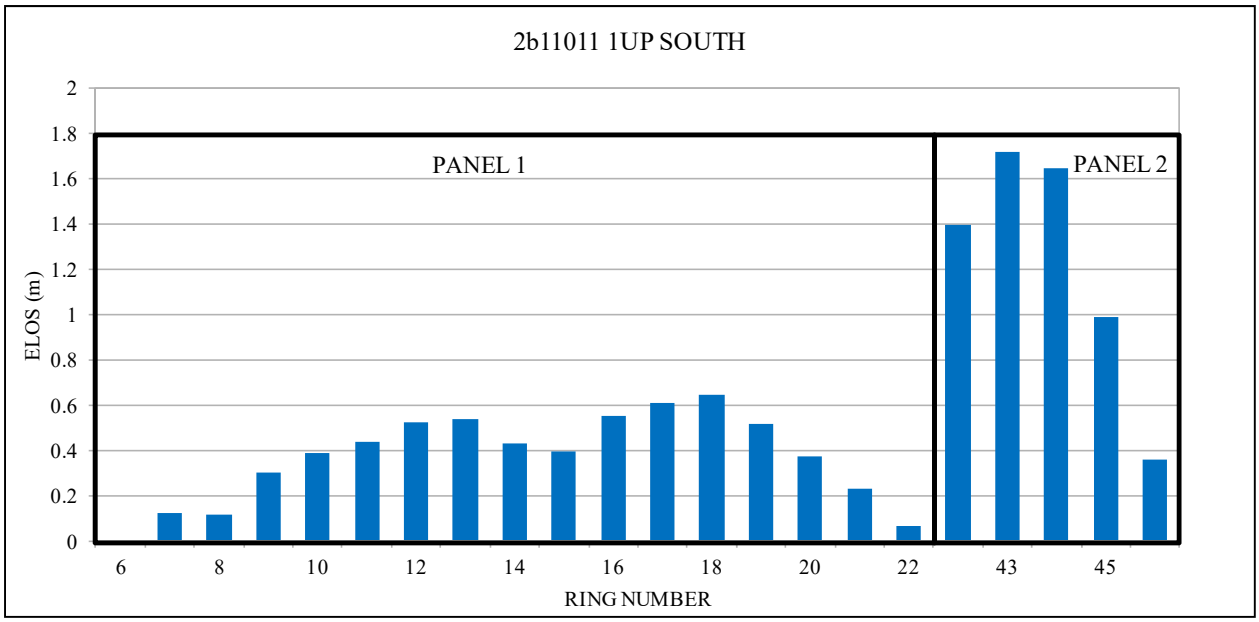

Figure A.12 A bar graph showing the ELOS against ring number for 2b11011 1UP south wall.

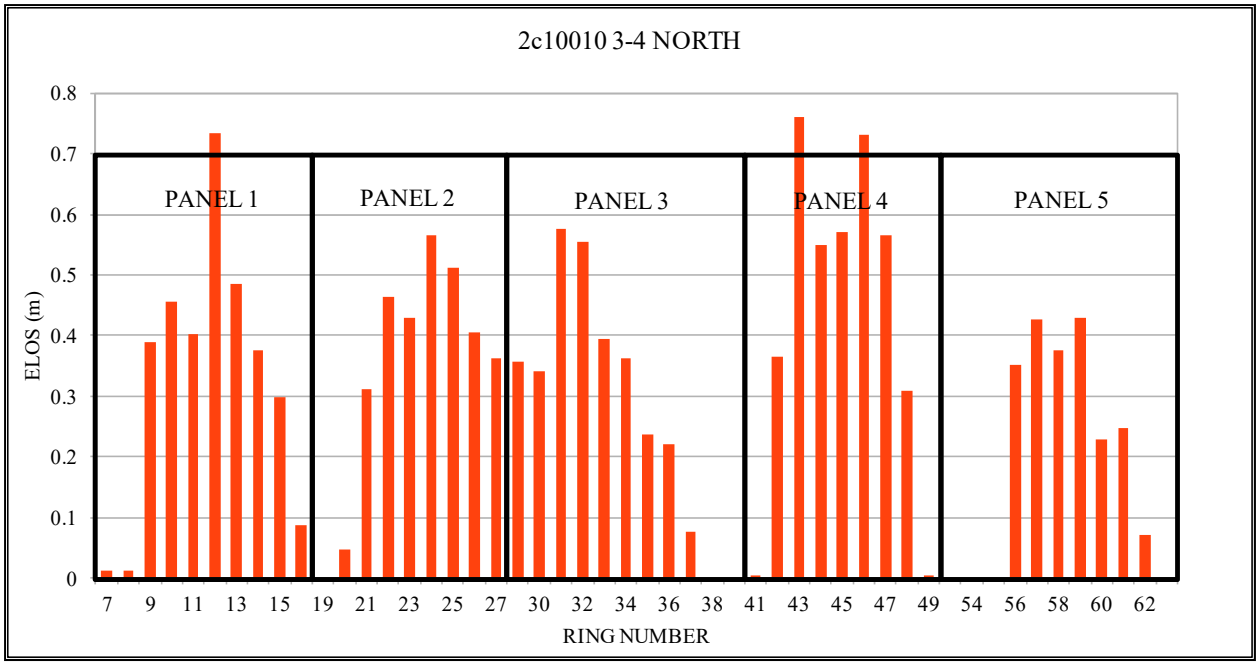

Figure A.13 A bar graph showing the ELOS against ring number for 2c10010 3-4 north wall.

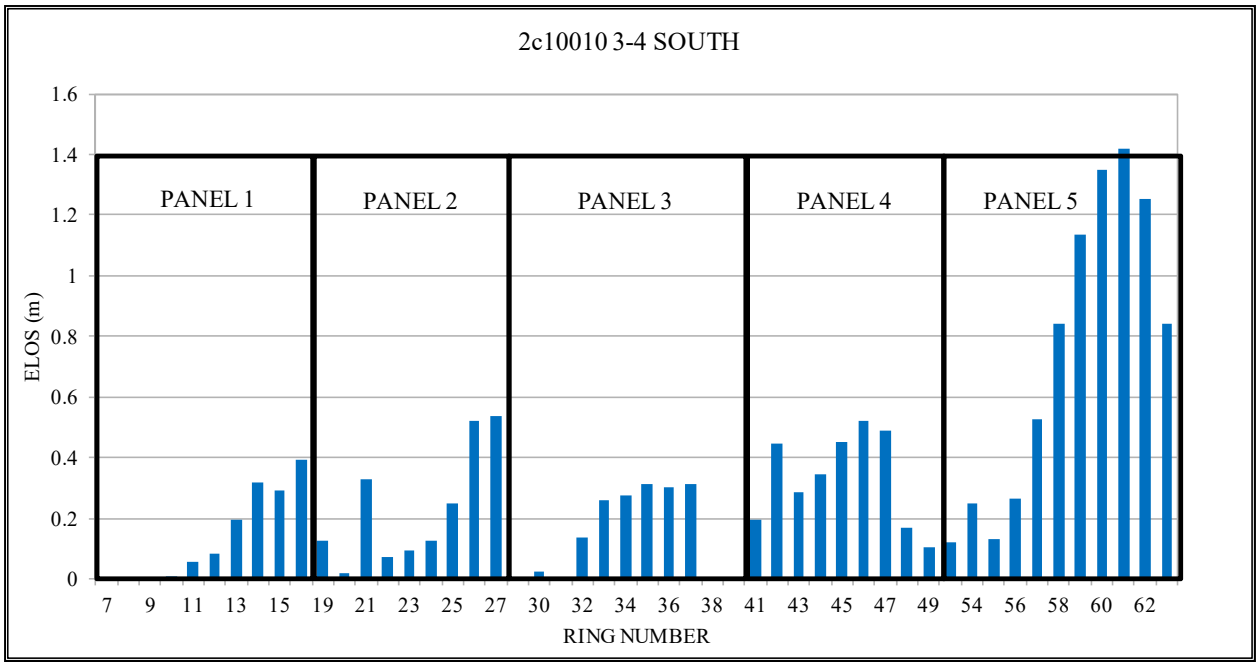

Figure A.14 A bar graph showing the ELOS against ring number for 2c10010 3-4 south wall.

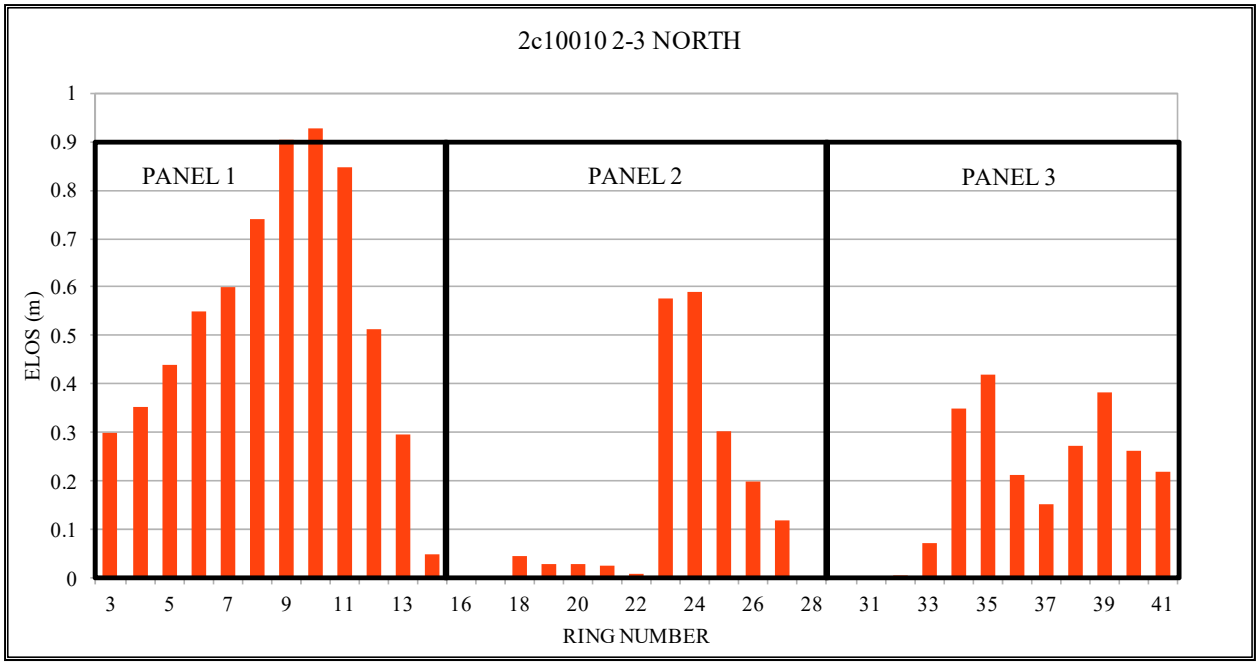

Figure A.15 A bar graph showing the ELOS against ring number for 2c10010 2-3 north wall.

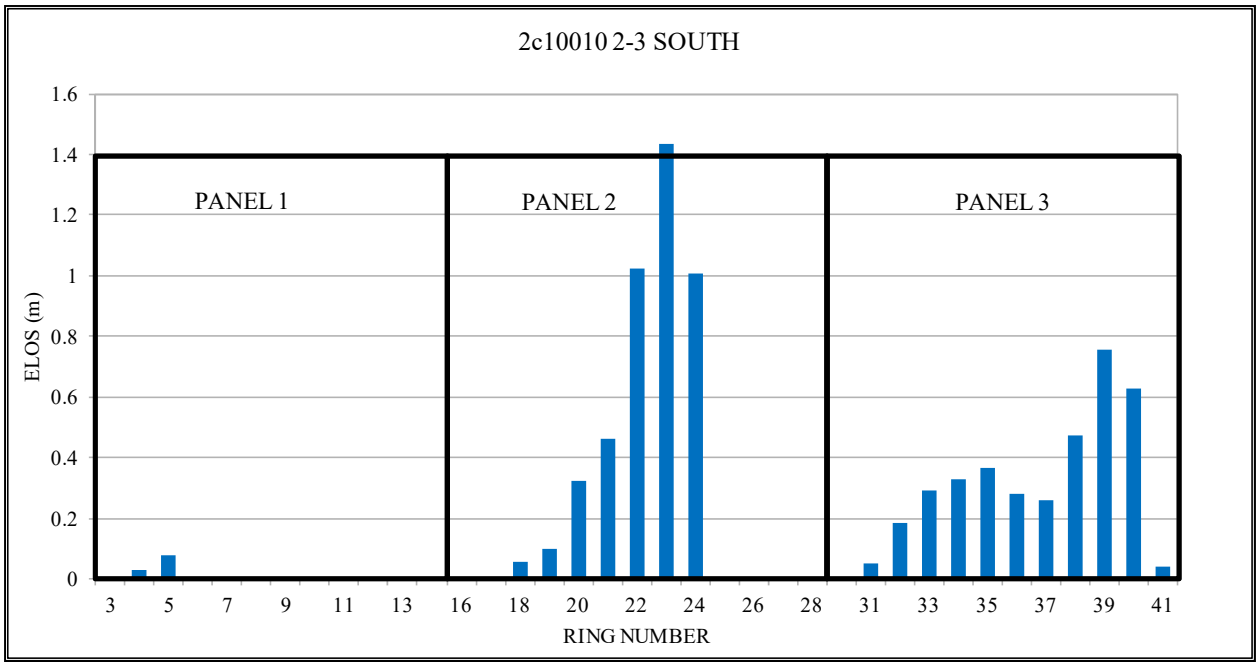

Figure A.16 A bar graph showing the ELOS against ring number for 2c10010 2-3 south wall.

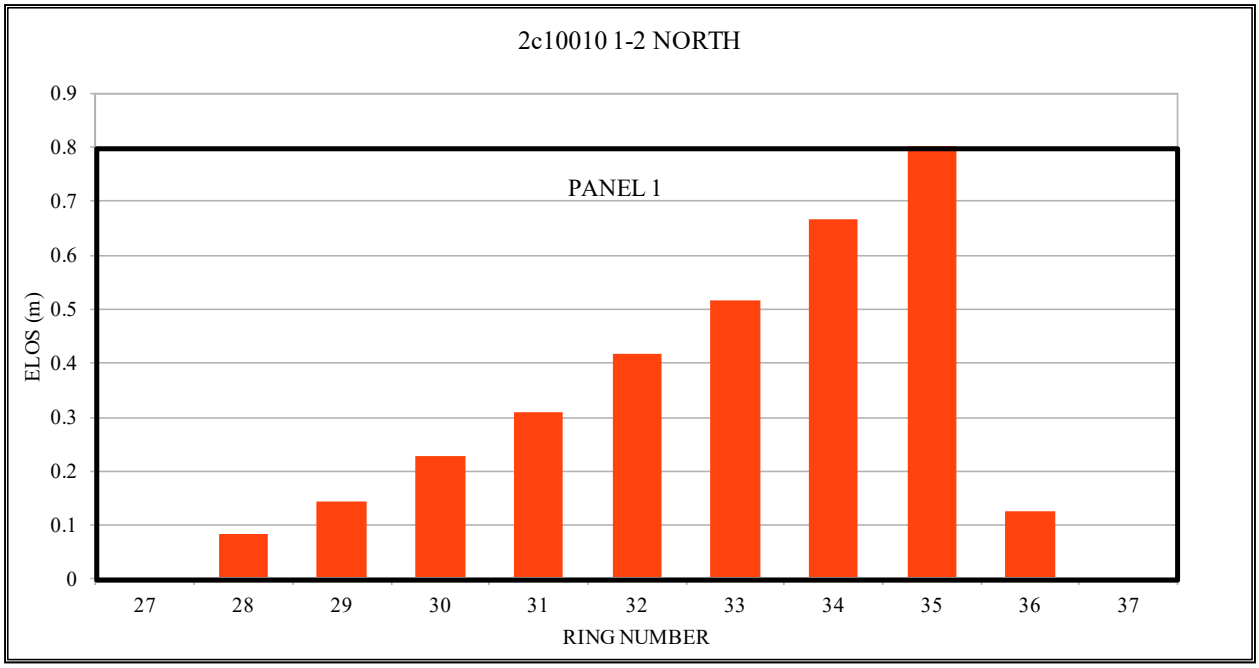

Figure A.17 A bar graph showing the ELOS against ring number for 2c10010 1-2 north wall.

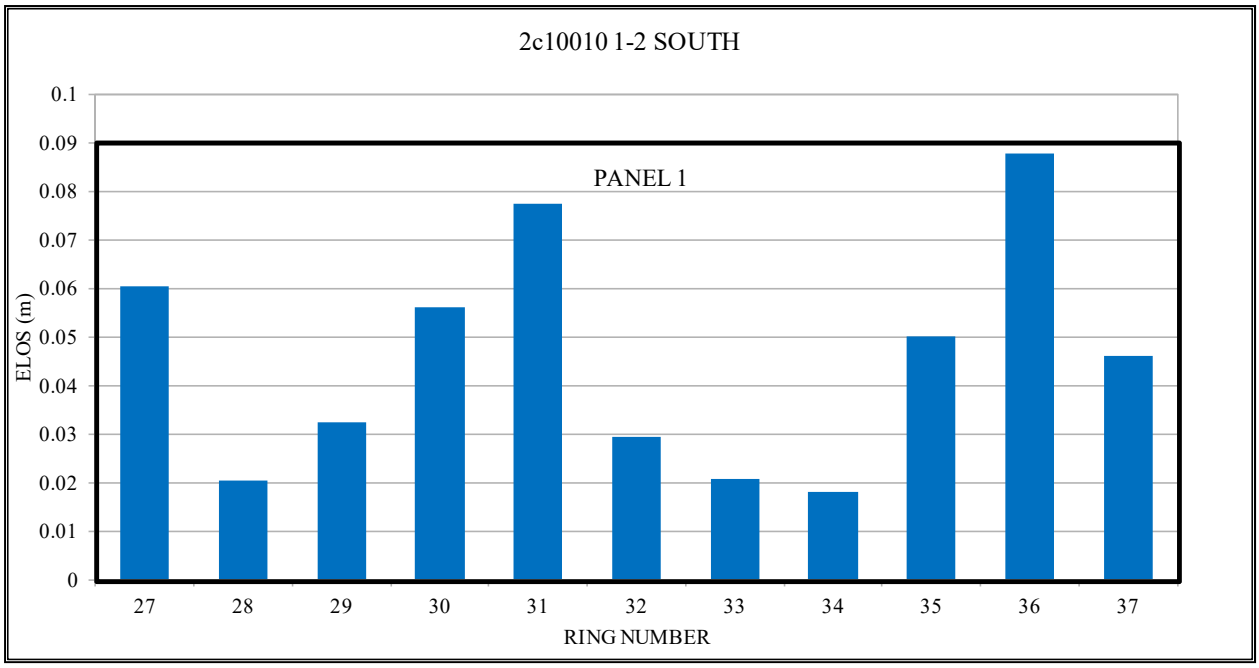

Figure A.18 A bar graph showing the ELOS against ring number for 2c10010 1-2 south wall.

APPENDIX B

DATA COLLECTION DATA

This portion of the appendices provides the data and figures from the data collection of rock mass properties from Seabee Gold Mine.

The following Figures B.1 – B.11 are the stereographs and JRC chart that are formed from the data collected. On the stereograph the poles of the joint orientations are plotted and contoured using the RocScience DIPS program. The average joint orientation of the joint set clusters was manually inputted. On the JRC chart the data was graphed onto a modified version of the chart; where the Jr/w portion of the chart has been extended to joint lengths of 0.3m, to account for the difficulty in obtaining measurements for joints that are greater than 1m in length. The Jr/r data was plotted on as a histogram on the Y – axis, this gives a visual indication of the number of recordings each JRC value obtained, the longer the bar the more readings.

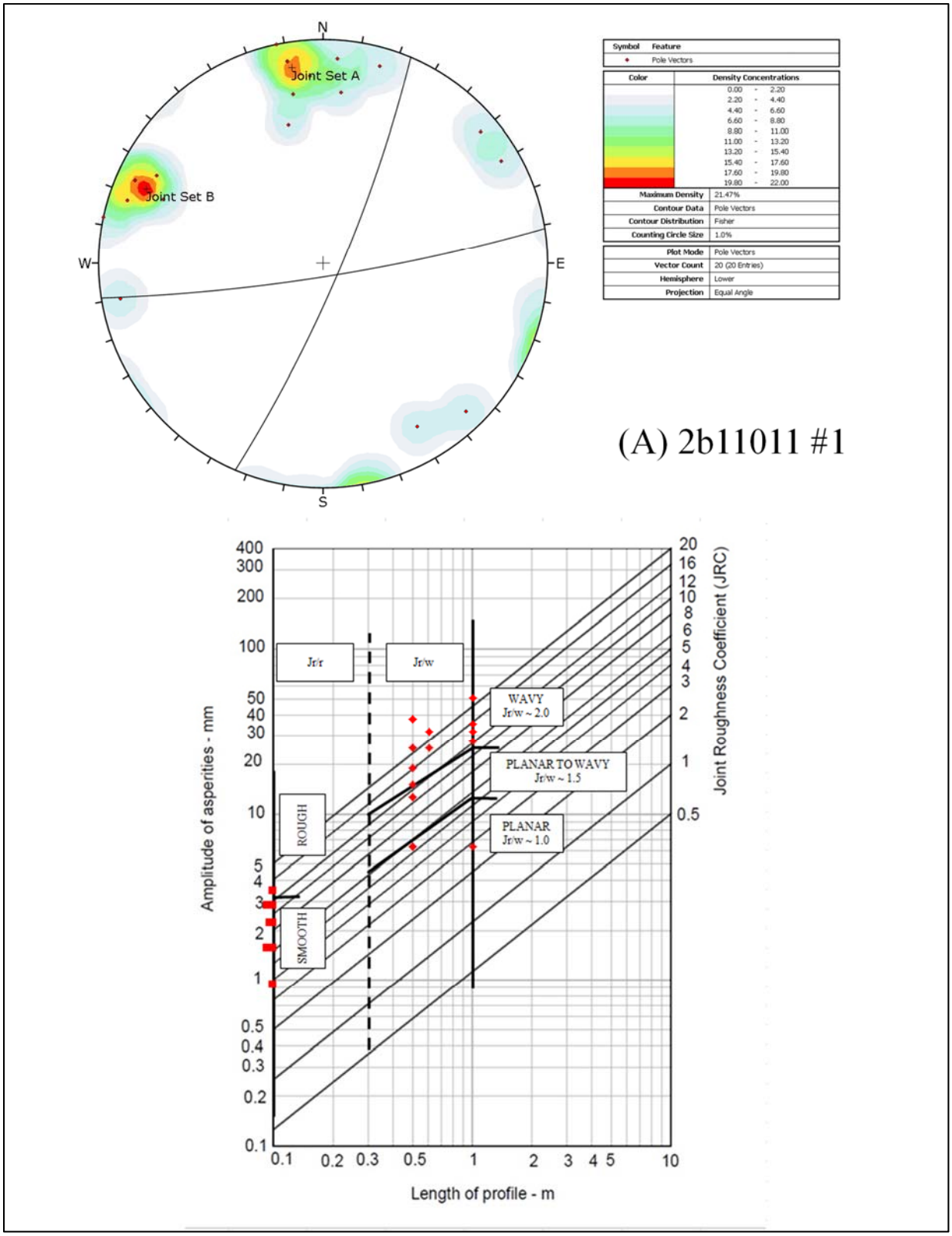

Figure B.1 Stereograph of joint orientation and JRC Chart for 2b11011 #1.

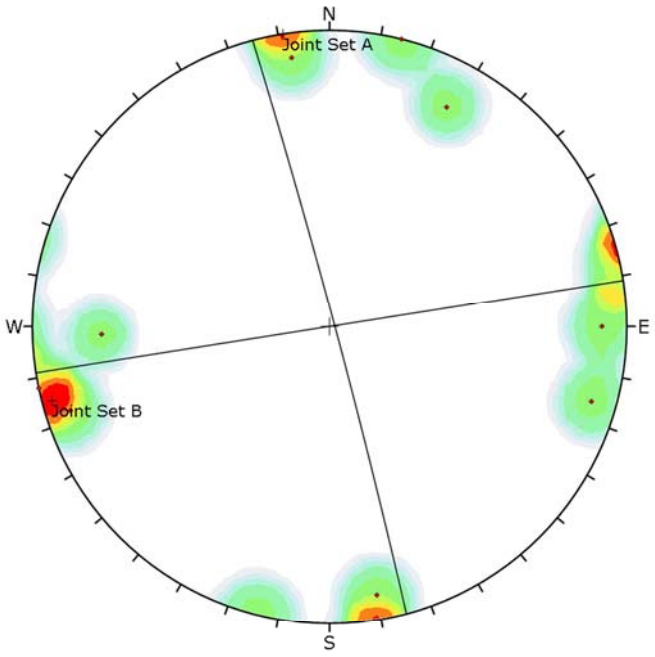

Symbol	Feature
◆	Pole Vectors

Color	Density Concentrations
	0.00 - 2.10
	2.10 - 4.20
	4.20 - 6.30
	6.30 - 8.40
	8.40 - 10.50
	10.50 - 12.60
	12.60 - 14.70
	14.70 - 16.80
	16.80 - 18.90
	18.90 - 21.00

Maximum Density	20.83%
Contour Data	Pole Vectors
Contour Distribution	Fisher
Counting Circle Size	1.0%

Plot Mode	Pole Vectors
Vector Count	9 (9 Entries)
Hemisphere	Lower
Projection	Equal Angle

(B) 2b11011 #2

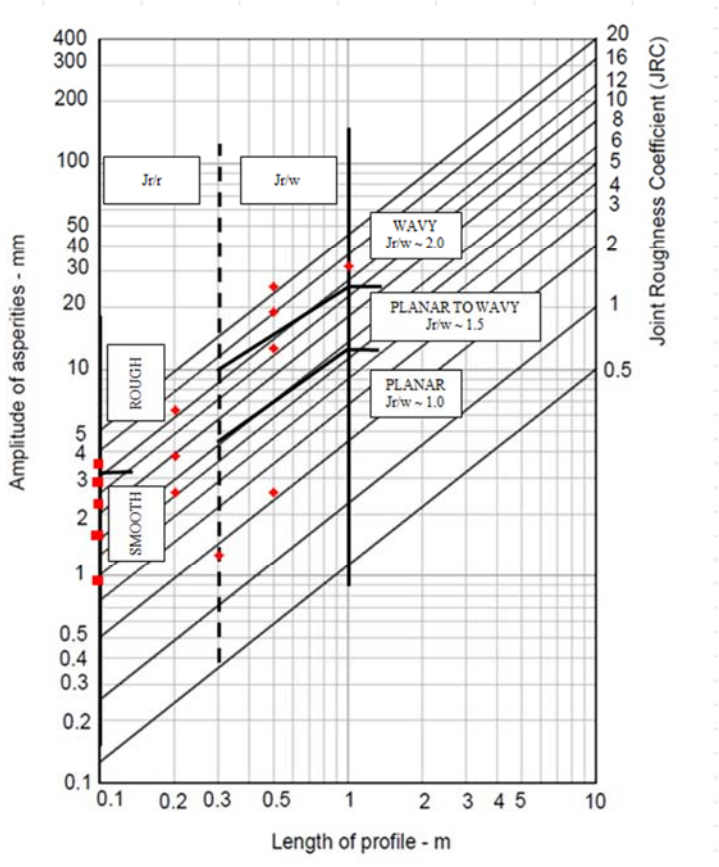

Figure B.2 Stereograph of joint orientation and JRC Chart for 2b11011 #2.

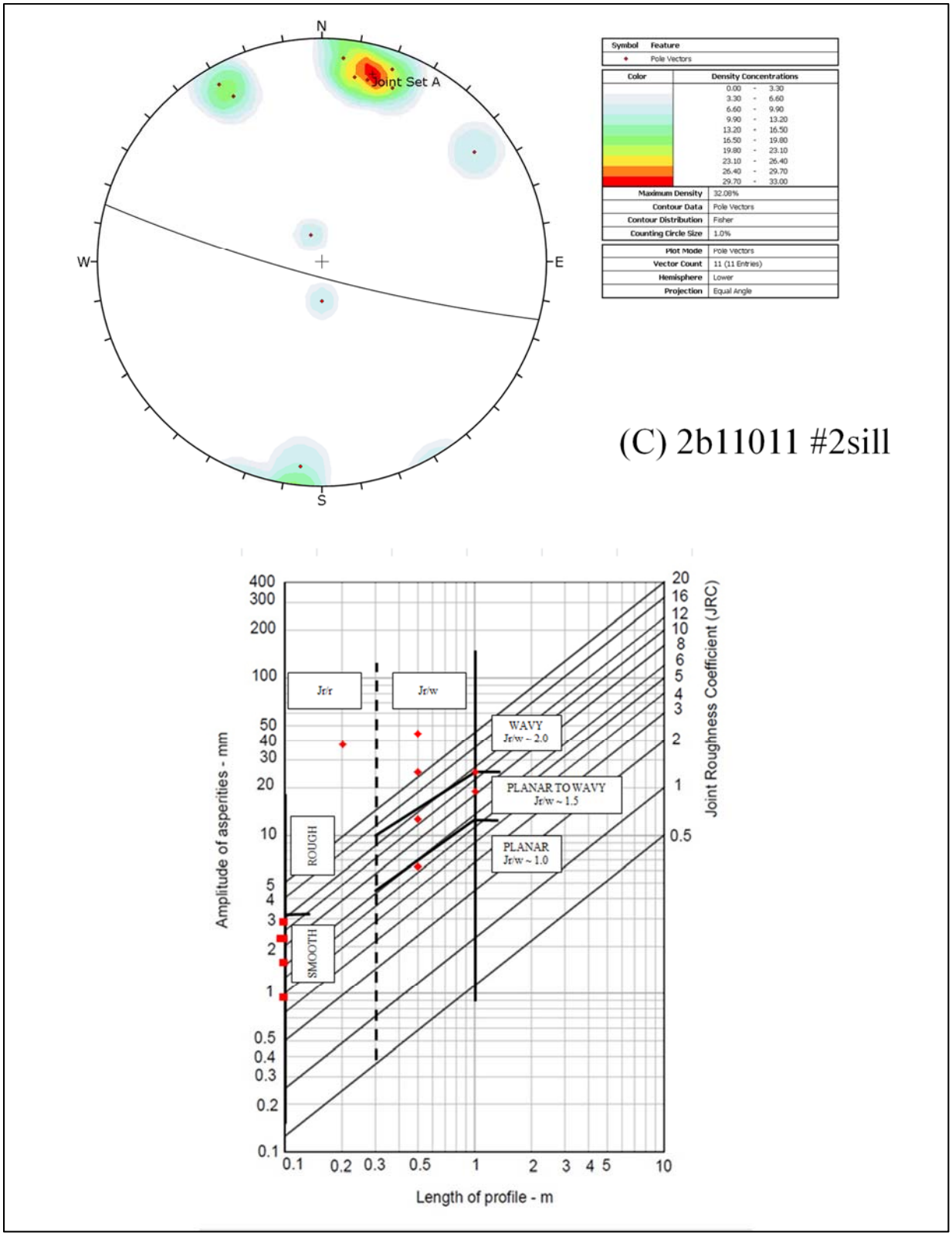

Figure B.3 Stereograph of joint orientation and JRC Chart for 2b11011 #2sill.

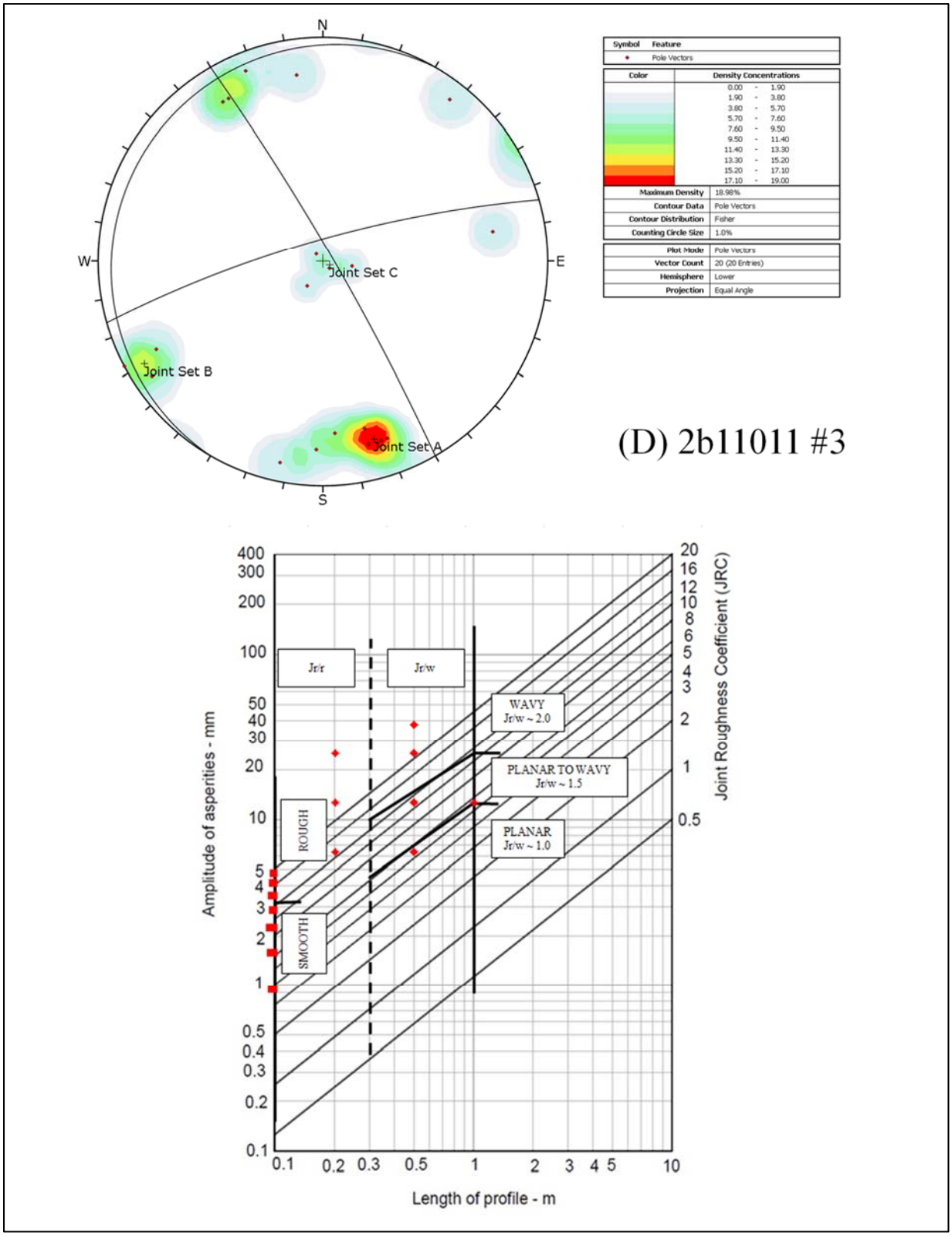

Figure B.4 Stereograph of joint orientation and JRC Chart for 2b11011 #3.

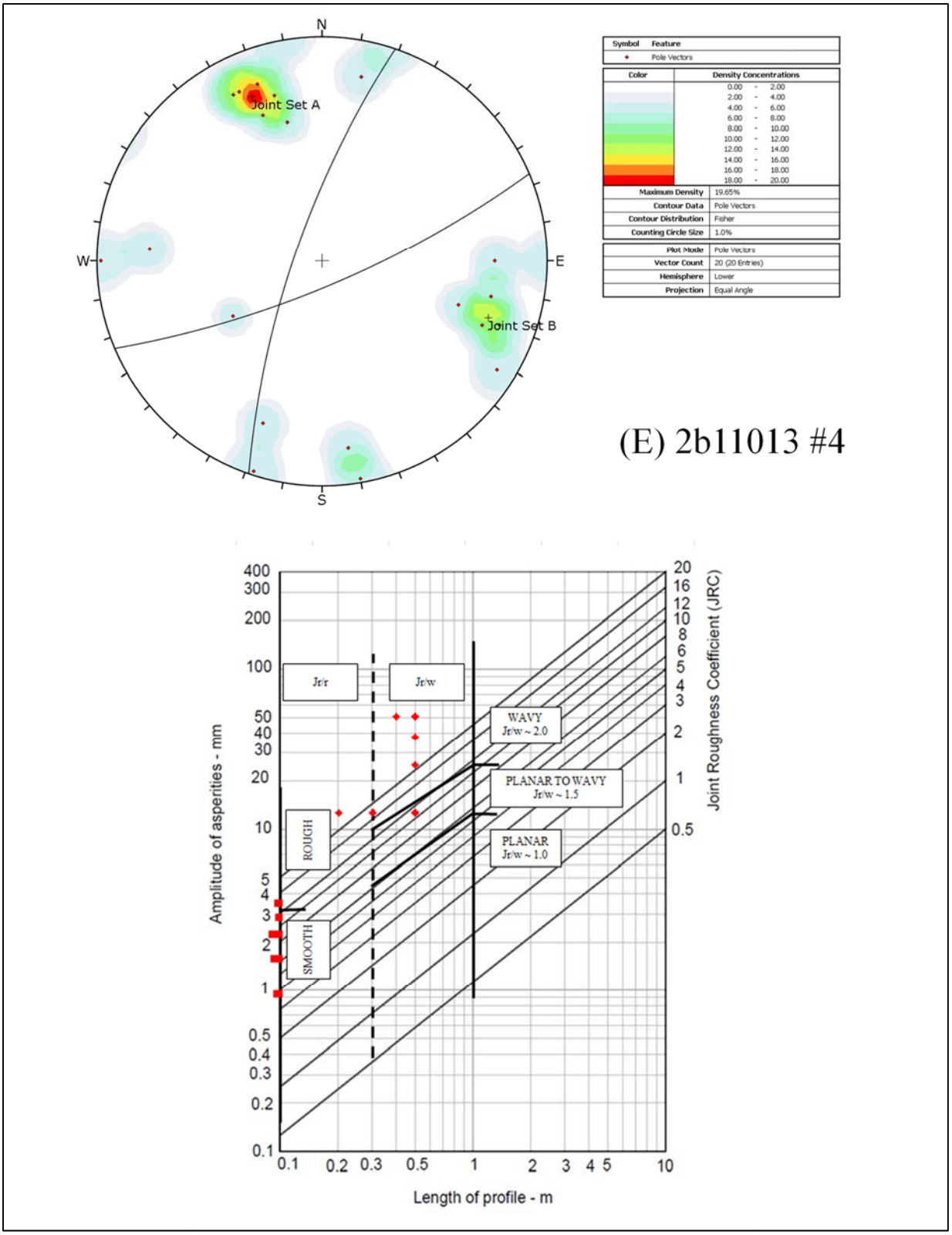

Figure B.5 Stereograph of joint orientation and JRC Chart for 2b11013 #4.

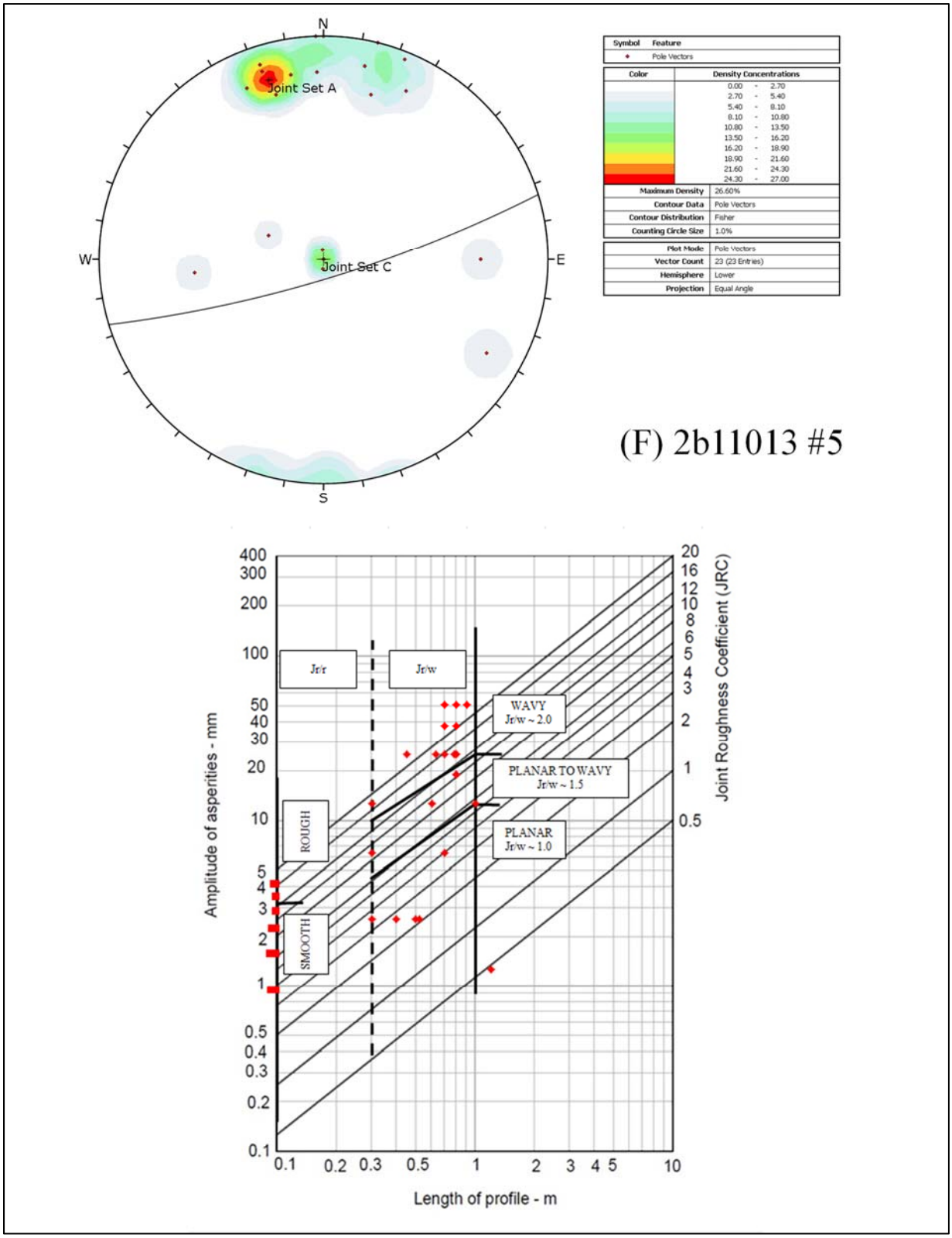

Figure B.6 Stereograph of joint orientation and JRC Chart for 2b11013 #5.

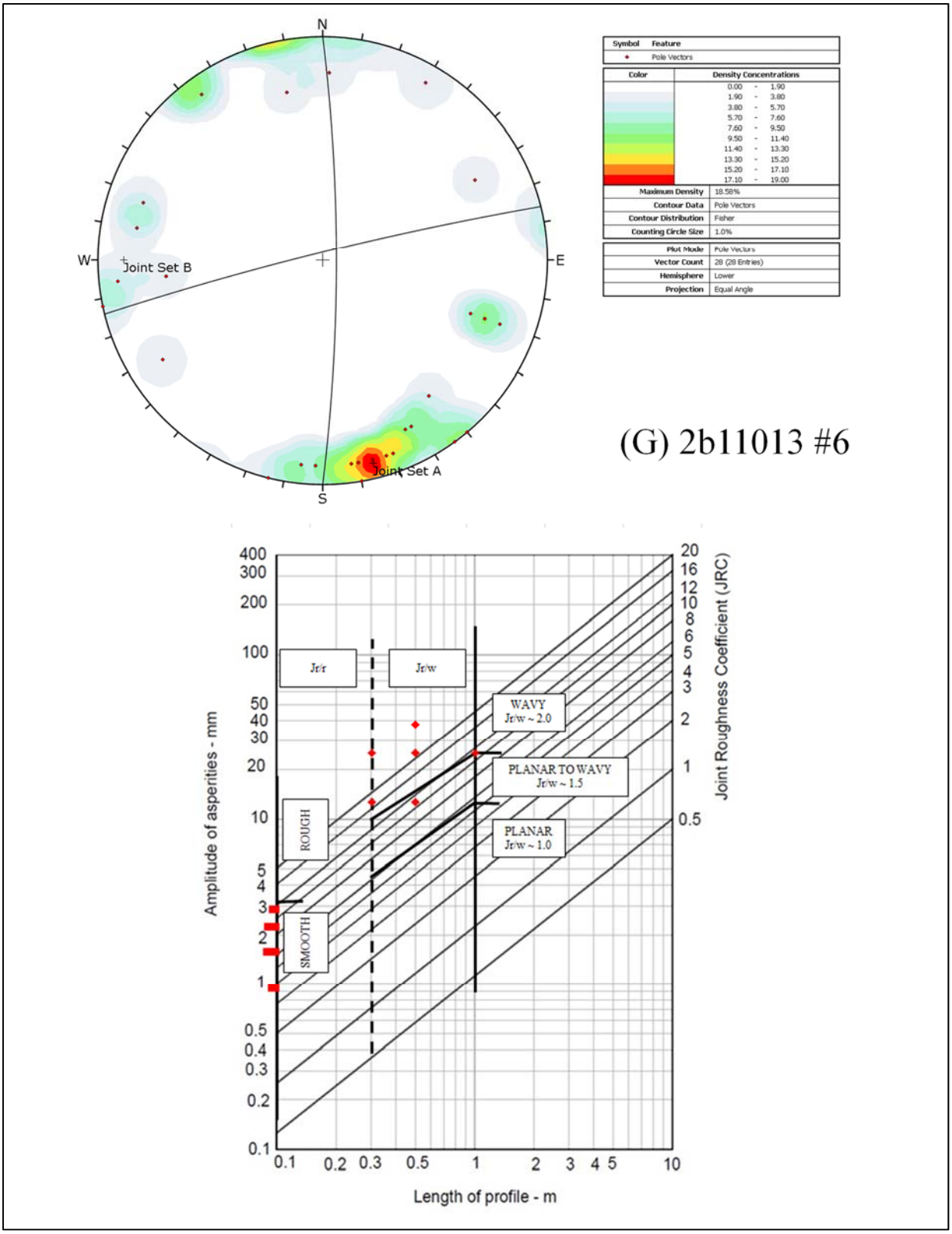

Figure B.7 Stereograph of joint orientation and JRC Chart for 2b11013 #6.

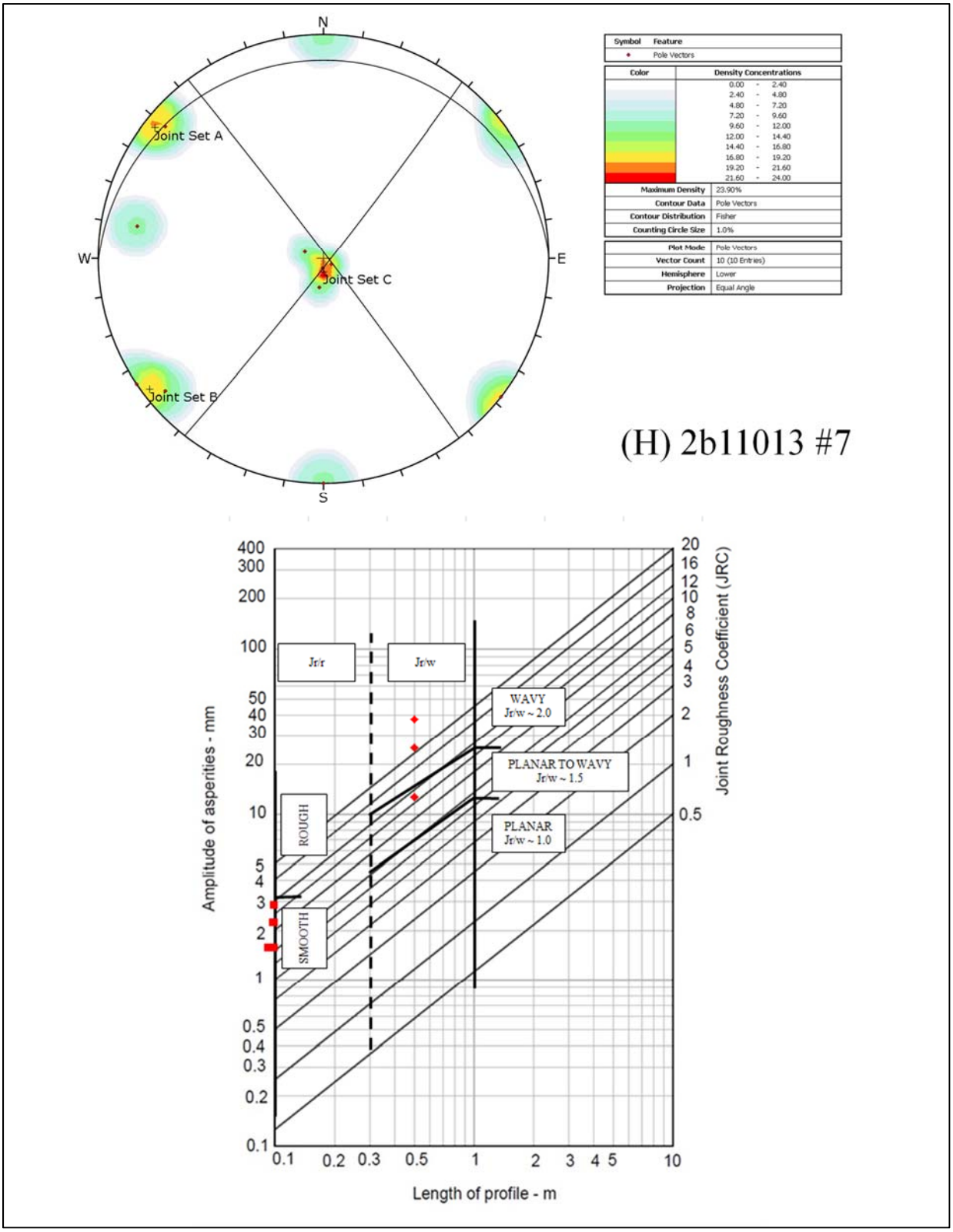

Figure B.8 Stereograph of joint orientation and JRC Chart for 2b11013 #7.

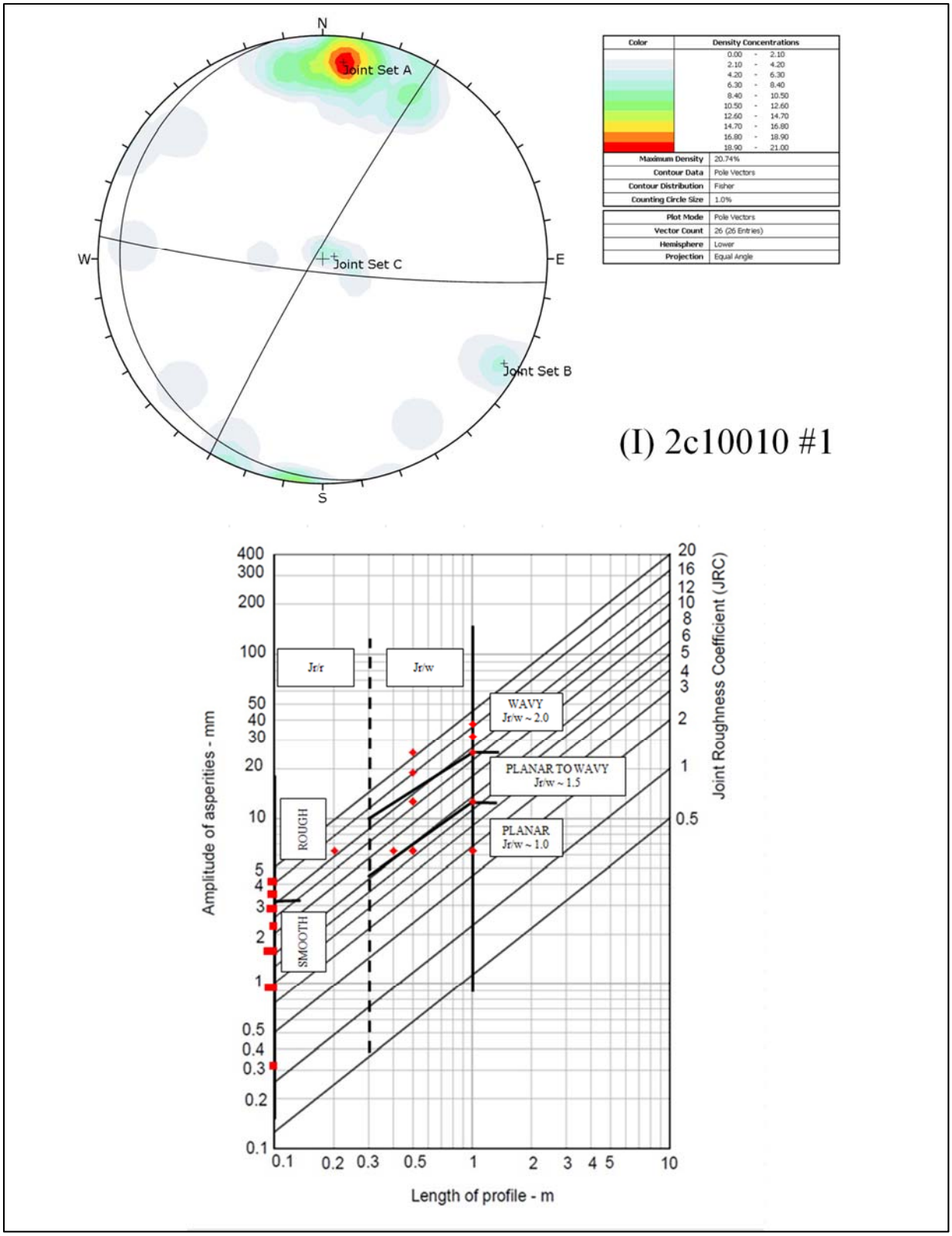

Figure B.9 Stereograph of joint orientation and JRC Chart for 2c10010 #1.

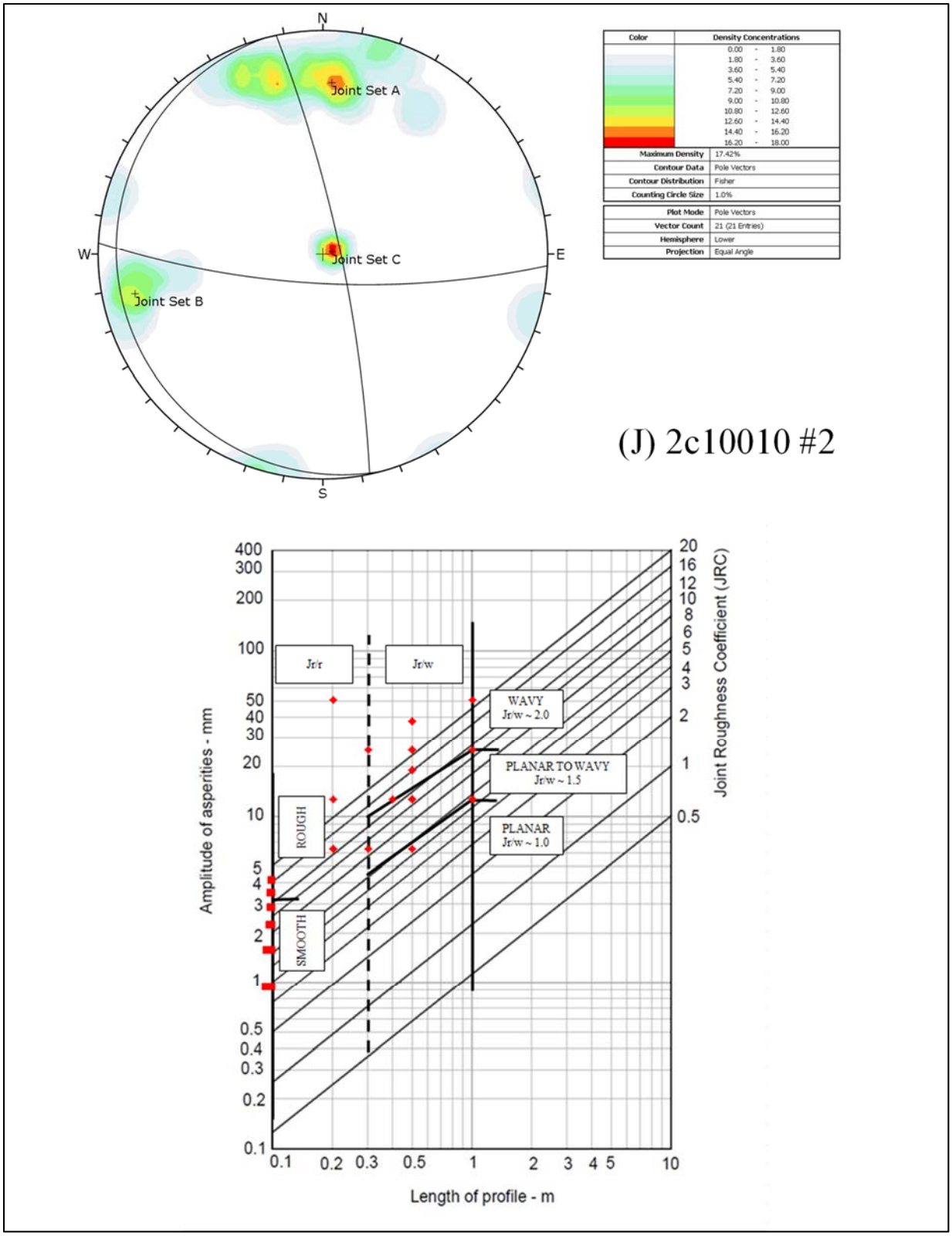

Figure B.10 Stereograph of joint orientation and JRC Chart for 2c10010 #2.

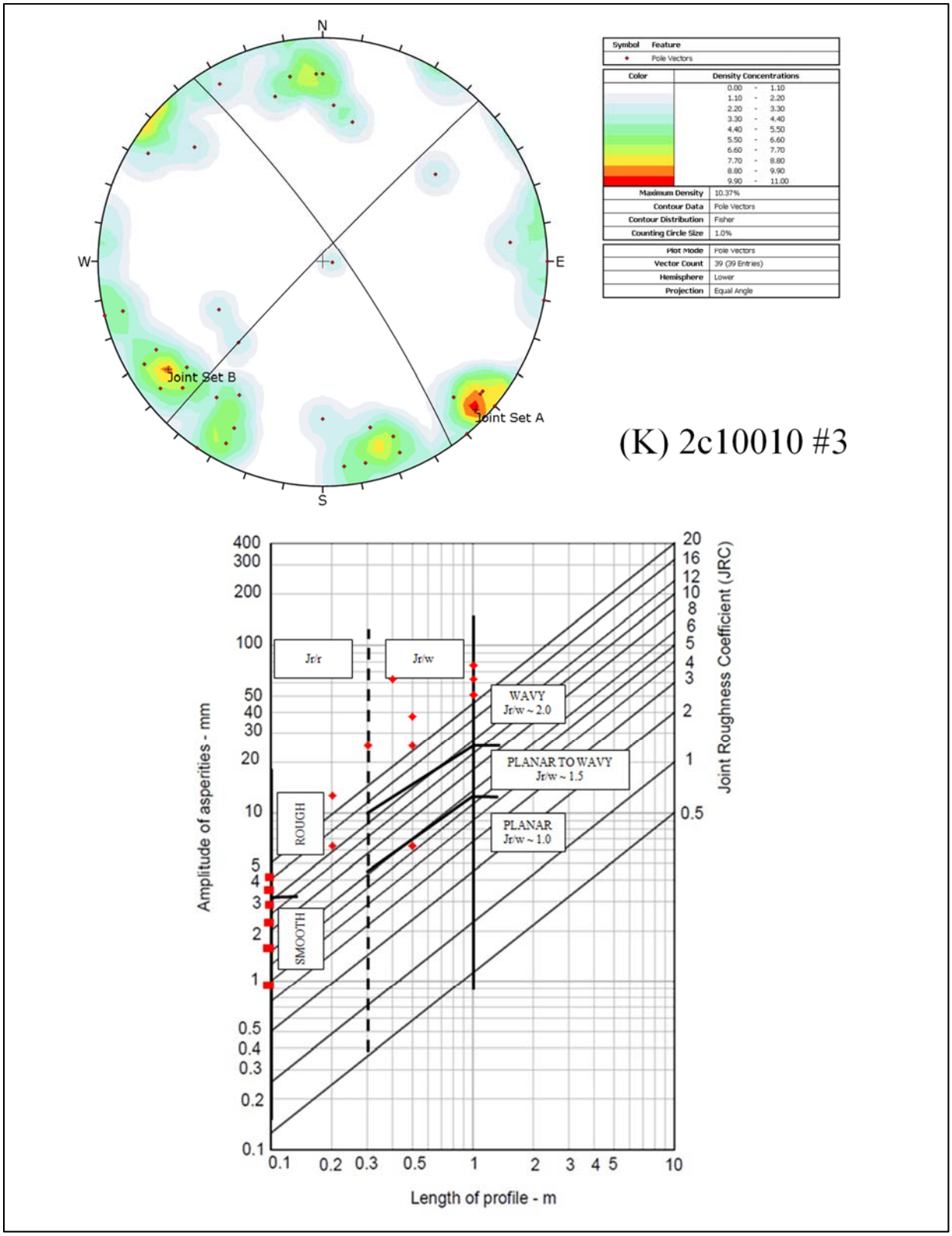

Figure B.11 Stereograph of joint orientation and JRC Chart for 2c10010 #3.

APPENDIX C
LABORATORY TESTING RAW DATA

This portion of the appendices provides the raw data and graphs from the laboratory testing performed on rock samples from Seabee Gold Mine.

The following Figures C.1 – C.15 are the stress – strain graphs for core samples that underwent UCS testing with attached strain gauges. The strain gauges were used to measure the elastic response of the rock while under compressive load. Four gauges were attached (two vertical and two horizontal) at mid – height along the sample at 90° intervals which were averaged to identify the radial strain and axial strain. The elastic modulus was calculated as the average modulus over the straight line elastic response. The Poisson's ratio was calculated as the ratio between the axial strain and radial strain over the straight line elastic response.

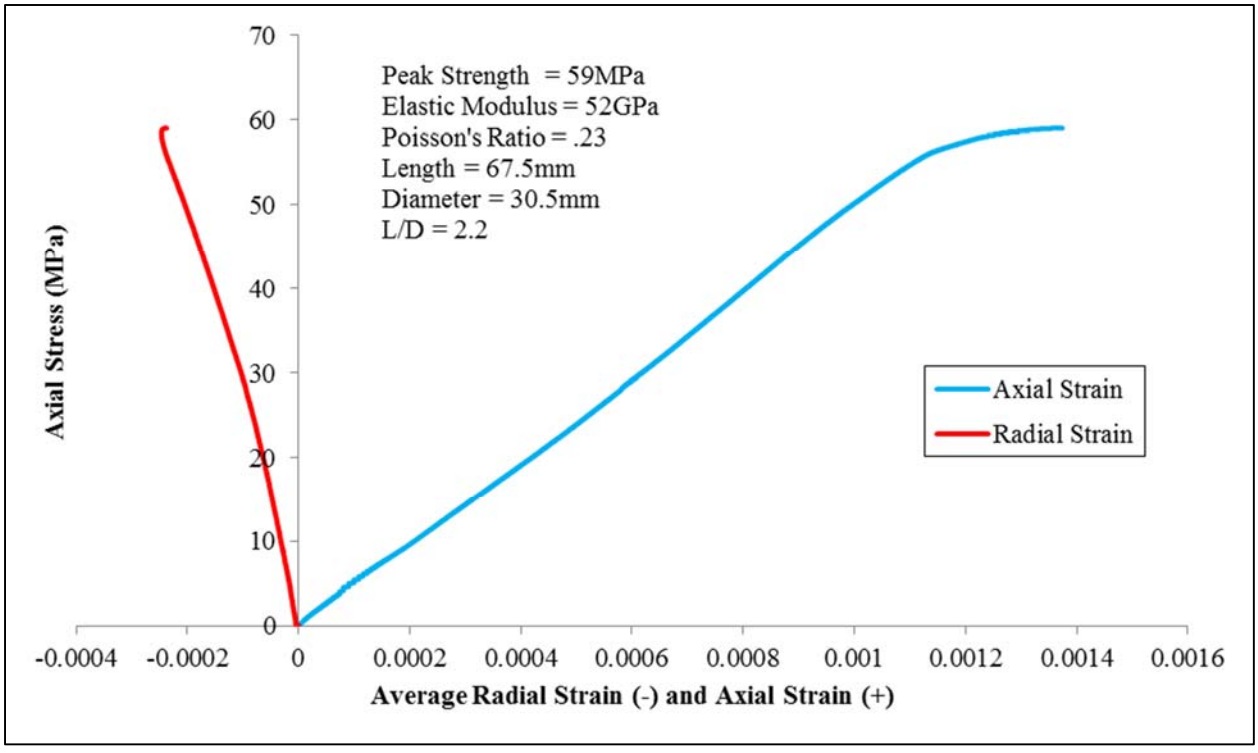

Figure C.1 Stress – strain graph for sample HW7.

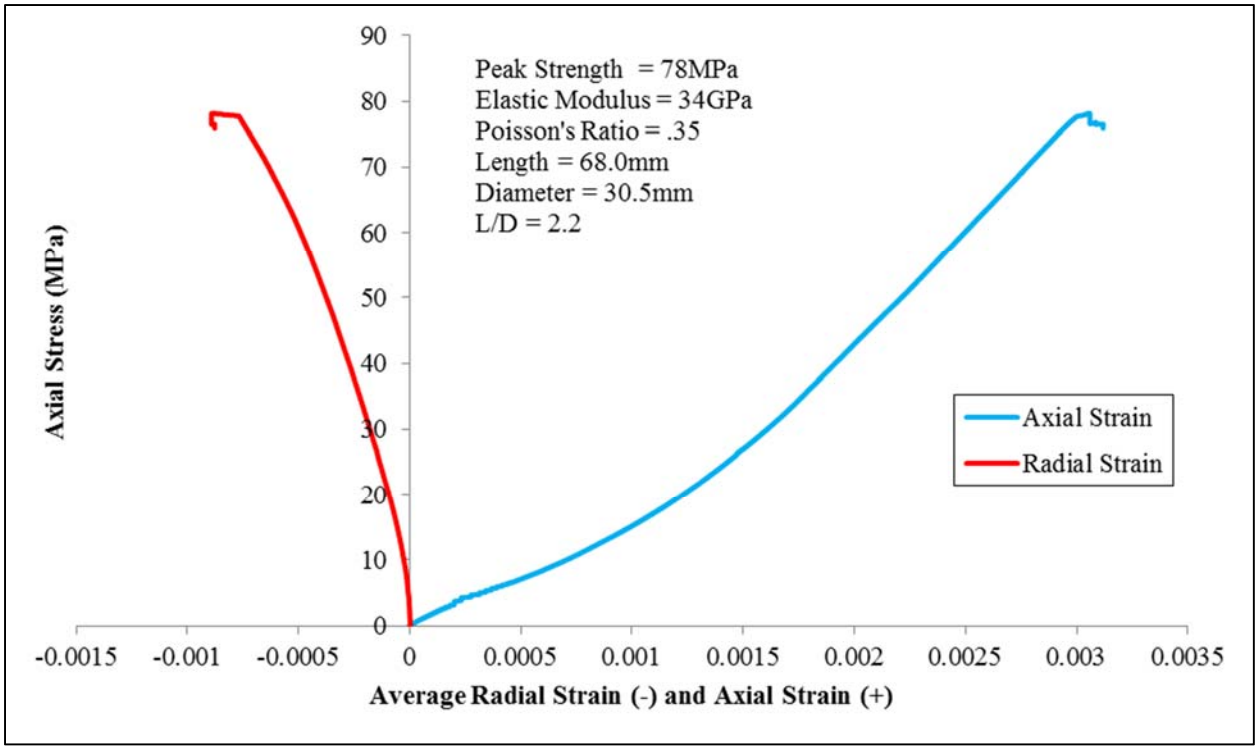

Figure C.2 Stress – strain graph for sample HW10.

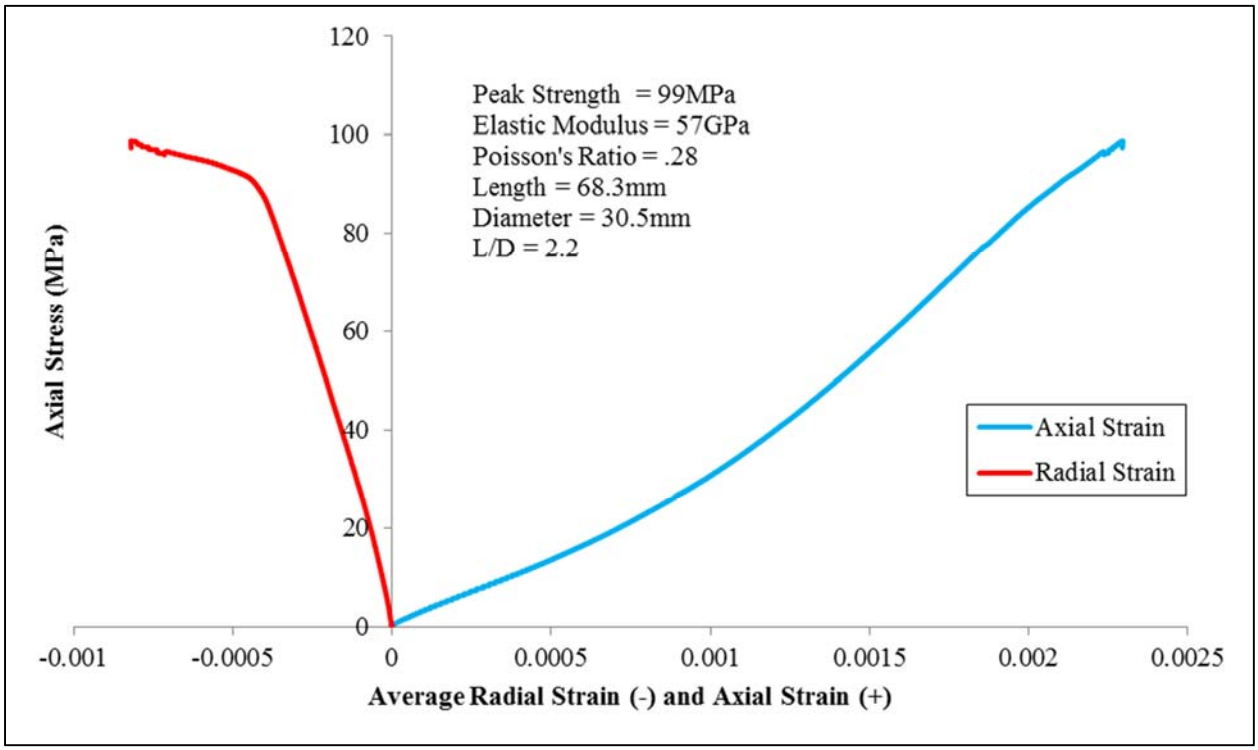

Figure C.3 Stress – strain graph for sample HW17.

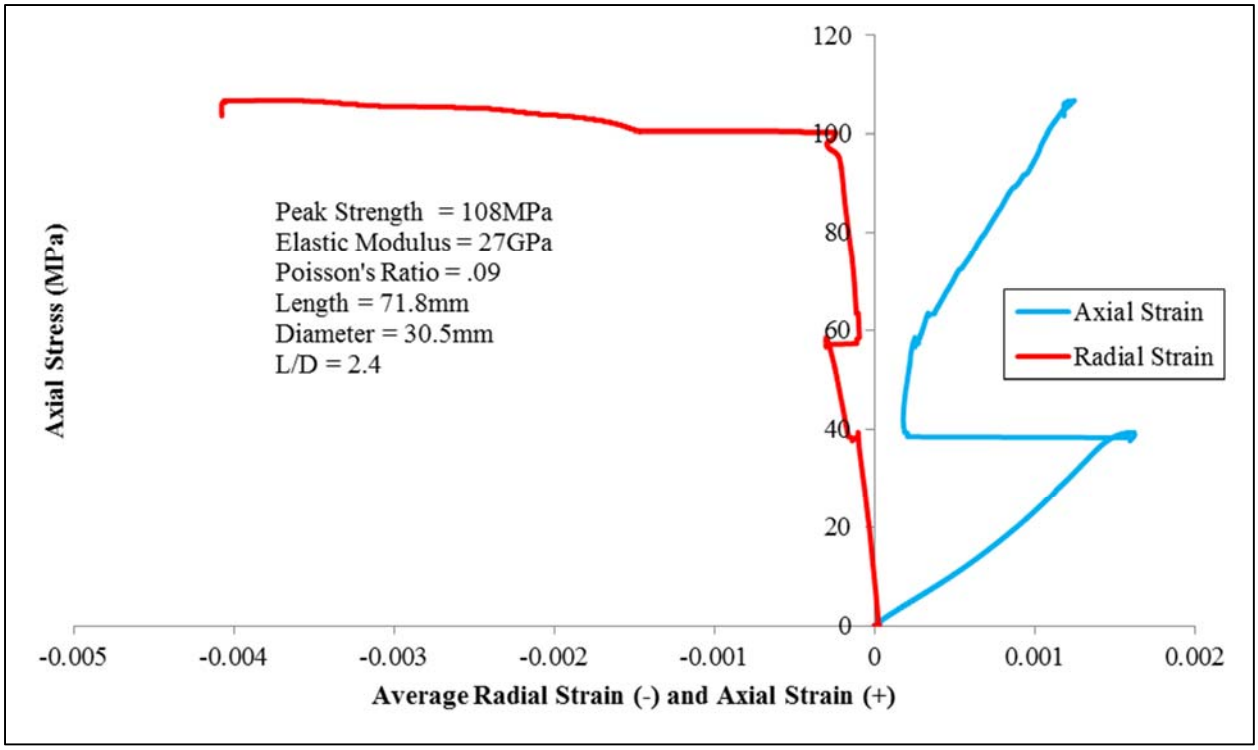

Figure C.4 Stress – strain graph for sample HW18.

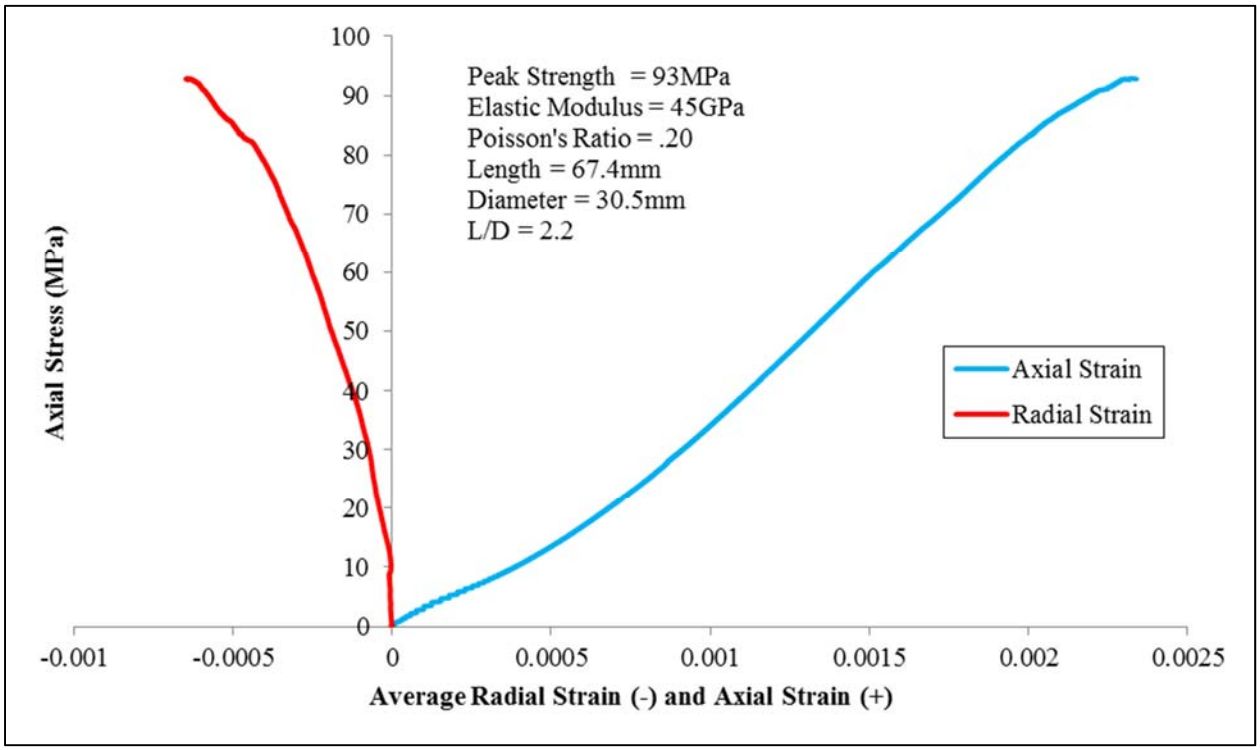

Figure C.5 Stress – strain graph for sample HW19.

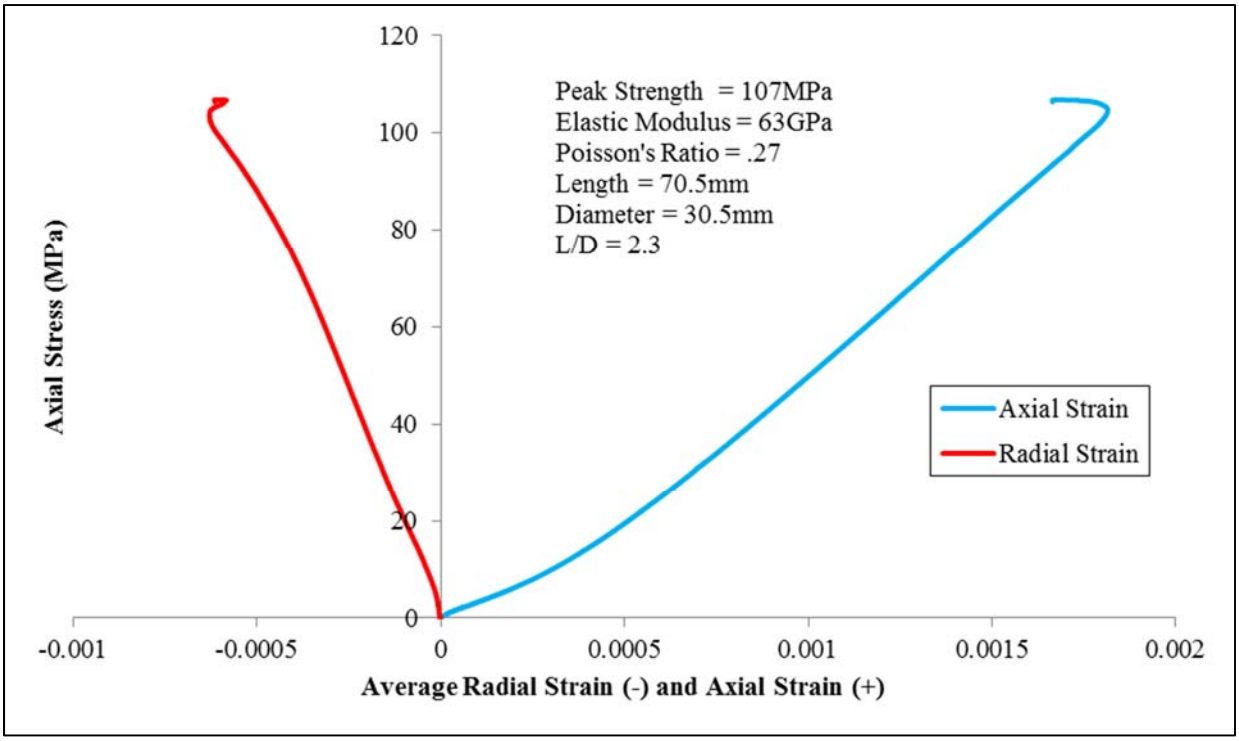

Figure C.6 Stress – strain graph for sample FW5.

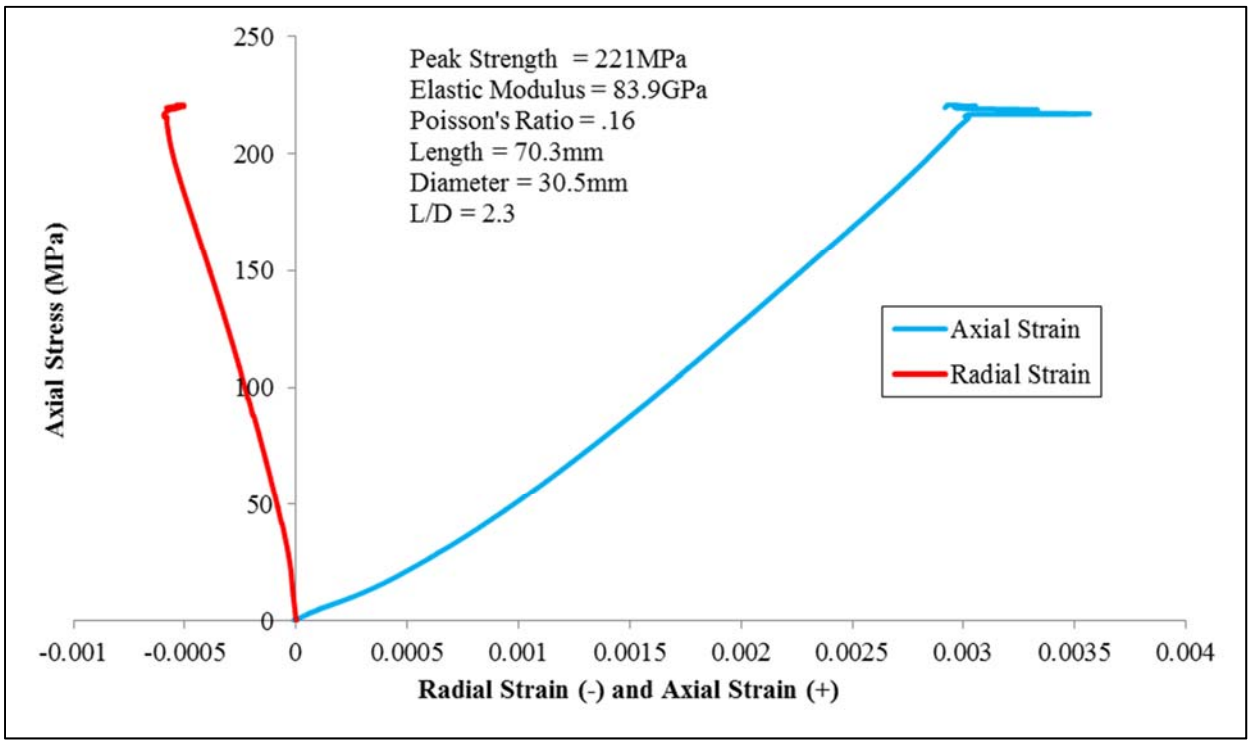

Figure C.7 Stress – strain graph for sample FW10.

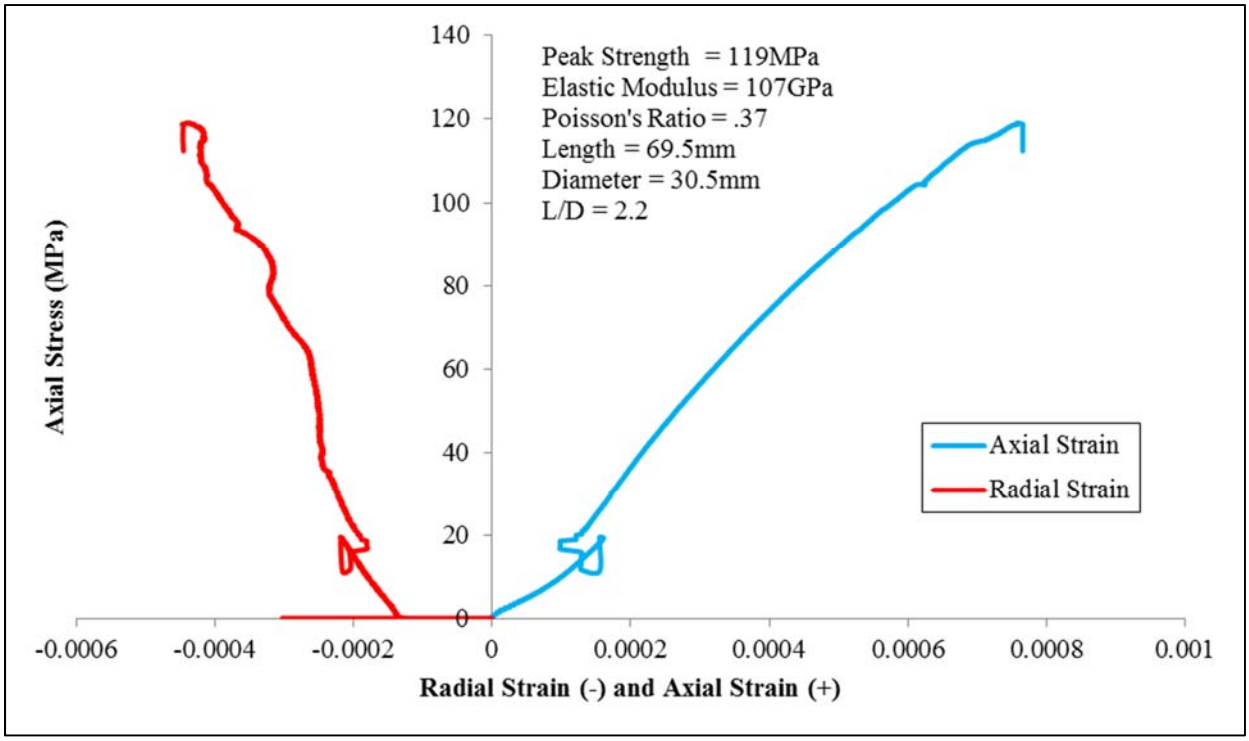

Figure C.8 Stress – strain graph for sample FW17.

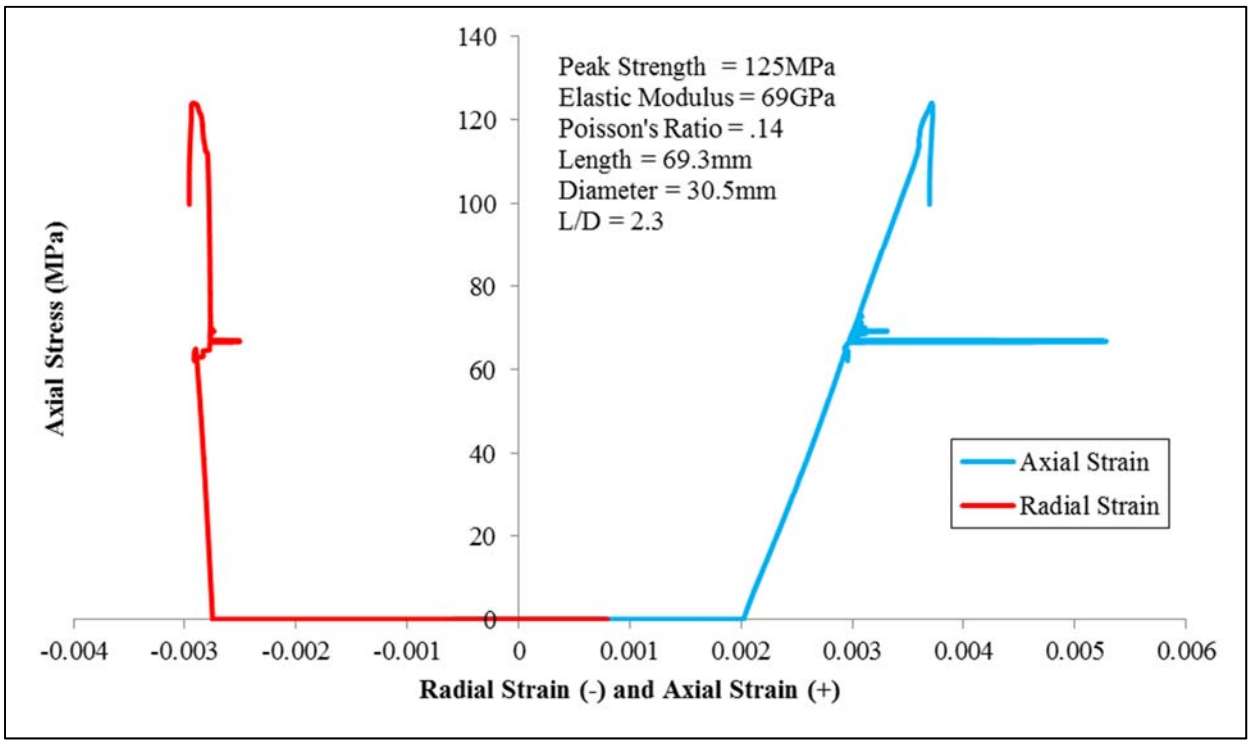

Figure C.9 Stress – strain graph for sample FW18.

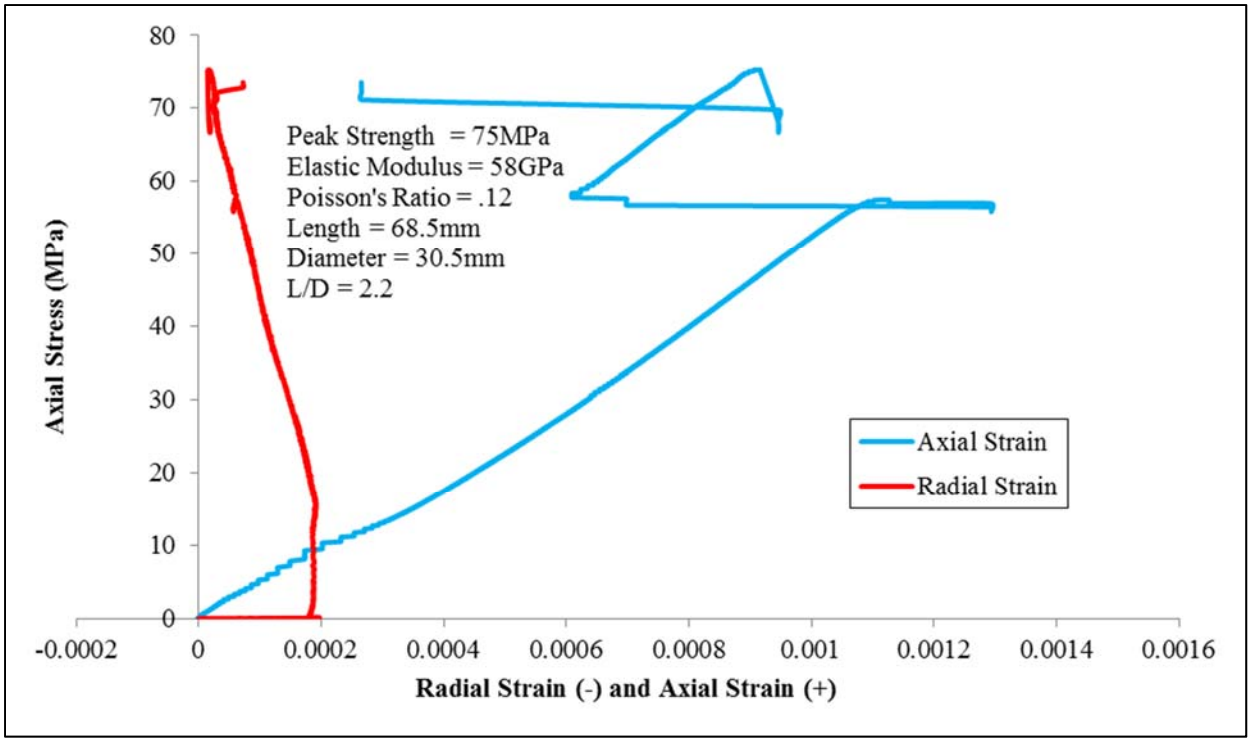

Figure C.10 Stress – strain graph for sample FW19.

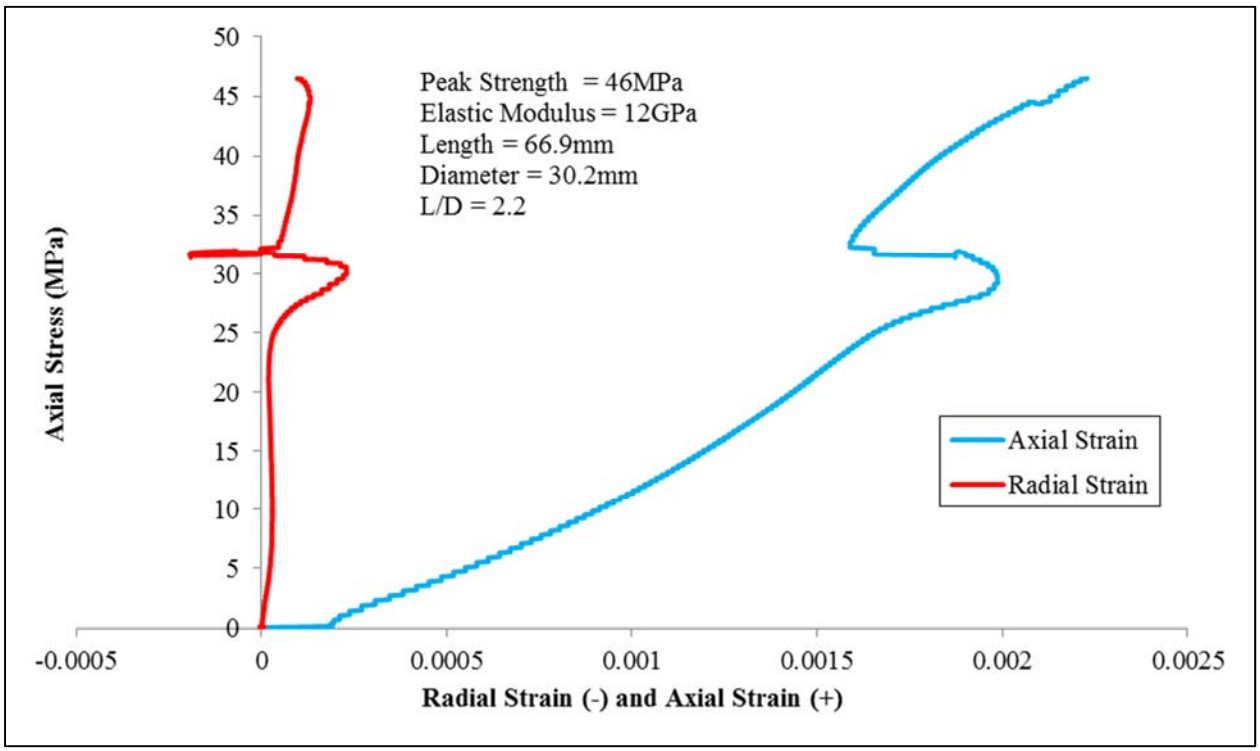

Figure C.11 Stress – strain graph for sample OZ20.

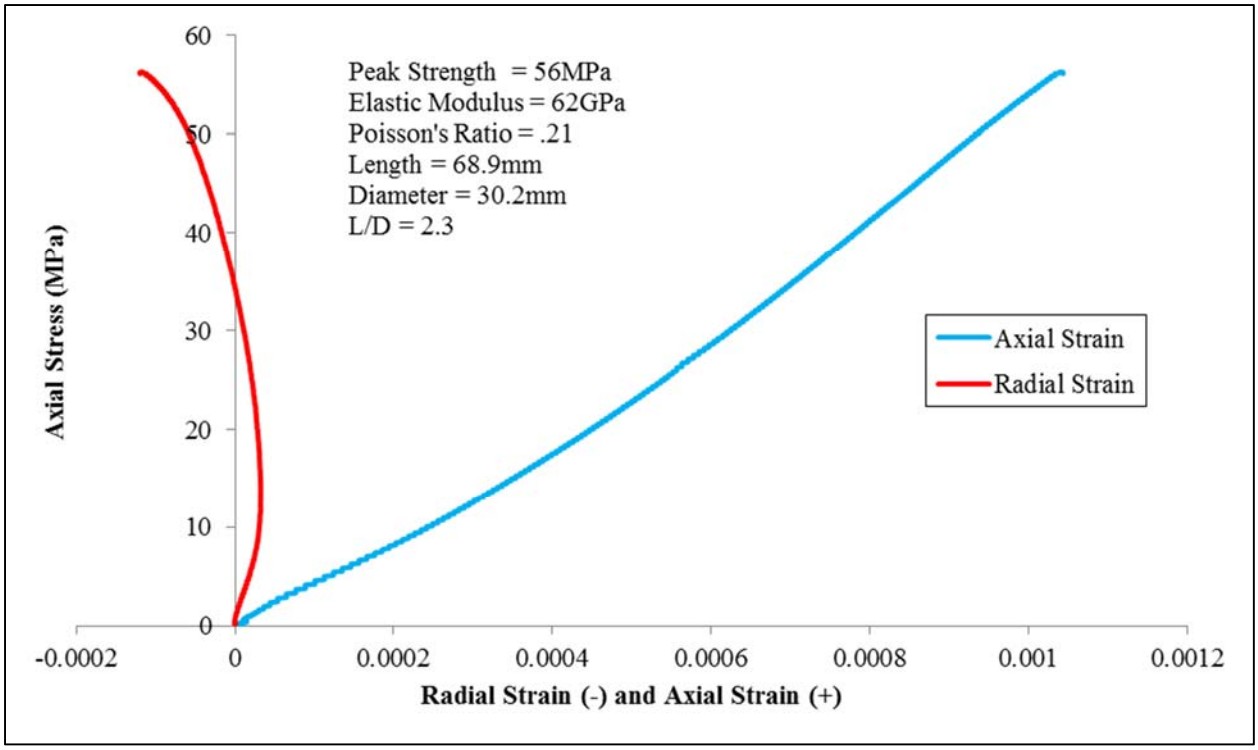

Figure C.12 Stress – strain graph for sample OZ21.

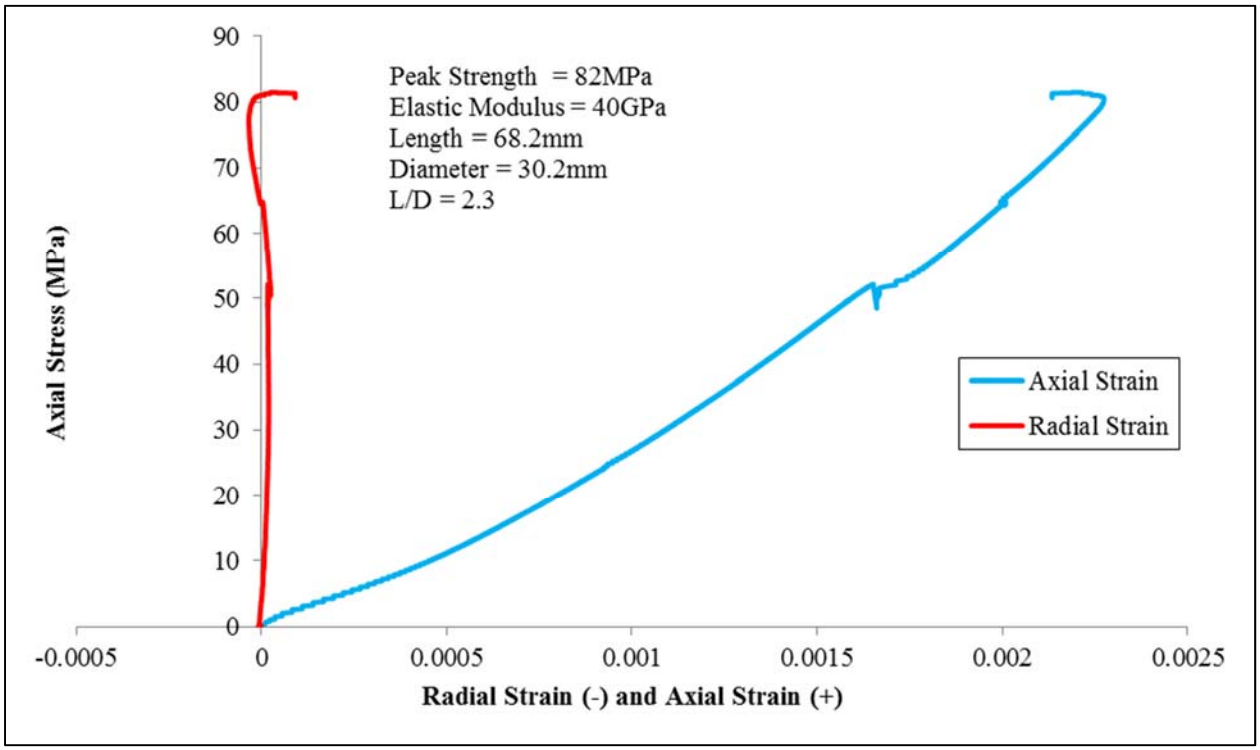

Figure C.13 Stress – strain graph for sample OZ22.

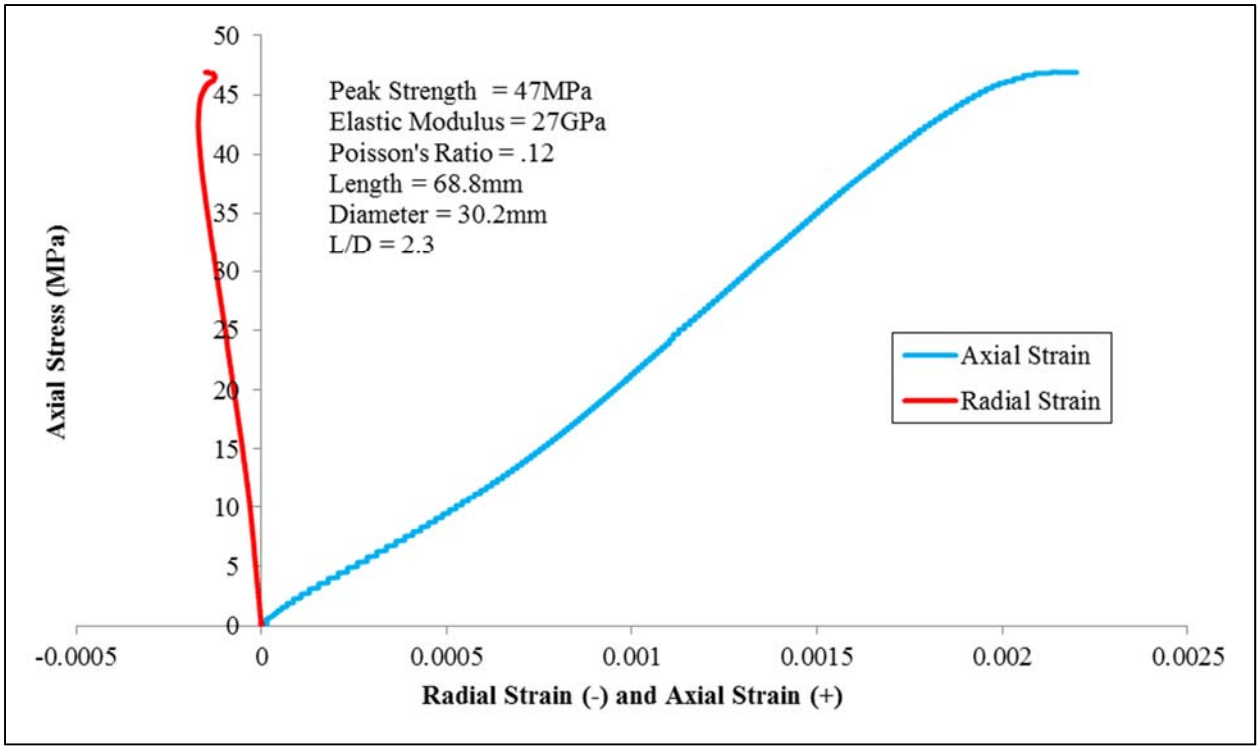

Figure C.14 Stress – strain graph for sample OZ23.

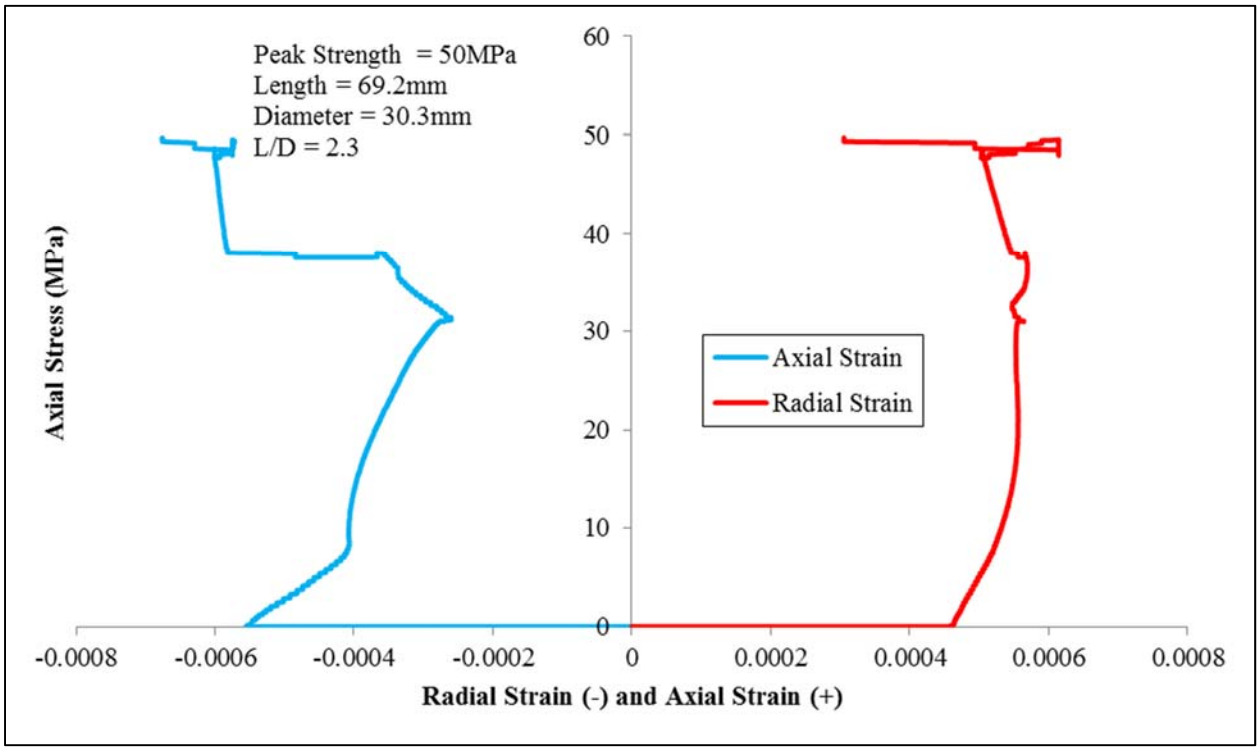

Figure C.15 Stress – strain graph for sample OZ24.

The following Tables C.1 –CA.3 contain the triaxial results for the three structures. Four samples were tested from each structure at different confining pressures. The corresponding Mohr – Coulomb plots are shown in Figures C.16 – C.18.

Table C.1 Triaxial testing results for the hangingwall structure.

Sample	Confining Pressure (psi)	Confining (kPa)	Vertical Load Final (lbs)	Vertical Load Final (kN)	Final Load Actual (kN)	Final Stress Vertical (MPa)
HW1	1560	10748	37196	165	148	203
HW2	2900	19981	11000	48	17	24
HW3	3827	26368	44848	199	158	216
HW4	4350	29971	61515	273	227	310

Table C.2 Triaxial testing results for the footwall structure.

Sample	Confining Pressure (psi)	Confining (kPa)	Vertical Load Final (lbs)	Vertical Load Final (kN)	Final Load Actual (kN)	Final Stress Vertical (MPa)
FW1	4354	29999	51156	228	181	247
FW2	2900	19981	94345	420	389	532
FW3	3641	25086	61515	274	235	320
FW4	1450	9990	52681	234	219	299

Table C.3 Triaxial testing results for the orezone structure.

Sample	Confining Pressure (psi)	Confining (kPa)	Vertical Load Final (lbs)	Vertical Load Final (kN)	Final Load Actual (kN)	Final Stress Vertical (MPa)
OZ11	1565	10782	48947	218	201	280
OZ12	2206	15199	65409	291	267	372
OZ13	3250	22392	73470	327	292	406
OZ14	656	4519	34508	154	146	204

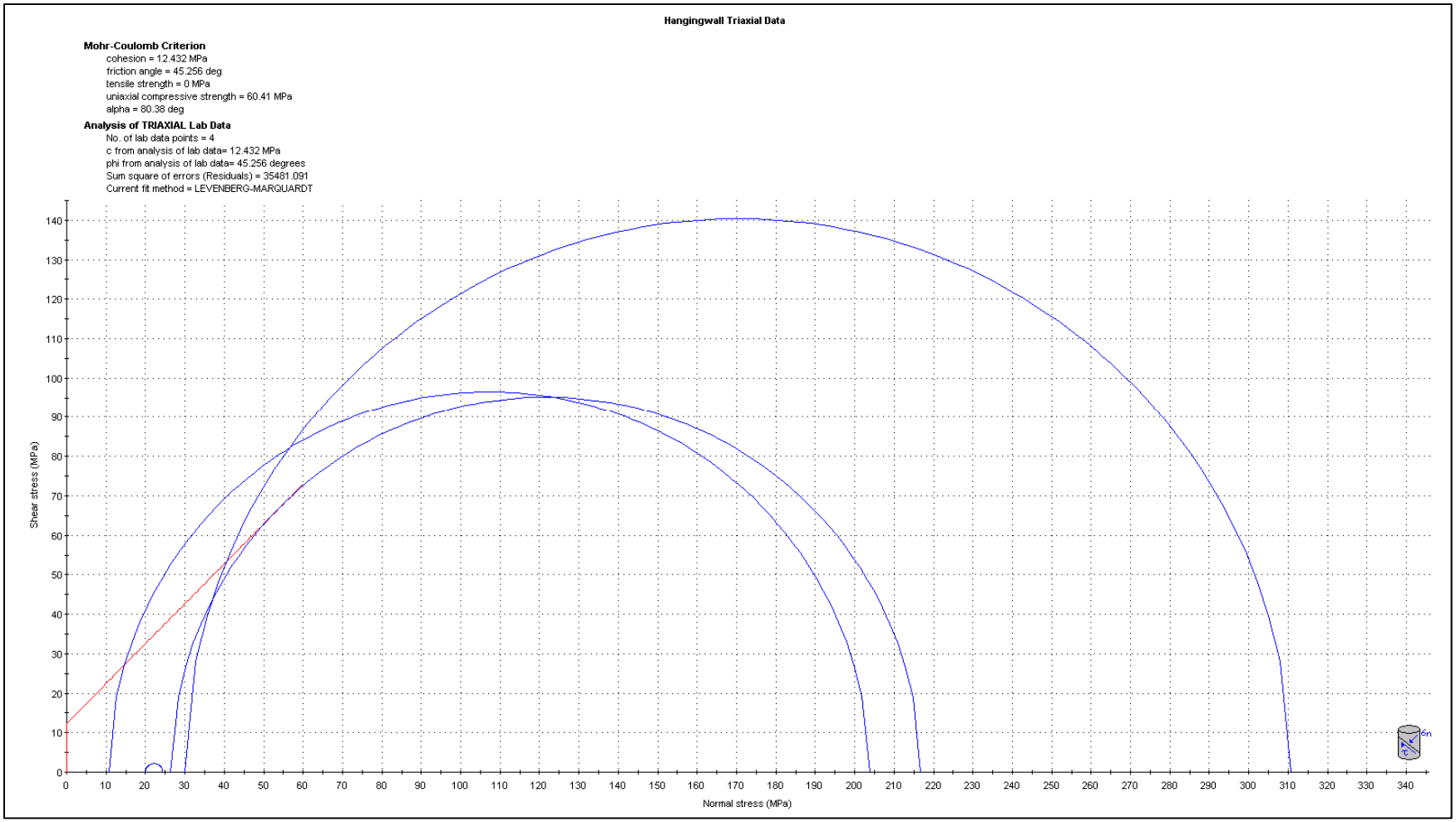

Figure C.16 Mohr – Coulomb plot of triaxial results for the hangingwall with analysis results.

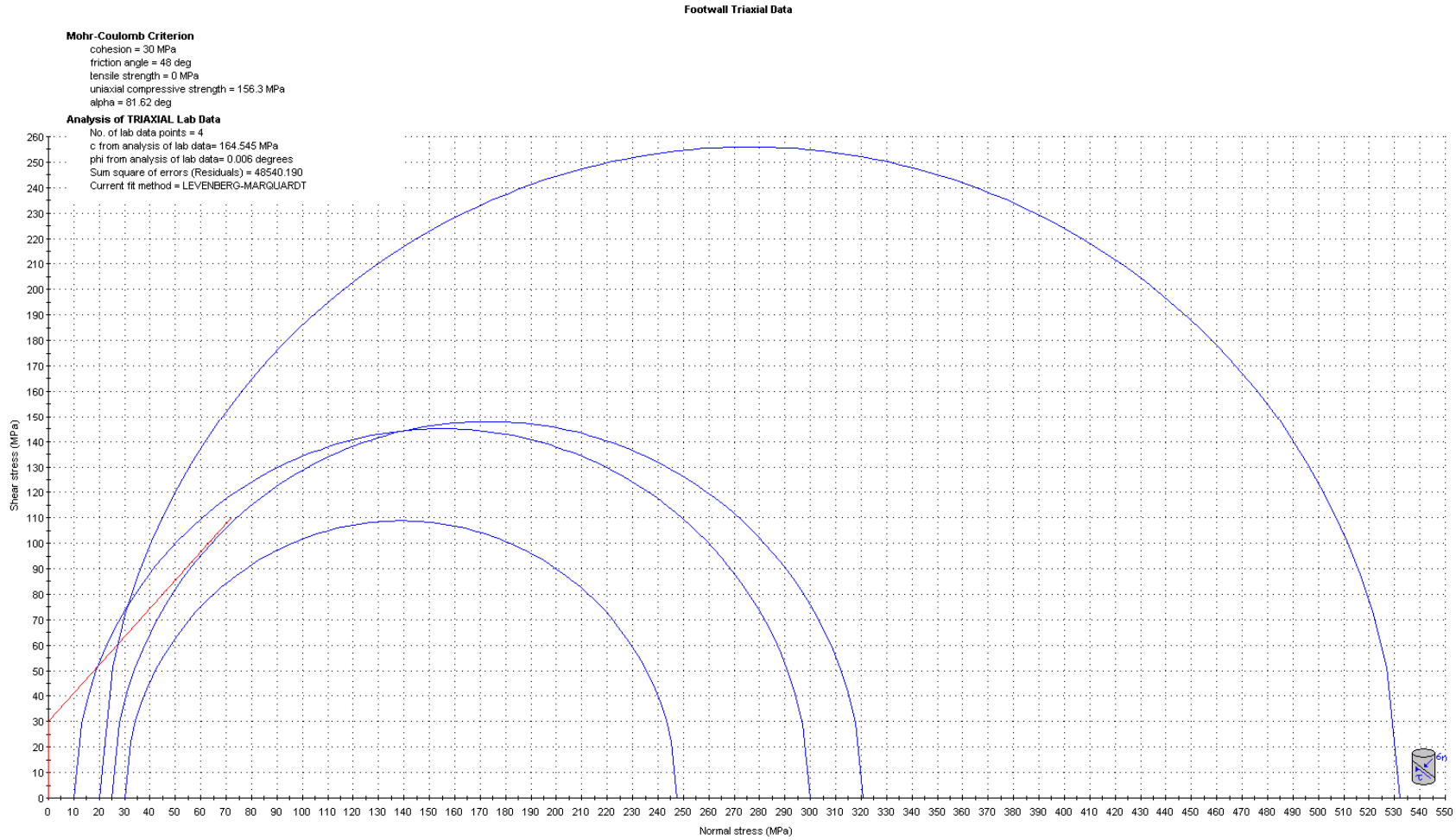

Figure C.17 Mohr – Coulomb plot of triaxial results for the footwall with analysis results.

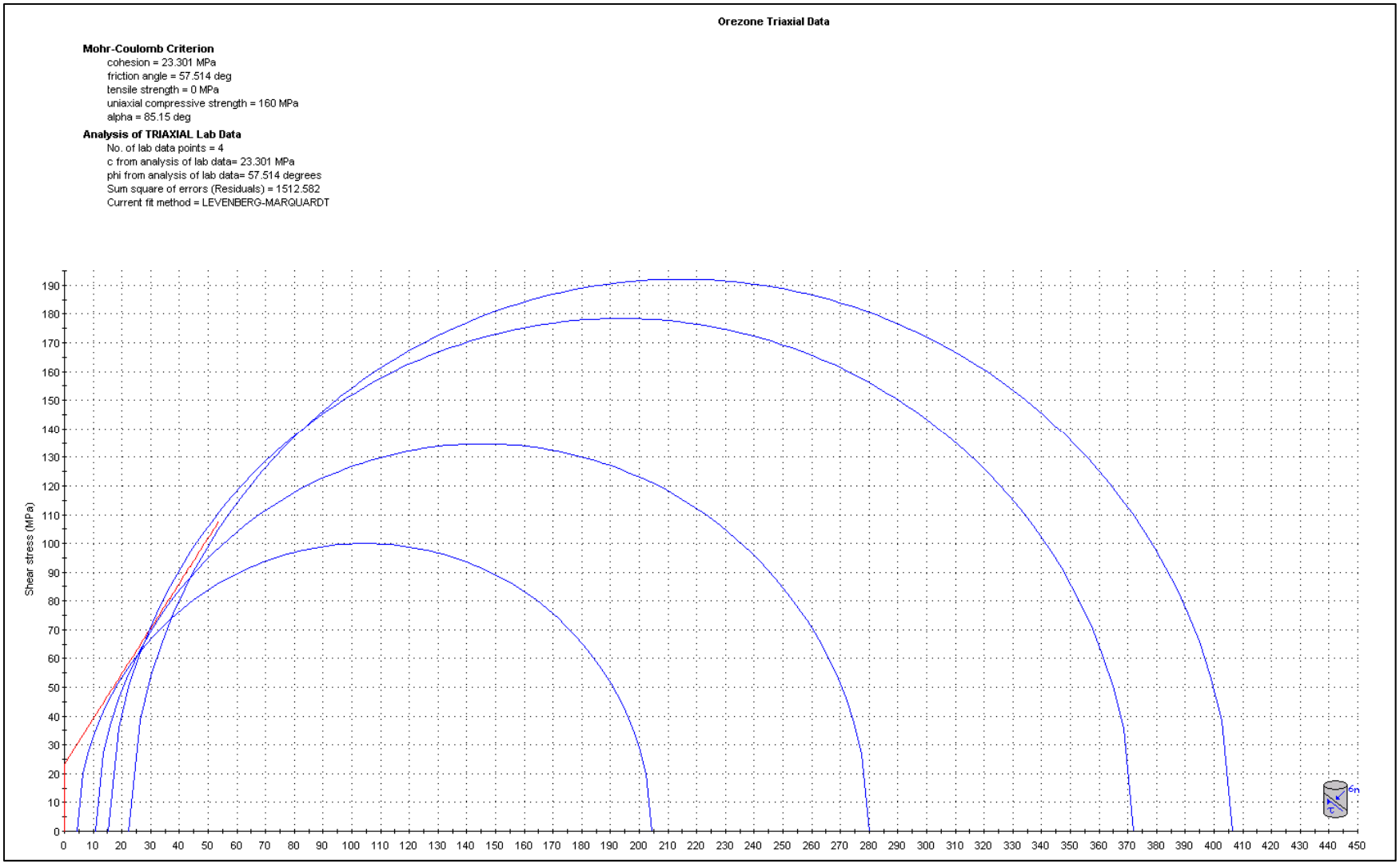

Figure C.18 Mohr – Coulomb plot of triaxial results for the orezone with analysis results.

The following Tables C.4 – C.6 contain the Brazilian results for the three structures. Ten samples were tested from each structure.

Table C.4 Brazilian testing results for the hangingwall structure.

Sample Name	Peak Load (lbs)	Peak Load (kN)	Splitting Tensile Strength (MPa)
HW11	2392	10.6	11.3
HW12	2577	11.5	12.4
HW13	2784	12.4	12.9
HW14	2071	9.2	9.4
HW15	3714	16.5	17.9
HW20	1502	6.7	11.8
HW21	1904	8.5	13.3
HW22	2468	11.0	16.6
HW23	1777	7.9	13.6
HW24	2227	9.9	14.9

Table C.5 Brazilian testing results for the footwall structure.

Sample Name	Peak Load (lbs)	Peak Load (kN)	Splitting Tensile Strength (MPa)
FW11	0	0	0
FW12	3363	15.0	17.0
FW13	4454	20.0	19.1
FW14	3171	14.1	14.9
FW15	3196	14.2	16.4
FW20	1852	8.2	13.3
FW21	1966	8.7	12.7
FW22	1901	8.5	12.0
FW23	1942	8.6	11.5
FW24	1879	8.4	11.4

Table C.6 Brazilian testing results for the orezone structure.

Sample Name	Peak Load (lbs)	Peak Load (N)	Splitting Tensile Strength (MPa)
OZ1	2433	10.8	18.9
OZ2	3745	16.7	22.3
OZ3	2204	9.8	15.1
OZ4	2572	11.4	16.2
OZ5	2418	10.8	17.0
OZ6	2855	12.7	18.5
OZ7	2315	10.3	15.9
OZ8	2841	12.6	18.2
OZ9	2361	10.5	15.7
OZ10	2648	11.8	18.5

The following Tables C.7 – C.9 contain the acoustic velocity results for the three structures. Fourteen samples were tested from each structure.

Table C.7 Acoustic velocity testing results for the hangingwall structure.

Sample	P-wave (μs)	S-wave (μs)	P-wave Velocity (m/s)	S-wave Velocity (m/s)	Young's Modulus (GPa)	Rigidity Modulus (Gpa)	Poisson's Ratio	Lame's Constant (GPa)	Bulk Modulus (GPa)
HW1	20.45	33.05	5326.44	3310.00	77	33	0.19	19	41
HW2	21.05	37.2	5095.97	2765.81	59	23	0.29	32	47
HW3	21.5	37.05	4936.88	2784.40	58	23	0.27	26	42
HW4	22.65	36.65	4672.79	2896.75	59	25	0.19	15	32
HW5	22.9	37.85	4434.19	2663.95	52	21	0.22	16	31
HW6	23.5	38.7	4277.64	2584.24	46	19	0.21	14	27
HW7	23.7	39.7	4142.33	2441.95	47	19	0.23	17	30
HW8	21.45	35.7	5069.04	3011.42	66	27	0.23	22	40
HW9	23.1	39.1	4472.61	2595.93	48	19	0.25	19	31
HW10	23.6	39.9	4199.38	2442.73	43	17	0.24	17	28
HW16	21.55	37.85	4777.39	2620.16	53	21	0.28	28	41
HW17	21.9	38.5	4707.59	2580.72	51	20	0.29	26	40
HW18	23.45	41.05	4476.01	2477.24	47	18	0.28	23	36
HW19	21.8	37.4	4683.33	2660.36	53	21	0.26	23	37

Table C.8 Acoustic velocity testing results for the footwall structure.

Sample	P-wave (μs)	S-wave (μs)	P-wave Velocity (m/s)	S-wave Velocity (m/s)	Young's Modulus (GPa)	Rigidity Modulus (GPa)	Poisson's Ratio	Lame's Constant (GPa)	Bulk Modulus (GPa)
FW1	21.75	35.25	4783.28	2958.62	63	26	0.19	16	34
FW2	22.60	36.50	4629.61	2878.12	58	24	0.19	14	31
FW3	20.80	34.70	5117.16	3027.37	66	27	0.23	23	41
FW4	20.45	32.35	5287.36	3399.01	78	34	0.15	14	37
FW5	23.35	35.70	4418.81	2980.13	56	26	0.08	5	23
FW6	21.85	34.40	4862.98	3144.07	66	29	0.14	11	31
FW7	21.40	33.70	4845.00	3133.03	66	29	0.14	11	31
FW8	22.30	34.45	4586.58	3050.89	60	27	0.10	7	25
FW9	21.00	37.25	5010.29	2703.97	55	21	0.29	30	45
FW10	22.30	36.15	4720.81	2918.67	58	24	0.19	15	31
FW16	21.90	37.80	4832.41	2721.17	54	21	0.27	25	39
FW17	18.75	31.15	6121.59	3637.70	95	39	0.23	32	58
FW18	19.40	32.65	5771.67	3362.14	82	33	0.24	31	53
FW19	20.60	32.50	5187.12	3348.17	74	33	0.14	13	35

Table C.9 Acoustic velocity testing results for the orezone structure.

Sample	P-wave (μs)	S-wave (μs)	P-wave Velocity (m/s)	S-wave Velocity (m/s)	Young's Modulus (GPa)	Rigidity Modulus (GPa)	Poisson's Ratio	Lame's Constant (GPa)	Bulk Modulus (GPa)
OZ11	20.45	33.05	5352.49	3326.19	78	33	0.19	19	41
OZ12	21.05	37.20	5019.78	2724.45	57	22	0.29	31	45
OZ13	21.50	37.05	4941.84	2787.20	59	23	0.27	26	42
OZ14	22.65	36.65	4638.69	2875.61	59	25	0.19	15	31
OZ15	22.90	37.85	4482.58	2693.02	53	22	0.22	17	31
OZ16	23.50	38.70	4189.44	2530.96	45	19	0.21	14	26
OZ17	23.70	39.70	4504.91	2655.70	51	21	0.23	18	32
OZ18	21.45	35.70	4964.41	2949.26	64	26	0.23	22	39
OZ19	23.10	39.10	4287.90	2488.72	46	18	0.25	18	30
OZ20	23.60	39.90	4129.63	2402.15	42	17	0.24	16	28
OZ21	22.35	36.70	4606.69	2793.91	56	23	0.21	17	32
OZ22	22.05	34.50	4656.66	3038.75	63	28	0.13	10	28
OZ23	23.75	37.10	4206.12	2745.31	50	22	0.13	8	22
OZ24	23.50	37.90	4298.14	2676.98	50	21	0.18	12	26

The following Tables C.10 – C.12 contain the UCS results for the three structures. Ten samples were tested from each structure, five with strain gauges and five without.

Table C.10 UCS testing results for the hangingwall structure.

Sample	Strain	Max Load (lbs)	Load (kN)	Stress (MPa)
HW5	No	3631	16	22
HW6	No	25512	114	155
HW8	No	27692	123	169
HW9	No	21525	96	131
HW16	No	16321	73	101
HW7	Yes	9730	43	59
HW10	Yes	12854	57	78
HW17	Yes	15989	71	99
HW18	Yes	17353	77	108
HW19	Yes	15002	67	93

Table C.11 UCS testing results for the footwall structure.

Sample	Strain	Max Load (lbs)	Load (kN)	Stress (Mpa)
FW6	No	19886	88	121
FW7	No	23824	106	145
FW8	No	35036	156	213
FW9	No	35925	160	219
FW16	No	6591	29	40
FW5	Yes	17559	78	107
FW10	Yes	36287	161	221
FW17	Yes	19552	87	119
FW18	Yes	20505	91	125
FW19	Yes	12360	55	75

Table C.12 UCS testing results for the orezone structure.

Sample	Strain	Max Load (lbs)	Load (N)	Stress (Mpa)
OZ15	No	12197	54	76
OZ16	No	15478	69	96
OZ17	No	15757	70	98
OZ18	No	11764	52	73
OZ19	No	12829	57	80
OZ20	Yes	7489	33	46
OZ21	Yes	9054	40	56
OZ22	Yes	13102	58	82
OZ23	Yes	7573	34	47
OZ24	Yes	8130	36	50

The following Tables C.13 – C.15 contain the point load results for the three structures. Nineteen to twenty one samples were tested from each structure.

Table C.13 Point load testing results for the hangingwall structure.

Sample	Box	Depth (m)	D_e (mm)	Load (kN)	$I_{s(50)}$ (MPa)	K Conversion Factor	UCS (MPa)	Orientation wrt Foliation
1	U11-037	162.50	30.5	7	5.9	18	106	Parallel
2	U11-037	162.65	30.5	8	6.7	18	121	Perpendicular
3	U11-037	162.90	30.5	6	5.0	18	91	Parallel
4	U11-037	163.15	30.5	6	5.0	18	91	Perpendicular
5	U11-037	163.50	30.5	3.5	2.9	18	53	Parallel
6	U11-037	163.50	30.5	7	5.9	18	106	Perpendicular
7	U11-037	163.70	30.5	7.5	6.3	18	113	Parallel
8	U11-037	163.90	30.5	6	5.0	18	91	Perpendicular
9	U11-037	164.10	30.5	7.5	6.3	18	113	Perpendicular
10	U11-037	164.45	30.5	8	6.7	18	121	Parallel
11	U11-357	166.70	30.5	3.8	3.2	18	57	Perpendicular
12	U11-357	166.85	30.5	8	6.7	18	121	Perpendicular
13	U11-357	167.05	30.5	7	5.9	18	106	Perpendicular
14	U11-357	167.15	30.5	6.8	5.7	18	103	Perpendicular
15	U11-357	167.25	30.5	6	5.0	18	91	Perpendicular
16	U11-357	167.35	30.5	10.5	8.8	18	159	Perpendicular
17	U11-357	168.10	30.5	7	5.9	18	106	Parallel
18	U11-357	168.52	30.5	6	5.0	18	91	Parallel
19	U11-357	168.30	30.5	10	8.4	18	151	Parallel
AVERAGE				6.9 ± 1.7	5.8 ± 1.4		105 ± 25	

Table C.14 Point load testing results for the footwall structure.

Sample	Box	Depth (m)	D_e (mm)	Load (kN)	$I_{s(50)}$ (MPa)	K Conversion Factor	UCS (MPa)	Orientation wrt Foliation
1	U11-037	174.25	30.5	12	10.1	22	222	Parallel
2	U11-037	174.57	30.5	8	6.7	22	148	Parallel
3	U11-037	174.98	30.5	8	6.7	22	148	Parallel
4	U11-037	175.06	30.5	9.75	8.2	22	180	Perpendicular
5	U11-037	175.42	30.5	11	9.2	22	203	Parallel
6	U11-037	175.65	30.5	4.5	3.8	22	83	Parallel
7	U11-037	176.09	30.5	8	6.7	22	148	Parallel
8	U11-037	176.09	30.5	12	10.1	22	222	Perpendicular
9	U11-037	176.30	30.5	56	47.0			Perpendicular
10	U11-037	176.65	30.5	13	10.9	22	240	Parallel
11	U11-357	176.65	30.5	10	8.4	11	92	Perpendicular
12	U11-357	152.10	30.5	14	11.8	11	129	No Foliation
13	U11-357	152.20	30.5	13	10.9	11	120	No Foliation
14	U11-357	152.30	30.5	10	8.4	11	92	No Foliation
15	U11-357	152.40	30.5	8	6.7	11	74	No Foliation
16	U11-357	152.50	30.5	10	8.4	11	92	No Foliation
17	U11-357	152.60	30.5	8.5	7.1	11	79	No Foliation
18	U11-357	152.80	30.5	9	7.6	11	83	No Foliation
19	U11-357	152.90	30.5	5.5	4.6	11	51	No Foliation
20	U11-357	153.90	30.5	10	8.4	11	92	No Foliation
21	U11-357	154.00	30.5	8	6.7	11	74	No Foliation
AVERAGE				9.6 ± 2.4	8.1 ± 2.0		129 ± 56	

Table C.15 Point load testing results for the orezone structure.

Sample	Box	Depth (m)	D_e (mm)	Load (kN)	$I_{s(50)}$ (MPa)	K Conversion Factor	UCS (MPa)	Orientation wrt Foliation
1	U11-357	169.60	30.5	4	3.4	8	27	Parallel
2	U11-357	169.70	30.5	9.5	8.0	8	64	Perpendicular
3	U11-357	169.80	30.5	8.5	7.1	8	57	Parallel
4	U11-357	169.90	30.5	8.5	7.1	8	57	Perpendicular
5	U11-357	170.00	30.5	5	4.2	8	34	Parallel
6	U11-357	169.40	30.5	5.5	4.6	8	37	Perpendicular
7	U11-357	169.30	30.5	6	5.0	8	40	Parallel
8	U11-357	167.90	30.5	17	14.3	8	114	Perpendicular
9	U11-357	167.50	30.5	15.5	13.0	8	104	Perpendicular
10	U11-357	166.60	30.5	7	5.9	8	47	Parallel
11	U11-357	166.70	30.5	9	7.6	8	60	Perpendicular
12	U11-357	166.85	30.5	12	10.1	8	81	Perpendicular
13	U11-357	167.05	30.5	17	14.3	8	114	Perpendicular
14	U11-357	167.15	30.5	17	14.3	8	114	Perpendicular
15	U11-357	167.25	30.5	13	10.9	8	87	Perpendicular
16	U11-357	167.35	30.5	11.5	9.7	8	77	Perpendicular
17	U11-357	168.10	30.5	12	10.1	8	81	Parallel
18	U11-357	168.20	30.5	11	9.2	8	74	Parallel
19	U11-357	168.30	30.5	10	8.4	8	67	Parallel
20	U11-357	168.40	30.5	13	10.9	8	87	N/A
AVERAGE				10.6 ± 4.0	8.9 ± 3.3		71 ± 26	

APPENDIX D

NUMERICAL STRESS MODELLING

This portion of the appendices provides the figures from the numerical stress modelling performed in ExamineTAB.

Figures D.1 to D.17 provide the induced stress that exists prior to mining each stope.

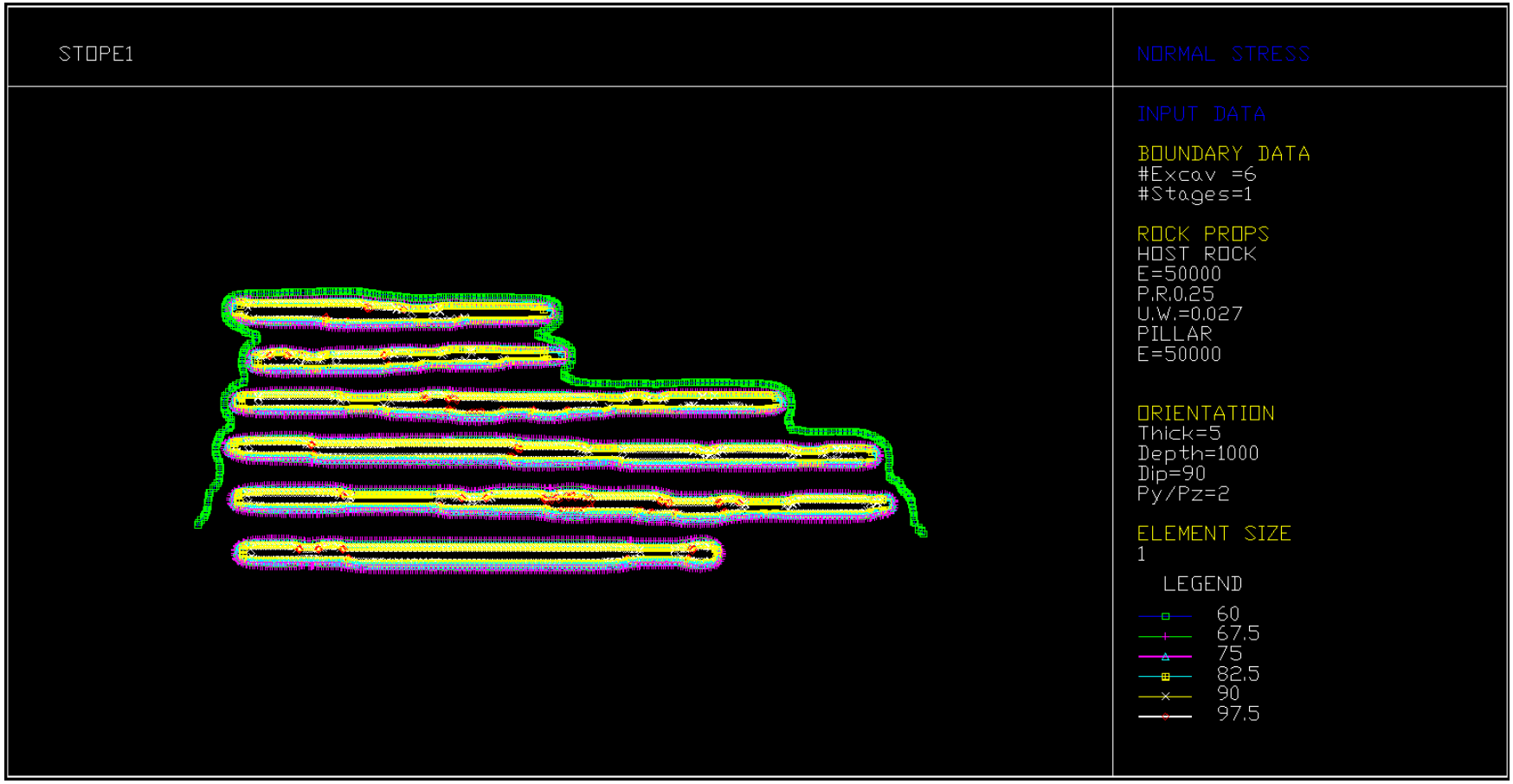

Figure D.1 Induced stresses prior to mining Stope #1.

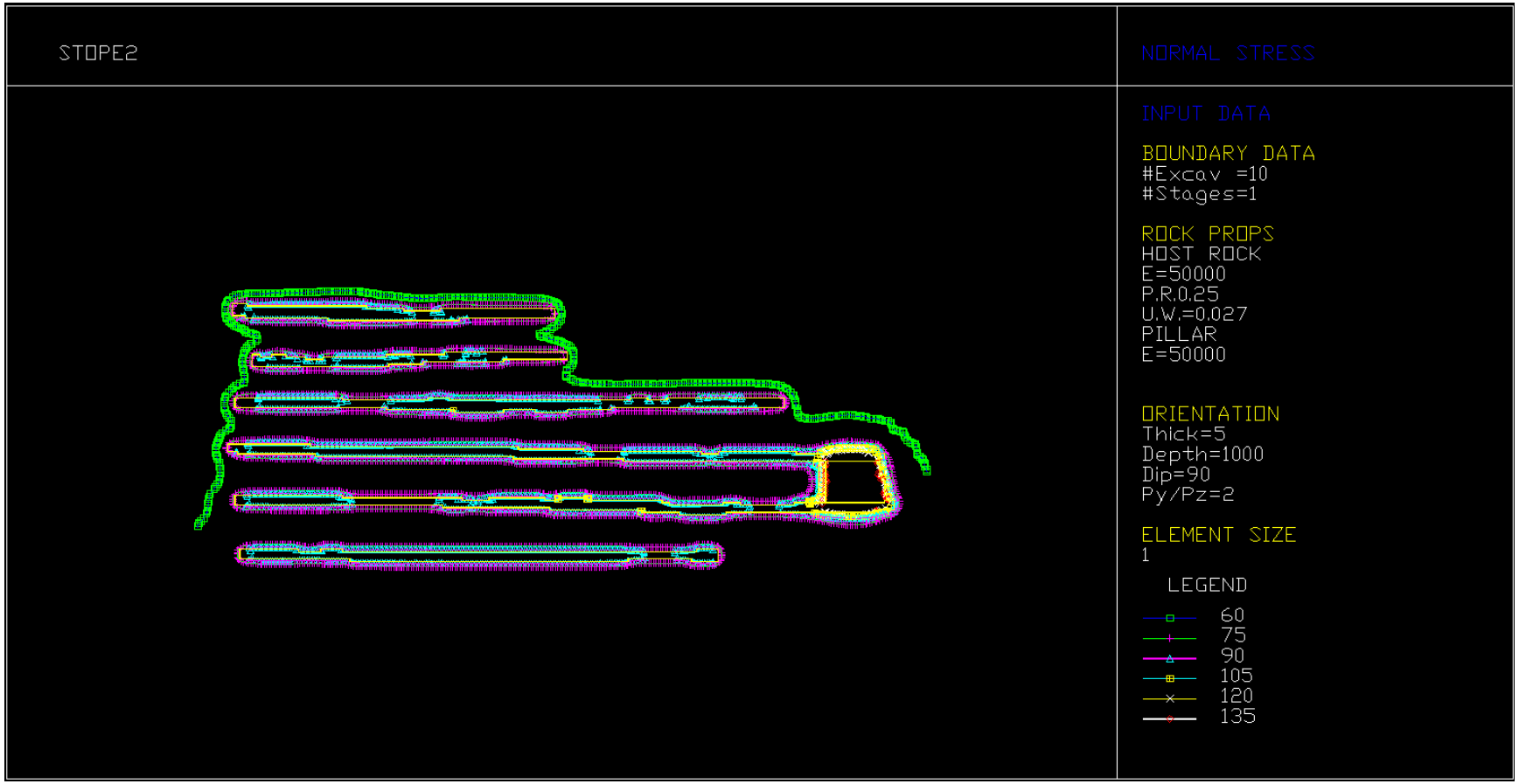

Figure D.2 Induced stresses prior to mining Stope #2.

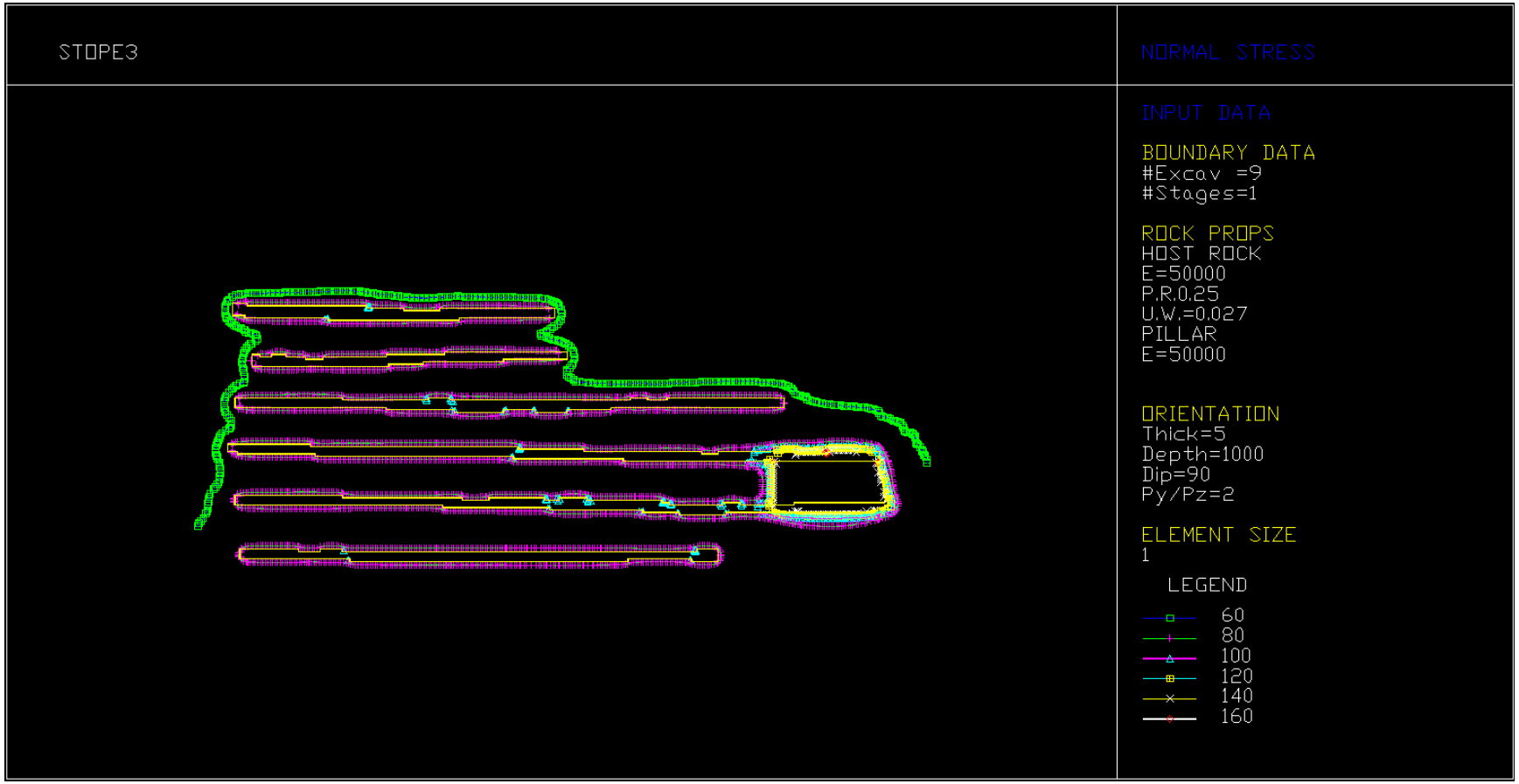

Figure D.3 Induced stresses prior to mining Stope #3.

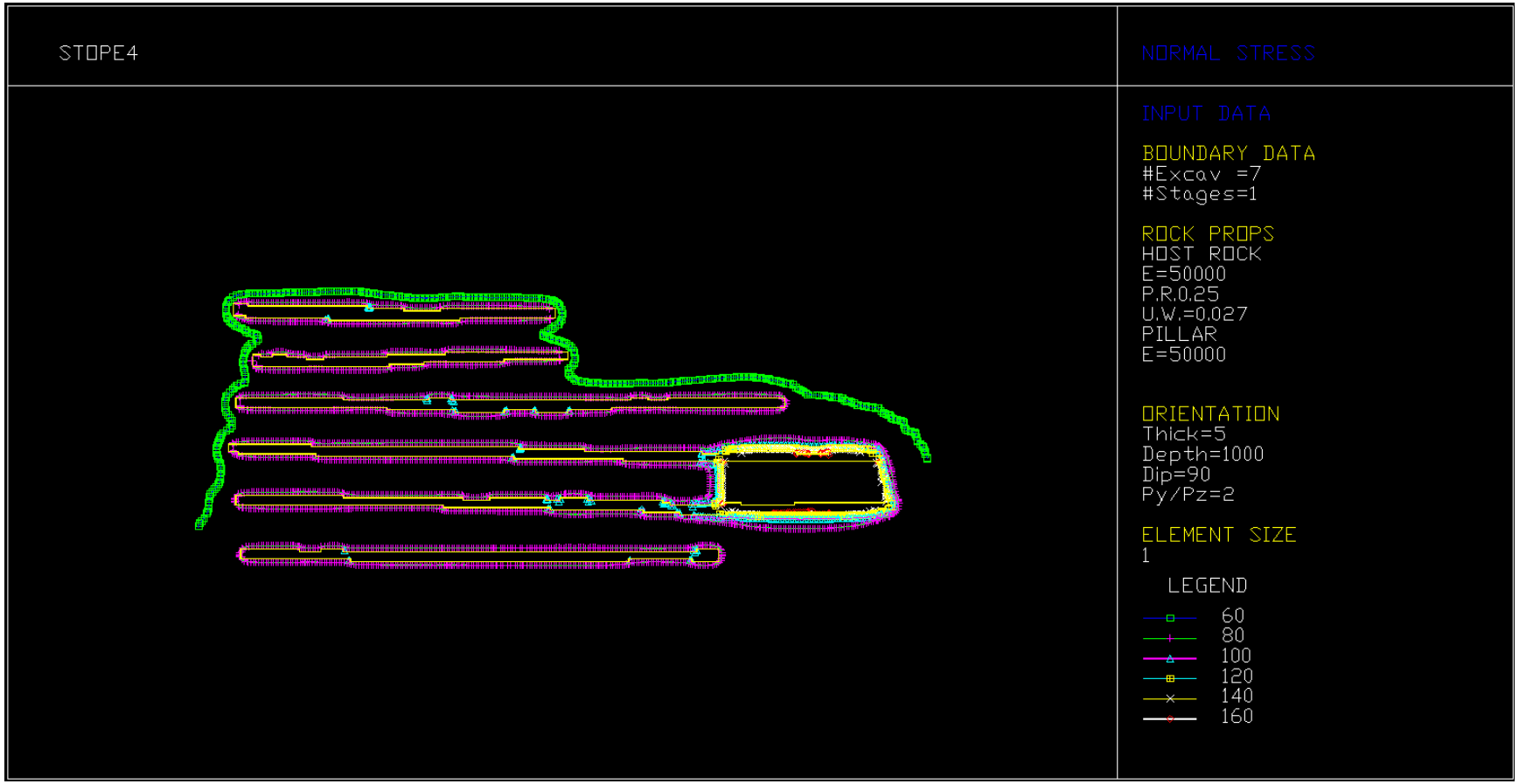

Figure D.4 Induced stresses prior to mining Stope #4.

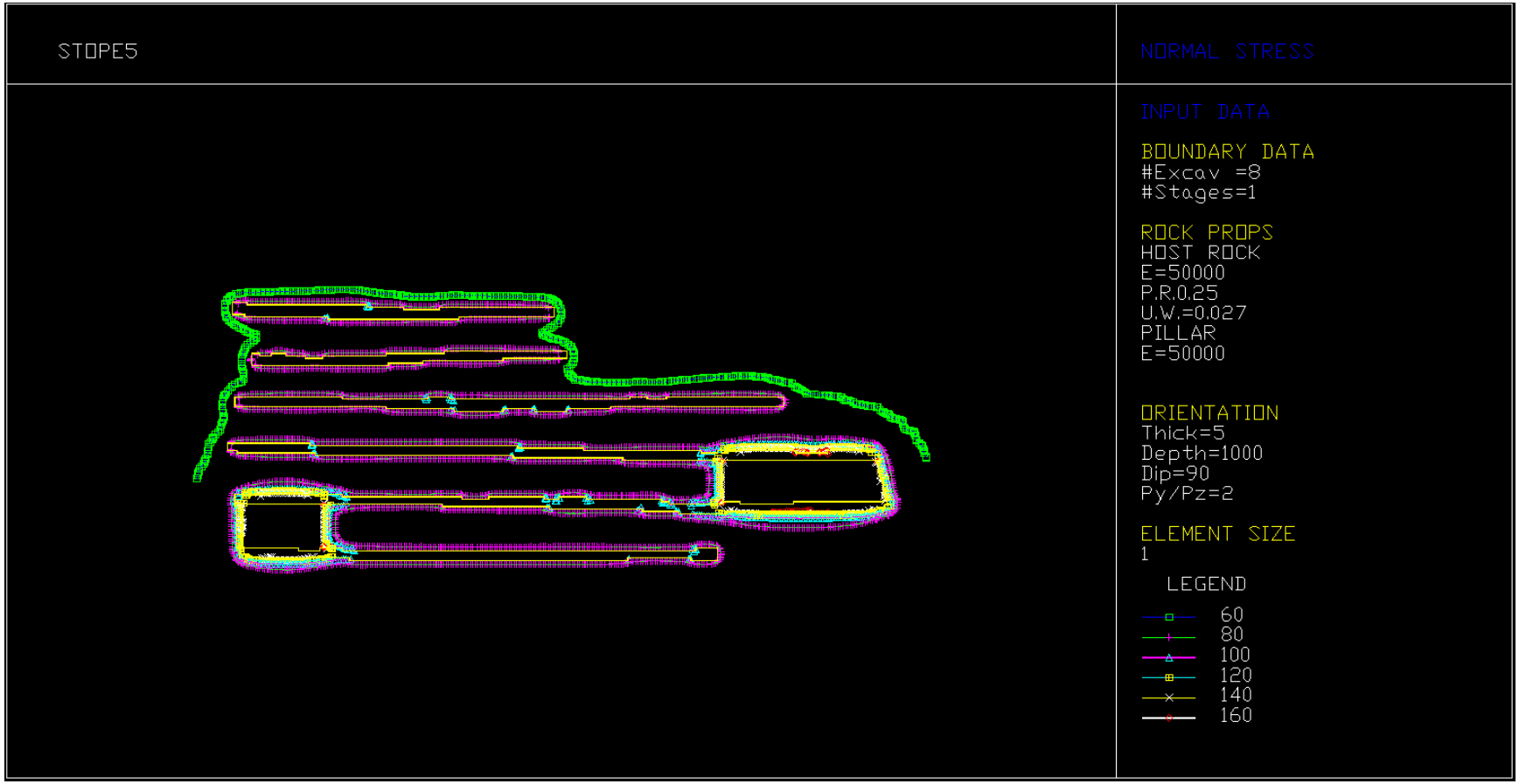

Figure D.5 Induced stresses prior to mining Stope #5.

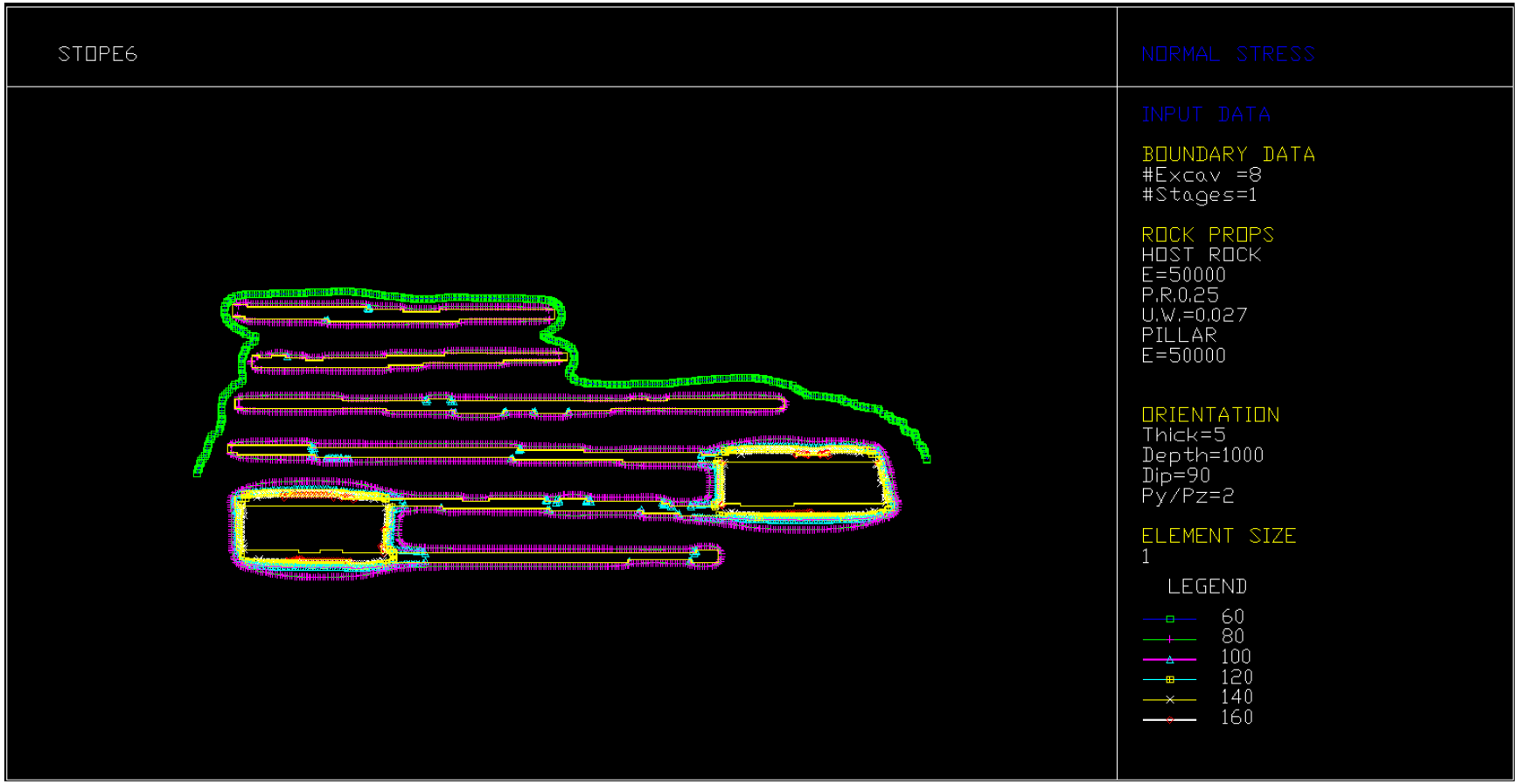

Figure D.6 Induced stresses prior to mining Stope #6.

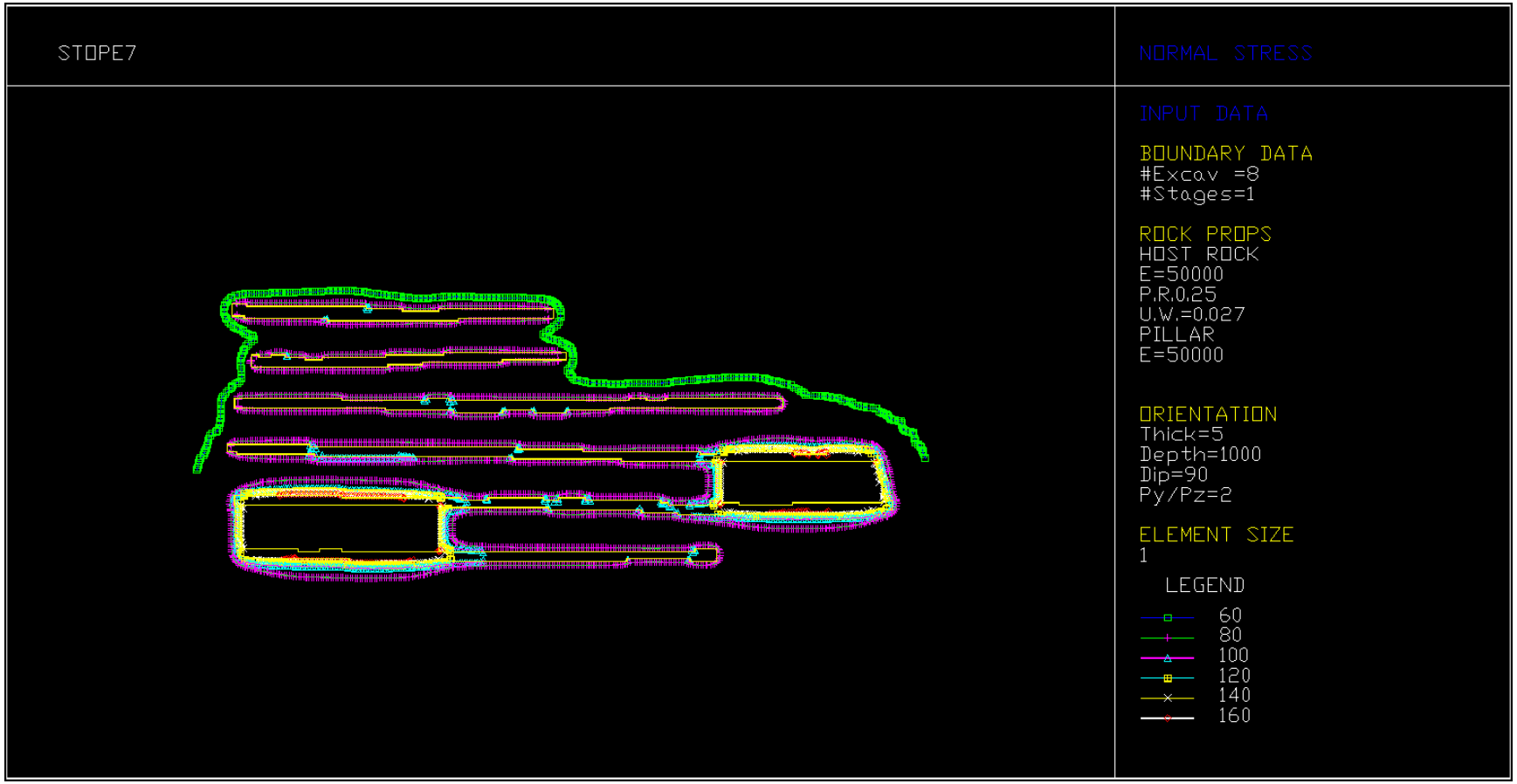

Figure D.7 Induced stresses prior to mining Stope #7.

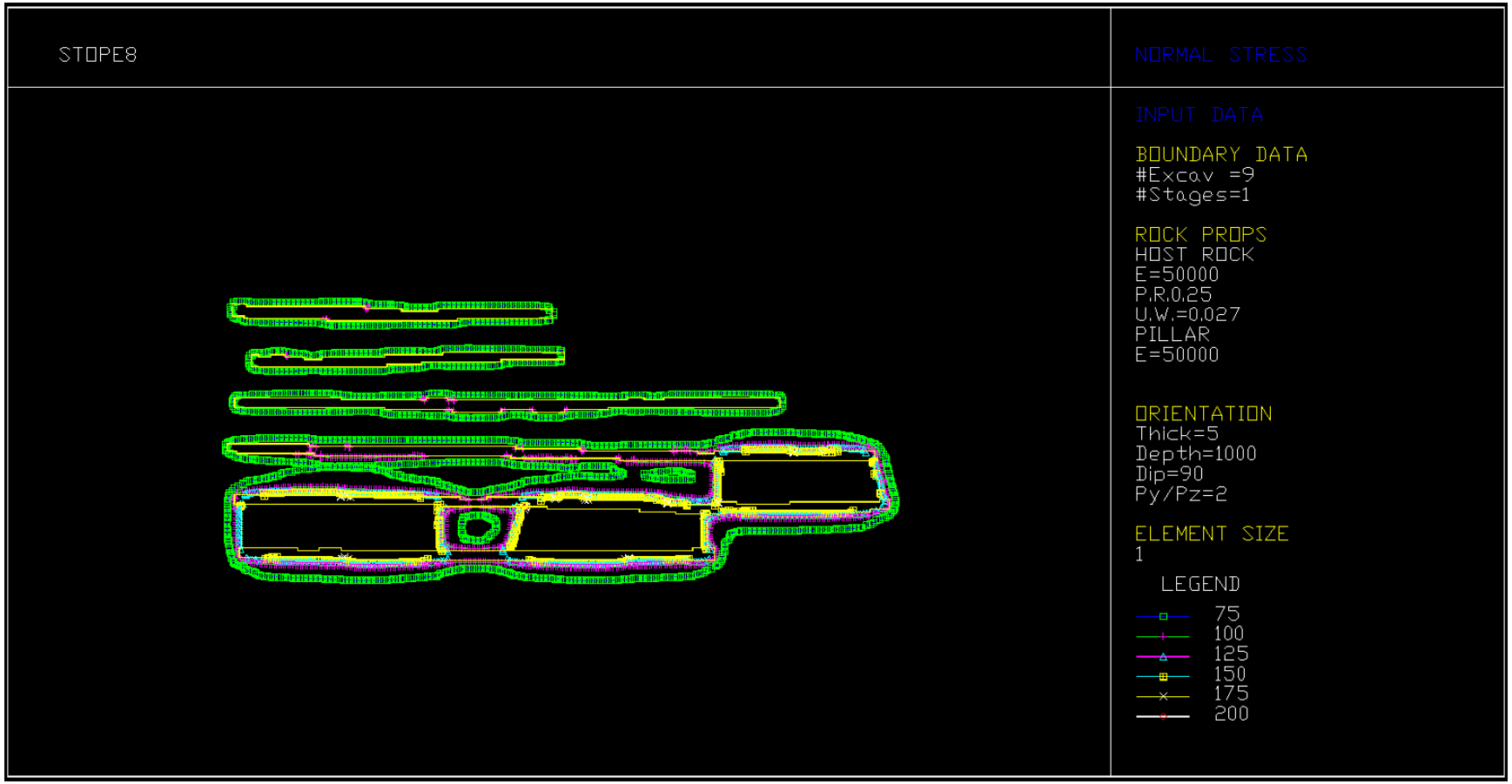

Figure D.8 Induced stresses prior to mining Stope #8.

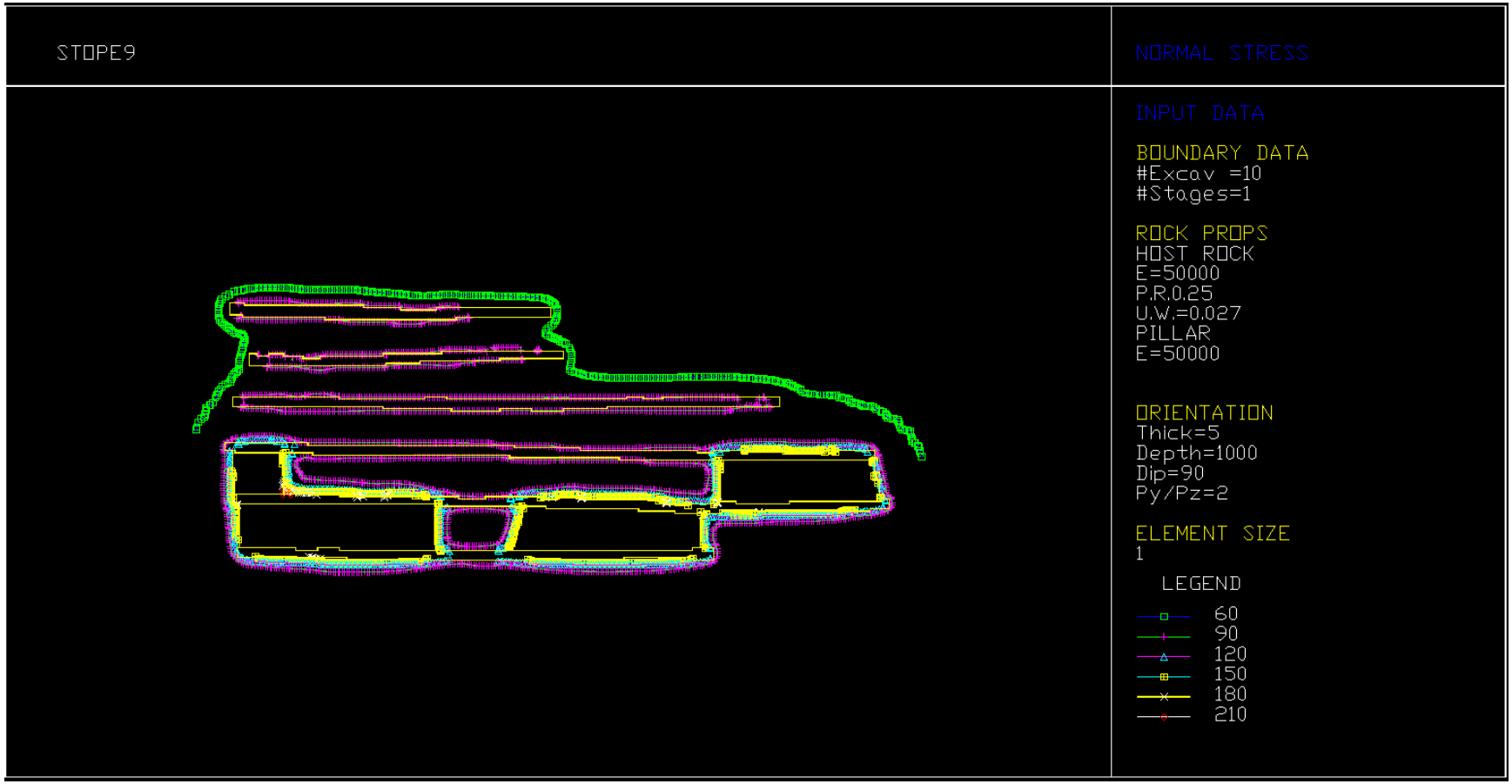

Figure D.9 Induced stresses prior to mining Stope #9.

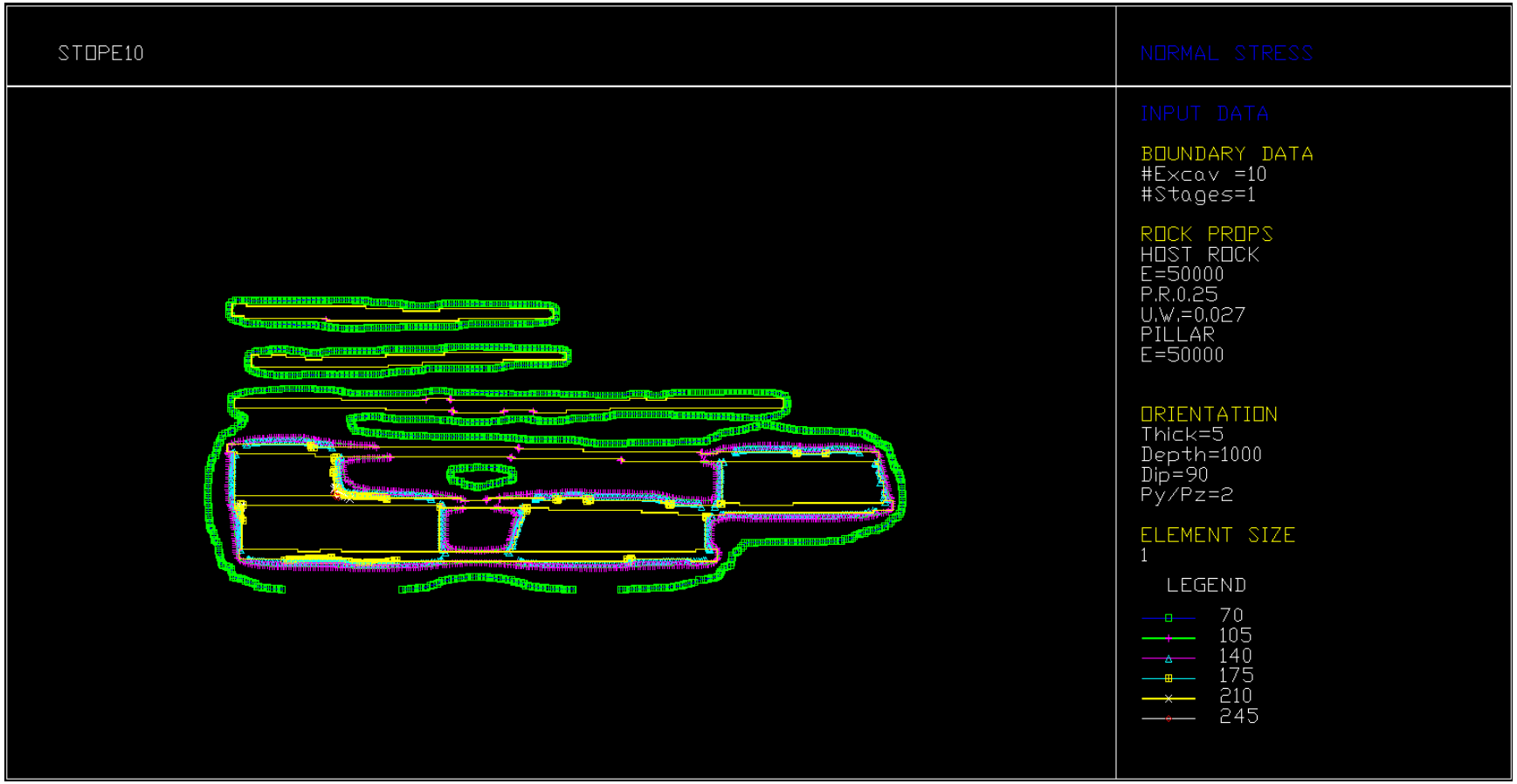

Figure D.10 Induced stresses prior to mining Stope #10.

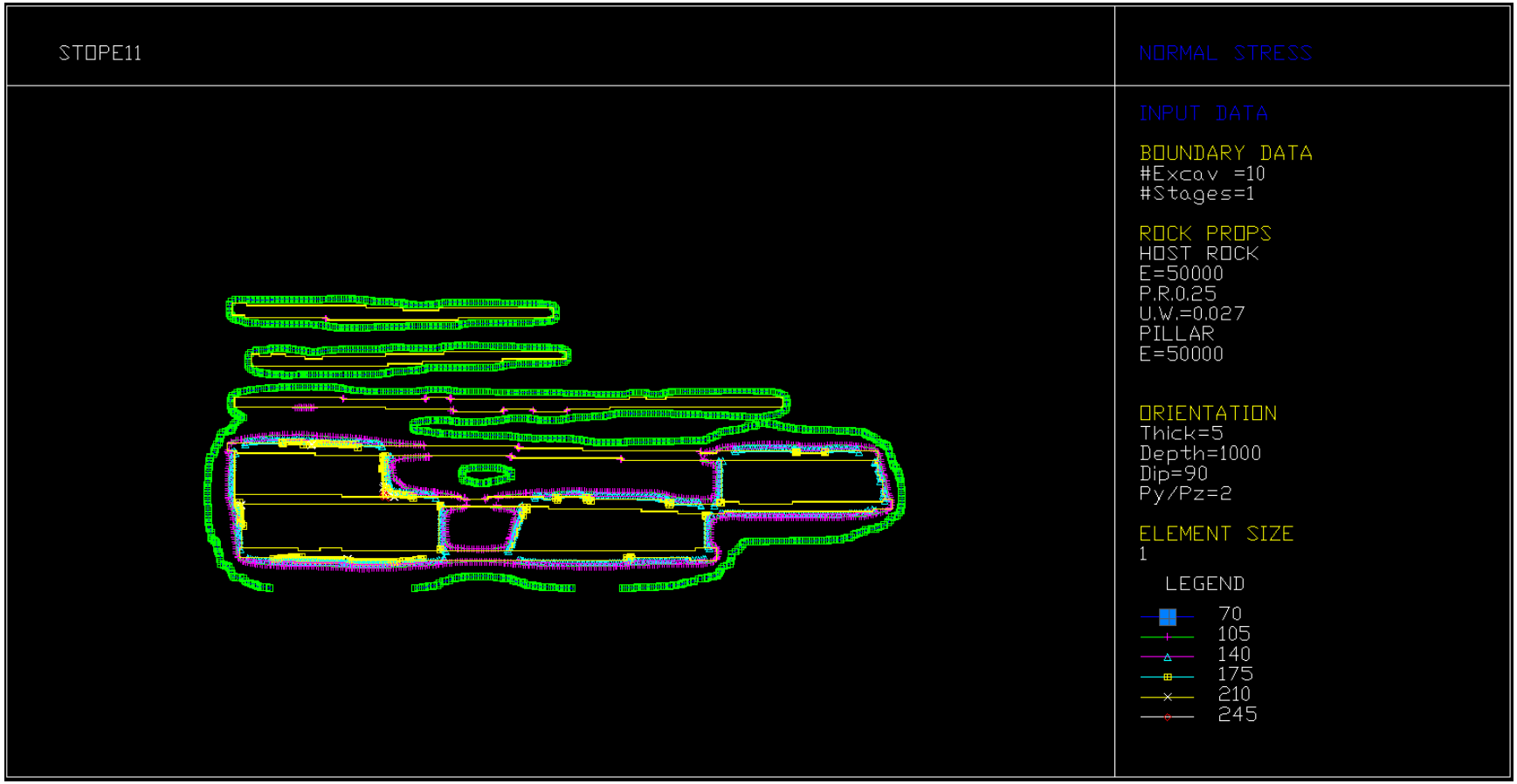

Figure D.11 Induced stresses prior to mining Stope #11.

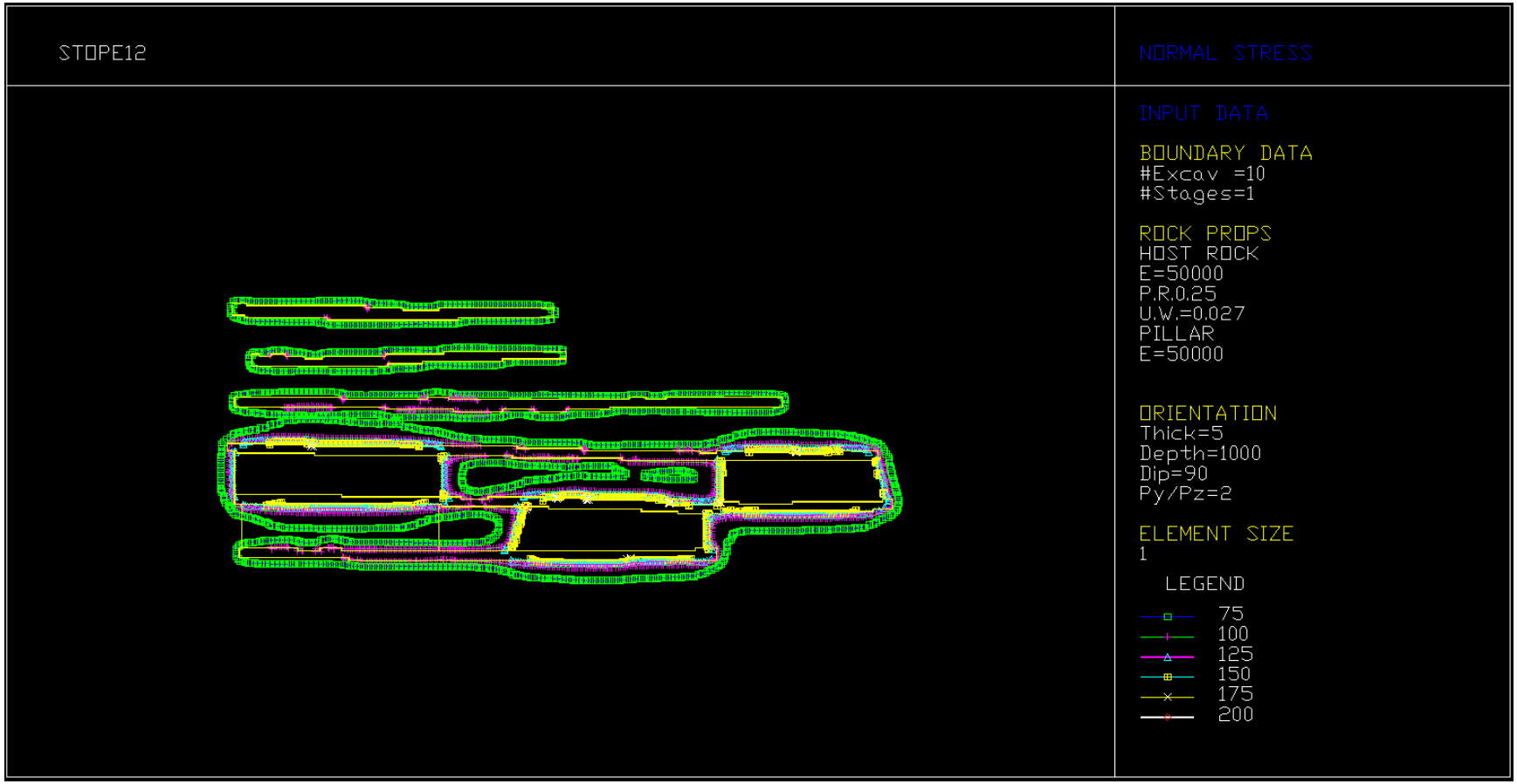

Figure D.12 Induced stresses prior to mining Stope #12.

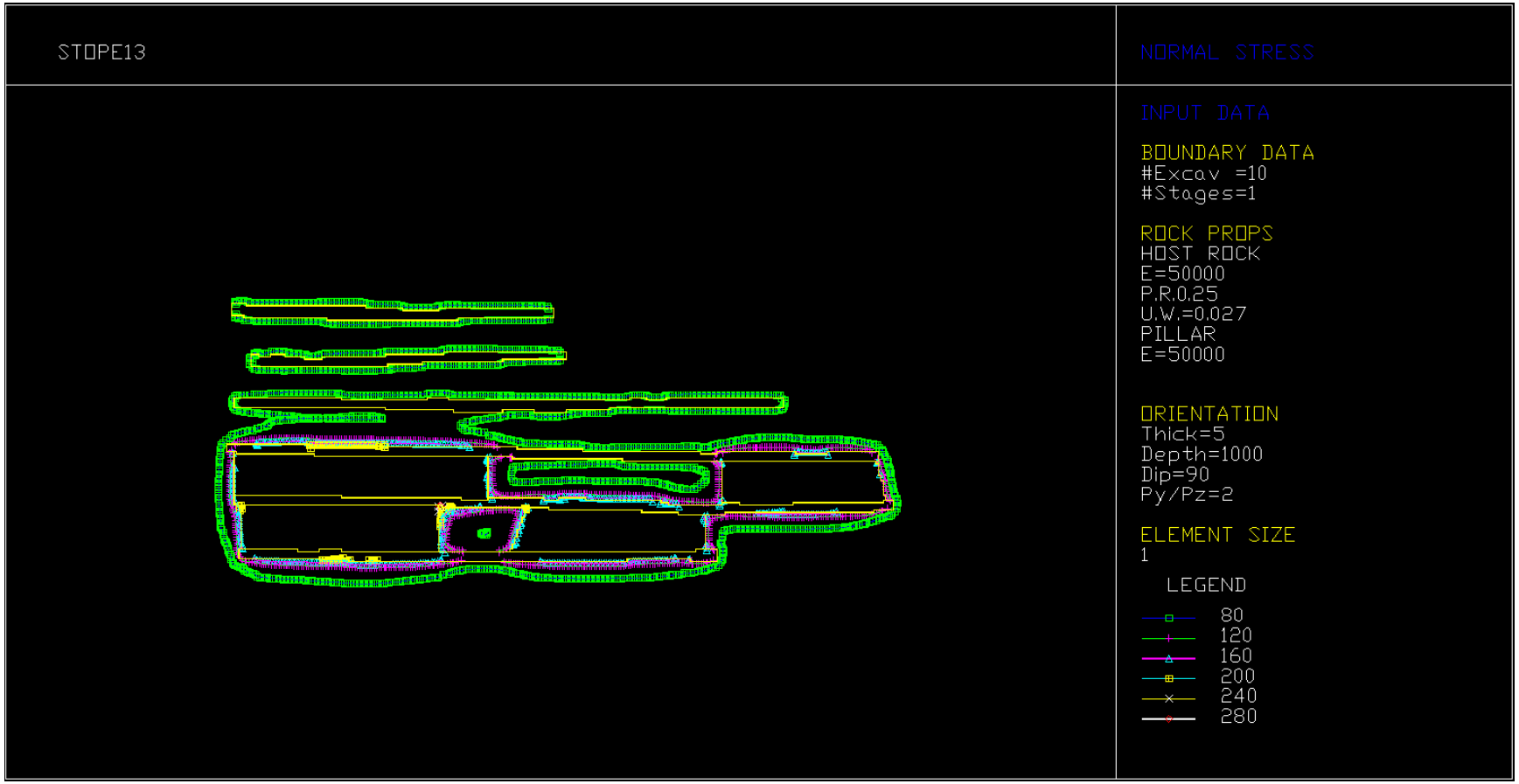

Figure D.13 Induced stresses prior to mining Stope #13.

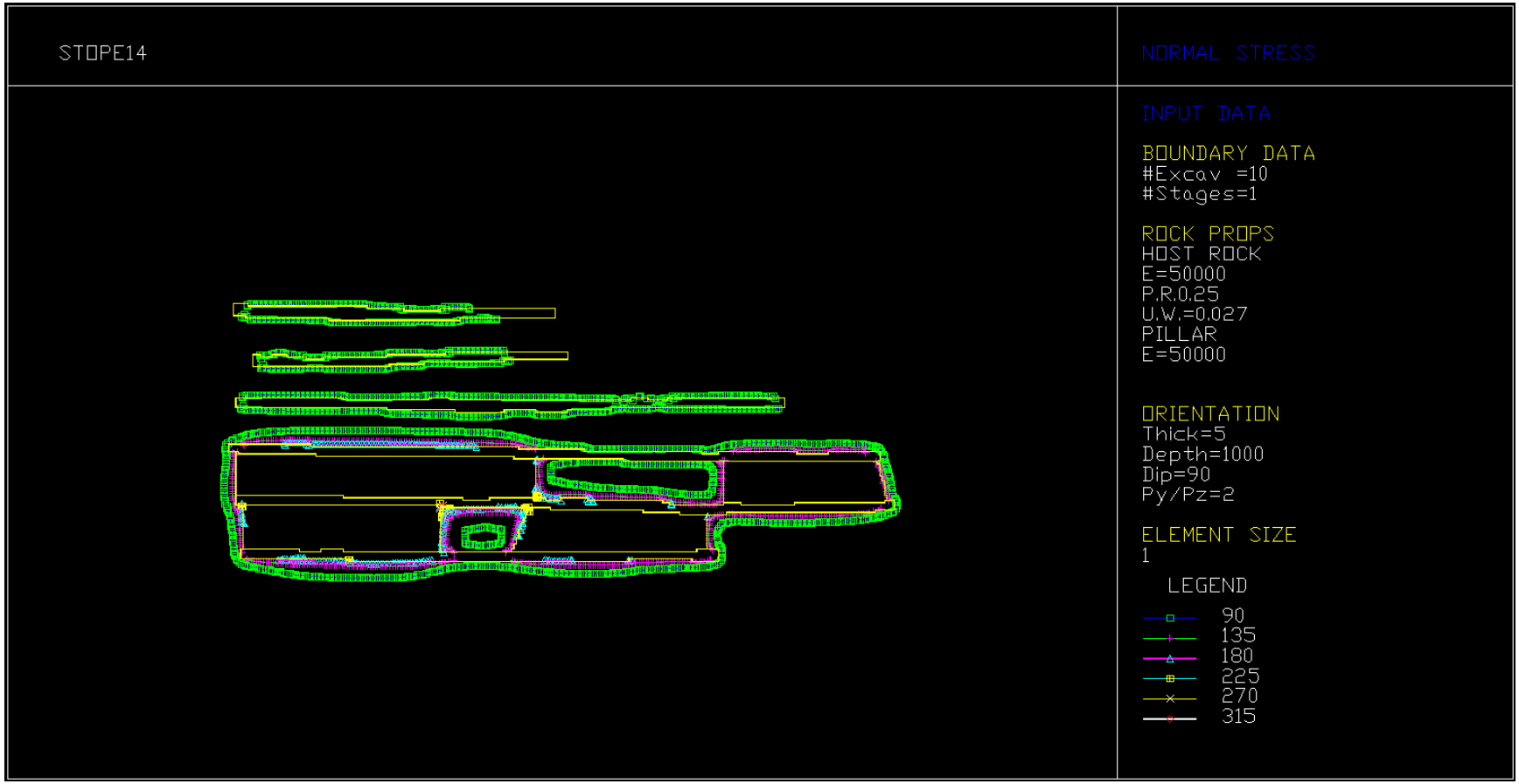

Figure D.14 Induced stresses prior to mining Stope #14.

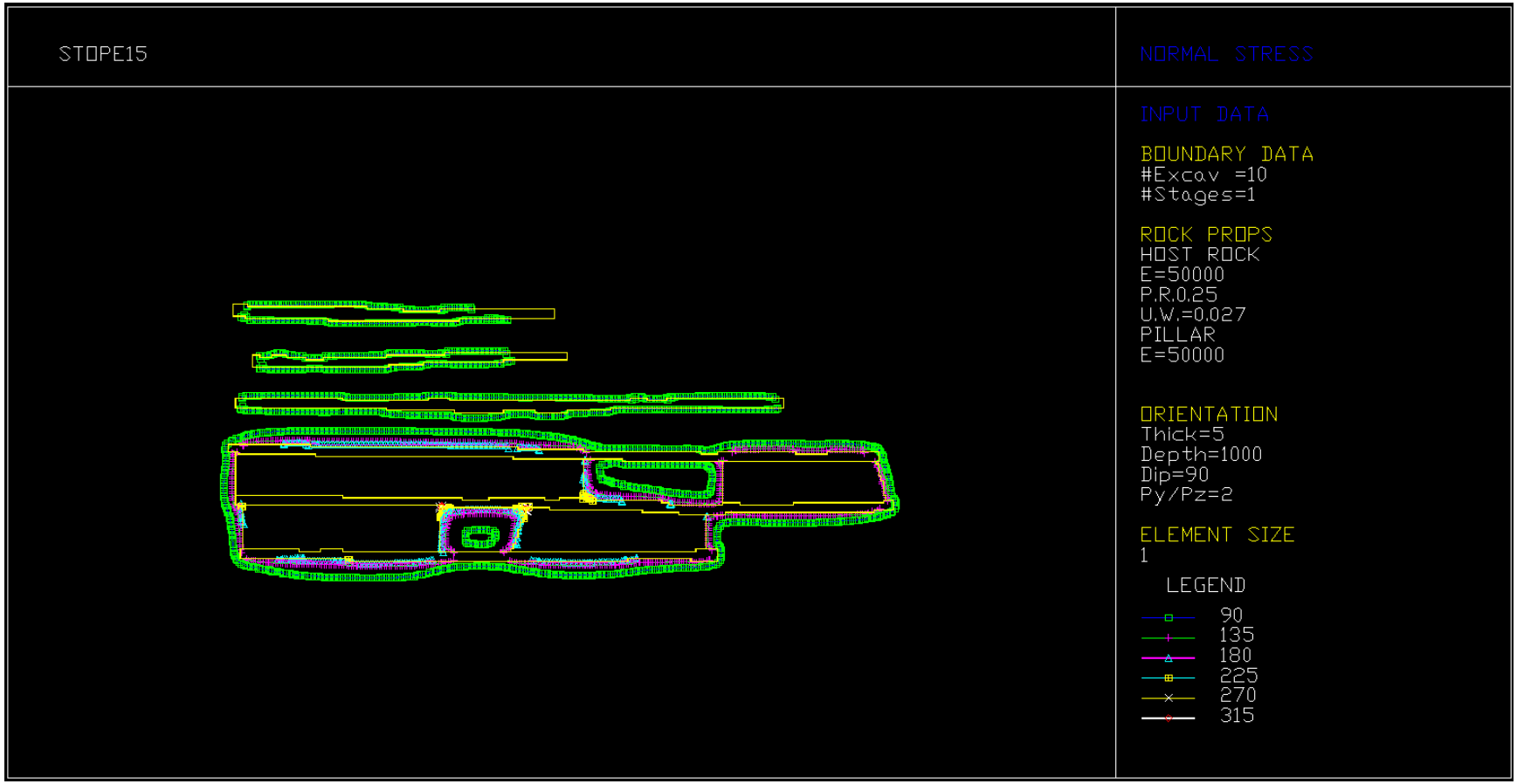

Figure D.15 Induced stresses prior to mining Stope #15.

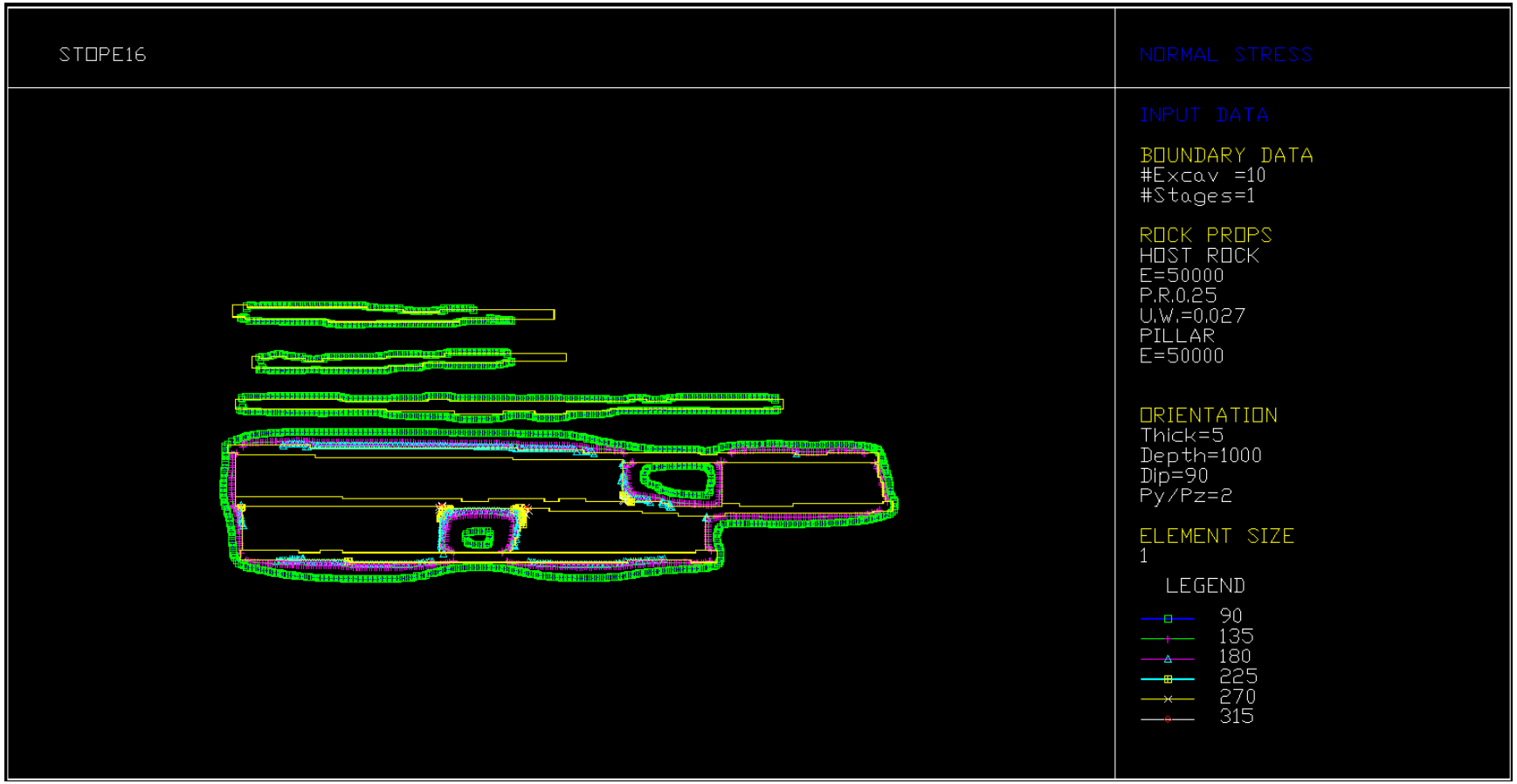

Figure D.16 Induced stresses prior to mining Stope #16.

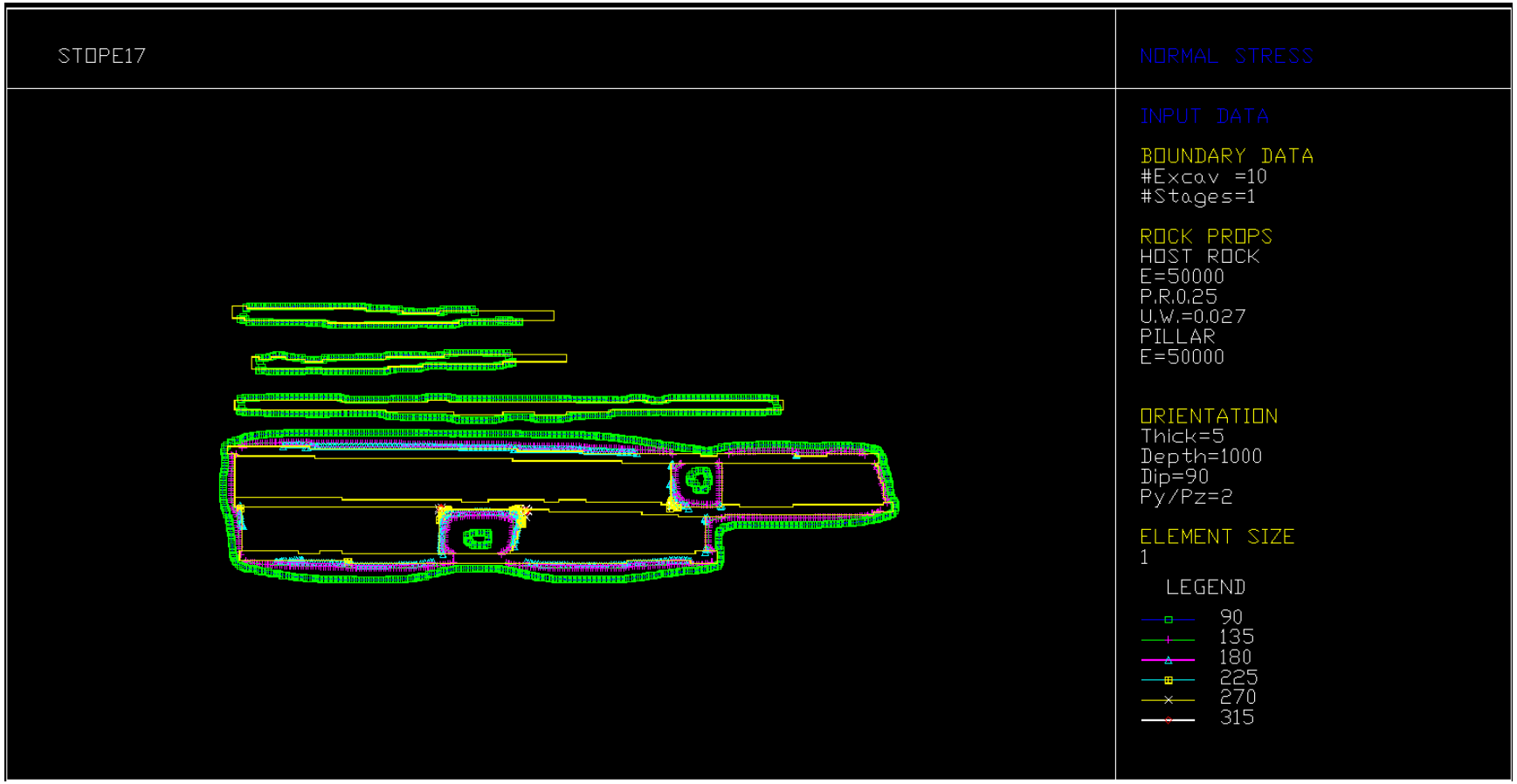

Figure D.17 Induced stresses prior to mining Stope #17.